Analysis of Tool Life for Tungsten Carbide Helical End Mills in Milling Aerospace Aluminum

by

Nevzat Bircan BUĞDAYCI

A Thesis Submitted to the
Graduate School of Science and Engineering
in Partial Fulfillment of the Requirements for
the Degree of

Master of Science
in
Mechanical Engineering

Koc University

August 2013

Koc University

Graduate School of Sciences and Engineering

This is to certify that I have examined this copy of a master's thesis by

Nevzat Bircan Buğdaycı

and have found that it is complete and satisfactory in all respects,

and that any and all revisions required by the final

examining committee have been made.

Committee Members:

____

İsmail Lazoğlu, Ph. D. (Advisor)

____

Demircan Canadinç, Ph.D.

____

Uğur Ünal, Ph. D.

Date: ________________________

ABSTRACT

In today's competitive aerospace and aircraft industries, demand in manufacturing products with high speed, high precision and lower cost is increasing. According to the Airbus reports, number of commertial aircrafts is doubled every 15 years. Milling is one of the major manufacturing processes in producing aerospace and aircraft parts such as all structural parts and jet engine components. In aerospace and aircraft industry, removing of 90-95% of the bulk material with milling is very common to lower the weight of parts. Therefore, milling is perhaps the most critical manufacturing process in these critical parts. Selections of optimal machining conditions and the appropriate tools based on scientific analysis are very critical for high quality part manufacturing with lower cost in shorter cycle times. When machining velocities are increased in order to reduce the process time, machining forces, heat generated and process temperatures all increase. The harsh machining environment accelerates the tool wear. As a result, worn tools generates higher forces and more deformations on parts and tools, may cause bad surface quality and scraped parts, and sometimes may results into catastrophic failures. Along with negative effects on the work safety, machining center and final product, the tool costs are one of the main contributors of the overall cost. Therefore, accurate prediction and optimization of the tool life are very important both from the scientific and industrial perspective.

In this thesis, tool lives of different helical end mills in milling aerospace grade aluminum alloy Al-7050 which is used in structural parts of aircrafts and aerospace systems are investigated experimentally. This research was sponsored by the Turkish Aerospace Industries (TAI). The workpiece material and milling tools are supplied by TAI. In this research, the forces acting during the milling of Al-7050 are modeled using mechanistic calibration technique taking the bottom edge cutting affects into account. The cutting force model is validated with the cutting experiments conducted on multi-axis CNC milling processes in Mori Seiki NMV5000 DCG. Moreover, the heat generated and temperature distributions in the tool geometry are predicted using the mechanic and thermal modeling methods. The thermal model outputs are compared with the available data in the literature and with the infrared thermal measurements performed in the Manufacturing and Automation Research Center. After the temperature field is established, an analysis on wear is performed. The predicted wear values are also compared with the experimental measurement results. The surface roughnesses of the manufactured parts are measured to observe the effect of wear on the finished part. Besides the scientific analysis on milling mechanics and thermal analysis, this research concludes that by selecting appropriate cutting tools and machining conditions significant saving (up to 85%) on tooling cost in industry is possible.

ÖZET

Günümüzün rekabetçi havacılık ve uzay endüstrisinde yüksek hız, yüksek hassasiyet ve düşük maliyette üretime olan talep gün geçtikçe artmaktadır. Airbus'un yayınladığı raporlara göre dünya üzerindeki yolcu uçaklarının sayısı her 15 senede bir iki katına çıkmaktadır. Frezeleme, jet motoru ve yapısal elemanlar gibi birçok uçak parçasının üretiminde kullanılan en yaygın ve önemli yöntemlerden biridir. Havacılık ve uzay endüstrisinde üretilen parçaların ağırlıklarının azaltılması için, kaba malzemenin hacimsel olarak %90-95'inin talaş olarak atılması sıklıkla gerçekleşen bir durumdur. Bu nedenle, en iyi üretim koşullarının ve en uygun kesici takımların seçiminin bilimsel temellere dayandırılması yüksek kaliteli ürünlerin düşük maliyet ve kısa süre içerisinde üretilmeleri açısından elzemdir. Üretim süresinin azaltılması için kesme hızlarının arttırılması ise kesme kuvvetleri, ortaya çıkan ısı ve işlem sıcaklıklarının tümünün artmasına neden olmaktadır. Oluşan bu zor şartlar takım aşınmasını hızlandırmaktadır. Böylece aşınan takımlar daha da yüksek kuvvetler oluşturmakta ve üretilen yüzeyin kalitesini düşürmektedirler. Bunlara ek olarak üretilen parça ve takım üzerindeki şekil bozuklukları ile hurdaya çıkan parça sayısı artmakta ve bazı durumlarda aşınan bu takımlar beklenmeyen ani ve büyük hasarlara yol açmaktadırlar. İş güvenliği, takım tezgâhı ve iş parçasının üzerindeki olumsuz etkilerinin yanı sıra, takım maliyetleri üretim maliyetlerinin önemli bir kısmını oluşturmaktadır. Bu nedenle takım ömürlerinin hassas tahmini ve eniyilemesi hem akademik hem de endüstriyel açıdan önemli bir araştırma konusudur.

Bu çalışmada uzay ve havacılık endüstrisinde yaygın olarak kullanılan Alüminyum 7050 alaşımının frezelenmesinde kullanılan parmak frezelerin ömürleri deneysel olarak incelenmiştir. Çalışma, Türk Havacılık Endüstrisi (TAI)'nin desteği ile gerçekleştirilmiş, kesici takımlar ile iş parçaları TAI tarafından sağlanmıştır. Öncelikle frezeleme sırasında takımların maruz kaldıkları kuvvetler freze alt yüzeyinin de etkileri göz önüne alınarak mekanistik kalibrasyon yöntemi ile modellenmiş ve bu kuvvetler Mori Seiki NMV5000 DCG dikey işleme tezgahında yapılan deneylerle doğrulanmıştır. Daha sonra bu değerler kullanılarak işlem sırasında açığa çıkan ısı ve takım üzerindeki sıcaklık dağılımı hesaplanmıştır. Hesaplanan sıcaklıklar, Koç Üniversitesi Üretim ve Otomasyon Araştırma Merkezi bünyesinde yapılan kızılötesi sıcaklık ölçümleri ile karşılaştırılmıştır. Bir sonraki adımda sıcaklık ve kuvvet bilgileri kullanılarak takım aşınması incelenmiş ve yapılan deneylerle karşılaştırılmıştır. Aşınmanın yüzey kalitesine olan etkisi üretilen yüzeylerin pürüzlülüklerin bakılarak incelenmiştir. Son olarak uygun kesme şartları ve kesici takımlar seçilerek takım maliyetlerinde %85'e varan iyileştirmeler yapılabileceği gösterilmiştir.

ACKNOWLEDGEMENTS

First of all I would like to express my sincere gratitude to my advisor, Prof. Dr. İsmail Lazoğlu for his guidance, encouragement and mentorship throughout my time in Koç University. I am also grateful to him for giving me this opportunity.

I also would like to thank Asst. Prof. Dr. Demircan Canadinç and Asst. Prof Dr. Uğur Ünal for reading this thesis and involving in my thesis committee.

I would also like to acknowledge Turkish Aerospace Industry and Koç University for their support during my graduate study. I am also grateful to KUYTAM and Anadolu University Department of Materials Science and Engineering for sharing their experiences, knowledge and research facilities.

I deeply appreciate my colleagues at the Manufacturing and Automation Research Center; especially Hasan Sinan Bank, Coşkun İslam, Ehsan Layegh, Suat Cömert, Ali Mamedov, Erdem Kundakçıoğlu and Mr. Muzaffer Bütün for all the things and time we shared.

I am also very grateful to Bige Deniz Ünlütürk, Buket Baylan, Ayten Bilgin and Serkan Külah for all the time and fun we had together.

Last but not the least; I am deeply grateful to my mother Kafiye, my brother Alican and my father Hidayet, for their endless love and support. This thesis is dedicated to them.

TABLE OF CONTENTS

LIST OF TABLES

LIST OF FIGURES

NOMENCLATURE

F	Total cutting forces
$F_B \quad F_S$	Total cutting forces acting on the bottom and side edge
θ	Angular position
i	Number of flutes
j	Number of axial disk elements
$dF_{S,T}, dF_{S,R}, dF_{S,Z}$	Differential cutting forces acting on the side edge in tangential, radial and axial directions
$dF_{B,T}, dF_{B,R}, dF_{B,Z}$	Differential cutting forces acting on the bottom edge in tangential, radial and axial directions
$K_{Sc,T}, K_{Sc,R}, K_{Sc,Z}$	Tangential, radial and axial cutting coefficients for side edge
$K_{Bc,T}, K_{Bc,R}, K_{Bc,Z}$	Tangential, radial and axial cutting coefficients for bottom edge
$K_{Se,T}, K_{Se,R}, K_{Se,Z}$	Tangential, radial and axial edge coefficients for side edge
$K_{Be,T}, K_{Be,R}, K_{Be,Z}$	Tangential, radial and axial edge coefficients for bottom edge
h_S, h_B	Side and bottom uncut chip thicknesses
w_S, w_B	Side and bottom widths of cut
A_p	Axial depth of cut
fpt	Feed per tooth
V_w, V_s, V_c	Cutting velocity and its components on the shear plane and rake face
F_s, F_f	Shear force and frictional force between tool rake face and chip
α_n	Normal rake angle

β_n	Normal friction angle
η, i	Chip flow angle and inclination angle
c, k, ρ	Specific heat capacity, thermal conductivity, mass density
α_r	Orthogonal rake angle
χ	Proportion of shearing heat entering into the workpiece
B	Proportion of frictional heat entering into the tool
τ, ϕ_n	Shear stress and shear angle
l_{cn}	Chip contact length
l	Shear plane length
$\dot{Q}_f, \dot{Q}_s$	Frictional and shearing heat generated
F_s, F_f	Force component on the shear plane and tool rake face

Chapter 1

INTRODUCTION

With the rapidly developing technologies, manufacturing field experienced major advancements in the recent years. On one side, with the progresses in the materials science, enhanced alloys that exhibit a variety of characteristics are introduced. Accordingly, advanced cutting tool materials and coatings are developed to machine these enhanced alloys. On the other side, larger, faster and more powerful machining centers are built every day. Limiting capacities of equipments used in machining are improving steadily. Thus, novel models are being suggested for modeling these improved materials' behaviors under recent cutting conditions.

Aerospace grade aluminum alloy Al-7050-T7451 is one of the critical materials for airplanes and spacecrafts. It is an Al-Zn-Mg-Cu high strength alloy and was developed by J.T Staley and co-workers at Alcoa in 1971 [1]. Having great resistance to high fatigue and corrosion, Al-7075 has higher Zn (5.7-6.7%) and Cu (2-2.6%) contents than its predecessor and contains Zr (0.08-0.15%) in place of Cr [2]. It is especially suitable for thicker parts where lower quenching rates are unavoidable. Having Zr instead of Cr reduces the strength loss with decreasing quench cooling rates since it acts as high-temperature precipitate-forming addition. Instead of containing Cr which may form $Al_{12}Mg_2Cr$ or Mn which may form $Al_{20}Cu_2Mn_3$, Zr does not combine with principal alloying elements and presents in spherical compact particles. These modifications improve fracture toughness and avoid stress corrosion cracking which is crucial for aircraft industry.

On the other hand, cemented tungsten carbide is first introduced in 1923 by Karl Schröter in Germany [3]. Schröter was working for Osram Lamp Works of Berlin and the company was searching for a substitute material in order to replace the diamond dies used for drawing of electric lamp filaments. This substitute was named Hartmetall until the name cemented carbide was suggested by General Electric researchers. Later Friedrich Krupp, A.G. Essen, obtained the patent rights and developed Widia (Wie Diamant - Diamond like) which is the ancestor of modern cemented tungsten carbide [4]. Today tungsten carbide is widely used in production of cutting tools because of its unique abilities. It has high toughness and hardness, and also maintains its hardness at elevated temperatures which is useful in cutting applications. Besides, it resists deflections and has high compressive strength making it the most preferred material for cutting tool applications.

Up to here the material side of the cutting process is discussed. However, the process parameters such as cutting type, cutting speeds and feed rates etc. are equally crucial in machining. There are various cutting types such as turning, milling, boring, drilling, etc. Each one of them serves for a specific purpose and has its parameters accordingly. Milling is one of the most widely used and versatile cutting type. It is defined as machining operation in which a workpiece is fed past a rotating cylindrical tool with multiple cutting edges. By its nature milling is an interrupted cutting operation; the cutting edges enter and exit workpiece during each revolution. It is believed that milling machines are evolved from rotary filing practices to reduce the effort and time spent hand filing. Initially manually controlled, milling machines experienced a revolution in early 1950's with a research conducted in MIT. At first, a numerical control machine and its controller were designed in 1949 in Gordon S. Brown's Servomechanisms Laboratory and then computer control is integrated into this system in 1959 [5]. This machine is considered as the ancestor of computer numeric control (CNC) machines we use today. Today as the controllers and computers develop, impossible spindle speeds and feed rates for the past are being used in workshops. As the cutting speeds increase, such as in high speed cutting operations, the cutting environment becomes harsher and the tool is subjected to cycles of impact forces and thermal shocks during the operation.

By definition, high speed cutting is defined as cutting with speeds that are higher than the ones used in conventional machining operations [6]. High speed machining is favored in industry since it lowers the process time, but due to the increased forces and temperatures machine tools wear out sooner or tool breaks during cutting. Therefore, developing a wear model and predicting the tool life is a significant research topic. One can use such a model to replace the tool to prevent a catastrophic failure or use this model to simulate different conditions in virtual environment and to improve the overall performance.

In this work, the mechanics of milling Al-7050 alloy with cemented carbide helical end mills is studied. First, the cutting forces are modeled including the bottom edge cutting effect. Then the heat generated during the cutting operation is calculated using these forces and fed as an input for the finite element model which calculates the temperature field for the tool geometry. Then using the temperature field data and the material properties an empirical equation describing the wear is solved for the flank face. Finally, the tool lives are calculated and the outputs of the model are validated with the wear tests performed.

The thesis is organized as follows;

Chapter 2 covers the background information and literature review on force prediction, temperature calculations and wear estimations. Initially, the models that predict forces are reviewed. Then, analytic and numeric temperature models are compared for temperature calculations. Finally, present wear models in the literature are covered. The past and present trends along with the outcomes of the models are discussed.

In Chapter 3, the mechanics of end milling operation is explained, emphasizing the mechanistic calibration method for the bottom edge cutting effect. The detailed methodology for this approach is given here.

Thermal modeling of milling process is discussed in Chapter 4. The outcomes of the force model are used as inputs in calculating the tool's temperature field. Validation of this model is presented using the temperature data available in the literature.

In Chapter 5, the effect of cobalt concentration in cemented carbides on tool wear in cutting Al-7050 is discussed. Using the temperature data and material properties an empirical relation for the tool wear is obtained. Chapter is concluded with the experimental verification of the relation.

Chapter 6 shows the industrial applications of this thesis by summarizing the industry academy collaboration project between Koc University Manufacturing and Automation Center (MARC) and Turkish Aerospace Industry (TAI).

Finally in Chapter 7, the thesis is concluded with a brief summary and future research directions.

Chapter 2

LITERATURE REVIEW

Accurate and fast estimation of the tool life is a critical part in production planning. By ISO 3685:1993 standard, tool life is related to the tool wear such that a tool is accepted to complete its life when the maximum crater depth reaches 300 microns in the flank face [7]. Therefore, tool life estimations are based on determining the wear on the flank face. There are various types of wear mechanism that can occur simultaneously or individually during a machining operation such as abrasion wear, adhesion wear, diffusion wear, etc. In order to eliminate the complexity of the wear problem the modeling is divided into smaller analyzes. Initially the forces created during the cutting process should be evaluated. Using these force values and the friction relations between the materials, the heat generated in the cutting region is estimated. This heat results in the formation of a temperature field on the tool. The temperature field is significant since the material properties are temperature dependent. Finally, using the stresses acting on the tool and the tool temperature values tool wear is estimated.

In this chapter a review of the literature relating to this study of tool life estimation is presented. This section will be divided into three subsections:

1. Cutting force modeling in machining processes

2. Temperature prediction models

3. Wear estimation models.

2.1 Cutting force modeling in machining processes

Studies towards production planning and prediction of the cutting forces during the machining operations are popular research topics for a long time. Fred W. Taylor [8] states that their investigations started around 1880s to answer the 3 questions that must be answered each day in every machine shop: "What tool shall I use? What cutting speed shall I use? What feed shall I use?".

In 1944, Merchant presented a mathematical analysis of the mechanics and geometry of the metal cutting process in his milestone work "Basic Mechanics of the Metal-Cutting Process" [9]. He based his analysis on fundamental quantities such as strain, shear rate, friction between tool and chip, the metal's shear strength, plastic deformation, etc. He investigated two main cases, namely, orthogonal cutting in which a straight-edged tool moves into workpiece perpendicular to tool's cutting edge and oblique cutting in which there is an angle between the cutting edge and the direction of relative motion between the tool and the workpiece.

These two cases became the topic of research for many scientists. Armarego [10] studied the "classical" orthogonal and oblique operations with the thin shear zone (plane) assumption. This idea of a single shearing plane simplified the complexity of the equations and made it easier to relate the forces and power in machining to the variables such as tool geometry, cut geometry and workpiece material.

Altintas summarized the work until now in his book titled as "Manufacturing Automation" in 2012 [11]. In this book he gave detailed explanations to the mechanics behind the cutting process, process modeling and chatter vibration. For force prediction of milling operations the tool is divided into differential disc elements and the contribution of each element to the cutting forces is evaluated. These differential forces are assumed to be linearly dependent on the uncut chip thickness. This linear dependency is described by edge and cutting coefficients.

Shamoto and Altintas [12] proposed a new shear angle prediction theory for oblique cutting operations. In this work, the mechanics of the oblique cutting are described by five expressions where three of these expressions can be derived from the kinematics of oblique cutting. The authors propose the application of maximum shear stress or minimum energy principle to solve for the remaining two. This approach allows the use of only the material properties, tool geometry and laws of deformation and do not require any empirical assumptions unlike the previous solutions.

Soldani [13] et al proposed an analytical approach to model orthogonal cutting process. The model calculates the forces using the plastic deformation characteristics of the material such as strain rate sensitivity, strain hardening and thermal softening. The model assumes the deformation occurs on a single thin band and the analysis is limited to stationary flow.

They also modeled the temperatures by applying a temperature dependent friction law at the tool-chip interface. The model is tested for different cutting conditions.

Mabrouki [14] et al studied the dry cutting of aeronautical aluminum alloys. They based the material behavior and failure criteria on Johnson-Cook law for the solution of the numerical problem. This model connects the material damage evolution and its fracture energy. Their numerical solution shows that the reasons behind the bending loads on the chip are due to the chip-workpiece contact and tool advancement. Also they concluded that there is a fragmentation phenomenon taking place above the rake face corresponding to the location where chip begins to curl up. Besides, this model can predict the residual stress distribution along the cut direction on the machined surface. The results were then compared with the experiments and a good correlation is observed.

Ehmann [15] et al summarized the work done in the modeling of dynamic metal cutting field. A general view of the evaluation of the modeling approaches are given along with the detailed examples on experimental, mechanistic, numerical and analytical methods.

Tuysuz and Altintas [16] presented a mechanics model for prediction of the cutting forces in feed, normal and axial directions. They modeled the chip thickness distribution, and cutting and indentation mechanics. The indentation of the cutting edge into the material is modeled analytically using elasto-plastic deformation of the work material. The geometry of indentation zone and the distribution of chip thickness are calculated taking the five-axis motion of the tool into account. This approach improved the prediction of axial forces to be more precise, which is also demonstrated over the cutting experiments conducted.

Engin and Altintas [17] generalized the mathematical model of most helical end mills used in the industry. After the end mill geometry is modeled by helical flutes wrapped around a parametric envelope, the coordinates of a cutting point along the parametric helical flute are mathematically expressed. Using these expressions, the chip thicknesses at each cutting point is evaluated including the vibrations of both cutter and workpiece. By summing the effect of these cutting points along the cutting edges, the cutting forces and vibrations for an arbitrary end mill can be predicted. The predicted and measured cutting forces, surface roughness and stability lobes for various types of mills are compared.

Shih-Ming Wang [18] proposed an improved dynamic cutting force model for end-milling operations. Instantaneous shear plane area and cutter geometry, vibration and friction between the tool and the chip is taken into account. A theoretical–empirical method for the determination of the parameters for cutting force calculation was proposed.

Li [19] et al proposed a new approach for modeling and simulation of the cutting forces in helical end milling processes. They modeled the cutting forces by discretizing each tool of a helical end mill into a number of slices along the cutter axis and predicted the machining characteristic factors from fundamental material properties, tool geometry and cutting conditions. Effect of each slice is modeled as an oblique cutting process. The total cutting forces are obtained as the sum of the forces at all the cutting slices of all the teeth. A windows based simulation system for the cutting forces in helical end milling is developed using the model. Experimental milling tests have been conducted to verify the simulation system.

Wan [20] et al proposed a simplified model for the calibration of cutting force coefficients and cutter runout parameters for cylindrical end milling using the instantaneous cutting forces measured instead of average ones. In this model, the cutting force coefficients are expressed as the power functions of instantaneous uncut chip thickness instead of a linear function. The novelty of this model is that the forces are calibrated directly for tangential, radial and axial components. Also a single cutting test is sufficient to calibrate for a wide range of cutting conditions.

Azeem [21] et al focused their work on a simplified method for the determination of cutting force coefficients in ball-end milling. They present a new method which requires a single half-slot cut for the calibration of coefficients that are valid over a wide range of cutting coefficients. Since the instantaneous cutting forces are used with the known helical cutting edge profile on the ball part of the mill, this method allows successive determination of the discrete values of the varying cutting mechanics parameters along the cutter axis. The effectiveness of the method is demonstrated experimentally with a series of verification tests.

Hamade [22] et al proposed a novel approach for the determination of the cutting constants. In their model instead of doing a large number of calibration tests to cover a wide range of cutting speeds, feed rates and rake angles, performing a small number of drilling tests are proposed. By using the changing cutting geometry along the drills cutting lip this method covers a wider range in a single test. The coefficient obtained from this method is compared with the coefficients from the orthogonal tests.

Fang and Wu [23] investigated the effect of tool edge geometry in machining forces and proposed a new slip-line model for chip formation in machining with chamfered tools. They compared the chamfered and honed tool edges and measured the forces during cutting operation with both of the tool types experimentally. They concluded that the uncut chip thickness value is close to the tool edge dimension. The experiments were conducted on three aluminum alloys 7075-T6, 6061-T6 and 2024-T351 and a good agreement between the model and experiments were reached.

Wan and Wei [24] systematically studied the peripheral milling process modeling with cutter runout. They focused on the calibration of the cutting force coefficients in the presence of cutter runout. They presented five different methods in detail. In two of the methods the cutting force coefficients are assumed to be functions of instantaneous uncut chip thickness whereas in the other models the cutting force coefficients are assumed to be constants. The engagement between the tool and the workpiece is considered without measuring the actual cutter runout in the newly presented models. Experiments are conducted and the results obtained from these five different methods are compared.

Yang [25] et al investigated the effect of cutter runout on peripheral milling of curved surfaces. The presence of runout in the cutter changes the position of the cutting points, making it harder to calculate process parameters such as the tool position, feed direction and instantaneous uncut chip thickness for continuously changing workpiece geometry. The improvements brought by the proposed method are shown by a comparative study of an existing method from the literature.

Imani and Layegh [26] developed a model for the end-milling process to anticipate surface roughness and errors. A realistic surface texture model is constructed using the cutting conditions and dynamic simulation of the flexible end-mill. It is shown that the model predicts the surface roughness parameters accurately.

Patwari [27] et al studied the influence of the chip formation process during end milling on chatter. They modeled the vibration characteristic of the machine tool system with finite elements and experimental modal analysis in order to identify the interaction of chip instabilities with the natural vibration of the system components. It has been concluded that chatter occurs during end milling due to the resonance of the machine tools system component when the frequency of chip formation is approximately equal to the natural frequency modes of the system components.

Budak and Altintas presented their key work on chatter in 1998 in two parts [28, 29]. In the first part an analytical and practical method for chatter stability prediction in milling is presented. The dynamic milling system is developed by modeling the workpiece and cutter as multi degree of freedom structures. The dynamic milling forces are treated as a system of periodic differential equations with a certain amount of delay. They modeled an analytical relation for chatter stability limit which is critical for production planning in the industry. In the second part, this model is applied on three common milling systems. For each case the analytical predictions are compared with numerical and time domain solution from the previous models in the literature. Analytical nature of the model decreases the calculation time requirement compared to the numerical models.

Cao and Altintas [30] presented a general model of the spindle bearing and machine tool system, including all of the components such as the rotating shaft, tool holder, angular contact ball bearings, housing and the machine tool mounting. By doing so they were able to model virtual cutting of a work material during the design stage and predict stiffness, mode shapes, frequency response function (FRF), static and dynamic deflections along the cutter and spindle shaft, contact forces on the bearings before physically building and testing the spindles. The proposed models are verified experimentally by conducting tests on an industrial spindle. The study shows that the accuracy of predicting the performance of the spindles requires integrated modeling of all elements and mountings on the machine tool and the frequency and amplitude of vibrations during machining are affected by the operating conditions of the spindle.

Ko [31] et al developed a novel virtual machining system. They presented their finding in a three part paper. The first part includes a new method for calculating general cutting coefficients which are independent of cutting conditions. They calculate the instantaneous uncut chip thickness using the movement of the cutter's center position. The novelty of the presented model is that the cutting condition independent coefficients are determined form a single cutting condition. The model is validated by various experiments.

Budak and Lazoglu [32] proposed a method for offline feed rate scheduling in ball end milling. By analytically modeling the forces in ball end milling it is possible to change the feed rate during machining in such a way that the cutting forces will remain the same during the whole operation. Using this method the machining time can be decreased drastically by adjusting the feed rate. The model is validated with tests under various cutting conditions.

Bao and Tansel [33] proposed an analytical cutting force model for micro-end-milling operations. They used the trajectory of the tool tip for the calculation of the chip thickness. By doing so the cutting forces are calculated accurately for higher feed per tooth to tool radius ratios. They compared the outputs of their model with cutting experiments.

Kang [34] et al presented a mechanistic model to determine the cutting forces in micro end milling. The model considers the tool-workpiece contact at the flank face and tool edge radius effect. The model is validated using a newly developed tool dynamometer for micro end milling.

Dang [35] et al proposed a novel mechanistic cutting force model for flat end milling which includes the effect of bottom edge cuttings into account. The flank cutting force coefficients are treated as an exponent function of instantaneous uncut chip thickness and the flank cutting forces are subtracted from the total measured forces. The bottom coefficients are obtained from the remaining forces and shown to be constants. It is shown that the bottom edge cutting has a remarkable effect on total cutting forces when the axial depth of cut is relatively small.

2.2 Temperature Prediction Models

Prediction of temperature distributions in milling is critical for process planning since the limiting criteria for many milling operations in the industry is the high tool temperatures. Combined with the high cyclic nature of the cutting forces, these temperatures induce thermal stresses that lead to cracking and chipping of the tool. Also at elevated temperatures binding material in the tool structure tends to diffuse into chip and work piece which leads to diffusion type wear. In this part the work done in the literature on the temperature modeling is presented.

Hou and Komanduri [36] solved Jaeger's classical heat source method to calculate the temperature rise at any point due to stationary or moving plane heat source of different shapes and heat intensities. Later this solution is extended using the Hahn's moving oblique band heat source method by including appropriate image heat sources in a three part paper. Throughout the modeling, the analysis is carried out separately for chip and tool and then combined. In the first part [37] the heat formed in the shear plane is introduced as a plane heat source and the temperature distribution on the tool and workpiece is calculated accordingly. The workpiece is extended beyond the shear plane and this allowed the temperature rise in the workpiece and chip to be calculated without any need for heat partition formula. In this way, the heat partition can be determined from the solution of this model as done in the second part of the paper. In the second part, for the chip Jaeger's moving band and for the tool a stationary rectangular heat source are used [38]. Also in second part the heat formation due to the friction on the rake face is calculated. The appropriate boundary conditions to match the temperature distribution on the chip and tool sides were selected. In the third part the temperature rise due to both friction and plastic deformation are combined [39]. The temperature distributions obtained from the model are verified with both conventional machining tests done on steel and ultra precision tests on aluminum.

Moufki [40] et al studied the orthogonal cutting analytically using a thermomechanical model for the primary shear zone and a contact problem model at the tool chip interface. In the model, instead of a constant friction, a temperature dependent friction law is derived and used to model the heat generation. The effect of cutting conditions and material behavior on temperature distribution, cutting forces and friction is investigated.

Lazoglu and Altintas [41] developed a numerical finite difference model to predict tool and chip temperature fields in continuous and interrupted machining operations. For orthogonal turning operations the heat transfer between the tool and chip is modeled by using a partition formula to define the heat interaction between the tool and the workpiece. The model takes the deformation energy created in the shear zone and the friction energy generated at the rake face into account. Later, the model is extended to milling by digitizing the time varying chip thickness into small discrete elements and modeling each element as a first-order dynamic system. The time constant of each of these elements are identified based on the thermal properties of the tool and work material, and the initial temperatures. The simulation results show satisfactory agreement with the experimental temperature measurements available in the literature.

Lazoglu and his group modeled the three dimensional temperature fields on the chip, tool and workpiece material during orthogonal cutting using finite difference method [42]. They also validated this model using high precision infrared camera to determine the temperature distribution in the tool [43]. Later this approach is extended to temperature prediction in three dimensional temperature predictions of oblique cutting processes [44]. This analytical approach which uses elliptic structural grid generation to solve the temperature field allows different cutter geometries to be implemented easily and the analytical nature of the model improves the computational time requirement.

Majumdar [45] et al investigated the heat generation and temperature distribution in metal cutting processes using a finite element model. The model solves the multi-dimensional steady state heat diffusion equation taking into account the heat losses by convection at the surfaces. The heat generations within primary and secondary zones are modeled separately and fed into the FE model.

2.3. Wear Estimation Models

There are lots of mathematical simulations and models conducted in the last decades to better understand the nature and effects of wear in machining processes. Mathematical models have been developed, empirical tests are designed and the use of these models has been investigated. Recently finite element is also used for analysis. In this section an overview of the literature on wear modeling is given.

Usui [46] et al developed a general model for the flank and crater wear of tungsten carbide tools for a wide variety of tool shapes and cutting conditions in practical turning operations. The model is based on the orthogonal cutting data and two wear constants. A theoretically derived wear characteristic equation is verified experimentally. For the derivation of the wear equation, an energy method is developed for the chip formation and cutting forces in turning with a single-point tool using the orthogonal cutting data. Using these forces, stress and the temperature on the wear face were calculated. Using the characteristic equation and these values the wear progress was predicted. The predictions were verified with experiments.

Dolinsek et al investigated the wear mechanisms in high speed cutting processes [47]. The main characteristic faced in HSC is the fact that the cutting speed becomes no longer the main factor on wear, but the tool movement also takes a part. It is concluded that the oxidation process of the coating and workpiece plays an important role of the excessive wear in end-milling tools. When this protective layer is removed further diffusion wearing process takes part.

Zareena and Veldhuis [48] investigated the tool wear mechanisms during the ultra precision machining of titanium. Due to their poor thermal conductivity and high strength at high temperatures titanium alloys are known to be difficult to machine materials. It is shown that the mechanism that initiates the wear is graphitization. As the wear progresses and the sharpness of the cutting lip's edge decreases more material adheres on the tool and surface quality of the workpiece decreases. Zareeena and Veldhuis tried to use a coating of perfluoropolyether coating to decrease this effect. It was shown that this coating increases the surface quality and may be considered as a viable alternative.

Wang et al [49] investigated the tool wear characteristic of CBN tools in high speed milling of titanium alloys. It is shown that binderless CBN tools show longer tool life at high cutting speeds in slot milling and the main wear mechanism occurring are the adhesion of the workpiece and diffusion of the tool material.

Thamizhmanii et al [50] studied the tool wear and surface roughness of AISI 8620 using coated ceramic tools. After conducting various tests under different cutting speeds, feed rate and depth of cuts, it was concluded that the surface roughness decreased when the cutting speed was increased, and the flank wear increased at higher cutting speeds, feed rates and higher depths of cut. It was shown that during turning built up edge formed and the wear was due to the diffusion of the work piece material.

Adesta et al [51] studied the tool wear of cermet inserts in high speed turning. They investigated the effect of negative rake angle on tool wear and surface quality. The wear rates in conventional and high speed cutting were compared and it was shown that tool wear is greater in high speed cutting. On the other hand the surface quality in high speed cutting was better than conventional cutting.

Gu et al [52] tested and compared the wear rates of milling inserts in cutting 4140 steel and expressed the tool life as a function of cutting speed for different types of inserts. They used wear maps to identify and represent different wear mechanisms such as attrition, abrasion, mechanical fatigue and thermal fracture. It was concluded that TiN and TiAlN coated inserts provide longer tool lives where ZrN coated inserts have similar performances to C5 carbide inserts.

Tang et al [53] studied the interaction between the tool flank wear and residual stresses in milling aluminum alloys. They measured the residual stresses on the surface and in-depth of the Al-7050-T7451 workpiece material using X-ray diffraction technique in combination with electro-polishing. The cutting forces during machining is measured and combined with the temperature distribution data obtained from the thermal image of the system in a finite element method. It was shown that the tool flank wear has a significant effect on residual stresses profiles. As the wear length increases, the residual stress on the machined surface shifts to tensile range, the residual compressive stress beneath the machined surface increases and the thickness of the residual stresses layer also increases. Also the magnitude and distributions of the residual stresses are closely correlated with cutting forces and temperature field. During the tests it was also observed that with the increasing tool wear all of the force components and the highest temperature on the surface of the workpiece increase significantly. It was shown that the thickness of the residual stress layer is determined mostly by the mechanical load whereas the superficial residual stress depends on the thermal loads.

Kountanya developed a general 3D model for a corner-radius, chamfered and edge-honed worn cutting tool using mathematical representation [54]. This new approach differs from the models in the literature that it introduces a geometric approach to the machining operations. Using this model the surface finish of the workpiece including the Brammertz (ploughing) and sideflow effects was simulated in typical hard turning. Flank and crater wear volume was accurately estimated.

Pavlov [55] et al demonstrated a way to use the simulation modeling in the tribology of metal cutting. The computer model combines the analytical wear mechanism models of abrasive, adhesive and diffusion wear. It is claimed that this approach allows the determination of total wear for changing cutting parameters effectively.

Umbrello [56] et al modeled the diffusion and abrasion wear of carbide uncoated tools via an inverse approach. Their model is calibrated using the experimental results of orthogonal cutting of AISI 1020 tubes and using this data different wear mechanisms are compared using a finite element approach.

Sviasakthivel [57] et al predicted the tool wear in terms of machining geometry. They employed central composite rotatable second order response surface methodology to create a mathematical model and verified the adequacy of the model using analysis of variance. The experiments were conducted on Al 6063 by high speed steel end mill cutter and tool wear was measured using tool maker’s microscope. Using this method the direct and indirect effects of the machining parameters with tool wear were analyzed, which may be utilized to optimize the process parameters to reduce tool wear.

Andrea Gatto [58] conducted an experimental study on the performance optimization in machining aluminum alloys to provide technological know-how for moulds production and show that the minimum tool wear is observed at high cutting speeds with low feed rates. However during the tests the total amount of wear did not reach to the critical values to consider the tool’s life to be over. Using a curve fit method the wear characteristics of cutting tools in milling Al7050, Al7076 and Al2219 are defined.

Krain and colleagues [59] reviewed prior work on the influence of operating parameters on tool life in milling Inconel 718 and added two sets of experimental studies to evaluate the effect of varying feed rate/chip thickness, radial depth of cut, tool material and geometry on the tool life and tool wear. In their first set of experiments they examined the effects of various feed rates and radial depths of cuts with a fixed tool workpiece duo. In the second set a number of different geometries were tested. Their study did not give a single "best" option but a few combinations that perform better than others.

Ozel et al [60] investigated the surface finishing and tool flank wear in finish turning of steels using multi-radii design ceramic wiper inserts. They developed multiple linear regression models and neural network models for predicting surface roughness and tool flank wear. Wiper tools produced surface roughness as low as 0.20 μm and the tool flank wear reached to tool life criterion around 15 min of cutting time at high cutting speeds due to elevated temperatures. Comparing the neural network based predictions of tool wear with non-training experimental data shows that the neural network models are suitable for a range of cutting conditions.

Lorentzon and Jarvstrat [61] introduced an empirical tool wear model in a commercial finite element code to predict tool wear. In this model the tool geometry is continuously updated to reflect the evolution of wear profile as pressure, temperature and relative velocities adapt to the change in geometry. This approach allowed different friction and wear models to be analyzed and compared. Their conclusion underlined that a more advanced friction model than Coulomb friction is necessary to get accurate wear predictions.

Molinari and Nouari [62] proposed a model for the diffusion wear in high speed cutting processes. In their model, diffusion at the tool–chip interface is controlled by the contact temperature and tool life is analyzed in terms of cutting conditions (cutting velocity, feed, and rake angle), friction characteristics and material properties. It is claimed that using this model, optimal cutting conditions can be found with respect to tool life and volume of material removed.

Luo et al [63] proposed a new flank wear rate model combining cutting mechanics simulation and an empirical model to predict tool flank wear. The wear constants in the proposed model are determined based on the machining data and simulation results and they indicate that cutting speed has a more dramatic effect on tool life than feed rate.

Sanchez et al [64] identified the effects of adhesion on the dry turning processes of different aerospace aluminum alloys using energy dispersive spectroscopy. They were able to distinguish different composition characteristics between built-up layer (BUL) and built-up edge (BUE) formation. The evolution of BUL and BUE with the time of machining has been studied.

Liew and Ding [65] studied the wear progression of PVD coated and uncoated tools during the milling of stainless steel at low speeds. They observed that doubling the cutting speed does not affect the tool wear significantly but increasing the hardness of the workpiece increases flank wear of the tool. Comparing the coated tools with the uncoated ones it was observed that abrasive wear was dominant for the coated tool for lower workpiece hardness. However when the workpiece hardness is increased to 55 HRC from 35 HRC tool wear occurred in three distinct stages of first abrasion, then cracking and chipping and finally the formation of surface cracks. Also the fracture resistance of the tool increases with the coating. The reason behind this increase is believed to be coating's preventing of crack formation. It is concluded that the ductility of the workpiece and tool wear affects the surface roughness and this conclusion is supported with experimental data.

Montgomery et al [66] examined a number of wear models highlighting some key details and techniques to ascertain wear rates and introduced modern approaches to wear measurement for coated engineering samples.

Li et al [67] experimentally studied the tool wear propagation and cutting force variations in the end milling of Inconel 718 with coated carbide inserts. The experimental results showed that the tool flank wear propagation in the up milling operations was more rapid than that in the down milling operations. It was concluded that the tool wear propagation was responsible for the increase of the mean peak force in successive cutting passes, while the thermal effects were the cause for the peak force variation within a single cutting pass.

Rao et al [68] investigated the tool performance in face milling of Ti–6Al–4V titanium alloy. Specific cutting energy, surface integrity and tool performance were measured. The experimental analysis was supported with 3D finite element model (FEM) simulations. A tool wear model is parameterized from FEM predictions of the tool–chip interface temperature, contact stress and chip velocity.

Li [69] summarized the tool wear modeling in the literature and presented the new development in predicting the tool wear evolution and tool life in orthogonal cutting with

FEM simulations. He also introduced the Hidden Markov models (HMMs) to estimate tool wear in cutting.

Lee et al presented a simple model for the abrasive wear of composite materials [70]. The model works on the basis of mechanics and mechanisms associated with sliding wear in ductile matrix composites containing hard brittle reinforcement particles. It is assumed that any portion of the reinforcement removed as wear debris cannot contribute to the wear resistance of the matrix. By modeling the plowing, interfacial cracking and particle removal wear mechanisms, this non-contributing portion of the reinforcement is estimated. In the model a single contribution coefficient, C is used to describe the contribution of the critical variables such as the relative size and nature of the matrix/reinforcement interface.

Crosskey and Gutierrez-Miravete [71] modeled temperature distribution inside the tool as a result of the forces and friction involved in the cutting process, along with the resulting diffusional flow of the cobalt binder from the WC tool. The model uses tool rake and flank face temperatures determined either experimentally or from other models as input and then couples the thermal problem with the solid state diffusion problem. It was observed that the computed results predict the effects of changes in cutting parameters on diffusional wear and the resulting tool life well.

Shao et al [72] described a cutting power model for face milling operation which is used for tool wear monitoring in milling operations under variable cutting conditions.

Wang et al [73] used binderless cubic boron nitride (BCBN) for high-speed milling of a Ti–6Al–4V and investigated the wear mechanism during slot milling in terms of cutting forces, tool life and wear mechanism. It was observed using the SEM and EDX that adhesion of workpiece and attrition are the main wear mechanisms of the BCBN tool when used in high-speed milling of Ti–6Al–4V and this type of tool manifests longer tool life at high cutting speeds.

Bouzakis et al [74] tried to adjust the cutting parameters for machining with PVD coated inserts to increase tool life by correlating the impact resistance of the film and the cutting performance at corresponding temperatures. They determined the cutting loads and temperatures during machining and the films' impact resistance by impact tests. It is shown that the tool lives can be increased by adjusting the cutting parameters according to PVD film's properties.

Xie et al used finite element method to simulate three chip formation analysis steps including initial chip formation, chip growth and steady-state chip formation in continuous chip formation process [75]. They obtained steady chip shape, cutting force, and heat flux at tool/chip and tool/workpiece interface along with temperature distribution in the cutting insert at steady state after introducing a heat transfer analysis. Next a Python-based tool wear estimate program is implemented which reads predicted cutting process variables, calculates tool wear based on wear rate model and then updates tool geometry. The predicted crater wear and flank wear are verified with experimental results.

Marksberry and Jawahir [76] presented a new method to predict tool-wear/tool-life performance in NDM by extending a Taylor speed-based dry machining equation. It was revealed that NDM can improve tool-life over four times compared to dry machining.

Fukui [77] et al investigated the impact of tribological properties of DLC coatings on cutting performance. The results obtained from pin-on-disk tests showed that DLC coated tools have a low coefficient of friction against aluminum alloy and therefore can be used to reduce adhesion between a tool and a work material. Cutting processes are analyzed via a finite element simulation that takes the chip shapes and cutting forces into account. It was shown that DLC coatings enhance the tool performance, the machined surface integrity and the tool life compared to an uncoated tool in the dry machining of the aluminum alloys.

Liu et al [78] experimentally examined the effects of tool nose radius and tool wear on residual stress distribution in hard turning of bearing steel. They measured the residual stresses beneath the machined surface using X-ray diffraction technique and electro-polishing technique. The results obtained in this study show that the tool nose radius affects the residual stress distribution especially at the early stage of cutting process.

Calatoru [79] et al observed unexpected chipping followed by catastrophic failure of the end mill during high speed end milling of aeronautical-grade aluminum alloy 7475-T7351 parts using tungsten carbide with cobalt binding (WC–Co) tools, while abrasive wear traces were absent. Their study shows that high temperatures generated during the cutting process activate the diffusion of aluminum into the tool material. As a result a eutectoid-containing cobalt aluminide (AlCo) with the cobalt used as binder is formed. This hard and brittle material weakens cobalt's role as binder between the carbide grains. With the exposure time and temperature of the contact, the penetration of the aluminum in the tool material becomes deeper, until the whole tool tip becomes fragile and subject to chipping and further to heavy damage.

Zhang et al [80] proposed a theoretical diffusion analysis for the wearing of tungsten carbide tools in high-speed machining of titanium alloys. Using scanning electron microscope and energy dispersive X-ray spectroscopy, it was shown that the pulling out and removing of the tungsten carbide (WC) particles due to cobalt diffusion dominated the crater wear mechanism on the rake surface of the cutting tool.

Sarhan et al [81] developed and experimentally verified an on-line monitoring strategy using the cutting force harmonics magnitudes as indicator to tool flank wear. They also studied the interrelationships between cutting force harmonic variation and tool wear in end milling. It was shown that certain harmonics increase significantly with flank wear while other harmonics remain unaffected.

Grzesik [82] characterized the surface roughness generated during hard turning (HT) operations performed with conventional and wiper ceramic tools at variable feed rate. In this research, the notch wear progress at the secondary trailing edges was found to produce individual irregularities and constitutes the altered surface profiles. Moreover, this research related the tool state in tool life time domain and the relevant surface roughness.

Rech et al [83] showed that a radius on the cutting edge prevents fast and unpredictable wear in milling inserts and revealed the existence of an optimum value of the radius experimentally. In parallel, they used 2D finite element cutting simulations based on Lagrangian thermo-viscoplastic formulation to analyze the tool-stress distributions within the tool coating and substrate.

Chapter 3

MECHANISTIC MODELING OF END MILLING FORCES

3.1 Introduction

End milling is a widely used machining operation in industries such as aerospace, die-mold production and automotive. It is critical for the production planning to accurately model the cutting forces in end milling, since this is the base for other critical analyses such as tool life calculations, thermal analysis and/or prediction of residual stresses.

For the modeling of the forces, the tool is divided into small disks in the axial direction and the contribution of each disk to the overall cutting forces is calculated. Then the sum of all of these contributions gives the overall cutting forces. The contribution of each disc depends on the uncut chip thickness of the disc, the width of the element and some coefficients described as the cutting coefficients.

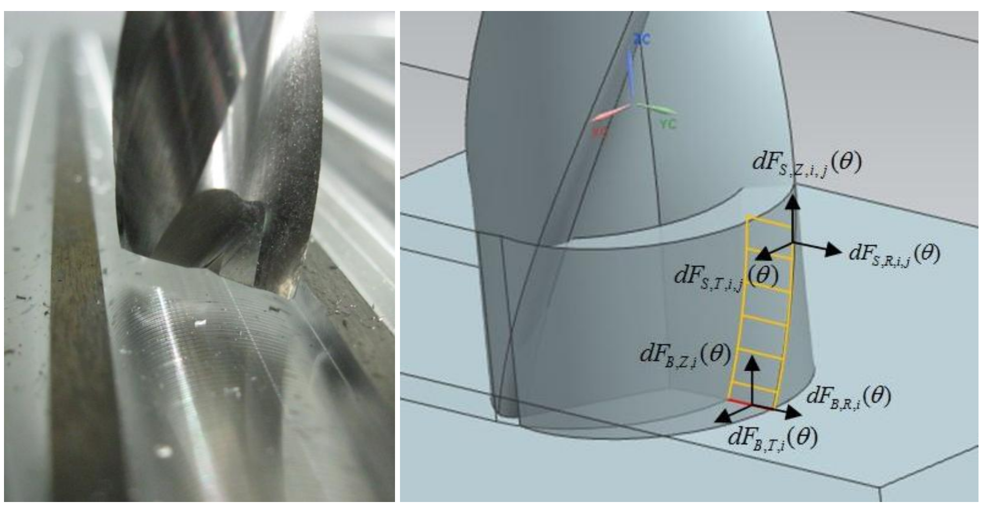

Figure 3.1 - Illustration of the differential discs

In literature, there are mainly two different approaches to calculate these coefficients. The first approach is the mechanistic approach. In this approach the coefficients are found by conducting calibration tests with the tool and workpiece to be modeled at different feed rates. The advantage of this model is its speed and simplicity. However, at the peak values where the average uncut chip thickness deviates from the instantaneous uncut chip thickness the results obtained from this method also deviate from the actual values.

The second approach is the orthogonal to oblique transformation. The advantage of this method is once the orthogonal data is obtained a wide range of geometries can be calculated using this method. However the results from this model have low accuracies for complex cutting geometries.

There are numerous studies on the prediction of cutting forces in end milling. However the effect of bottom edge in end milling is a less studied case. In most of the studies available in the literature the bottom edge effect is neglected. In 2010 Dang et al [36] studied this problem but they proposed a power function for the calculation of chip thickness. This approach requires a number of tests to be conducted in order to form the power function.

In this chapter the cutting forces acting on an end mill is calculated using the mechanistic calibration method, including the bottom edge cutting effect. It is believed that inclusion of the bottom edge cutting effect would reflect the actual physics of the cutting phenomena more accurately.

3.2 Modeling of the cutting forces

The cutting forces are assumed to be the sum of side edge cutting forces and bottom edge cutting forces.

$$\vec{F} = \vec{F}_S + \vec{F}_B \tag{3.1}$$

3.2.1 Modeling of the side edge forces

For the modeling of the side edge, the tool is divided into discs in the axial direction. For each flute and rotation angle the contribution of these elements are calculated separately. The contribution of each disc for a given angular position (θ) is as following;

$$dF_{S,i,j} = \begin{bmatrix} dF_{S,T,i,j}(\theta) \\ dF_{S,R,i,j}(\theta) \\ dF_{S,Z,i,j}(\theta) \end{bmatrix} = \left\{ \begin{bmatrix} K_{Sc,T,i,j} \\ K_{Sc,R,i,j} \\ K_{Sc,Z,i,j} \end{bmatrix} \cdot h_{S,i,j}(\theta) + \begin{bmatrix} K_{Se,T,i,j} \\ K_{Se,R,i,j} \\ K_{Se,Z,i,j} \end{bmatrix} \right\} \cdot w_{S,i,j} \tag{3.2}$$

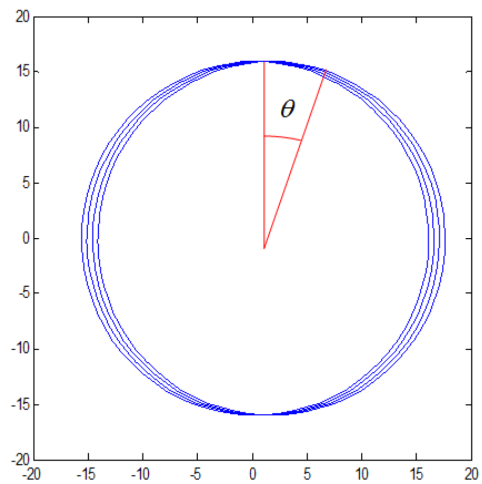

Figure 3.2 – Illustration of the trochoidal movement of the cutting lip for a 16 mm diameter tool

In this equation $dF_{S,i,j}$ means the side edge cutting force acting on the ith flute at the jth depth of cut, and consists of three components in the radial [R], tangential [T] and axial [Z] directions.

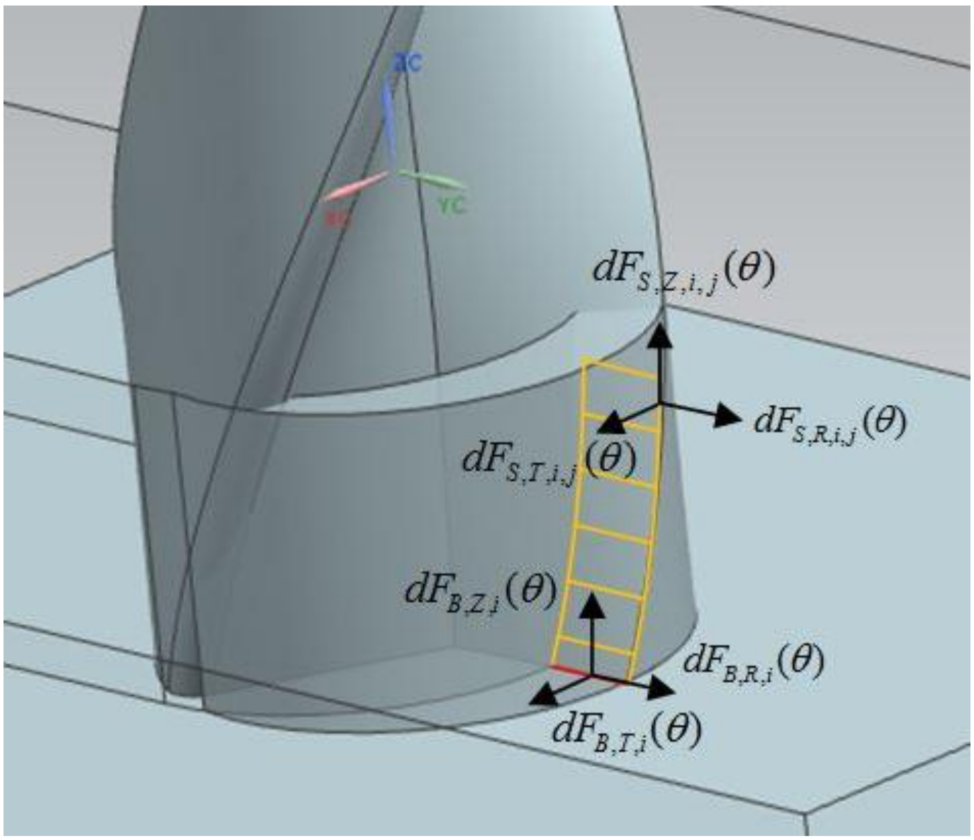

Figure 3.3 – Differential cutting forces acting on the side and bottom elements

The value of each component depends on the cutting coefficients for that edge ($K_{Sc,T,i,j}$, $K_{Sc,R,i,j}$, $K_{Sc,Z,i,j}$, $K_{Se,T,i,j}$, $K_{Se,T,i,j}$, $K_{Se,T,i,j}$), the uncut chip thickness $h_{S,i,j}(\theta)$ and the width of cut $w_{S,i,j}$. At the side edge the width of cut is constant and found by dividing the axial depth of cut to the number of discs. On the other hand the uncut chip thickness is constantly changing, starting from 0 at the beginning of slot milling to its maximum of feed per tooth value at the 90° rotation angle and going back to 0 again. Accordingly for each angular position for a end mill with n flutes and m number of axial discs the side edge cutting forces can be calculated as follows;

$$F_S = \sum_{\theta=1}^{360} \sum_{n=1}^{i} \sum_{m=1}^{j} (K_{Sc,i,j} \cdot fpt \cdot \sin(\theta) + K_{Se,i,j}) \cdot w_{S,i,j} \tag{3.3}$$

3.2.2 Modeling of the bottom edge forces

The effect of bottom edge cutting to the overall cutting forces is modeled as below;

$$dF_{B,i} = \begin{bmatrix} dF_{B,T,i}(\theta) \\ dF_{B,R,i}(\theta) \\ dF_{B,Z,i}(\theta) \end{bmatrix} = \begin{bmatrix} K_{Bc,T,i,j} \\ K_{Bc,R,i,j} \\ K_{Bc,Z,i,j} \end{bmatrix} \cdot h_{S,i,j}(\theta) + \begin{bmatrix} K_{Be,T,i,j} \\ K_{Be,R,i,j} \\ K_{Be,Z,i,j} \end{bmatrix} \tag{3.4}$$

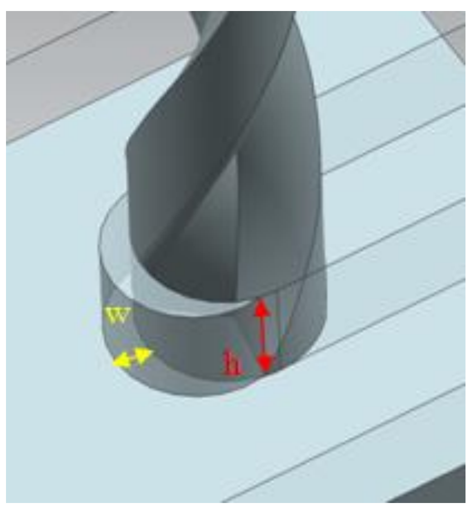

Figure 3.4 - Illustration of the uncut chip thickness for the bottom edge

In this equation $dF_{B,i}$ stands for the effect of the bottom edge of ith flute to the overall cutting forces, and has three components in tangential, radial and axial directions. The value of each component depends on the cutting coefficients ($K_{Bc,T,i}$, $K_{Bc,R,i}$, $K_{Bc,Z,i}$, $K_{Be,T,i}$, $K_{Be,R,i}$, $K_{Be,Z,i}$) and the uncut chip thickness $h_{S,i}$. Accordingly by summing the contributions of the bottom edge at each rotation angle for each flute the total contribution of the bottom edge to the overall cutting forces are evaluated.

$$F_B = \sum_{\theta=1}^{360} \sum_{n=1}^{i} K_{Bc} \cdot fpt \cdot \sin(\theta) + K_{Be} \qquad (3.5)$$

3.3 Mechanistic calibration tests

Mechanistic calibration tests on slot milling were conducted on Mori Seiki NMV5000 DCG 5 axis CNC machining center. The cutting force signals were collected using rotary type dynamometer and high speed data acqusition board at four different depths of cut (A_p =0.5, 1.0, 1.5, 2.0 mm) and 3 different feed per tooth rates (fpt =0.10, 0.15, 0.25 mm/rev).

Figure 3.5 - Experimental setup for milling

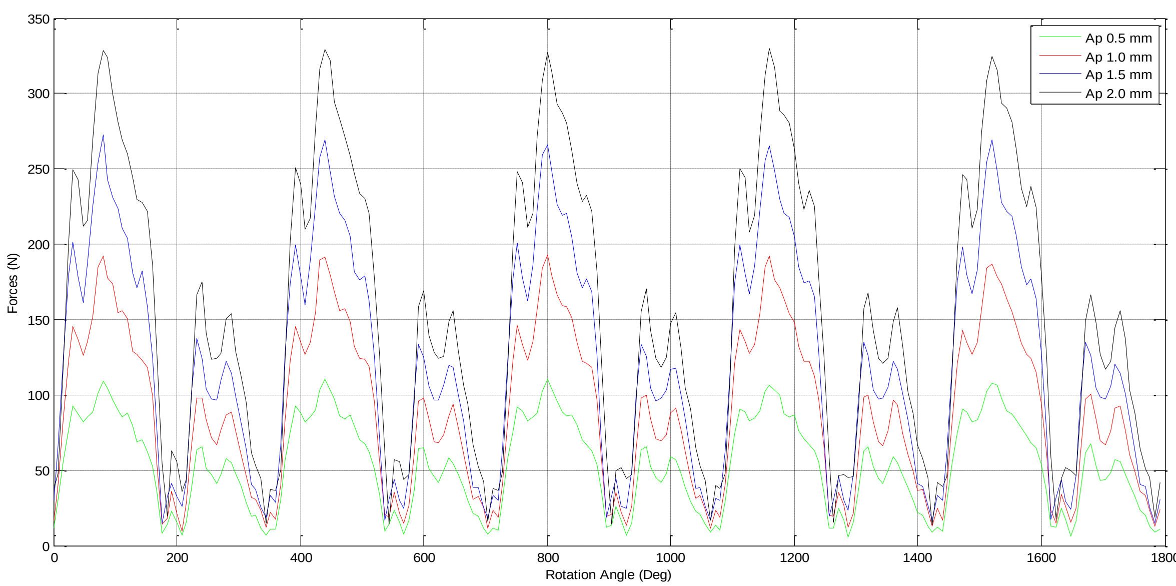

Figure 3.6 - Sample resultant cutting forces for tool D at 0.10 mm/rev at 8000 rpm.

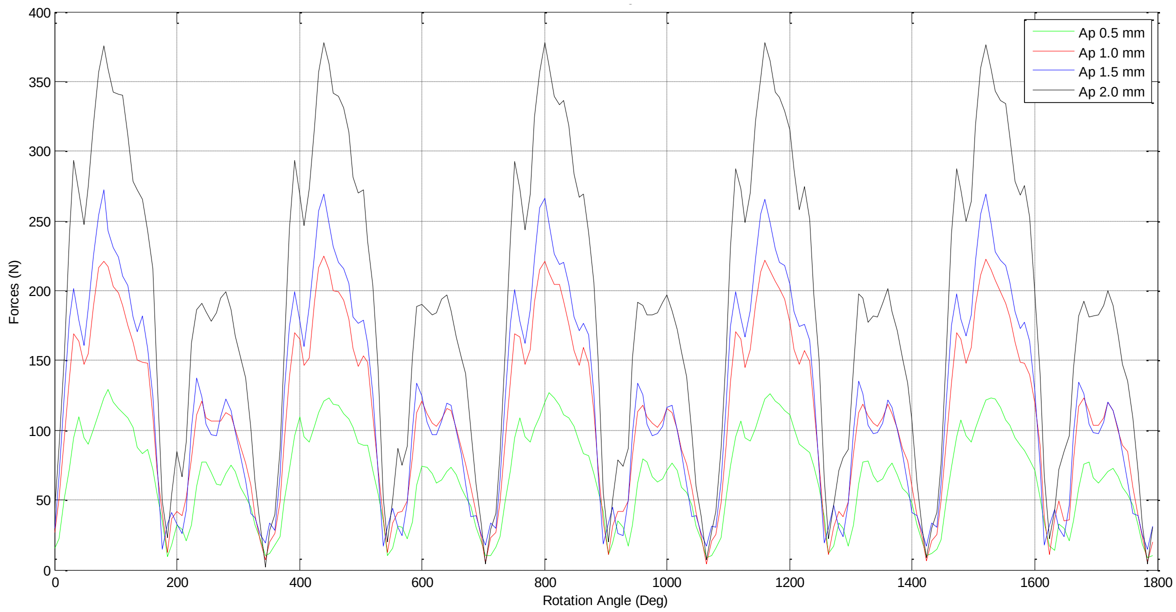

Figure 3.7 - Sample resultant cutting forces for tool D at 0.15 mm/rev at 8000 rpm.

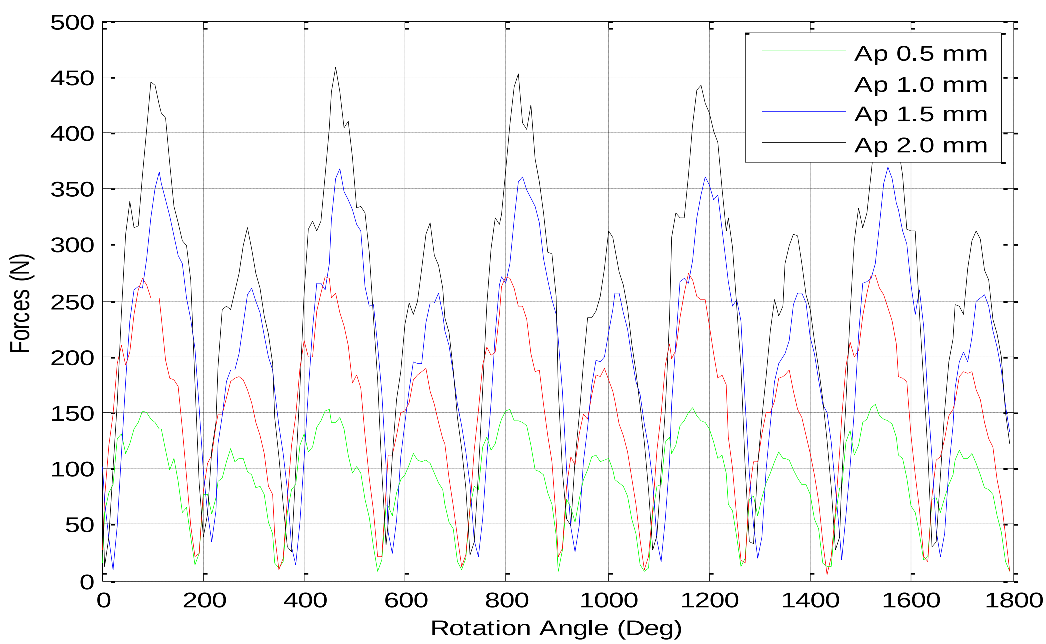

Figure 3.8 - Sample resultant cutting forces for tool D at 0.25 mm/rev at 8000 rpm.

By subtracting the A_p=0.5 test results from the A_p=1.0 test results, the cutting forces acting on a width of 0.5 mm on the side edge is measured. This operation is repeated for the other 0.5 mm widths between A_p=1.5-1.0 and A_p=2.0-1.5. It is seen that the forces acting on a width of 0.5 mm is the same independent of the axial level as expected. By dividing this result to the width of cut of 0.5 mm the cutting coefficients independent of the width of cut are obtained.

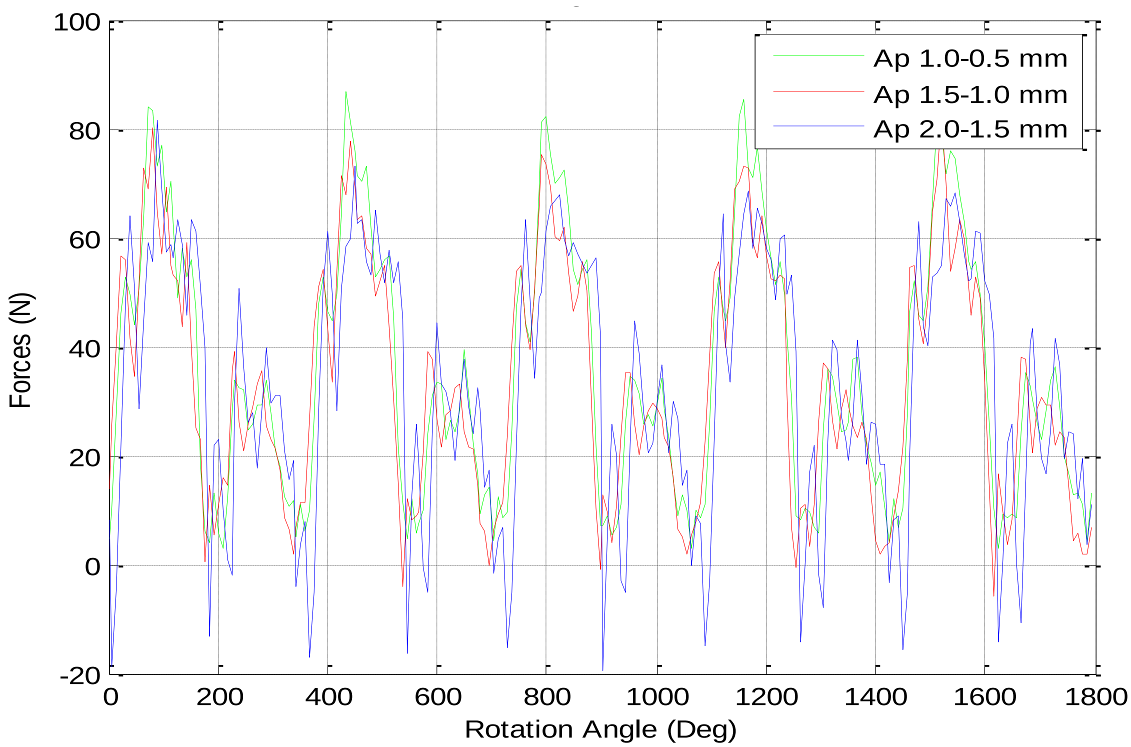

Figure 3.9 – Sample resultant forces for tool D at 0.10 mm/rev at 8000 rpm at 0.5 mm thickness discs

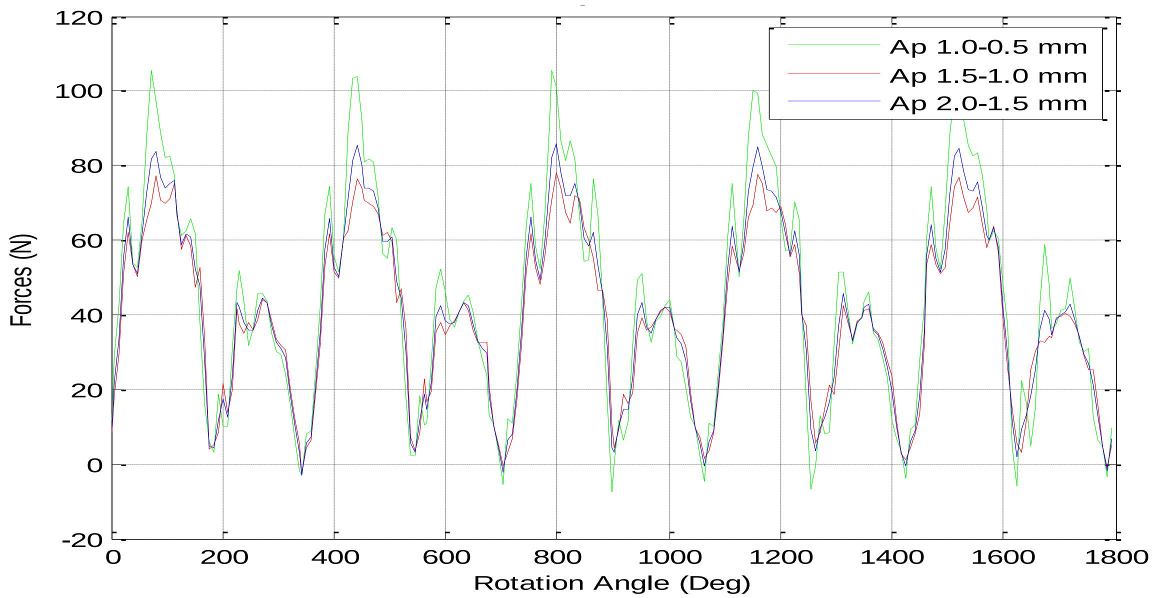

Figure 3.10 - Sample resultant forces for tool D at 0.15 mm/rev at 8000 rpm at 0.5 mm thickness discs

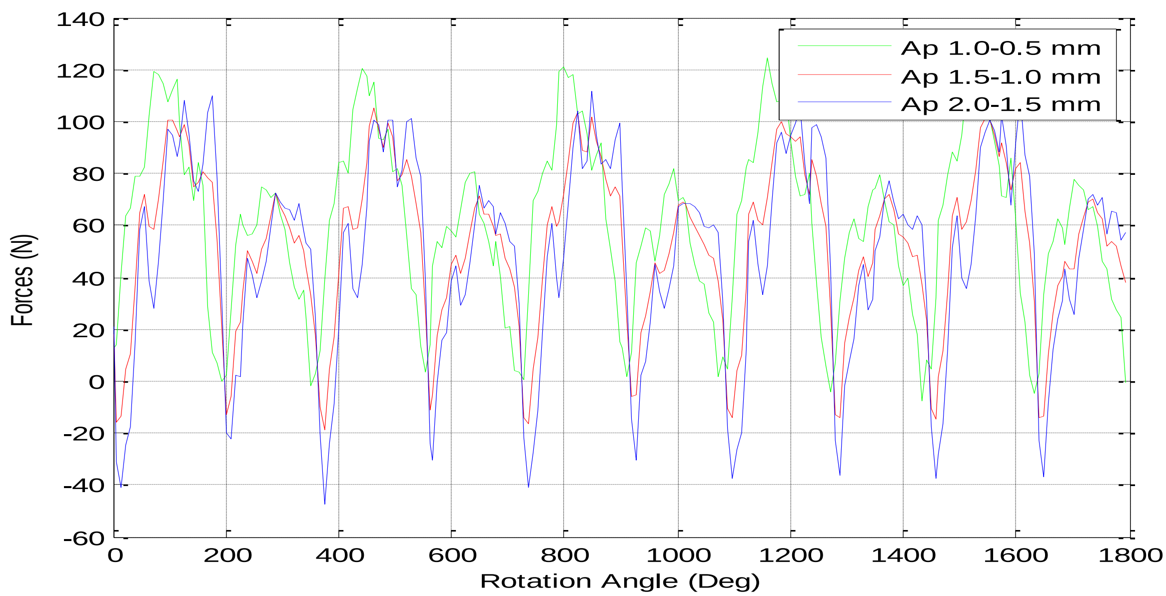

Figure 3.11 – Sample resultant forces for tool D at 0.25 mm/rev at 8000 rpm at 0.5 mm thickness discs

After the resultant forces are obtained, average resultant cutting forces are calculated using the trapezoid rule. These average forces are than used to calculate cutting coefficients by fitting a best fit line. The slope of this line gives the cutting coefficients, whereas the y axis intersection gives the edge coefficients.

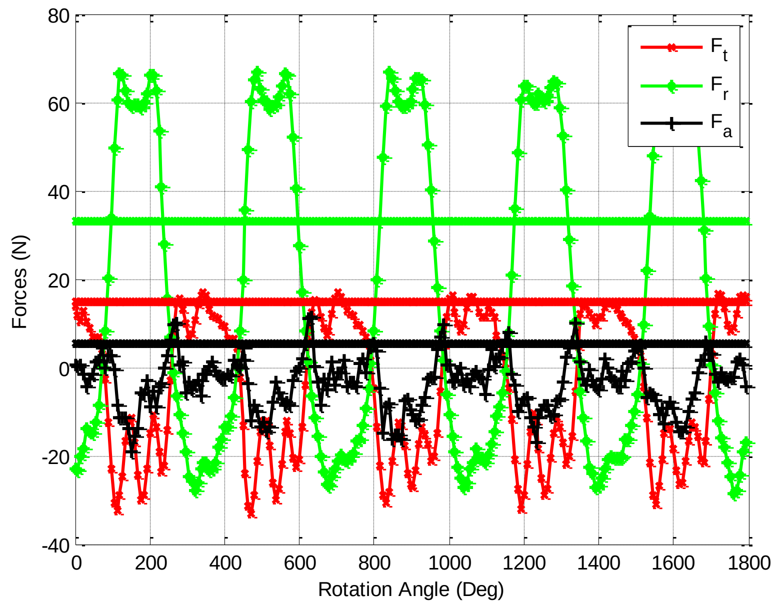

Figure 3.12 – Average side cutting forces for tool D at 0.10 mm/rev at 8000 rpm

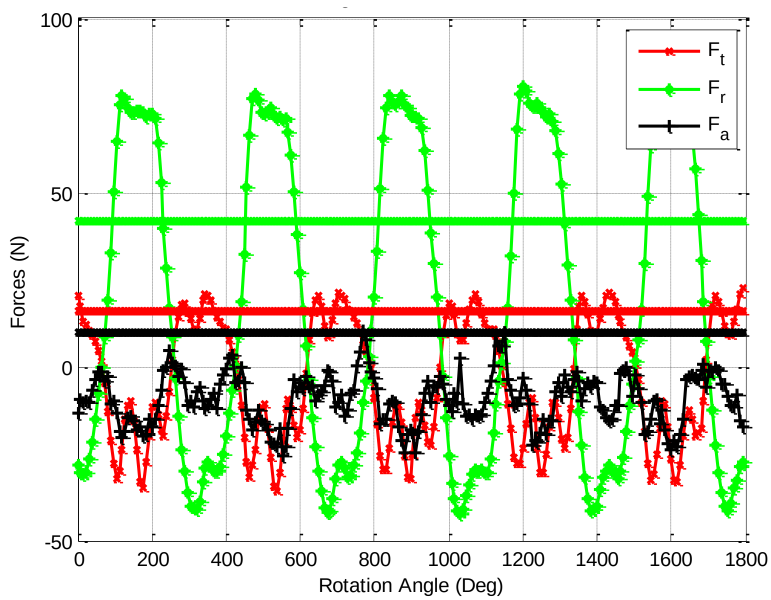

Figure 3.13 – Average side cutting forces for tool D at 0.15 mm/rev at 8000 rpm

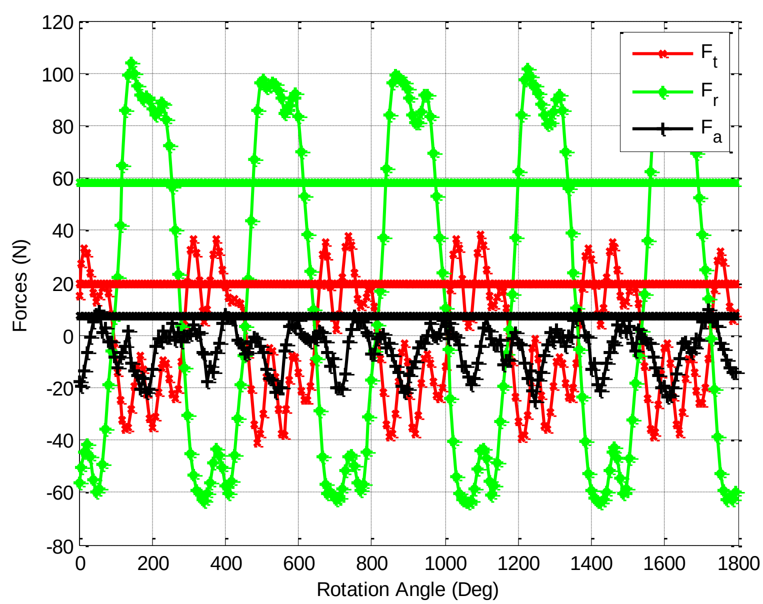

Figure 3.14 – Average side cutting forces for tool D at 0.25 mm/rev at 8000 rpm

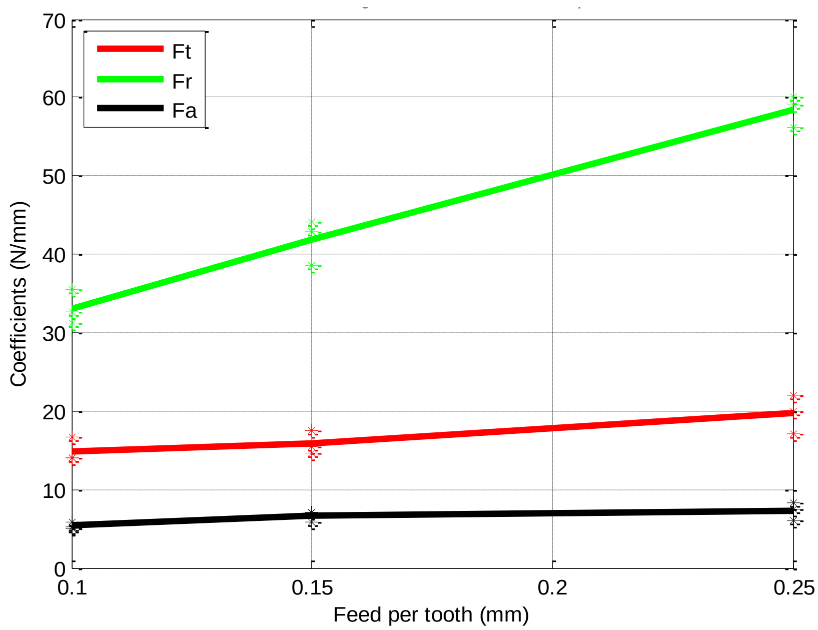

Figure 3.15 - Side cutting coefficients for tool D at 8000 rpm

Calibration methodology

1. Conduct slot milling cutting tests at two different axial depths of cut (A_p , kA_p)

2. Subtract the force data of the two tests to obtain the cutting forces acting on a disc with a width of $(k-1)\cdot A_p$

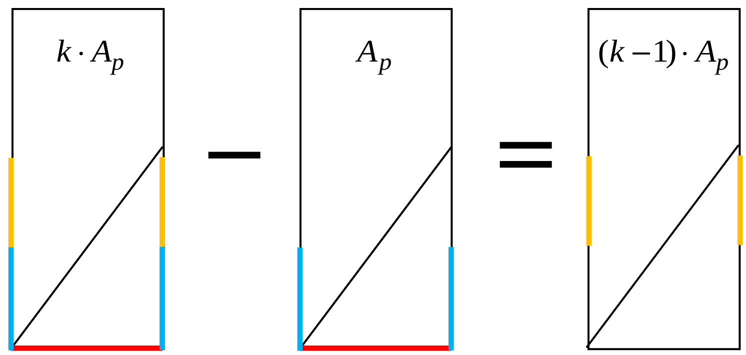

3. Divide these force values to $(k-1)$ to isolate the side edge cutting forces for test with A_p. (Divide and multiply by k for test $k\cdot A_p$)

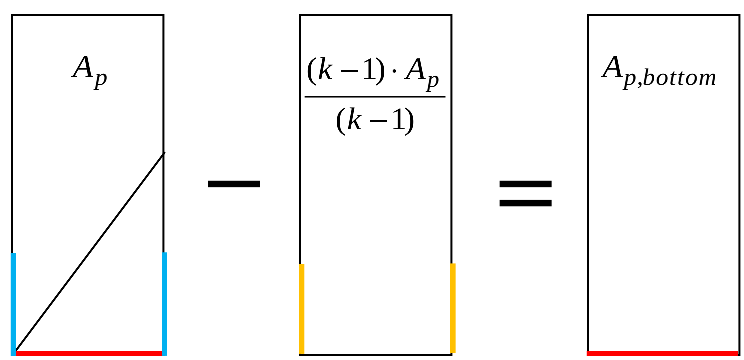

4. Subtract these force values from test with A_p values to isolate the effect of bottom edge cutting.

Figure 3.16 – Summary of the calibration methodology

3.4 Validation of the cutting force modeling

For the validation of the model, cutting tests are conducted with 6 different tool brands (A-F) at the conditions given below in Table 3.1. The results obtained from the model and the experimental force values are plotted in Figures 3.16-3.88.

Table 3.1 - Conditions for the calibration and validation tests

Spindle Speed	8000 rpm
Feed rates (mm/rev)	0.10 / 0.15 / 0.25
Axial depths of cut (mm)	0.5 / 1 / 1.5 / 2

Table 3.2 - Cutting coefficients of tools

	$K_{Sc,R}$	$K_{Sc,T}$	$K_{Sc,Z}$	$K_{Se,R}$	$K_{Se,T}$	$K_{Se,Z}$	$K_{Bc,R}$	$K_{Bc,T}$	$K_{Bc,Z}$	$K_{Be,R}$	$K_{Be,T}$	$K_{Be,Z}$
A	912.6	659.8	73.7	5.4	5.2	4.9	12.3	31.4	12.6	0.51	0.63	5.21
B	598.7	452.7	40.3	1.61	2.33	5.02	6.2	25.3	9.1	0.41	0.52	4.12
C	702.3	451.7	59.4	20.1	24.7	0.79	11.3	27.3	10.6	0.45	0.7	4.61
D	867.6	600.7	58.7	22.6	28	0.82	10.2	12.8	10	0.83	0.79	4.1
E	592.4	445.6	40.2	1.49	2.21	4.98	5.9	24.7	8.6	0.39	0.49	4.08
F	903.2	645.5	70.3	5.1	4.9	4.7	11.2	30.6	10.8	0.48	0.62	4.9

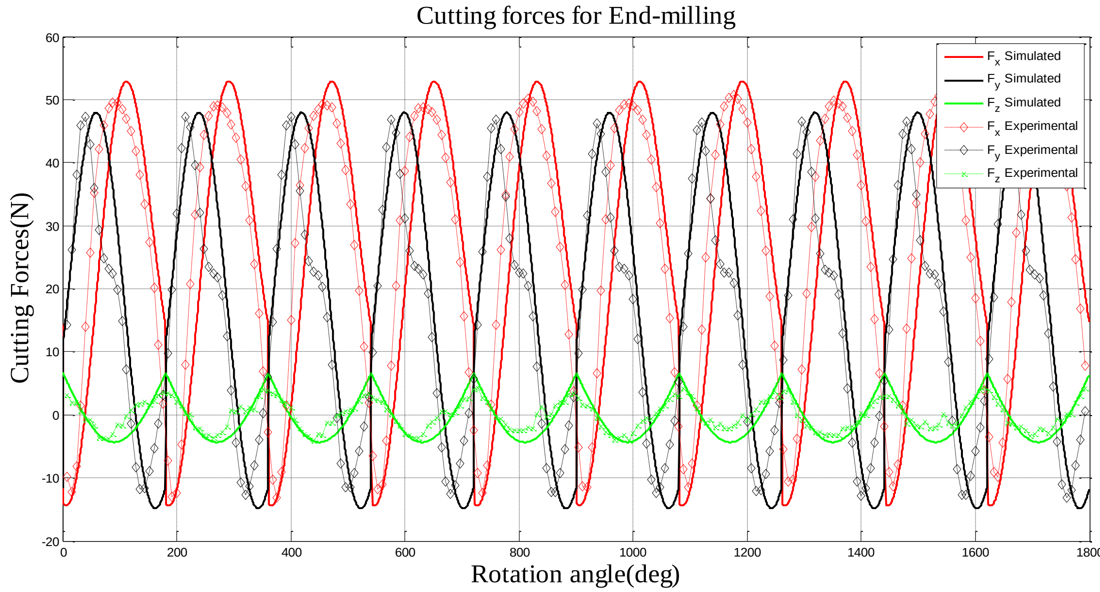

Figure 3.17 – Cutting forces of tool A at 0.10 mm/rev feed rate and 0.5 mm A_p

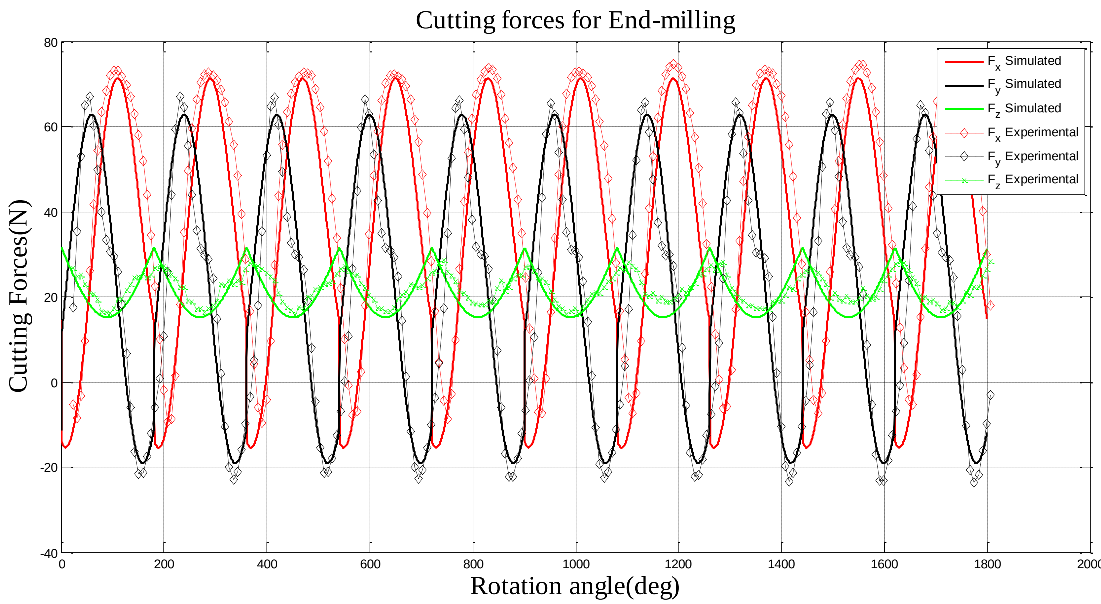

Figure 3.18 – Cutting forces of tool A at 0.15 mm/rev feed rate and 0.5 mm A_p

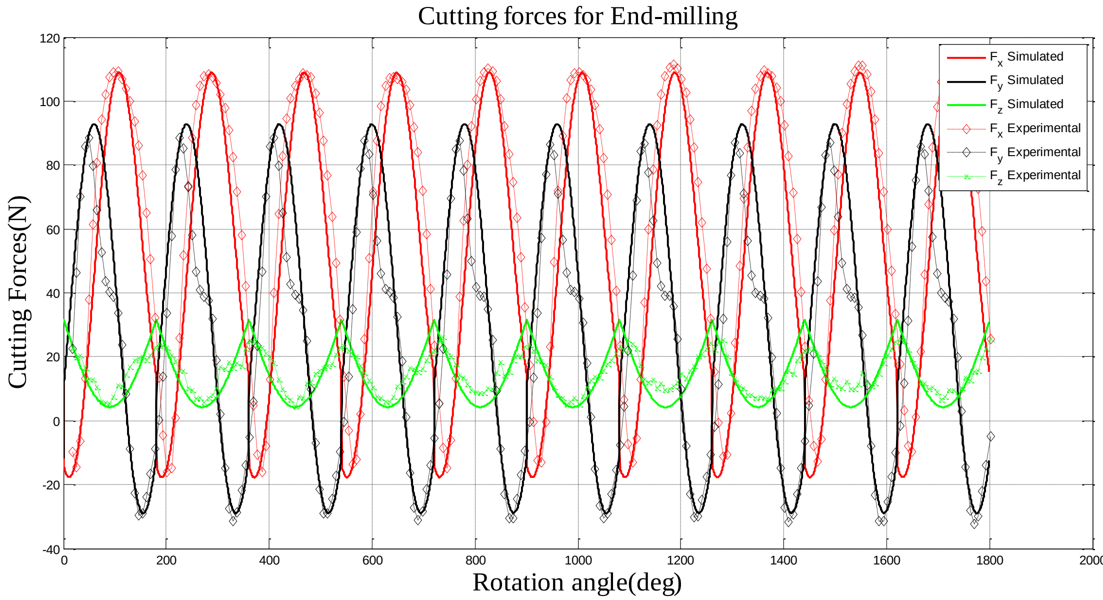

Figure 3.19 – Cutting forces of tool A at 0.25 mm/rev feed rate and 0.5 mm A_p

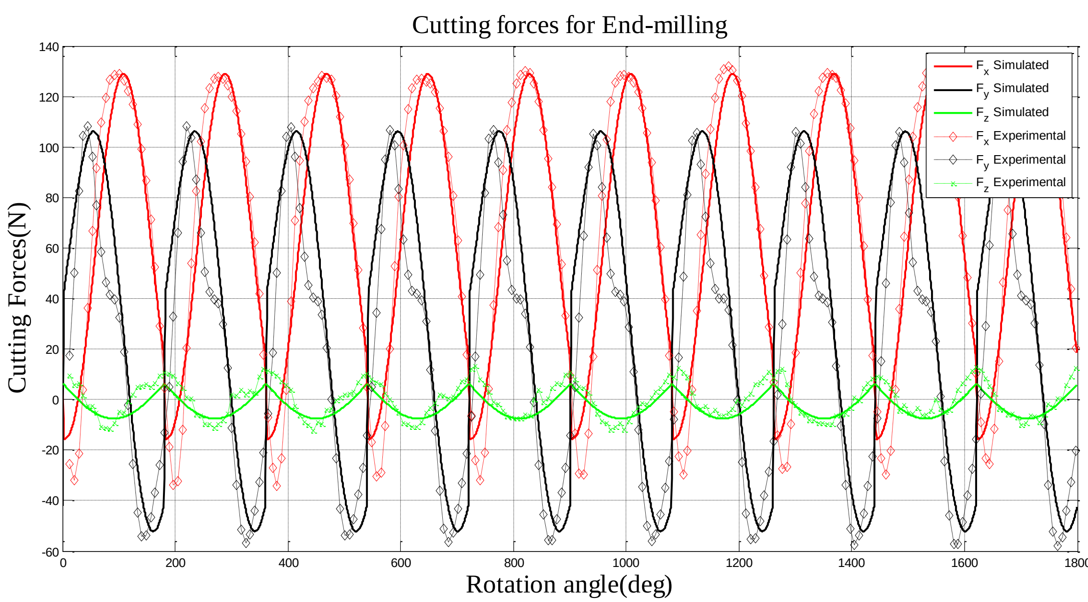

Figure 3.20 – Cutting forces of tool A at 0.10 mm/rev feed rate and 1 mm A_p

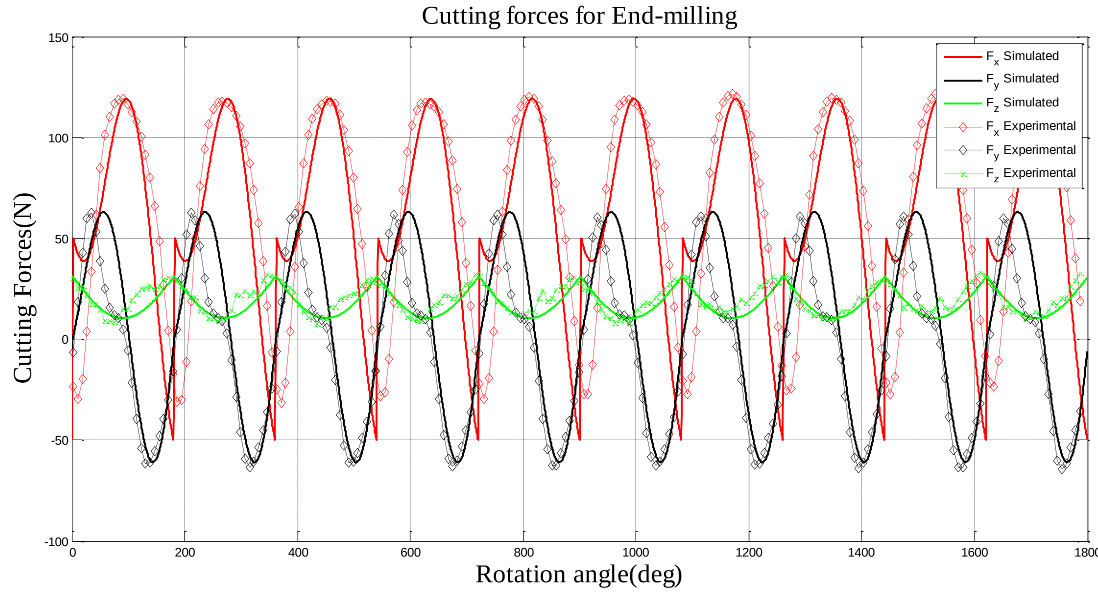

Figure 3.21 – Cutting forces of tool A at 0.15 mm/rev feed rate and 1 mm A_p

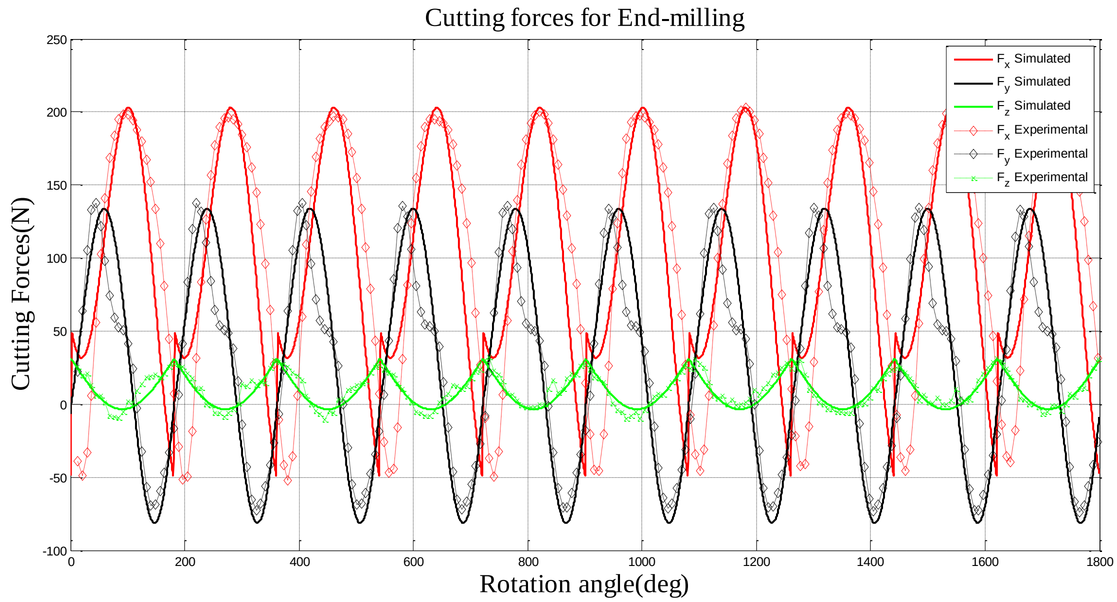

Figure 3.22 – Cutting forces of tool A at 0.25 mm/rev feed rate and 1 mm A_p

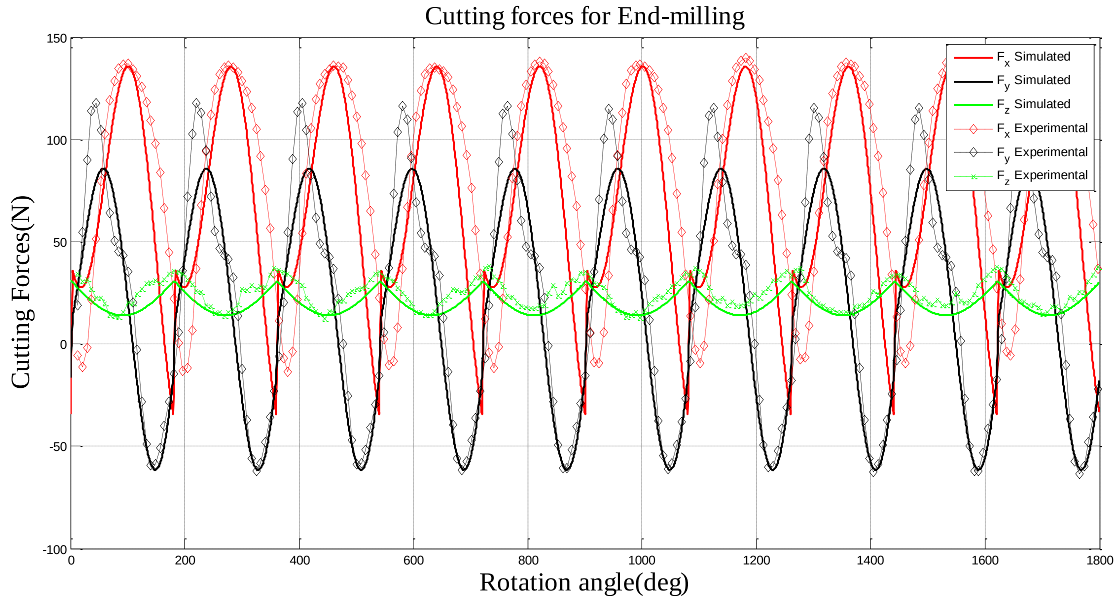

Figure 3.23 – Cutting forces of tool A at 0.10 mm/rev feed rate and 1.5 mm A_p

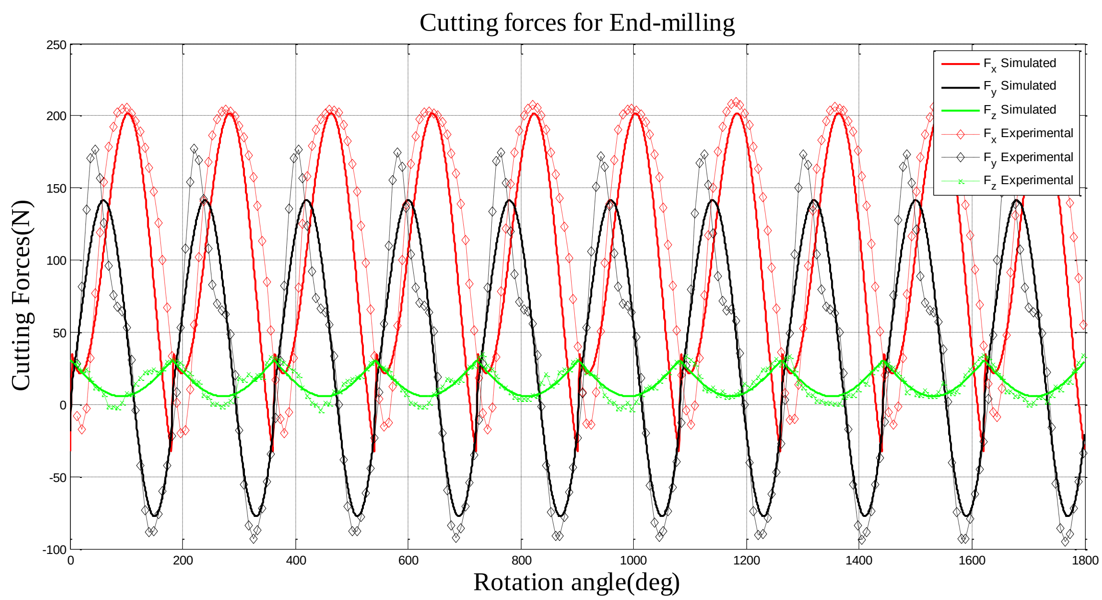

Figure 3.24 – Cutting forces of tool A at 0.15 mm/rev feed rate and 1.5 mm A_p

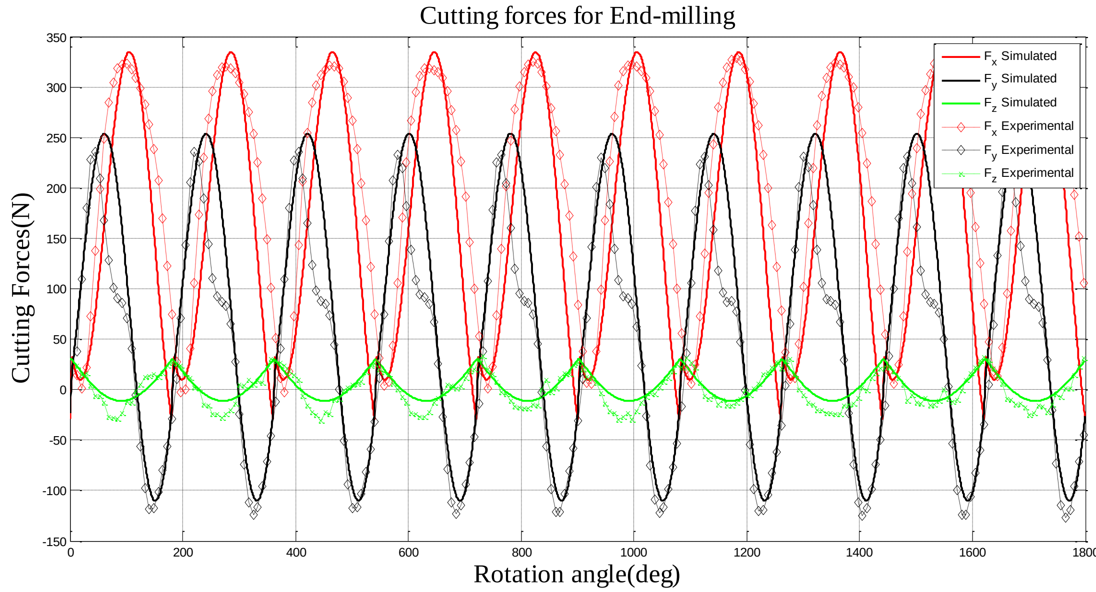

Figure 3.25 – Cutting forces of tool A at 0.25 mm/rev feed rate and 1.5 mm A_p

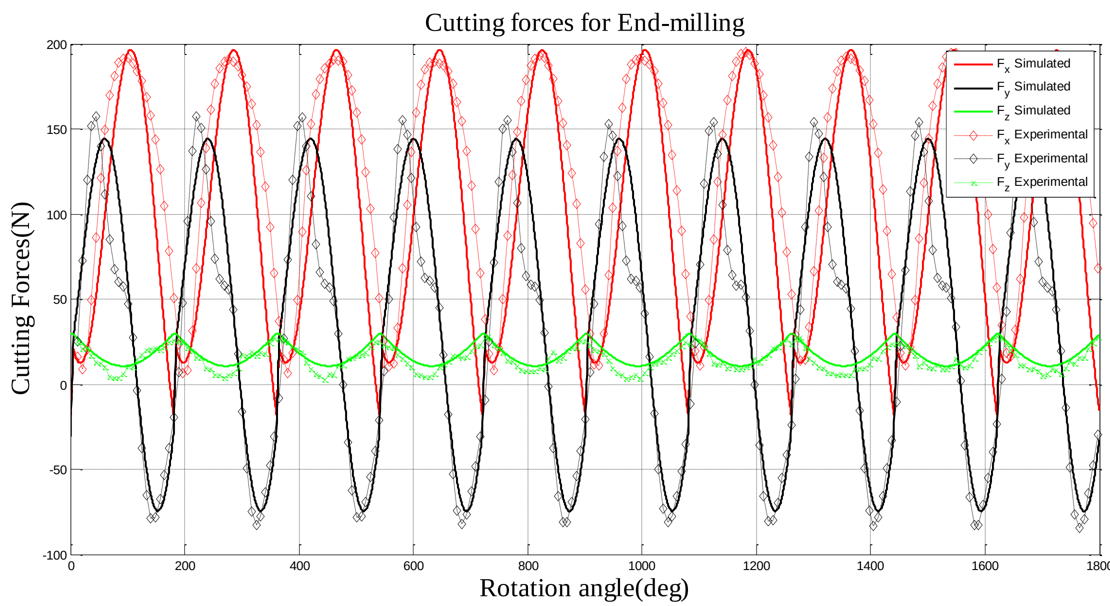

Figure 3.26 – Cutting forces of tool A at 0.10 mm/rev feed rate and 2 mm A_p

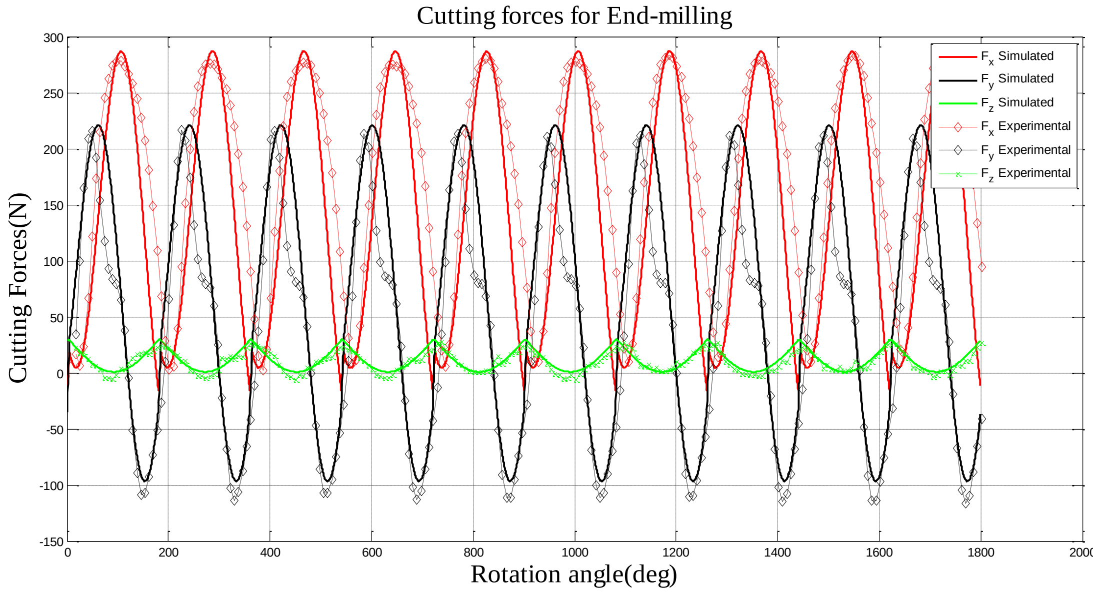

Figure 3.27 – Cutting forces of tool A at 0.15 mm/rev feed rate and 2 mm A_p

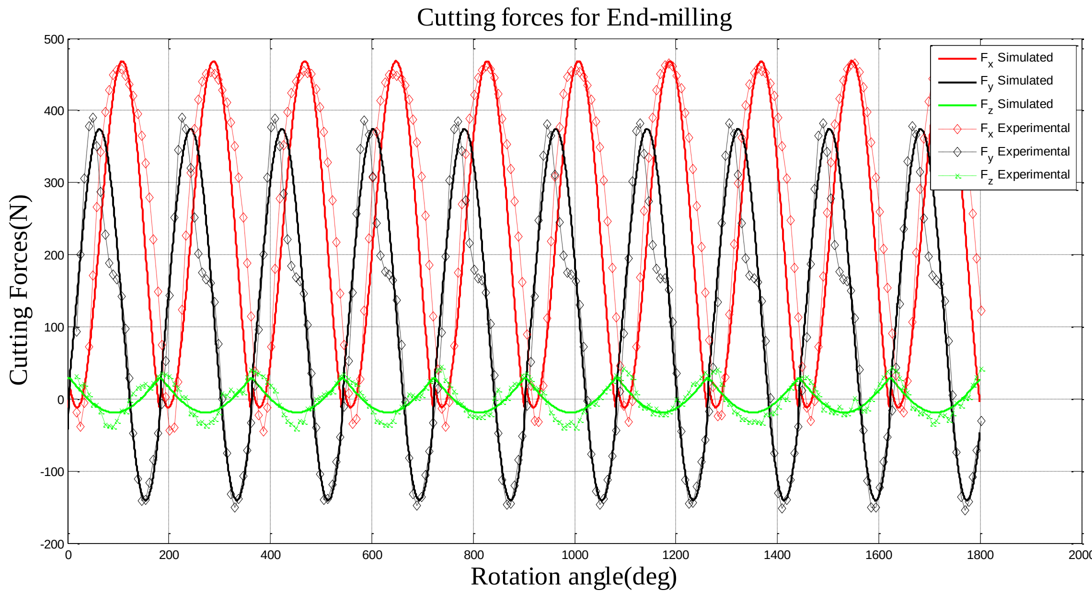

Figure 3.28 – Cutting forces of tool A at 0.25 mm/rev feed rate and 2 mm A_p

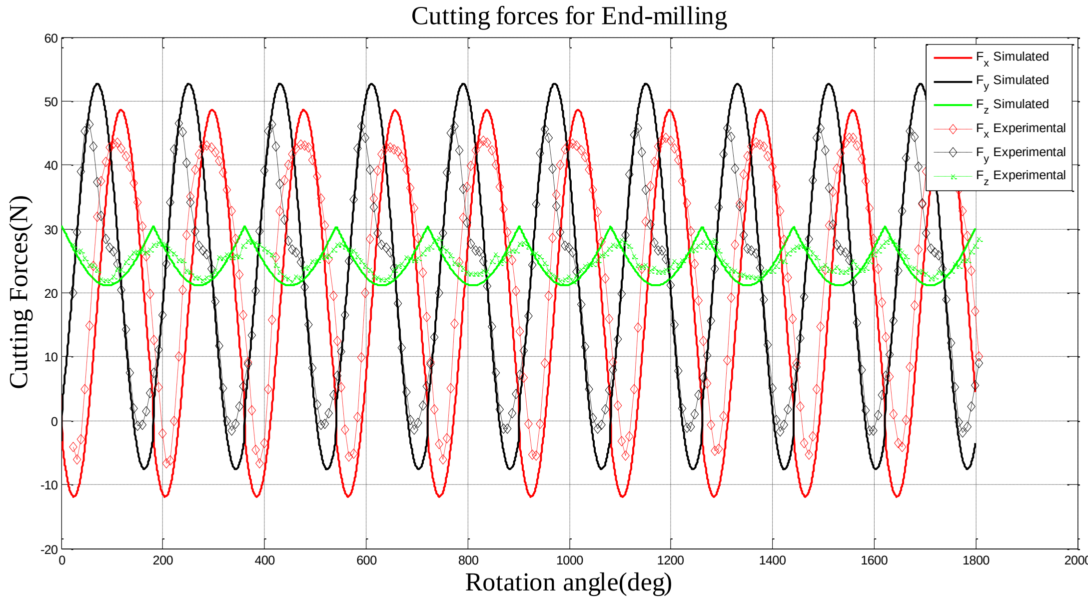

Figure 3.29 – Cutting forces of tool B at 0.10 mm/rev feed rate and 0.5 mm A_p

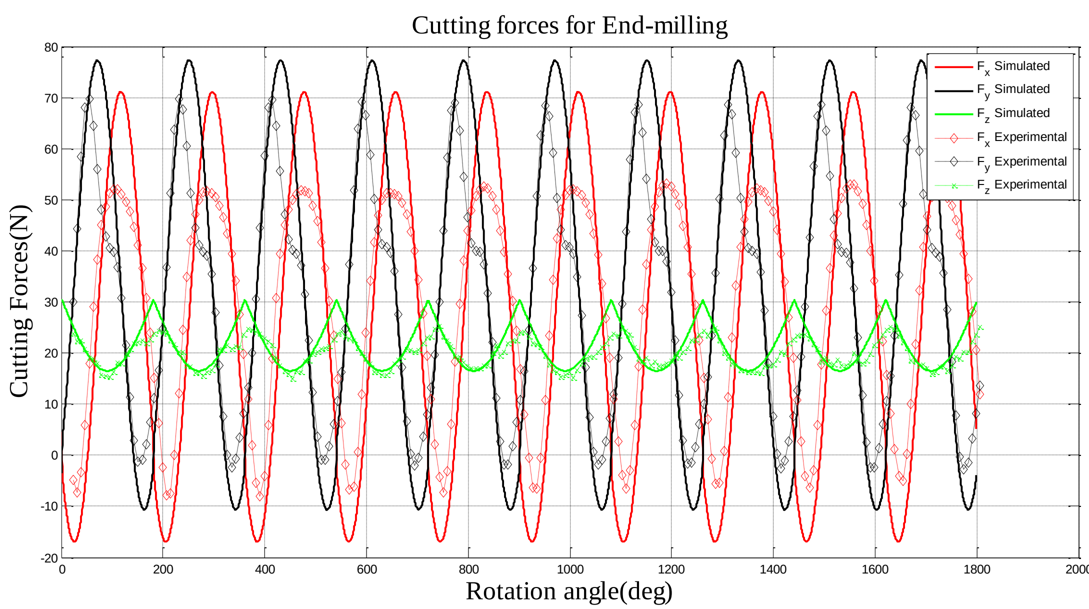

Figure 3.30 – Cutting forces of tool B at 0.15 mm/rev feed rate and 0.5 mm A_p

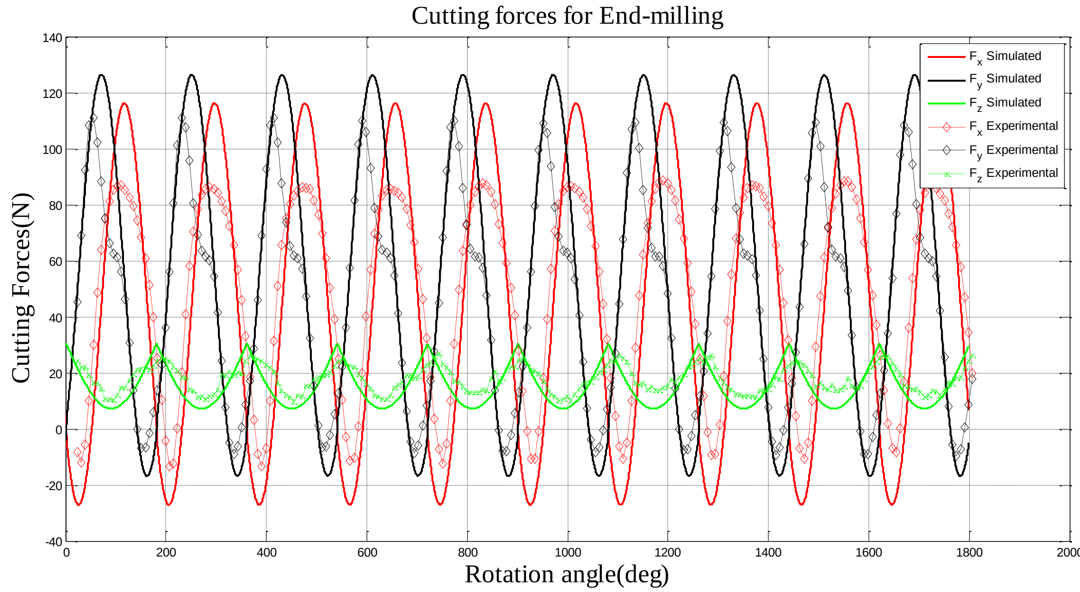

Figure 3.31 – Cutting forces of tool B at 0.25 mm/rev feed rate and 0.5 mm A_p

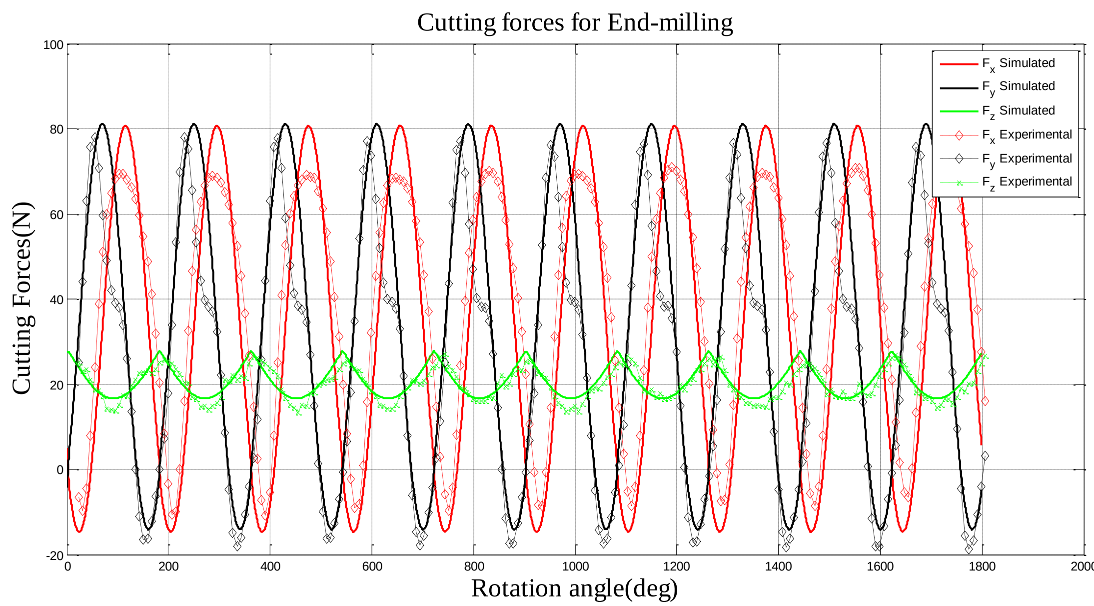

Figure 3.32 – Cutting forces of tool B at 0.10 mm/rev feed rate and 1 mm A_p

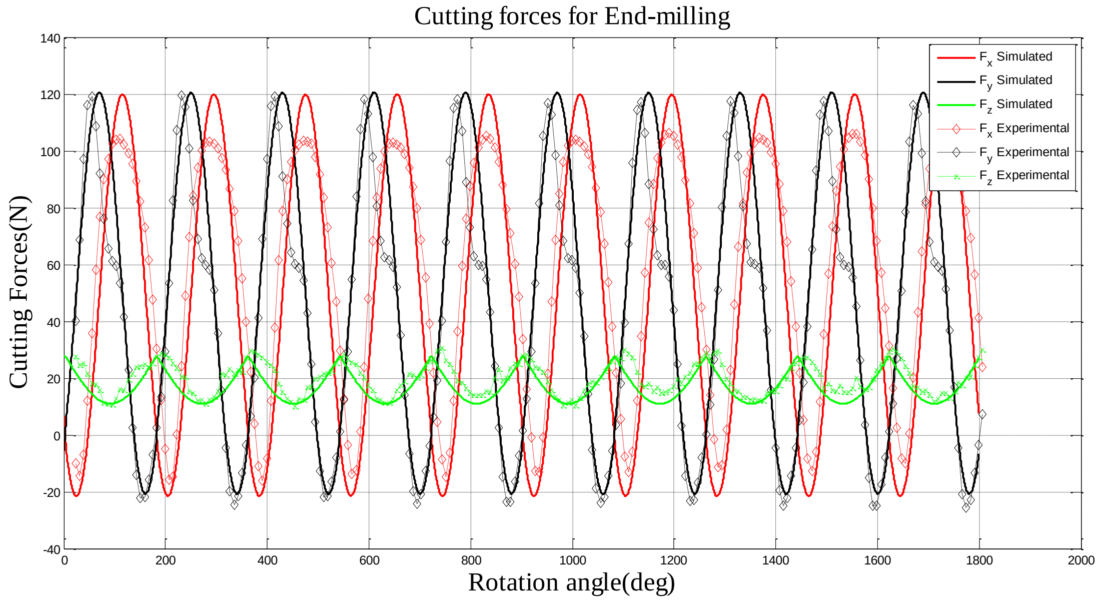

Figure 3.33 – Cutting forces of tool B at 0.15 mm/rev feed rate and 1 mm A_p

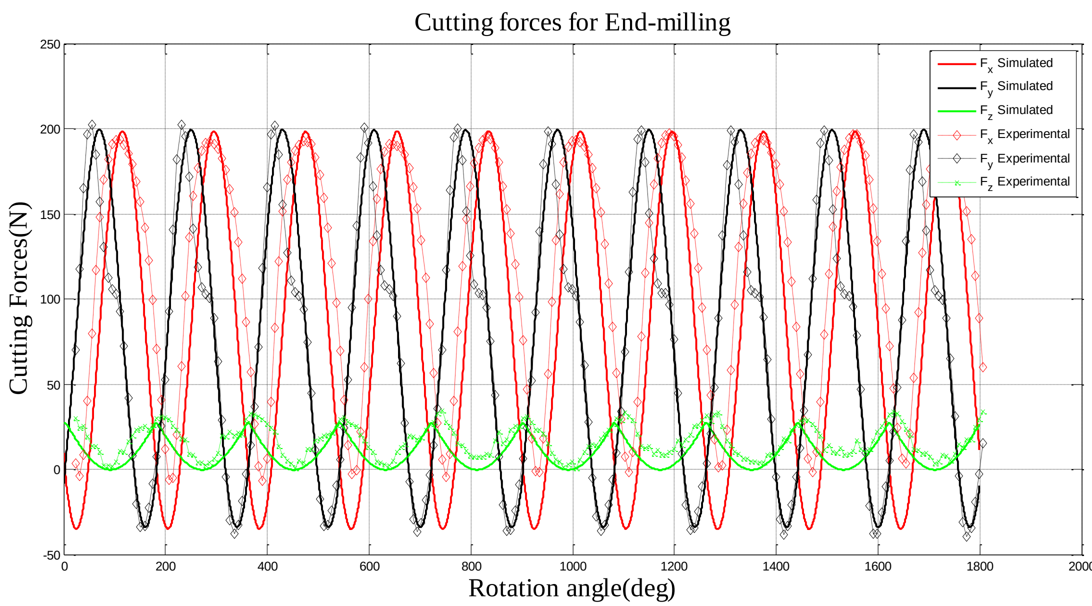

Figure 3.34 – Cutting forces of tool B at 0.25 mm/rev feed rate and 1 mm A_p

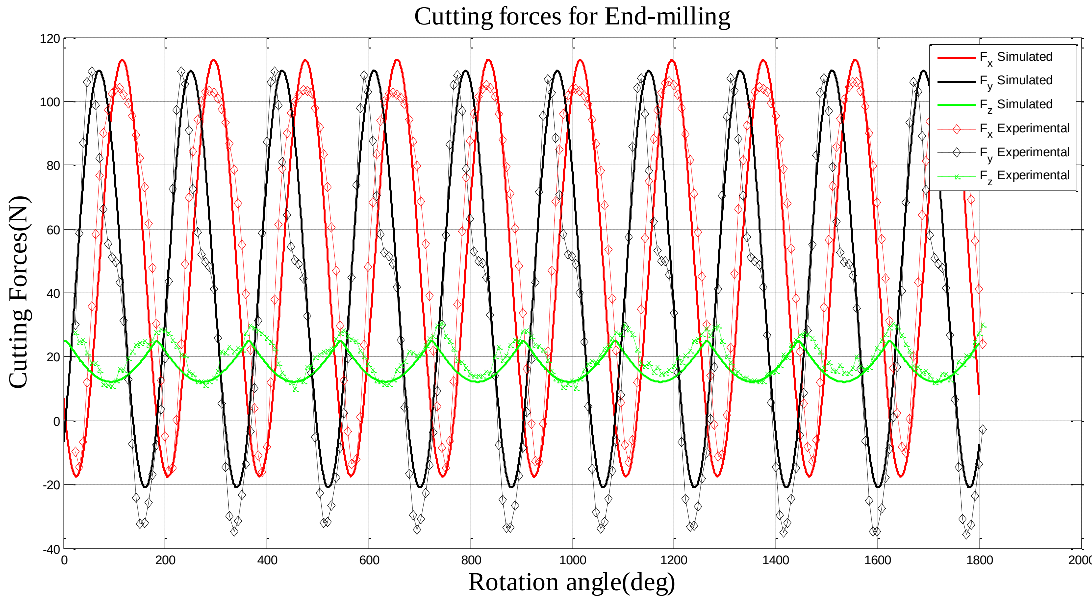

Figure 3.35 – Cutting forces of tool B at 0.10 mm/rev feed rate and 1.5 mm A_p

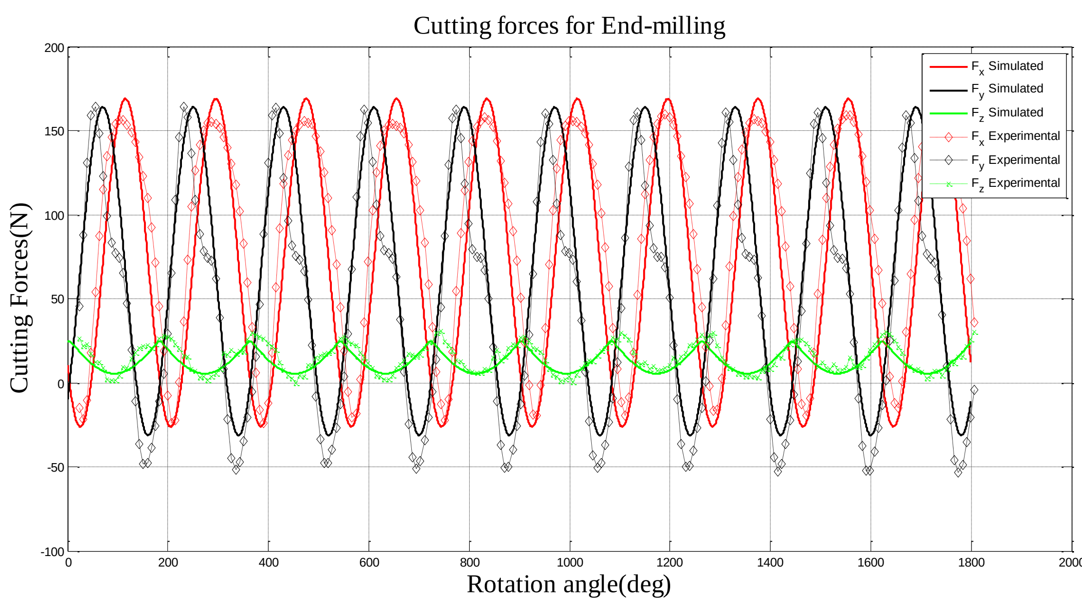

Figure 3.36 – Cutting forces of tool B at 0.15 mm/rev feed rate and 1.5 mm A_p

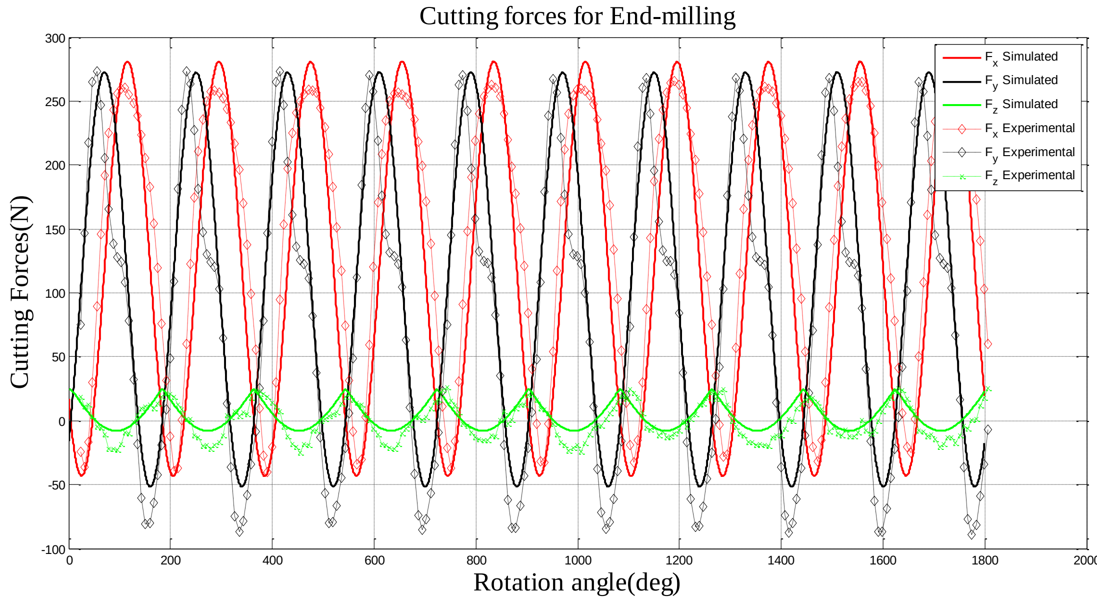

Figure 3.37 – Cutting forces of tool B at 0.25 mm/rev feed rate and 1.5 mm A_p

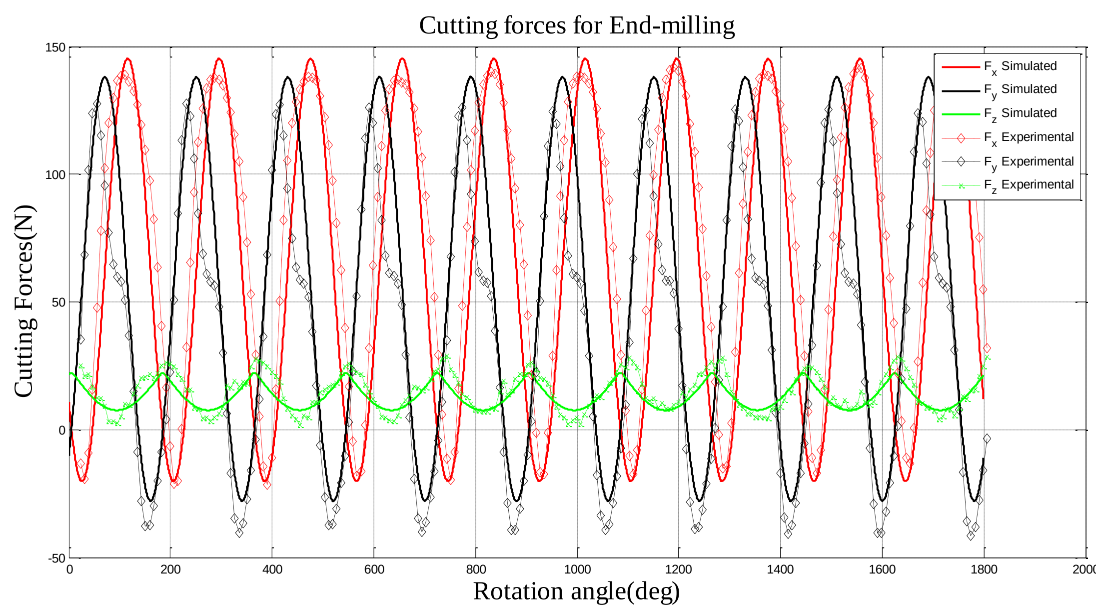

Figure 3.38 – Cutting forces of tool B at 0.10 mm/rev feed rate and 2 mm A_p

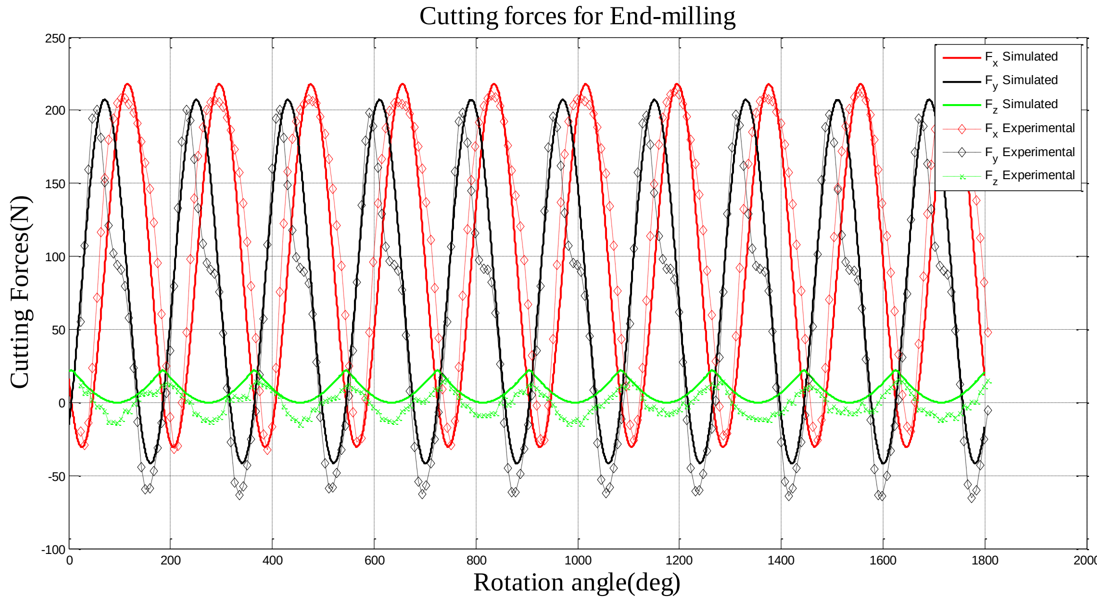

Figure 3.39 – Cutting forces of tool B at 0.15 mm/rev feed rate and 2 mm A_p

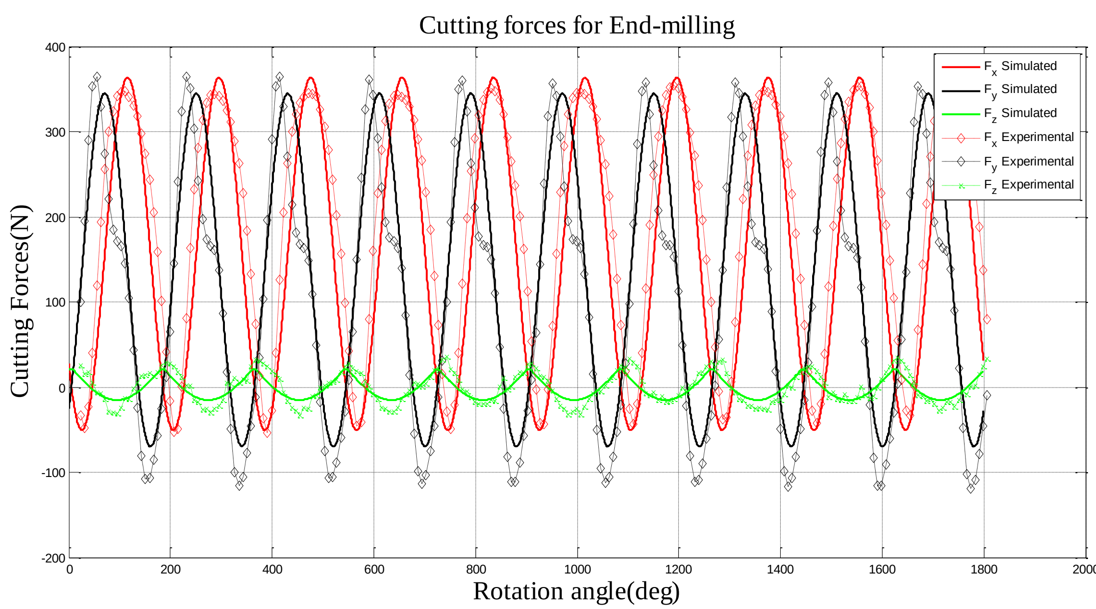

Figure 3.40 – Cutting forces of tool B at 0.25 mm/rev feed rate and 2 mm A_p

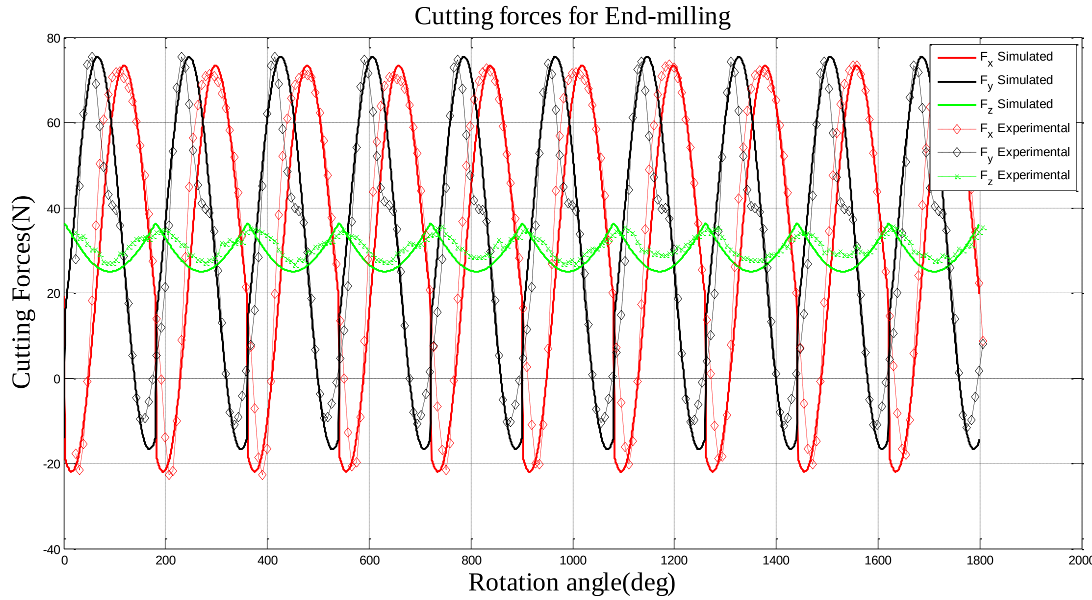

Figure 3.41 – Cutting forces of tool C at 0.10 mm/rev feed rate and 0.5 mm A_p

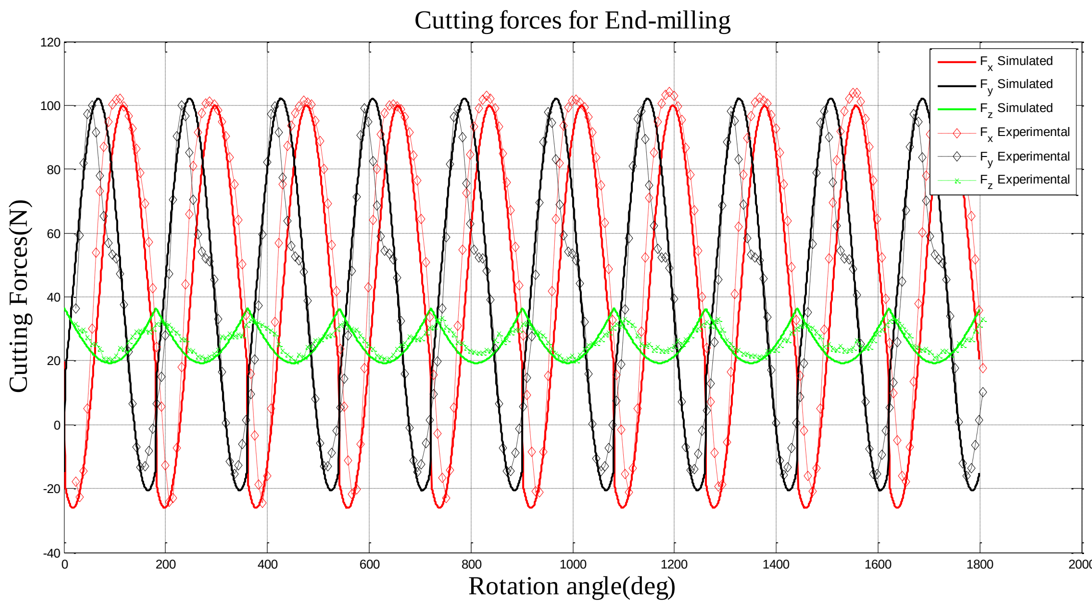

Figure 3.42 – Cutting forces of tool C at 0.15 mm/rev feed rate and 0.5 mm A_p

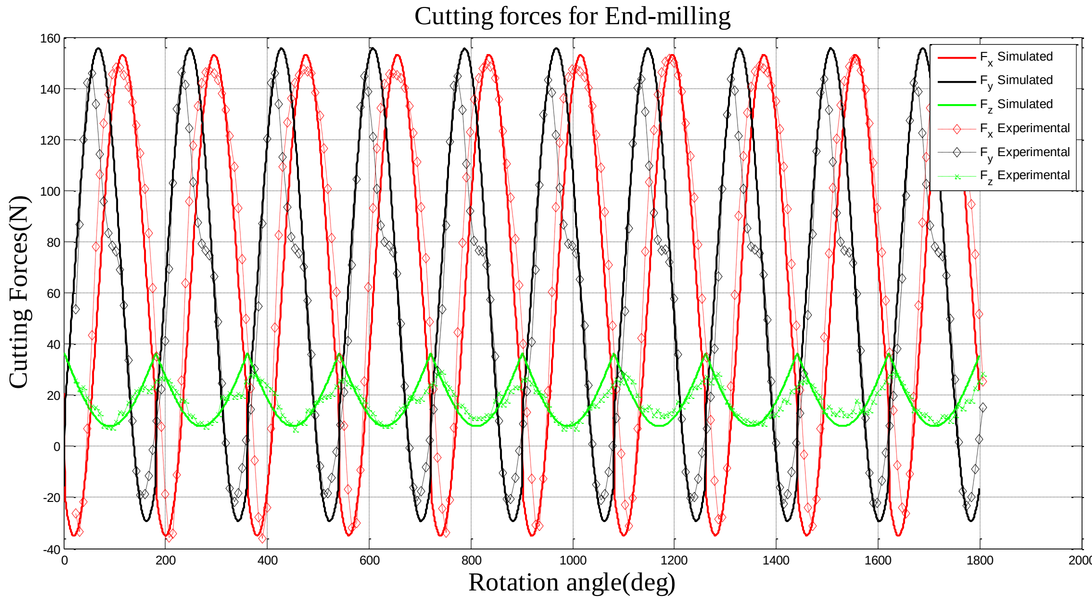

Figure 3.43 – Cutting forces of tool C at 0.25 mm/rev feed rate and 0.5 mm A_p

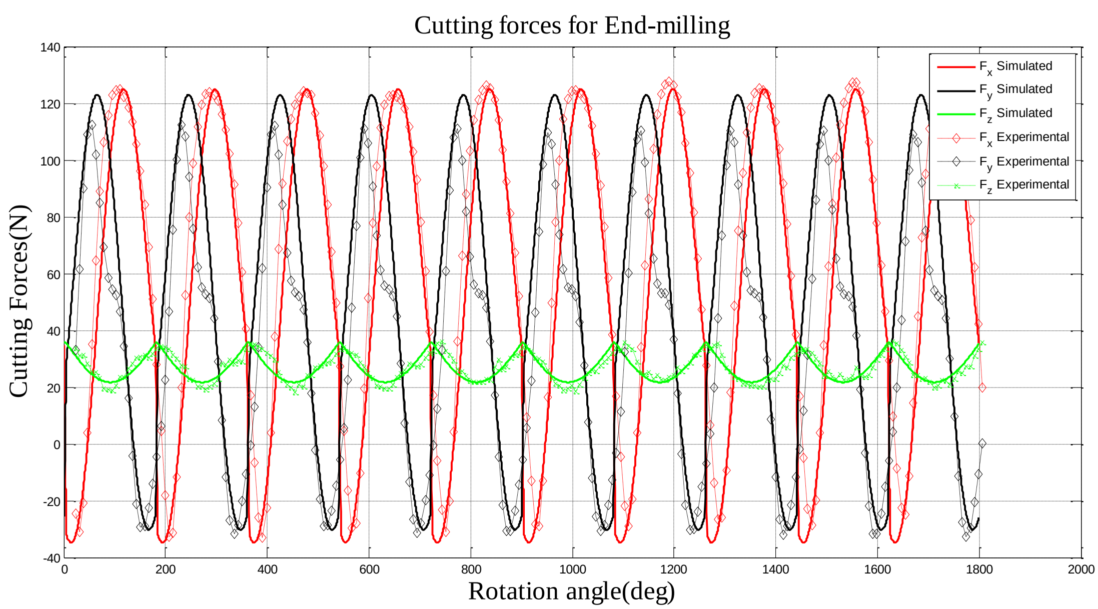

Figure 3.44 – Cutting forces of tool C at 0.10 mm/rev feed rate and 1 mm A_p

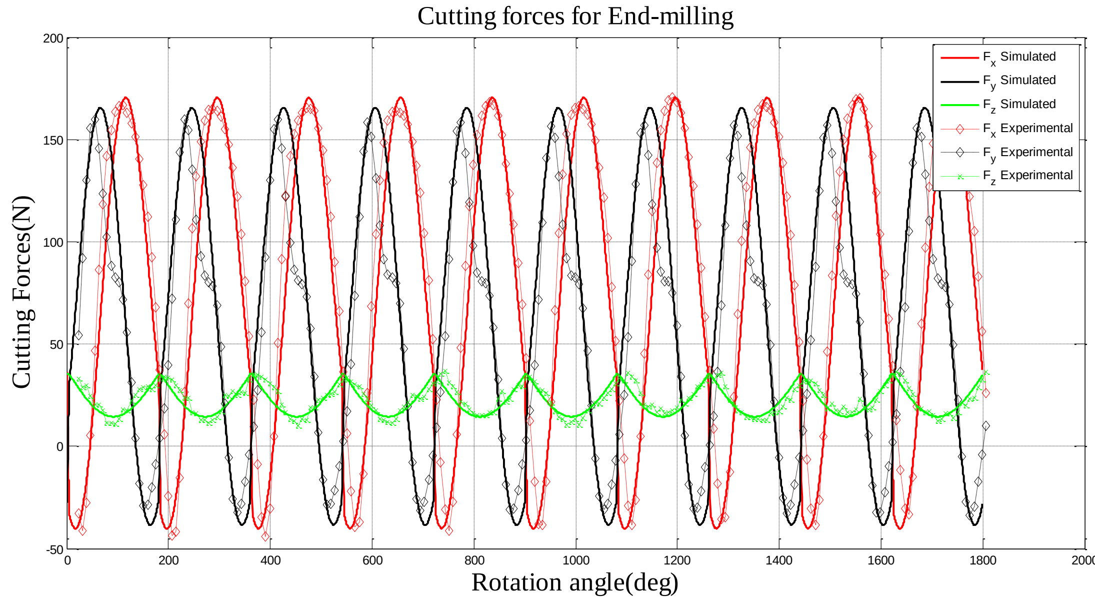

Figure 3.45 – Cutting forces of tool C at 0.15 mm/rev feed rate and 1 mm A_p

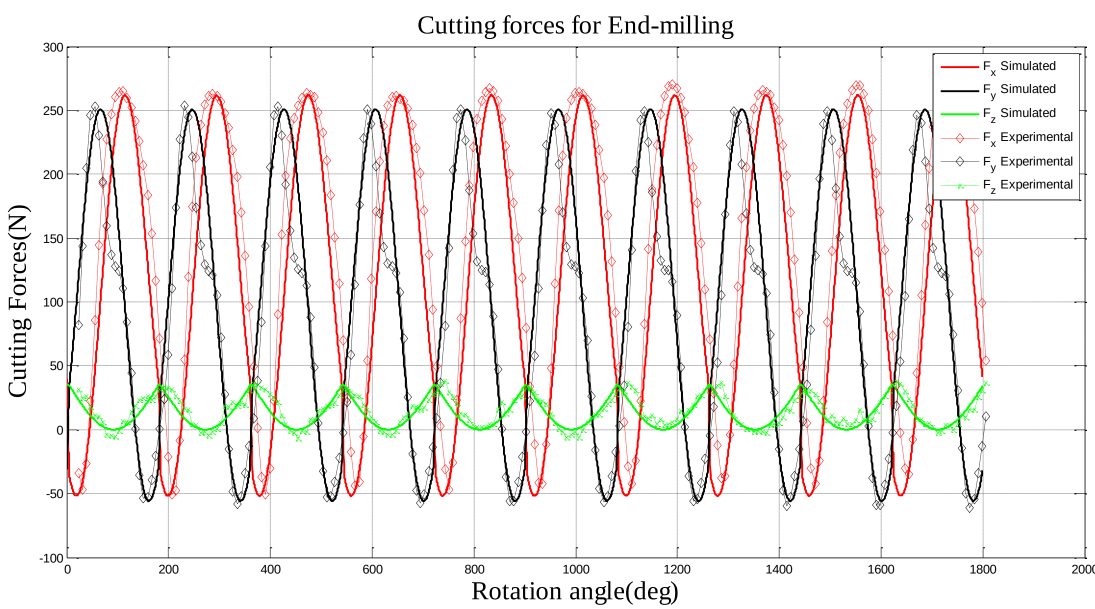

Figure 3.46 – Cutting forces of tool C at 0.25 mm/rev feed rate and 1 mm A_p

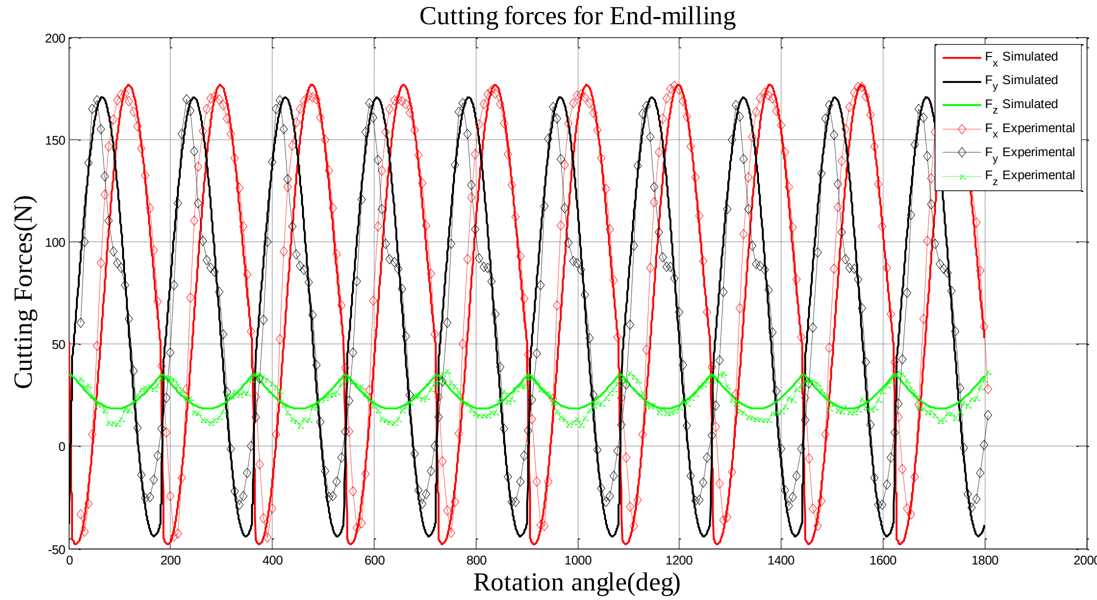

Figure 3.47 – Cutting forces of tool C at 0.10 mm/rev feed rate and 1.5 mm A_p

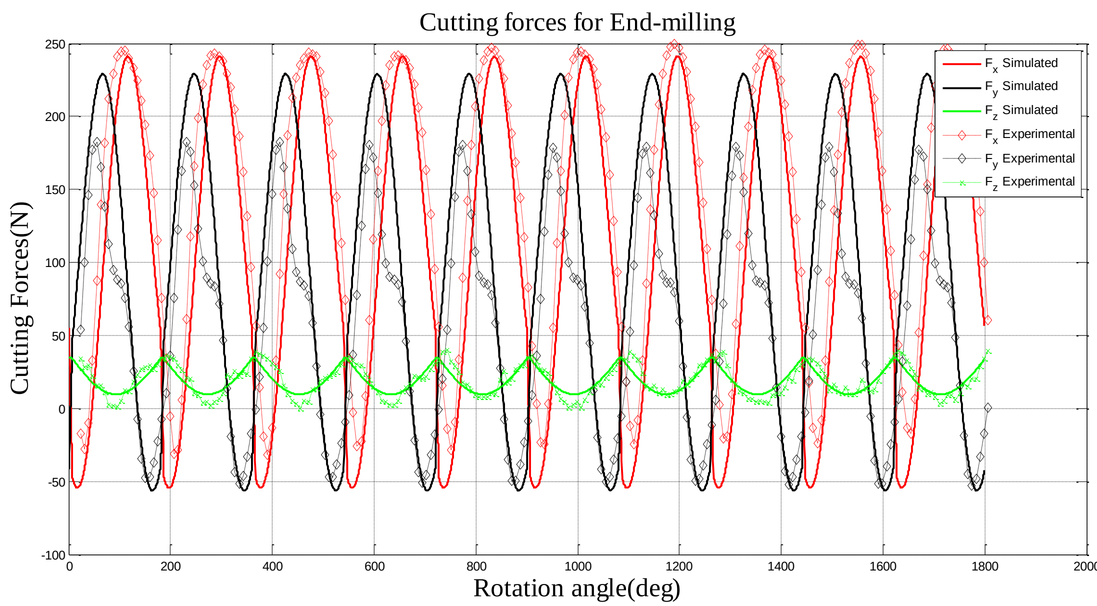

Figure 3.48 – Cutting forces of tool C at 0.15 mm/rev feed rate and 1.5 mm A_p

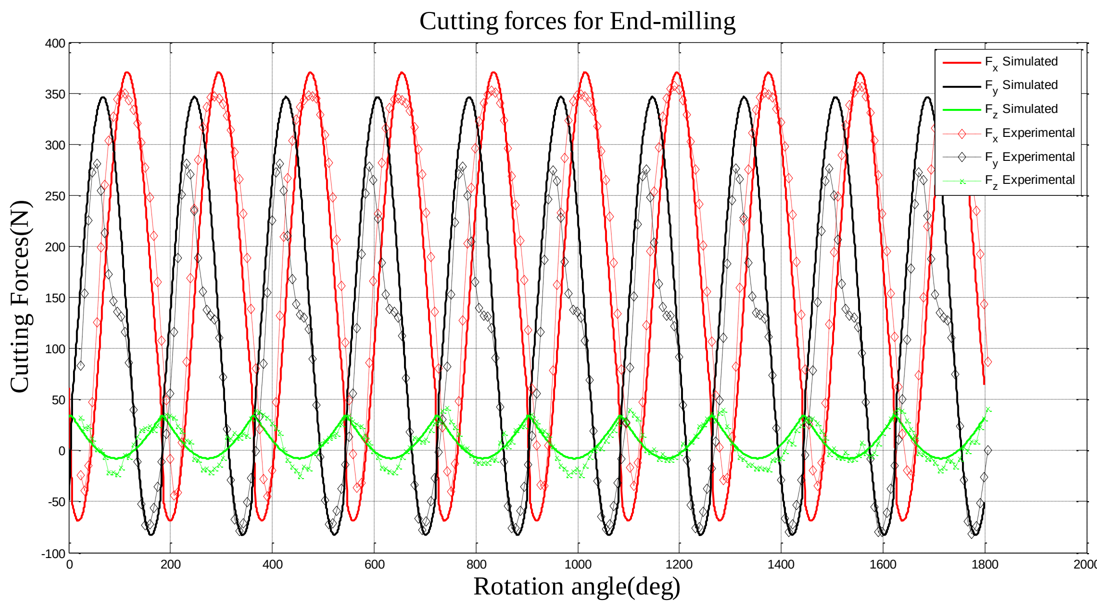

Figure 3.49 – Cutting forces of tool C at 0.25 mm/rev feed rate and 1.5 mm A_p

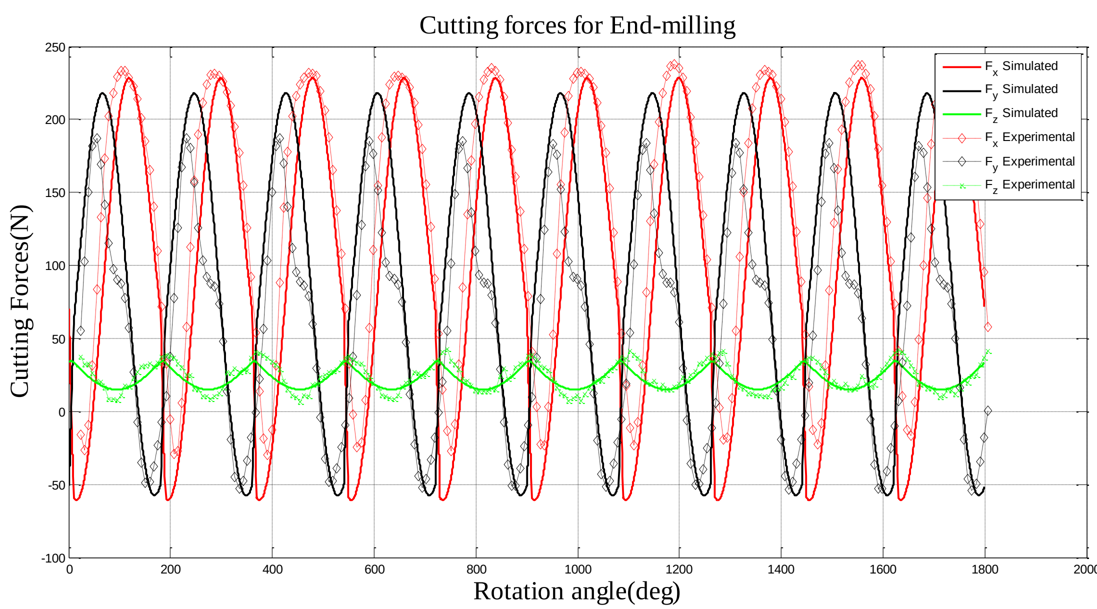

Figure 3.50 – Cutting forces of tool C at 0.10 mm/rev feed rate and 2 mm A_p

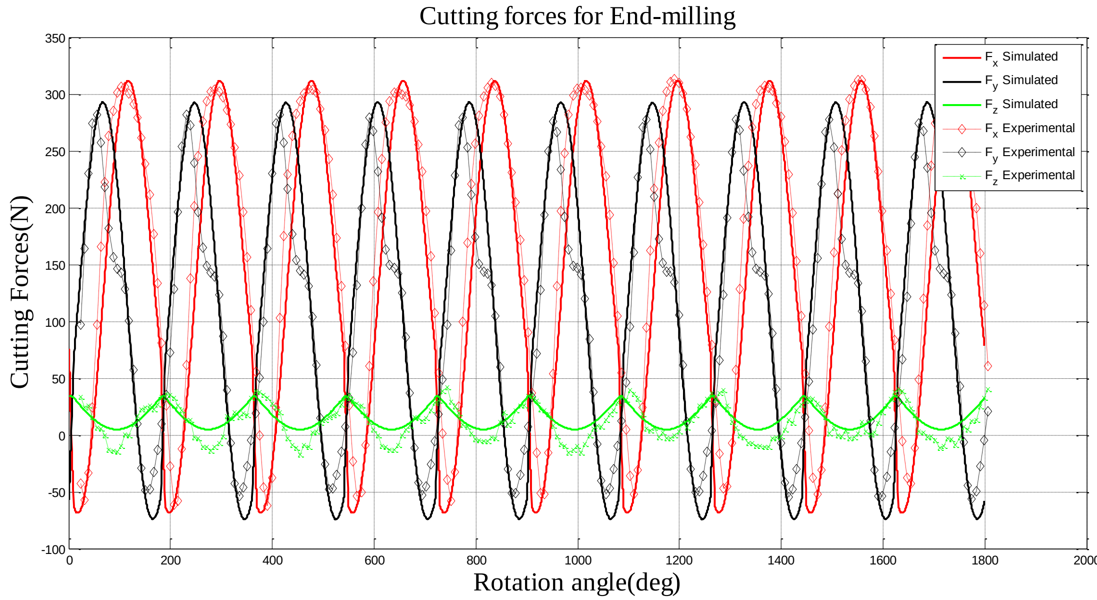

Figure 3.51 – Cutting forces of tool C at 0.15 mm/rev feed rate and 2 mm A_p

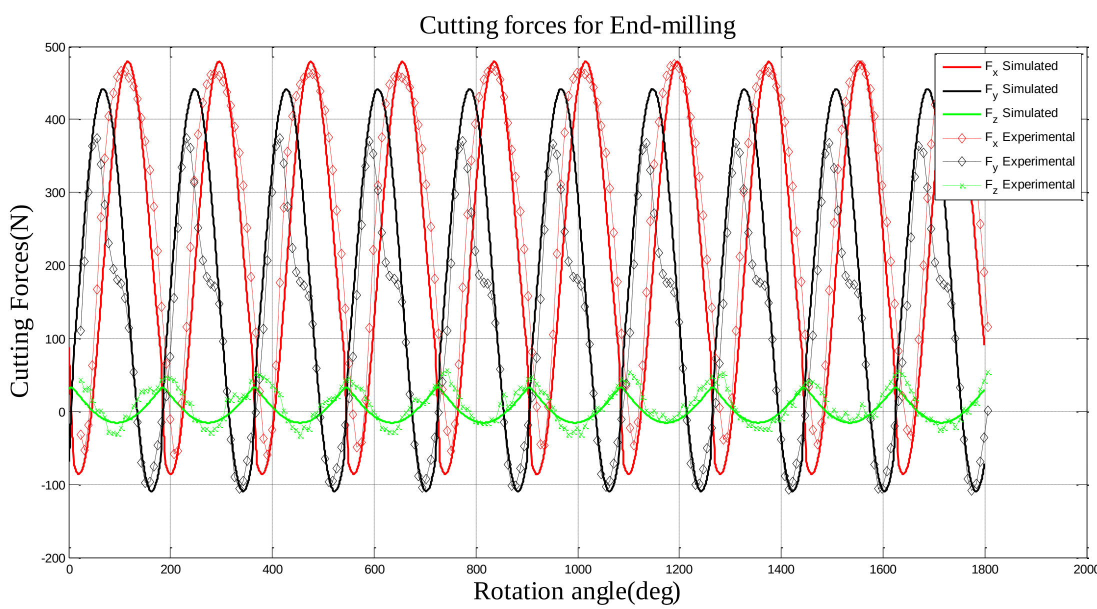

Figure 3.52 – Cutting forces of tool C at 0.25 mm/rev feed rate and 2 mm A_p

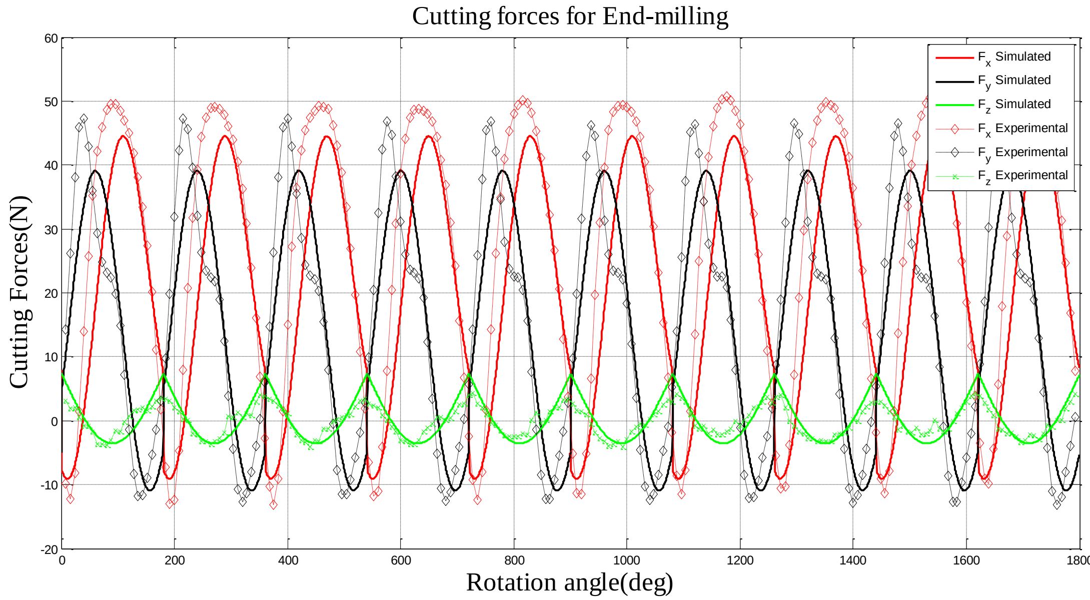

Figure 3.53 – Cutting forces of tool D at 0.10 mm/rev feed rate and 0.5 mm A_p

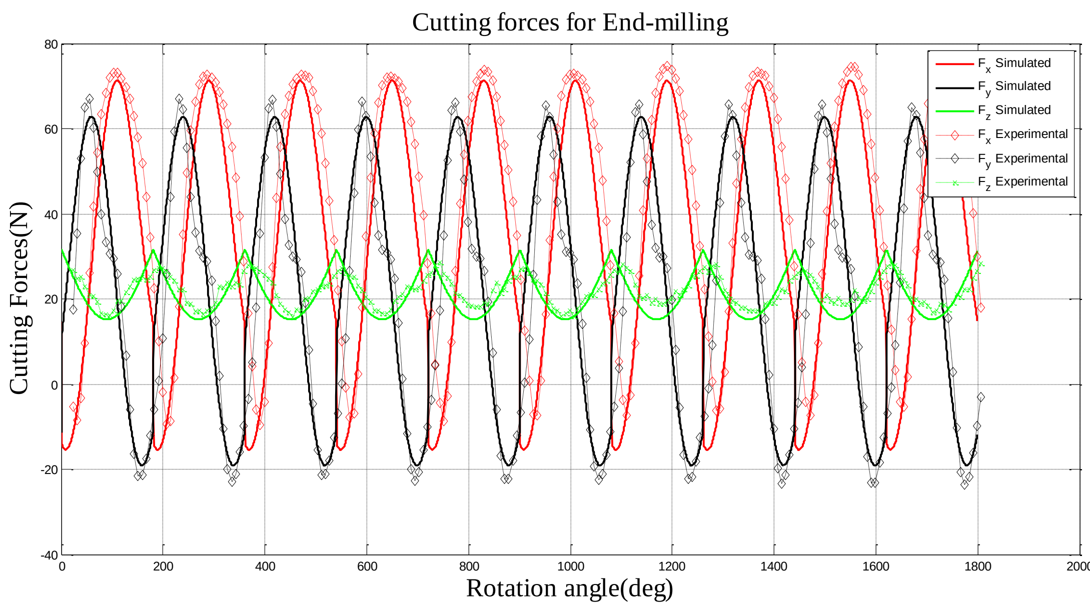

Figure 3.54 – Cutting forces of tool D at 0.15 mm/rev feed rate and 0.5 mm A_p

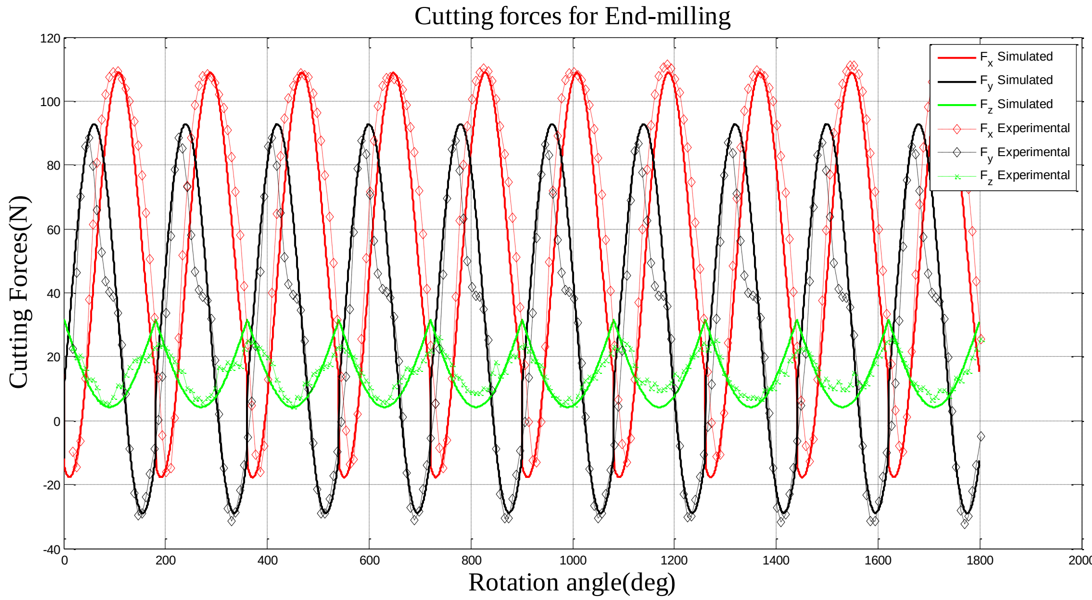

Figure 3.55 – Cutting forces of tool D at 0.25 mm/rev feed rate and 0.5 mm A_p

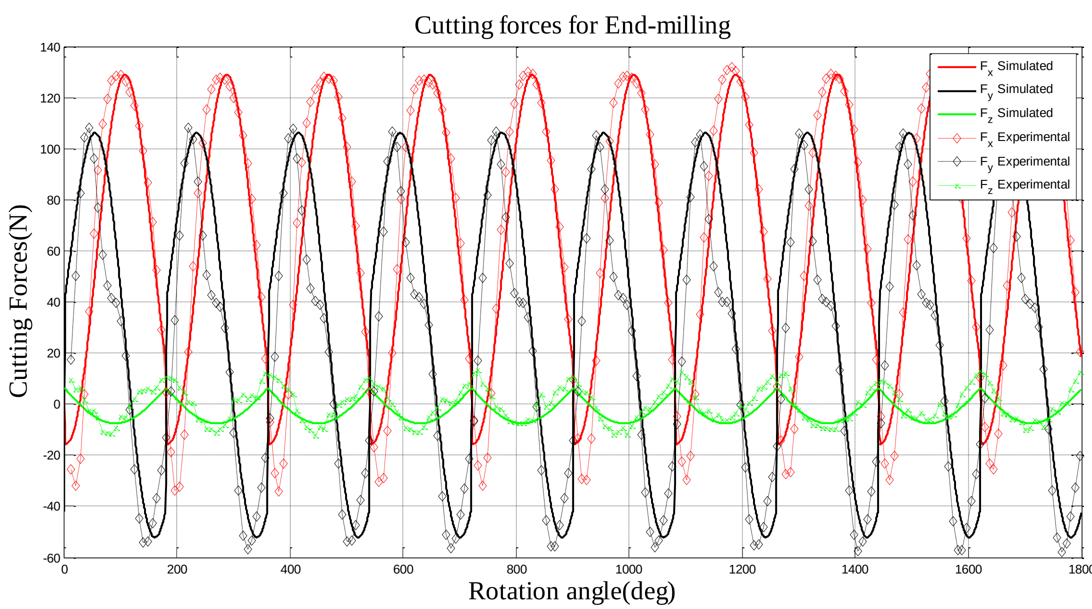

Figure 3.56 – Cutting forces of tool D at 0.10 mm/rev feed rate and 1 mm A_p

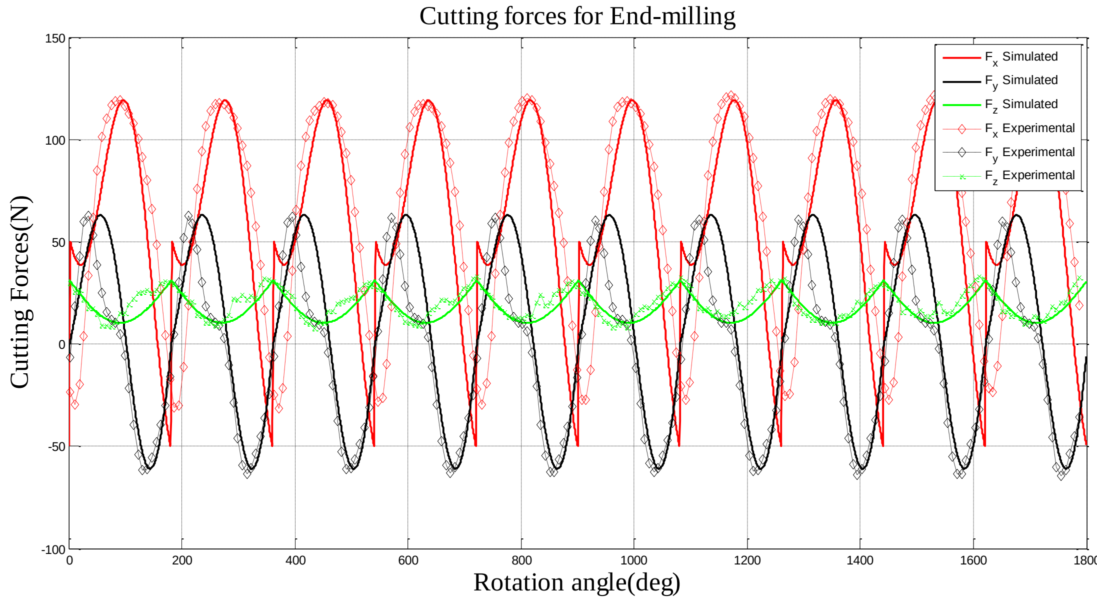

Figure 3.57 – Cutting forces of tool D at 0.15 mm/rev feed rate and 1 mm A_p

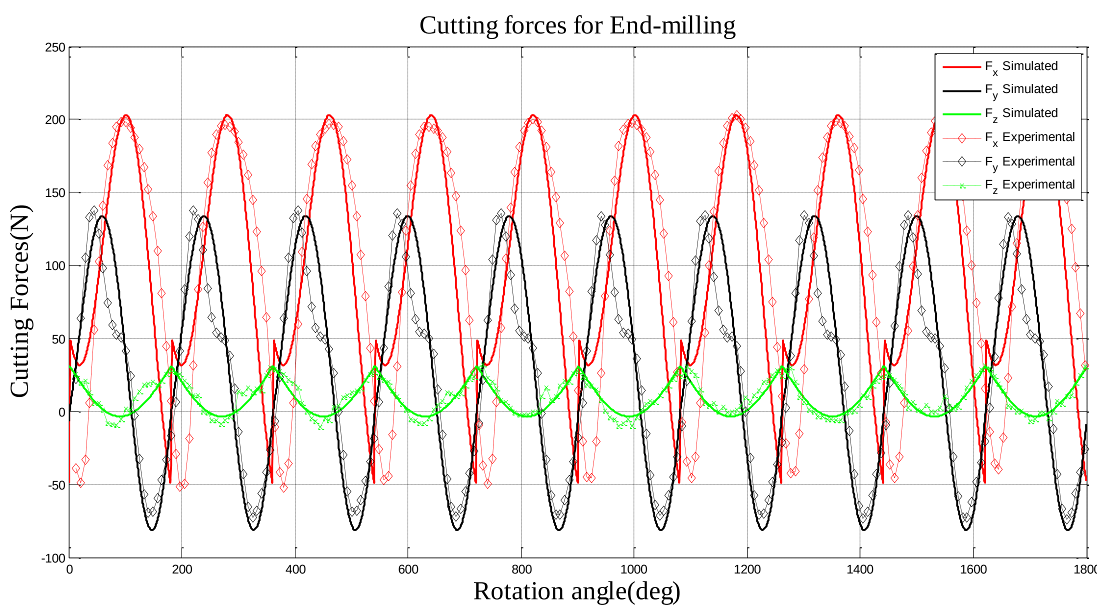

Figure 3.58 – Cutting forces of tool D at 0.25 mm/rev feed rate and 1 mm A_p

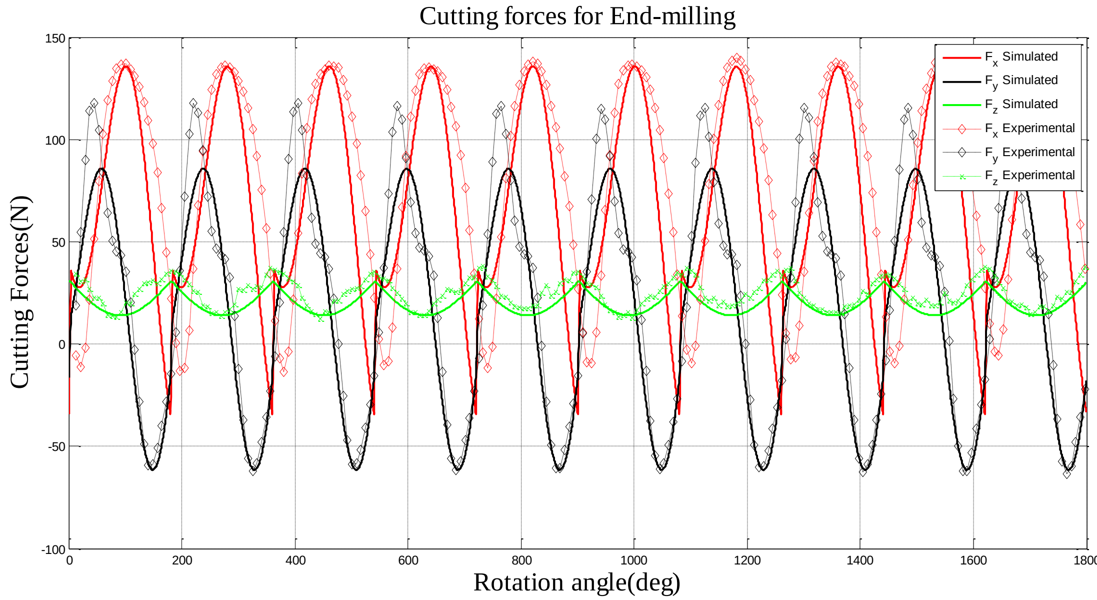

Figure 3.59 – Cutting forces of tool D at 0.10 mm/rev feed rate and 1.5 mm A_p

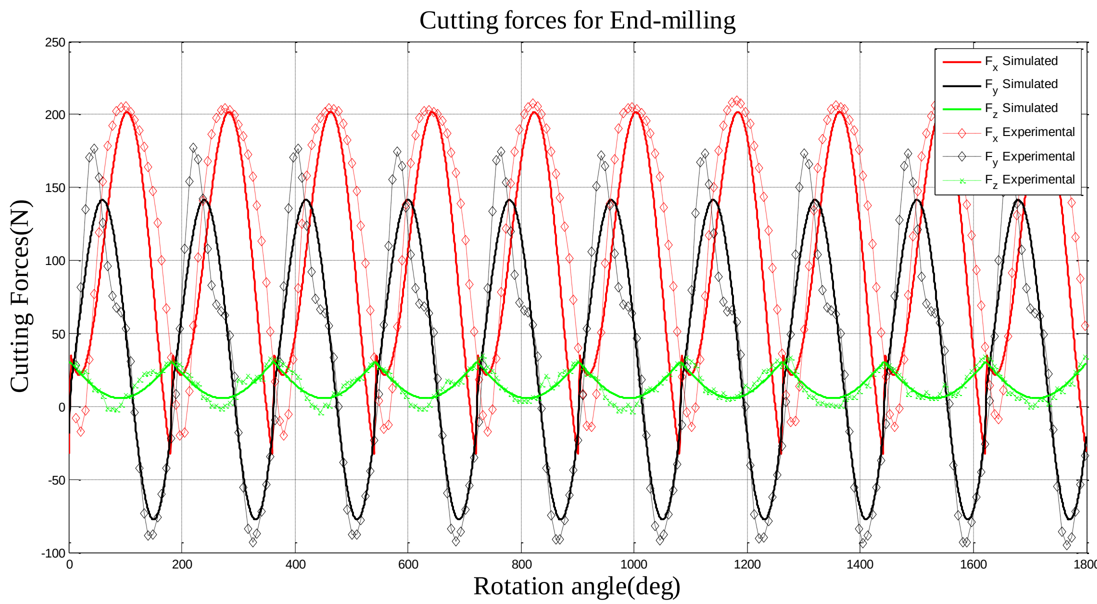

Figure 3.60 – Cutting forces of tool D at 0.15 mm/rev feed rate and 1.5 mm A_p

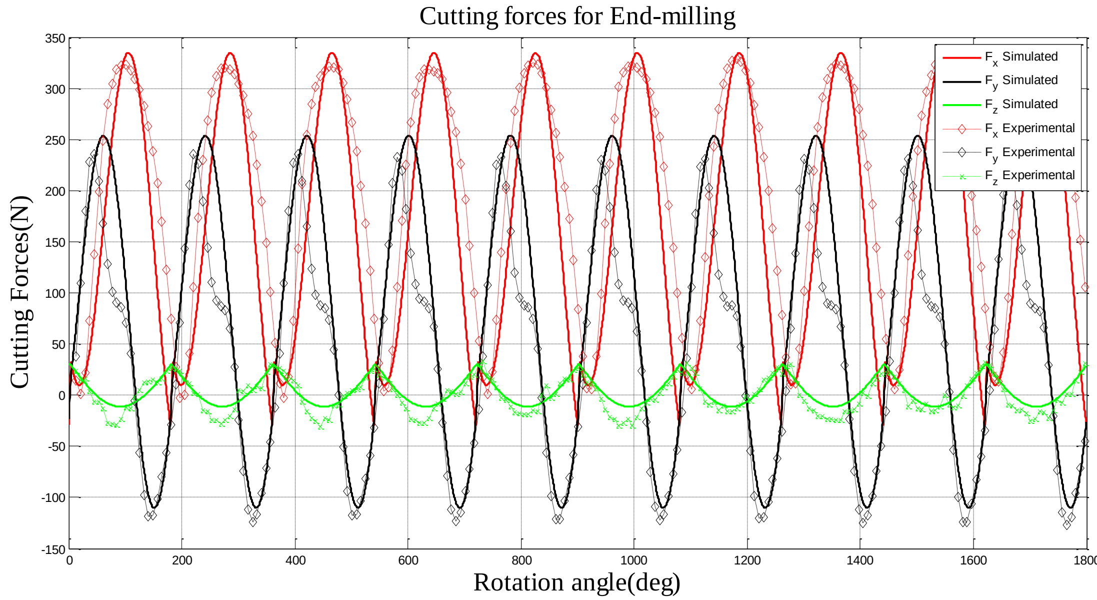

Figure 3.61 – Cutting forces of tool D at 0.25 mm/rev feed rate and 1.5 mm A_p

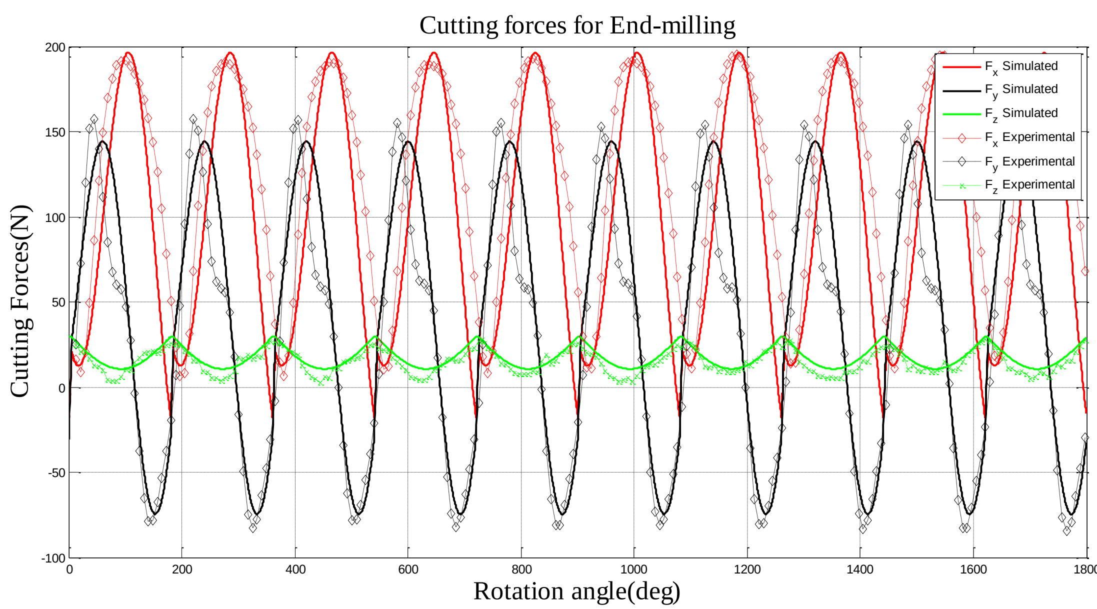

Figure 3.62 – Cutting forces of tool D at 0.10 mm/rev feed rate and 2 mm A_p

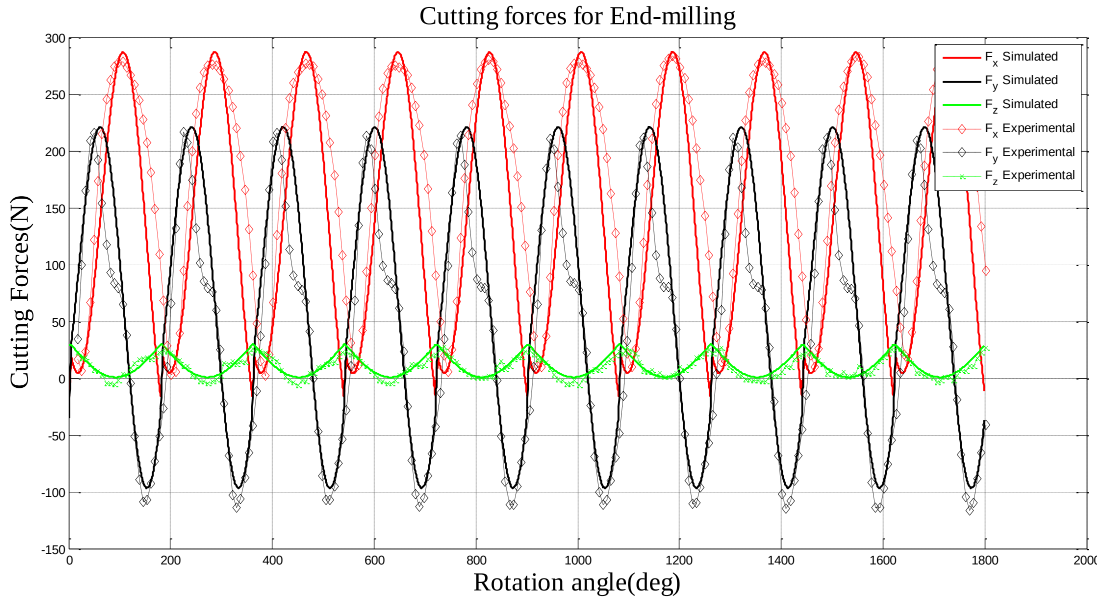

Figure 3.63 – Cutting forces of tool D at 0.15 mm/rev feed rate and 2 mm A_p

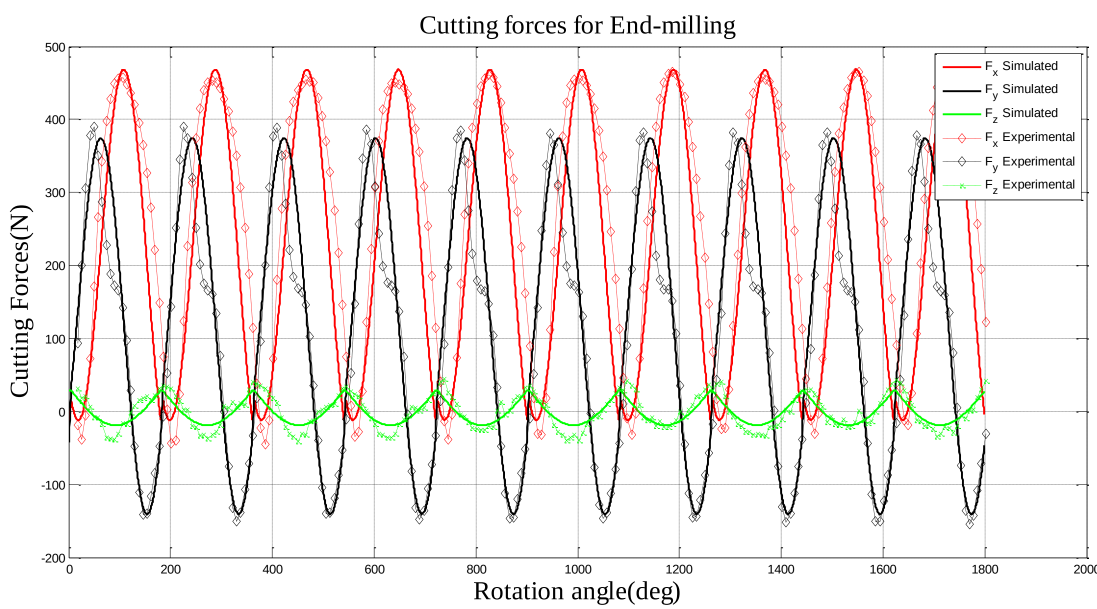

Figure 3.64 – Cutting forces of tool D at 0.25 mm/rev feed rate and 2 mm A_p

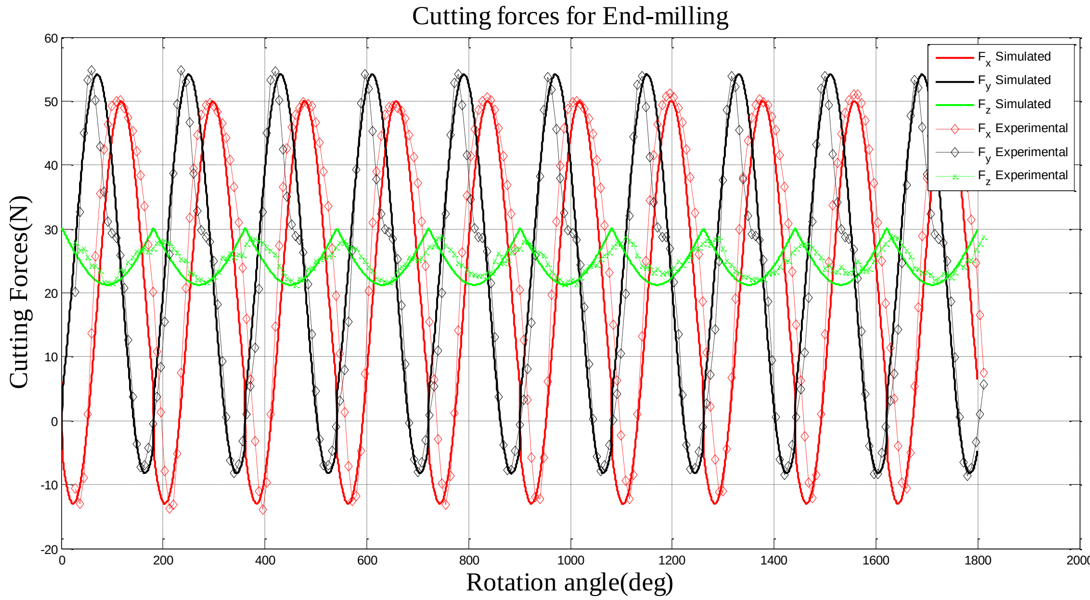

Figure 3.65 – Cutting forces of tool E at 0.10 mm/rev feed rate and 0.5 mm A_p

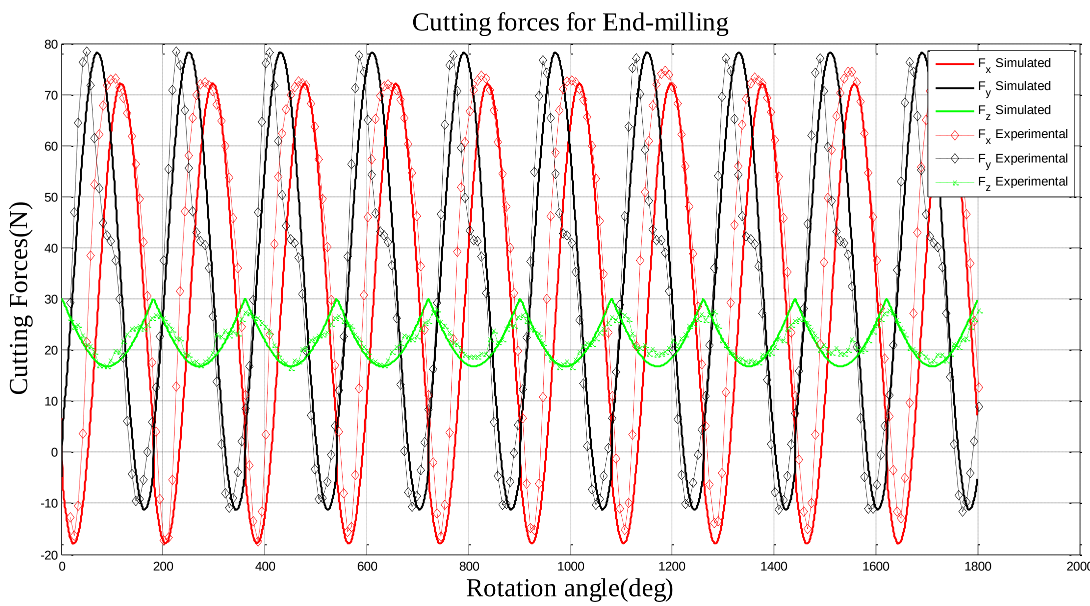

Figure 3.66 – Cutting forces of tool E at 0.15 mm/rev feed rate and 0.5 mm A_p

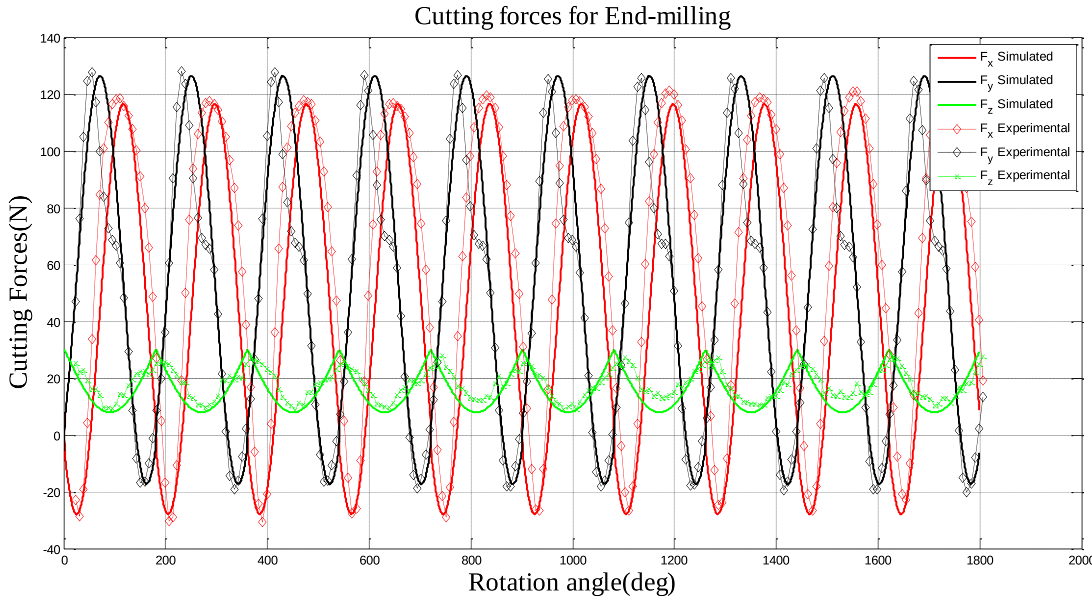

Figure 3.67 – Cutting forces of tool E at 0.25 mm/rev feed rate and 0.5 mm A_p

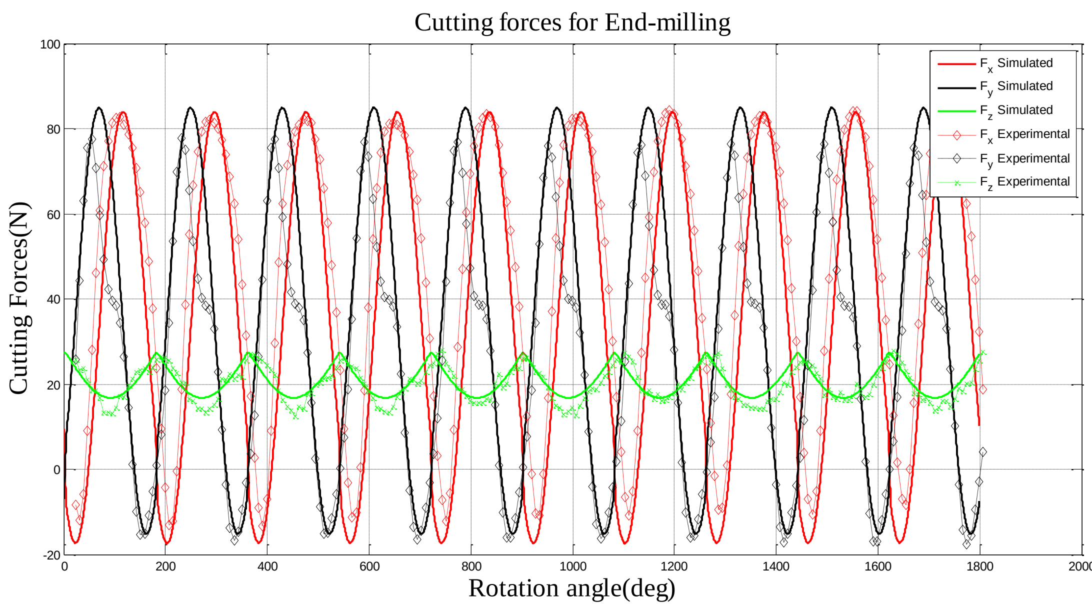

Figure 3.68 – Cutting forces of tool E at 0.10 mm/rev feed rate and 1 mm A_p

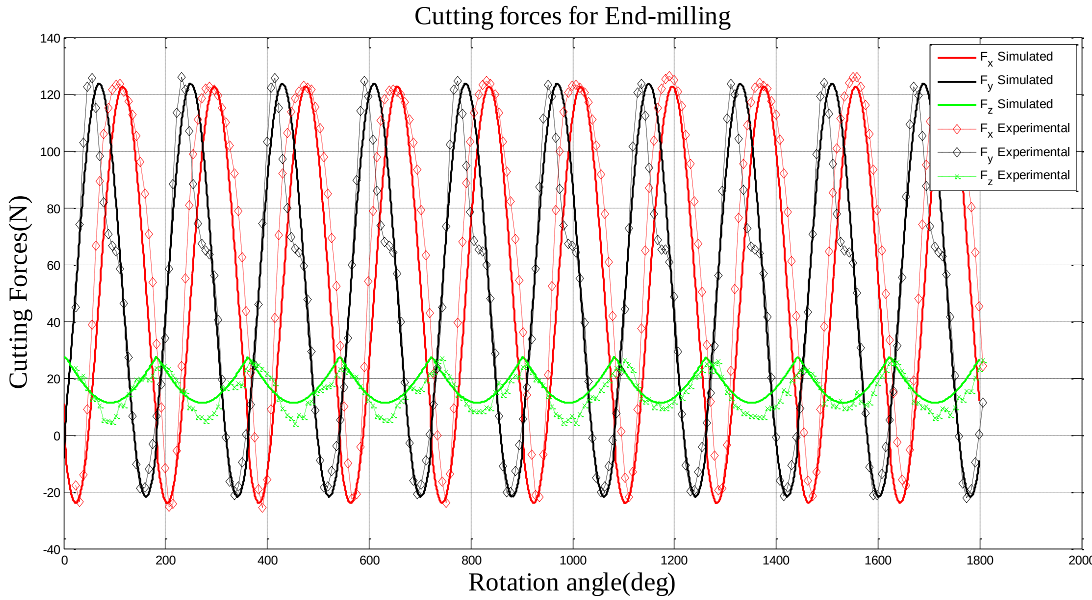

Figure 3.69 – Cutting forces of tool E at 0.15 mm/rev feed rate and 1 mm A_p

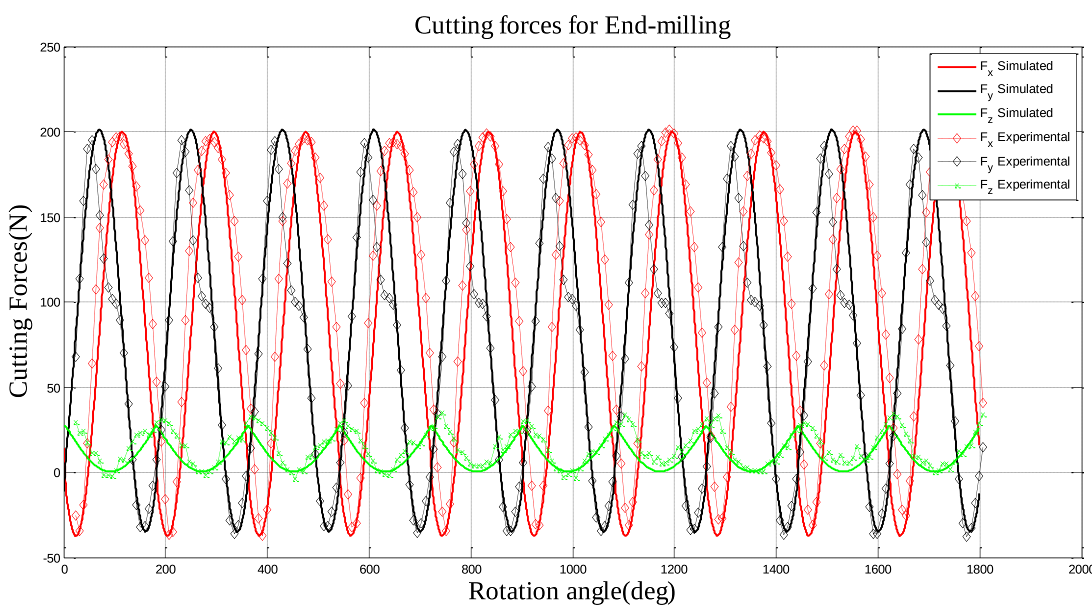

Figure 3.70 – Cutting forces of tool E at 0.25 mm/rev feed rate and 1 mm A_p

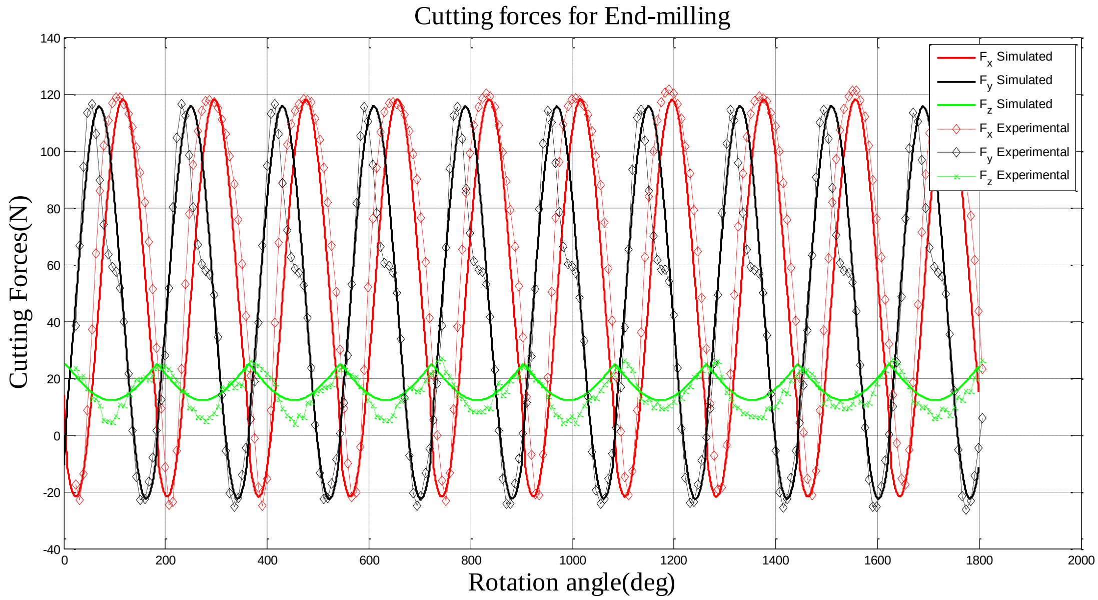

Figure 3.71 – Cutting forces of tool E at 0.10 mm/rev feed rate and 1.5 mm A_p

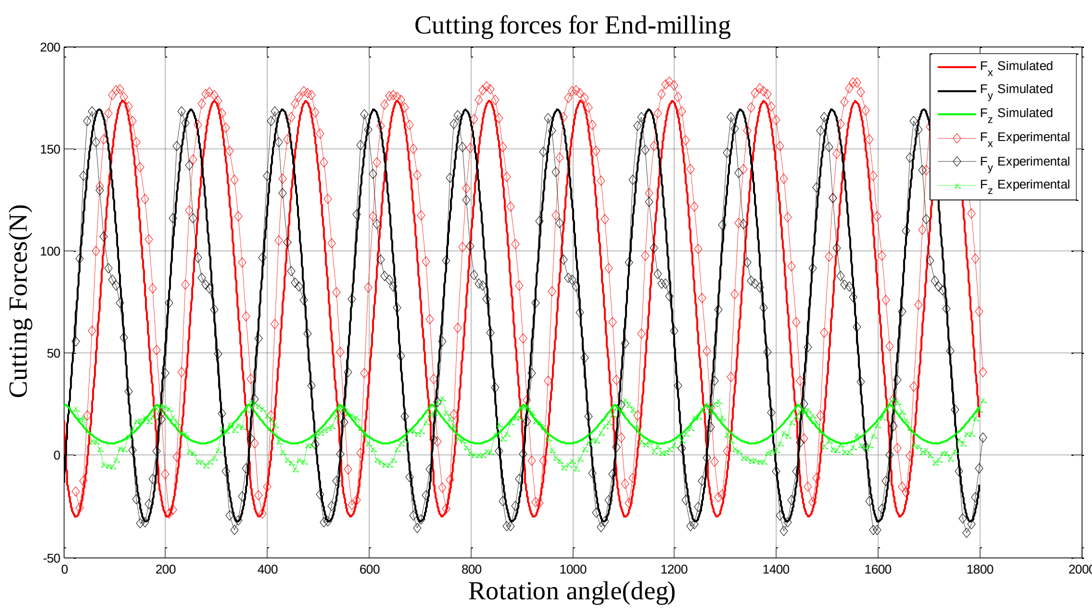

Figure 3.72 – Cutting forces of tool E at 0.15 mm/rev feed rate and 1.5 mm A_p

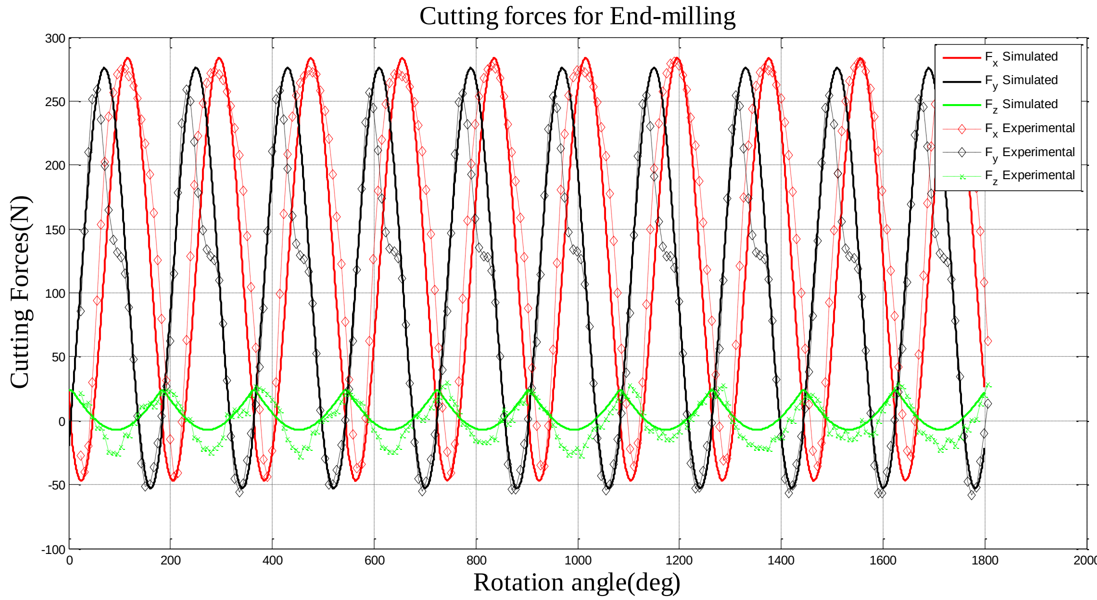

Figure 3.73 – Cutting forces of tool E at 0.25 mm/rev feed rate and 1.5 mm A_p

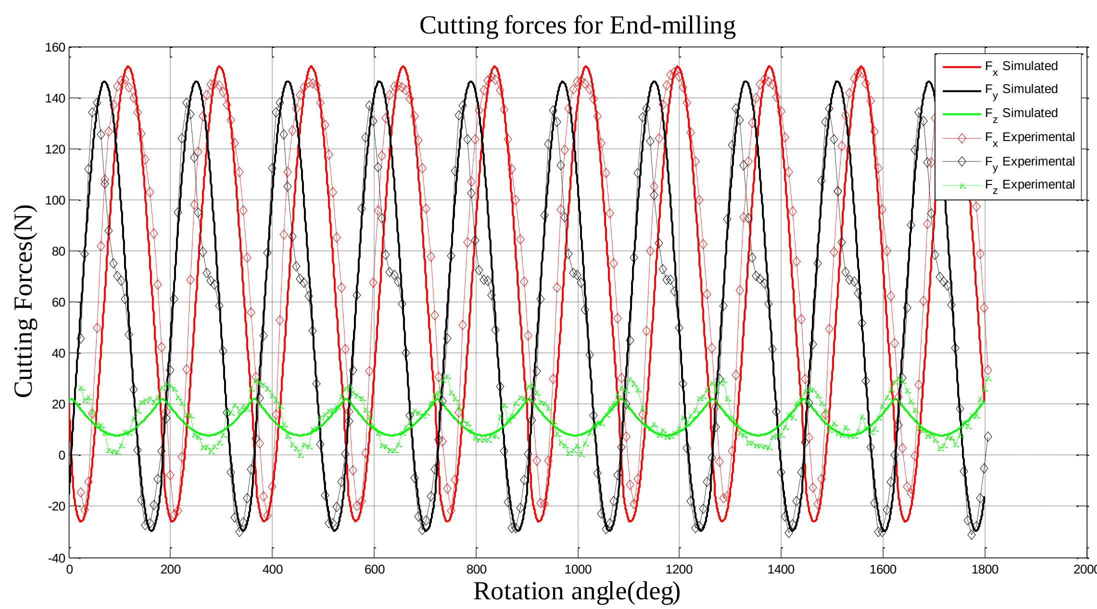

Figure 3.74 – Cutting forces of tool E at 0.10 mm/rev feed rate and 2 mm A_p

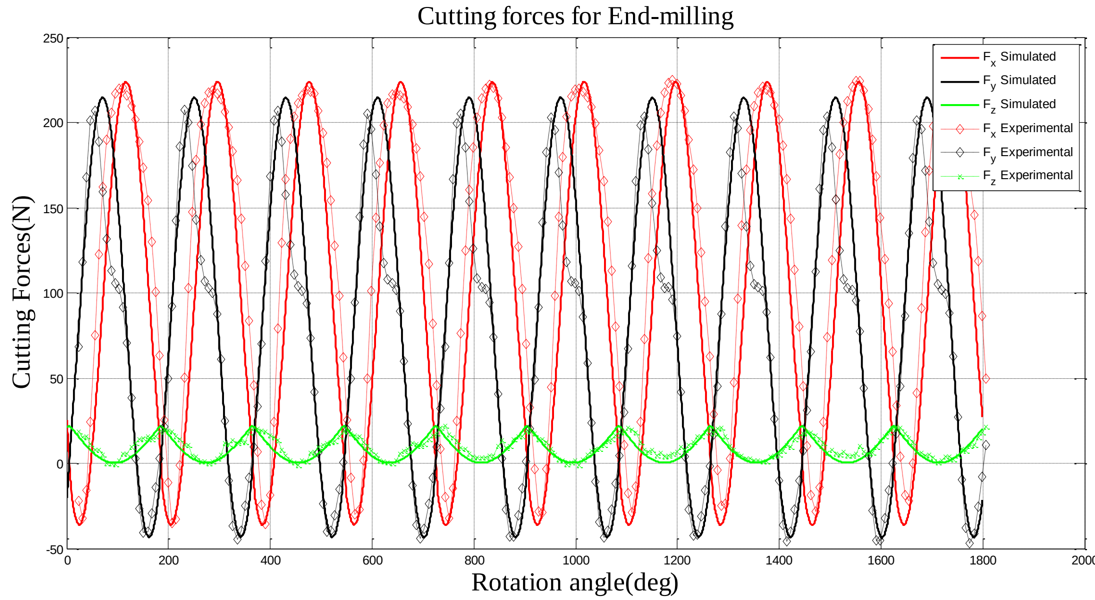

Figure 3.75 – Cutting forces of tool E at 0.15 mm/rev feed rate and 2 mm A_p

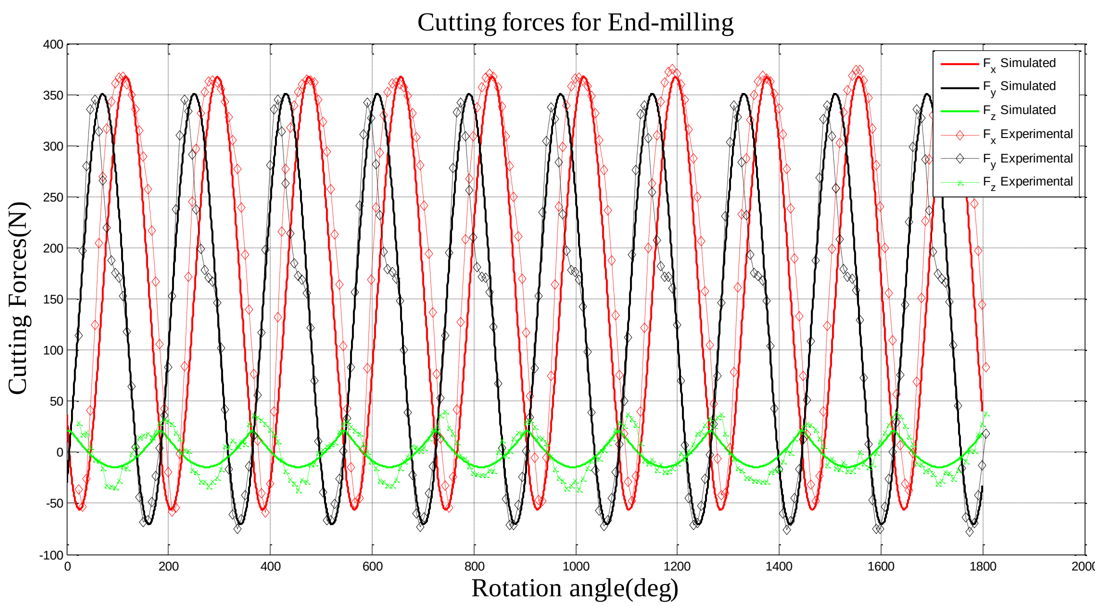

Figure 3.76 – Cutting forces of tool E at 0.25 mm/rev feed rate and 2 mm A_p

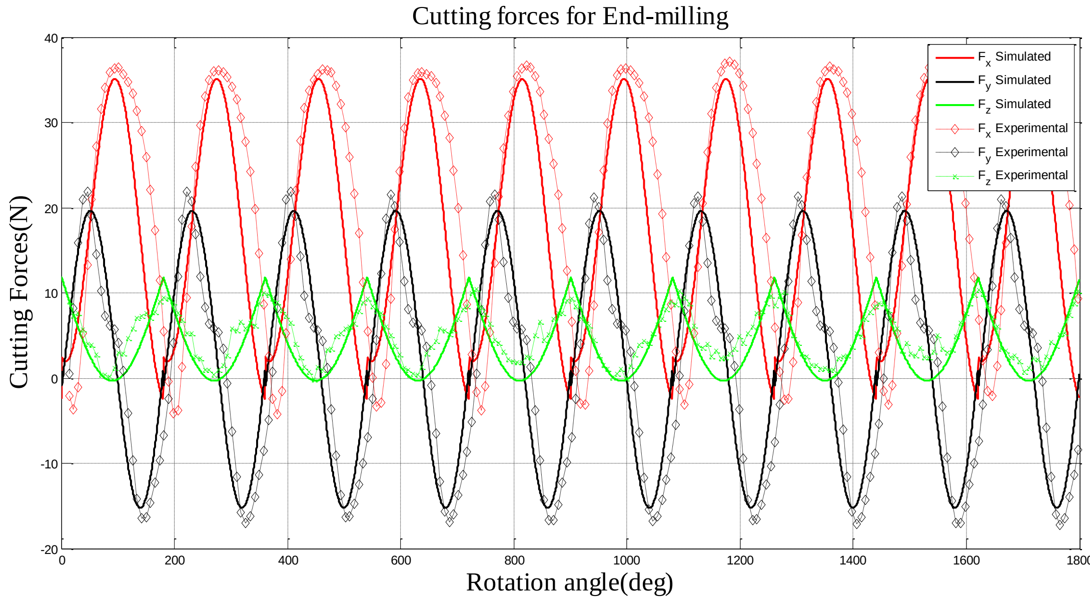

Figure 3.77 – Cutting forces of tool F at 0.10 mm/rev feed rate and 0.5 mm A_p

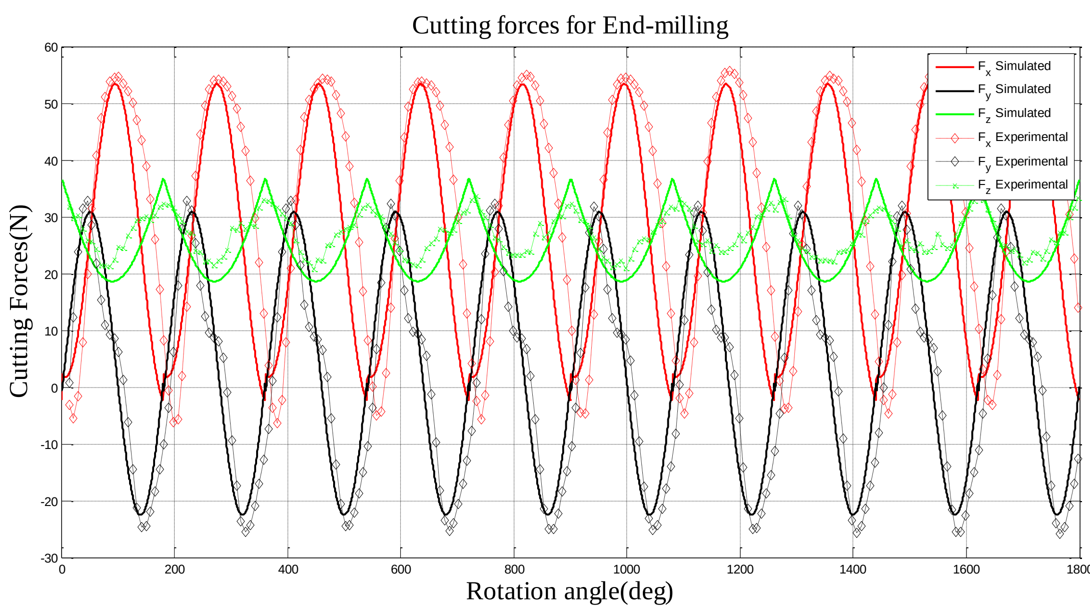

Figure 3.78 – Cutting forces of tool F at 0.15 mm/rev feed rate and 0.5 mm A_p

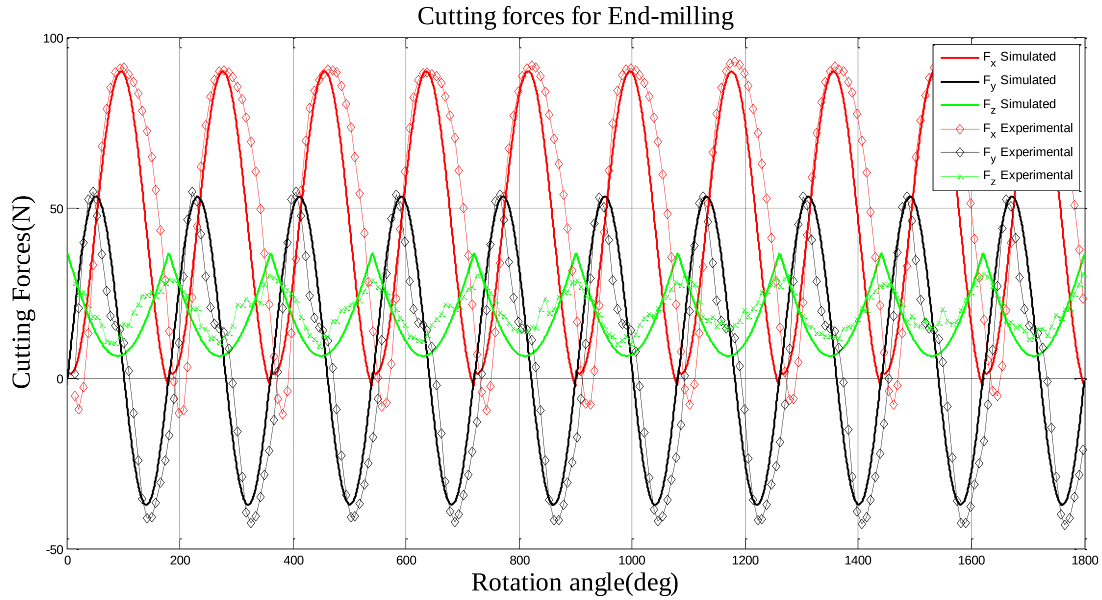

Figure 3.79 – Cutting forces of tool F at 0.25 mm/rev feed rate and 0.5 mm A_p

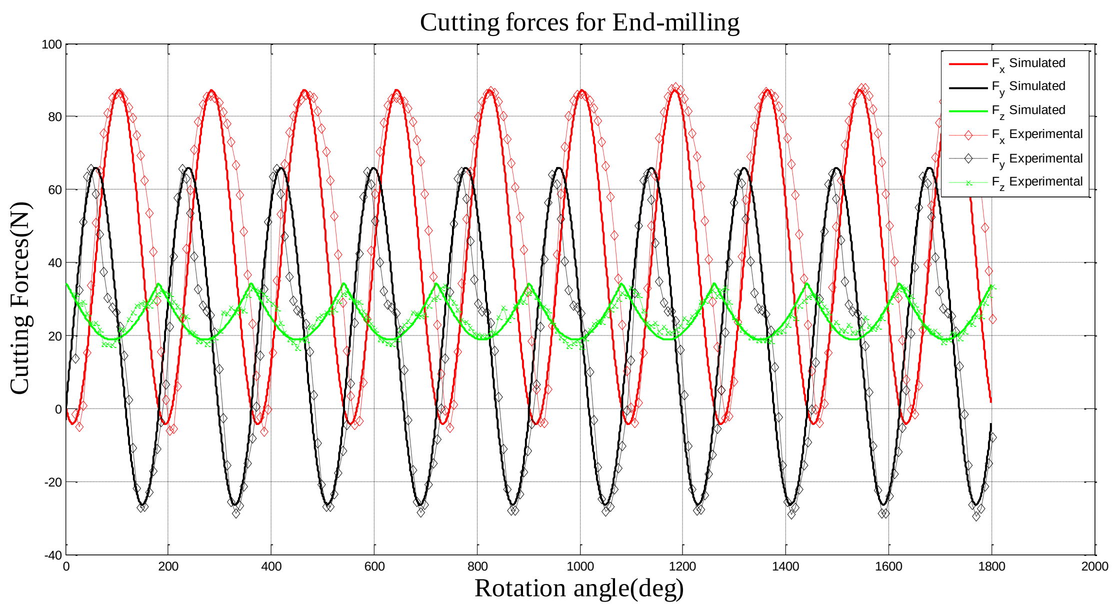

Figure 3.80 – Cutting forces of tool F at 0.10 mm/rev feed rate and 1 mm A_p

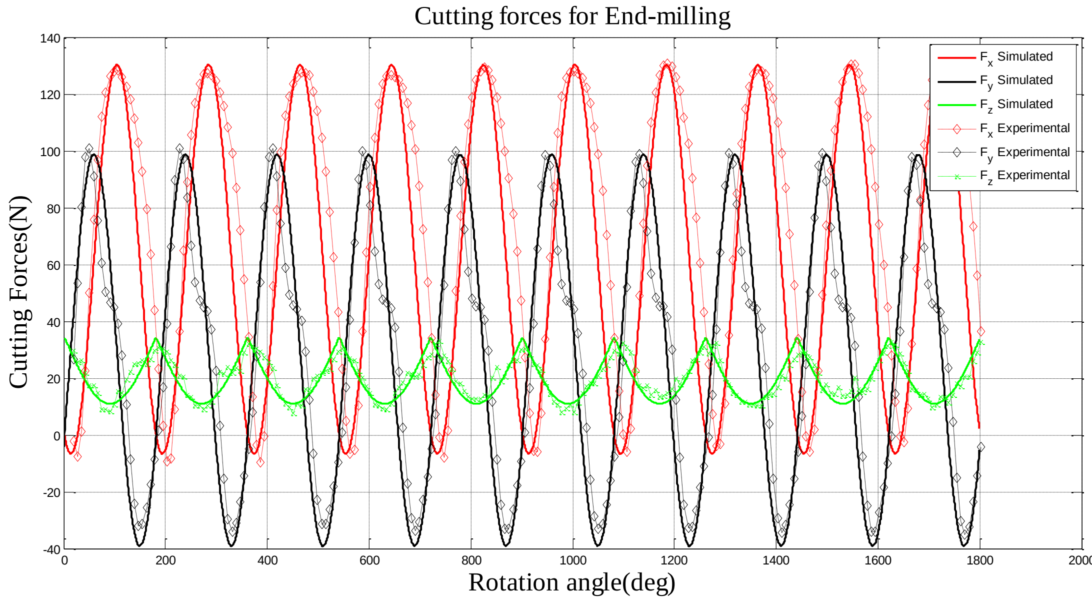

Figure 3.81 – Cutting forces of tool F at 0.15 mm/rev feed rate and 1 mm A_p

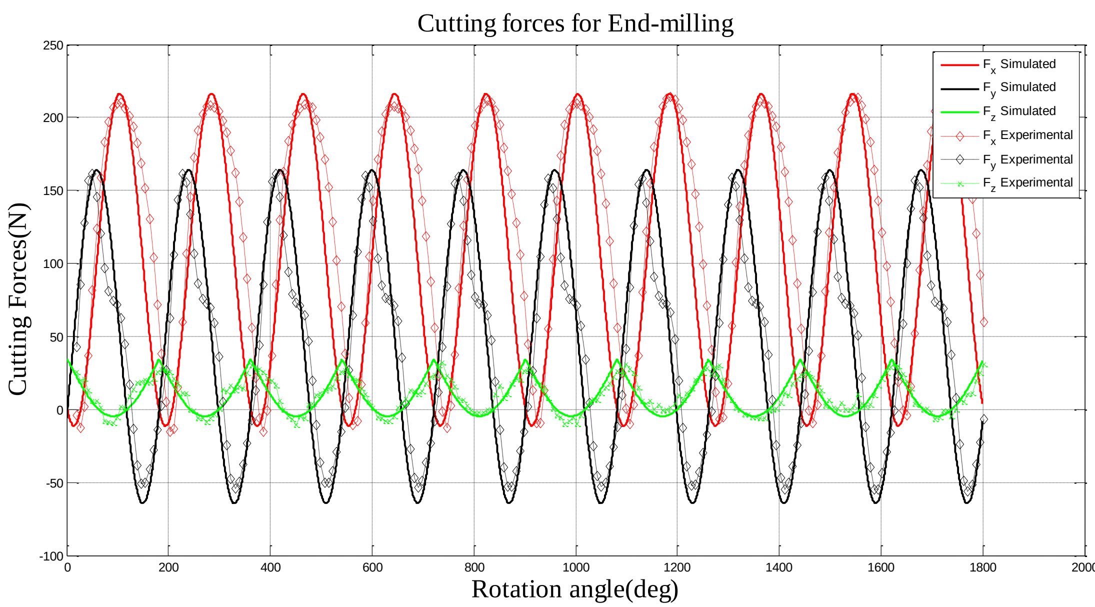

Figure 3.82 – Cutting forces of tool F at 0.25 mm/rev feed rate and 1 mm A_p

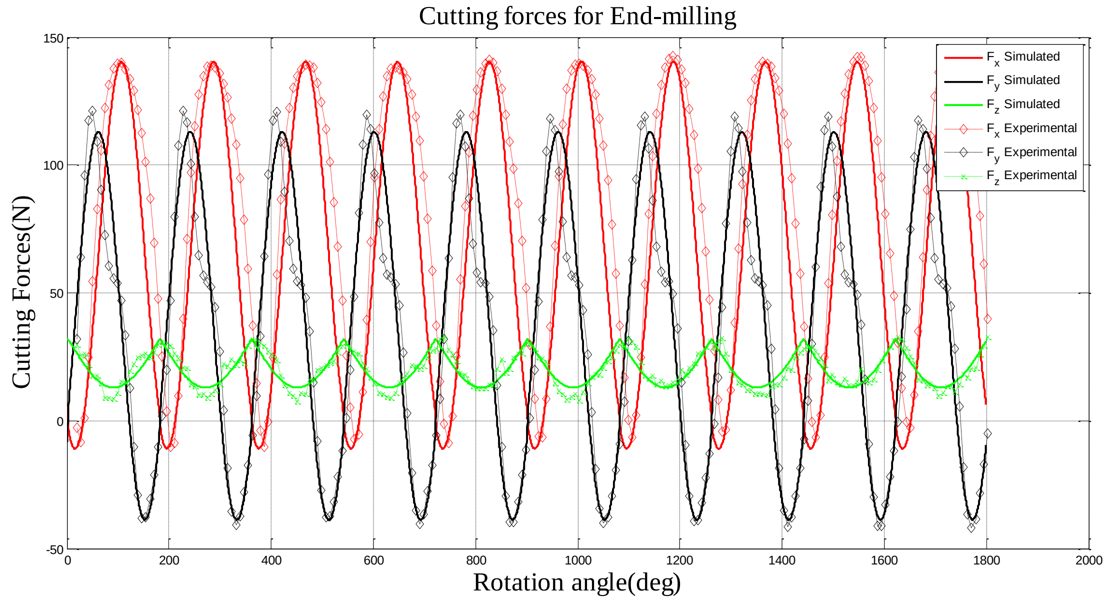

Figure 3.83 – Cutting forces of tool F at 0.10 mm/rev feed rate and 1.5 mm A_p

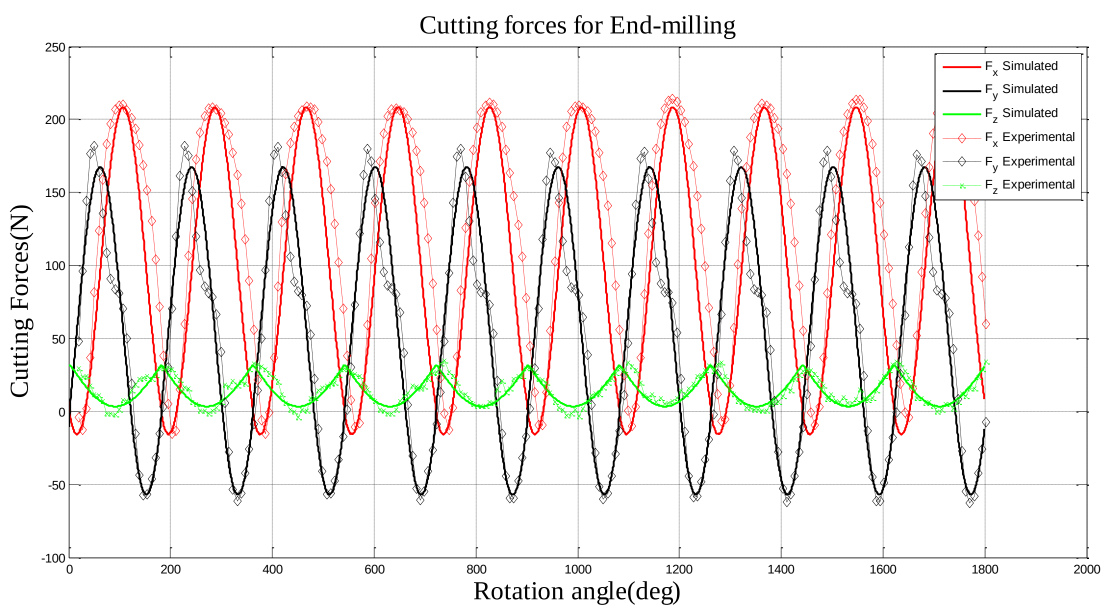

Figure 3.84 – Cutting forces of tool F at 0.15 mm/rev feed rate and 1.5 mm A_p

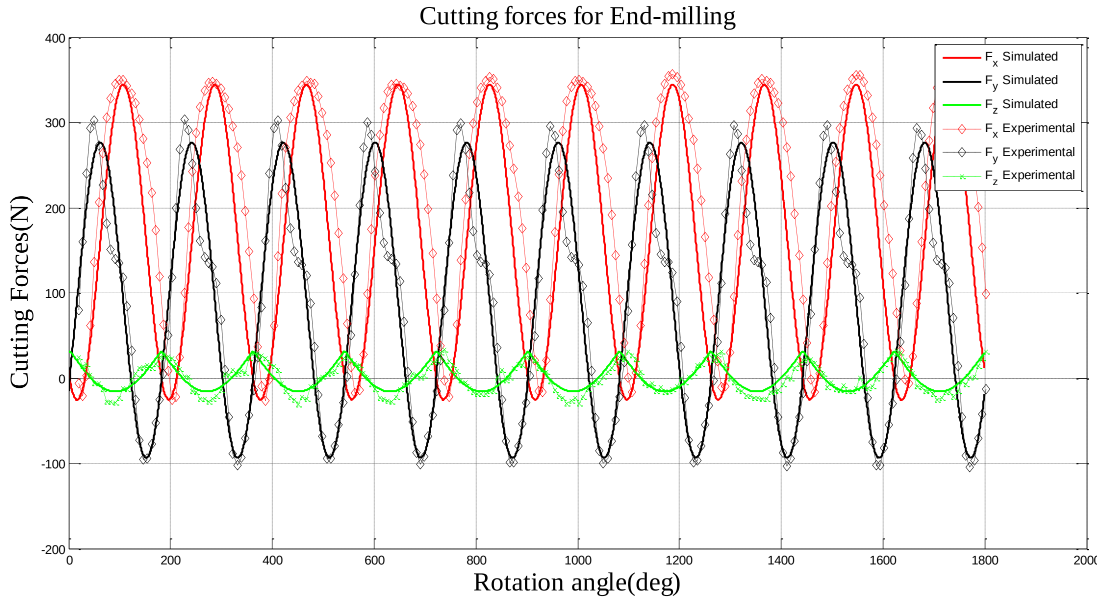

Figure 3.85 – Cutting forces of tool F at 0.25 mm/rev feed rate and 1.5 mm A_p

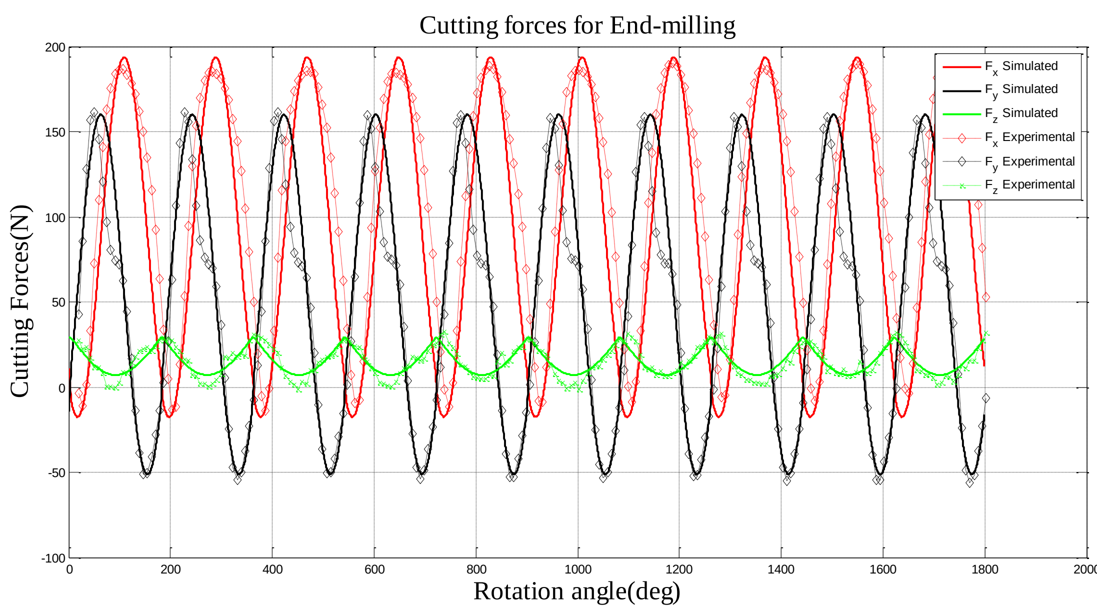

Figure 3.86 – Cutting forces of tool F at 0.10 mm/rev feed rate and 2 mm A_p

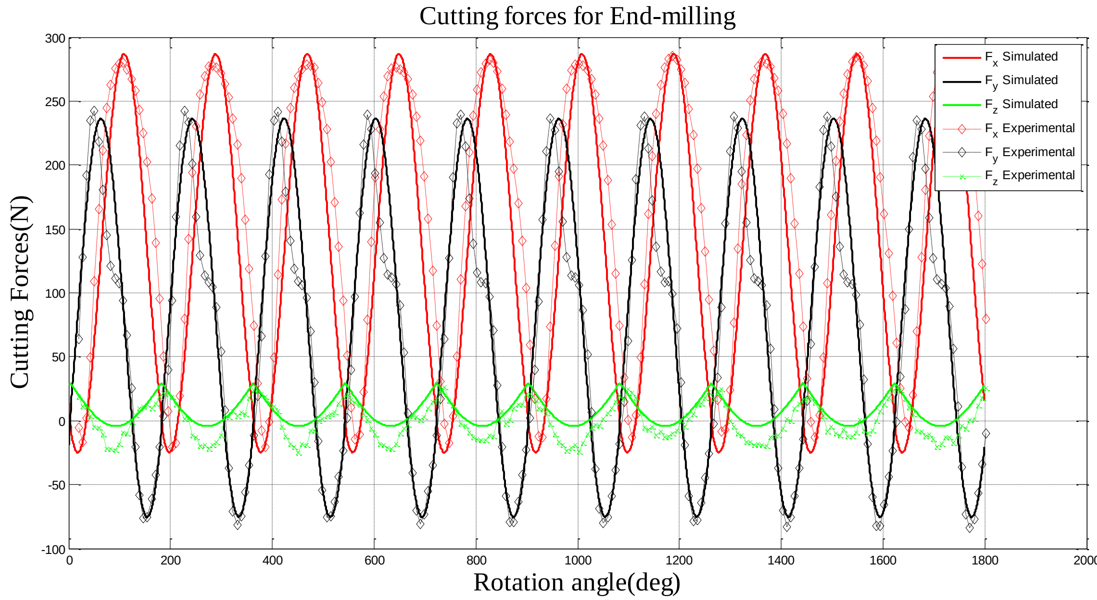

Figure 3.87 – Cutting forces of tool F at 0.15 mm/rev feed rate and 2 mm A_p

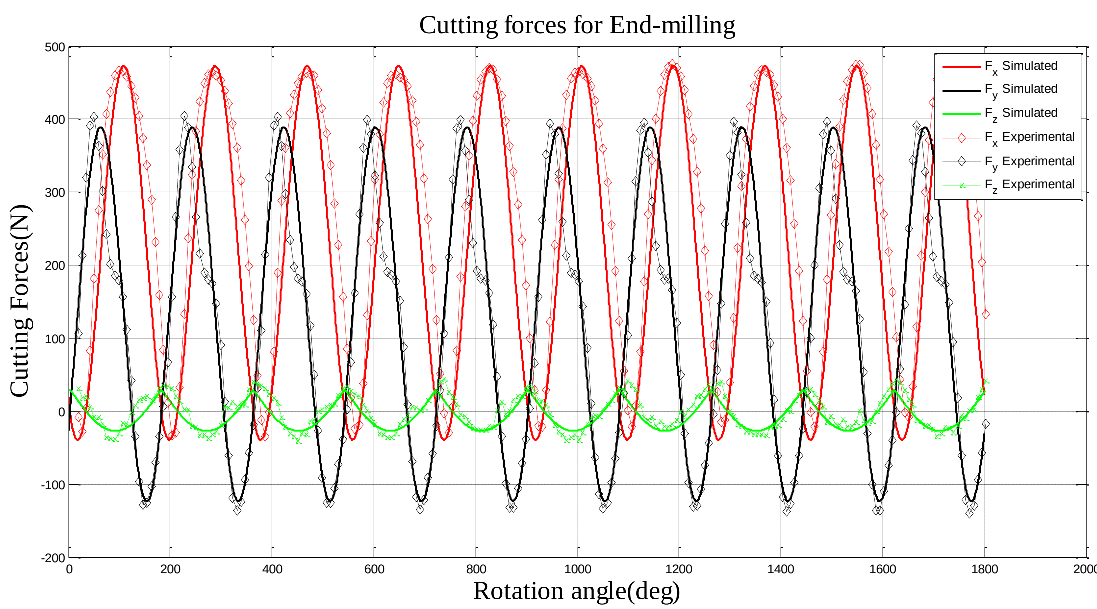

Figure 3.88 – Cutting forces of tool F at 0.25 mm/rev feed rate and 2 mm A_p

From the graphs it is seen that the model is in a good agreement with the experimental results. There are slight deviations in the maximum and minimum points especially for the lowest and highest feed rate values. This deviation can be correlated to one of the major downsides of the mechanistic calibration using average cutting constants which is the fact that the average cutting coefficients deviate from the instantaneous cutting constants at these extremes. As a future research direction, instantaneous cutting coefficients may be utilized for force modeling.

Chapter 4

THERMAL MODELING OF END MILLING

4.1 Introduction

Determination of the temperature fields during machining is one of the most important challenges for accurate metal cutting simulations. Coupled with excessive deformations taking place in a very small area, the high temperatures exhibit a highly non-linear complex modeling problem in metal cutting. The high temperatures during cutting process affect both the tool and the workpiece. On the workpiece side, these high temperatures induce thermal loads in addition to the mechanical loads and deform the workpiece, thus create dimensional errors. On the tool side high temperatures decrease tool life via various strongly temperature dependent wear mechanisms.

In this study, the temperature field on the rake face of a helical flat end mill is modeled using a semi-analytical approach. The cutting forces are modeled analytically and heat generated is calculated. Using a heat partition approach and a finite element model the maximum temperatures and the temperature fields on the rake face of the tool are calculated. For the first time in literature the heating effect of the bottom edge is also taken into account. It is shown that this effect becomes more important as the axial depth of cut gets smaller. The model is verified using experimental data on orthogonal cutting.

4.2. Heat balance equation

As a result of the first law of thermodynamics or in other words energy conservation law, it is stated that adding the rate at which thermal and mechanical energy enters to control volume to the rate at which thermal energy is generated within the control volume and subtracting the rate at which thermal and mechanical energy leaves the control volume equals to the rate of increase of energy stored within the control volume.

$$\dot{E}_{in} + \dot{E}_{generated} - \dot{E}_{out} = \dot{E}_{stored} \tag{4.1}$$

For the calculation of the temperature distribution in the tool based on the given boundary conditions, it is assumed that the medium is homogenous and the temperature field is expressed as T(x,y,z) in the Cartesian coordinates. For the infinitesimal differential element with volume of dx.dy.dz, qx, qy and qz stands for the heat conduction rates which are perpendicular to the control surfaces as shown in Figure 4.1. Considering heat conduction occurs in the presence of a temperature gradient, and using Taylor series expansion, the first order approximation of the flow rates for the three orthogonal directions are as follows

$$q_{x+dx} = q_x + \frac{\partial q_x}{\partial x} dx \tag{4.2}$$

$$q_{y+dy} = q_y + \frac{\partial q_y}{\partial y} dy \tag{4.3}$$

$$q_{z+dz} = q_z + \frac{\partial q_z}{\partial z} dz \tag{4.4}$$

ignoring the higher order terms.

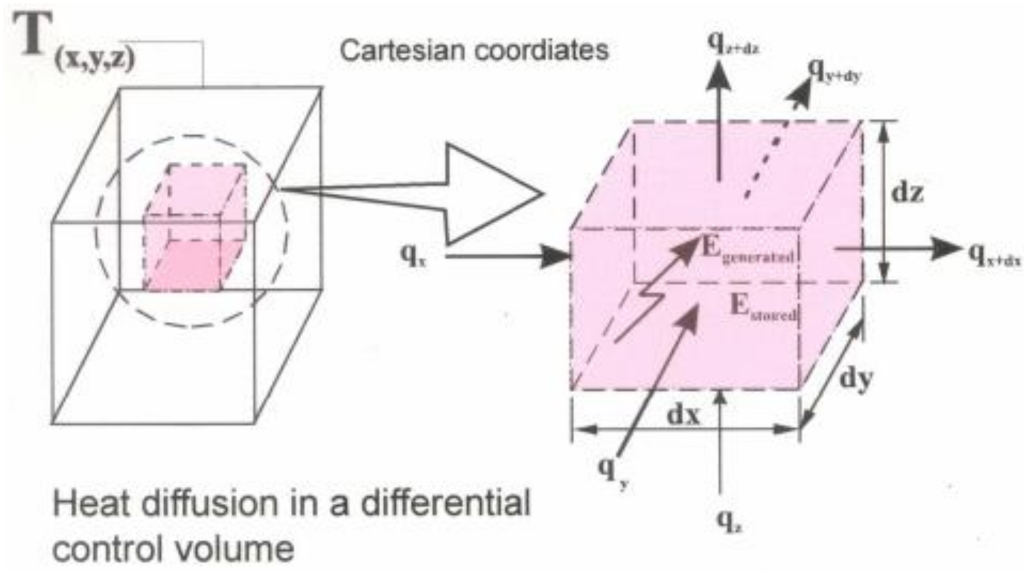

Figure 4.1 - Heat diffusion in differential control zones in Cartesian coordinates [88]

Accordingly the energy conservation equation can be rewritten as;

$$q_x + q_y + q_z + \dot{q} \cdot dx \cdot dy \cdot dz - q_{x+dx} - q_{y+dy} - q_{z+dz} = \rho \cdot c_p \cdot \frac{\partial T}{\partial t} \cdot dx \cdot dy \cdot dz \qquad (4.5)$$

Or in partial form as;

$$-\frac{\partial q_x}{\partial x} dx - \frac{\partial q_y}{\partial y} dy - \frac{\partial q_z}{\partial z} dz + \dot{q} \cdot dx \cdot dy \cdot dz = \rho \cdot c_p \cdot \frac{\partial T}{\partial t} \cdot dx \cdot dy \cdot dz \qquad (4.6)$$

The heat conduction rates can be calculated using Fourier's Heat Conduction Law,

$$q_x = -k \cdot dy \cdot dz \cdot \frac{\partial T}{\partial x} \qquad (4.7)$$

$$q_y = -k \cdot dx \cdot dx \cdot \frac{\partial T}{\partial y} \tag{4.8}$$

$$q_z = -k \cdot dx \cdot dy \cdot \frac{\partial T}{\partial z} \tag{4.9}$$

Therefore the heat balance equation becomes:

$$\frac{\partial (k \frac{\partial T}{\partial x})}{\partial x} + \frac{\partial (k \frac{\partial T}{\partial y})}{\partial y} + \frac{\partial (k \frac{\partial T}{\partial z})}{\partial z} + \dot{q} = \rho \cdot c_p \cdot \frac{\partial T}{\partial t} \tag{4.10}$$

With the assumption of constant heat conduction coefficient in the medium the equation transforms into;

$$\frac{\partial^2 T}{\partial x^2} + \frac{\partial^2 T}{\partial y^2} + \frac{\partial^2 T}{\partial z^2} + \frac{\dot{q}}{k} = \frac{1}{\alpha} \cdot \frac{\partial T}{\partial t} \tag{4.11}$$

where α is the thermal diffusivity defined as $\frac{k}{\rho \cdot c_p}$.

4.3. Heat generations in the primary and secondary zones

During the thermal modeling stage, the process is assumed to have orthogonal geometry. Thus following statements are presumed;

- The shearing takes place at an infinitely thin shear plane.
- There is a constant average friction over the tool chip contact zone.
- On the shear plane the stress distribution is uniform.

Accordingly the heat generation rates in the primary and secondary zones are defined as follows;

$$\dot{Q}_s = F_s V_s = \frac{\tau \cdot h \cdot V_w \cdot \cos(\alpha_n)}{\sin(\phi_n)\cos(\phi_n - \alpha_n)} \tag{4.12}$$

$$\dot{Q}_f = F_f V_c = \frac{\tau \cdot h \cdot V_w \cdot \sin(\beta_n)}{\cos(\phi_n + \beta_n - \alpha_n)\sin(\phi_n - \alpha_n)} \tag{4.13}$$

where F_s, F_f, V_w, V_s and V_c are the shear force in the shear plane, the frictional force between the tool rake face and the chip contact zone, the cutting velocity, the cutting velocity component along the shear plane and the cutting velocity component along the rake face, respectively. τ, ϕ_n, α_n and β_n are the shear stress in the shear plane, shear angle, normal rake angle and normal friction angle, respectively.

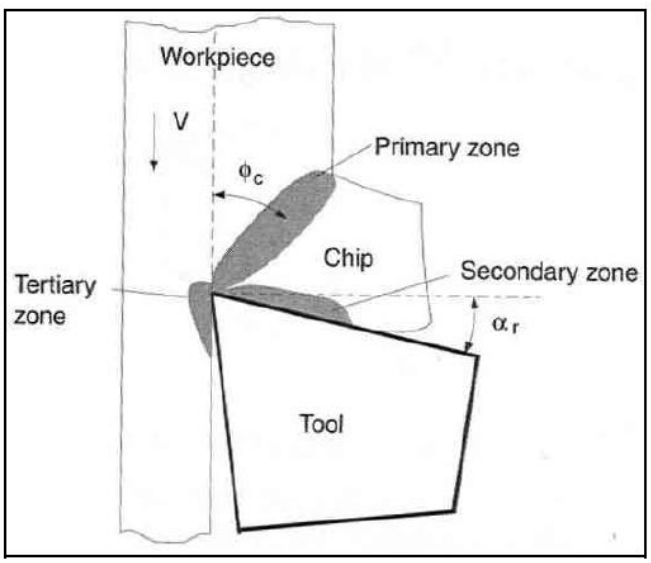

Figure 4.2 - Illustration of the shear zones [11]

For the calculation of the tool temperature distribution, the friction heat partition should be known. In order to calculate this, it is assumed that the temperature values at the tool chip contact zone are equal to each other due to thermodynamic equilibrium. The temperature rise over the chip is due to the heat input from friction and shearing. The average temperature rise of the chip per unit depth of cut due to shearing is determined by Oxley's energy partition function [42];

$$\Delta\overline{T} = \frac{\dot{Q}_s \cdot (1-\chi)}{\rho \cdot c_c \cdot h \cdot V_w} \tag{4.14}$$

where ρ is the mass density and c_c is the specific heat capacity of the workpiece material, respectively. χ represents the portion of the heat generated in the primary shear zone that enters to the chip and is defined as;

$$\chi = 0.5 - 0.35 \cdot \log_{10}(R_t \cdot \tan(\phi_n)) \text{ for } 0.004 \leq R_t \cdot \tan(\phi_n) \leq 10 \tag{4.15}$$

$$\chi = 0.5 - 0.15 \cdot \log_{10}(R_t \cdot \tan(\phi_n)) \text{ for } R_t \cdot \tan(\phi_n) \geq 10 \tag{4.16}$$

$$R_t = \frac{h \cdot V_w}{\zeta} \tag{4.17}$$

$$\zeta = \frac{k_c}{\rho \cdot c_c} \tag{4.18}$$

4.4. Tool temperature model

The frictional heat flow rate into the tool is given by;

$$\dot{Q}_t = \frac{B_t \cdot \dot{Q}_f \cdot \delta x}{l_{cn} \cdot k_t} \tag{4.19}$$

Where

$$l_{cn} = \frac{2 \cdot h \cdot \sin(\phi_n + \beta_n - \alpha_n)}{\cos(\beta_n) \cdot \sin(\phi_n)} \tag{4.20}$$

$$l \ = \frac{h \cdot \cos(\phi_n - \alpha_n)}{\sin(\phi_n)} \tag{4.21}$$

are the tool-chip contact length and shear plane length, β_n is the normal friction angle and α_n is the normal rake angle. V_w is the cutting velocity, ϕ_n is the shear angle and k_c is the thermal conductivity.

4.5. Simulation results and discussions

Temperature measurement in machining is a very challenging problem in the machining research community. Most of the limited work done on the temperature measurement is for the two dimensional turning processes. Number of research for temperature measurement in milling is even more limited. In fact there is no work done on the measurement of temperature distribution on the rake face of helical flat end mills. Therefore in order to validate the accuracy of the finite element model proposed in this thesis, the study by Dinc and Lazoglu is used [88]. Then the results for the milling simulations for various conditions are presented.

4.5.1 Orthogonal turning simulations

For the validation of the model, the experimental data by Dinc and Lazoglu is used. The finite element model is also compared with the finite difference model developed by Dinc [88]. The simulations are carried out for different cutting conditions, with different tool geometries for Al 7075. In Table 4.2, the conditions for the temperature experiments are given in detail. The cutting conditions are chosen such that cutting temperatures observed will be smaller than 523 ºC, which is the maximum temperature that can be detected by the infrared (IR) camera. The simulations are done for the same cutting conditions. The simulations and experimental results are compared for every single experiment. The simulation results include the temperature distribution graphs and the maximum simulated temperature in the tool rake face is also given. For the experimental results, an IR image of the tool is given for every experiment. The maximum tool rake face temperatures measured in IR experiments are compared with the simulation results.

Table 4.1 - Thermal properties of the tool and the workpiece

	Tool	Workpiece
Conductivity (W/mK)	84	130
Specific heat capacity (J/kgK)	480	960
Density (kg/m^3)	15700	2753

Table 4.2 – The conditions in the temperature measurement experiments for Al-7075

Experiment No.	Rake Angle (deg)	Cutting Velocity (m/min)	Feed (mm/rev)	Clearance Angle (deg)
1	6	200	0,05	5.7
2	6	200	0,1	5.7
3	6	200	0,15	5.7
4	6	200	0,2	5.7
5	18	200	0,05	5.7
6	18	200	0,1	5.7
7	18	200	0,15	5.7
8	18	200	0,2	5.7

Table 4.3 – Orthogonal test results for Al-7075

Material	Tool Rake Angle [deg]	Chip Ratio	Shear Angle [deg]	Average Friction Angle [deg]	Shear Stress [Mpa]
Al-7075	6	0.57	31.5	33	287.1
	18	0.55	32	40.5	266.8

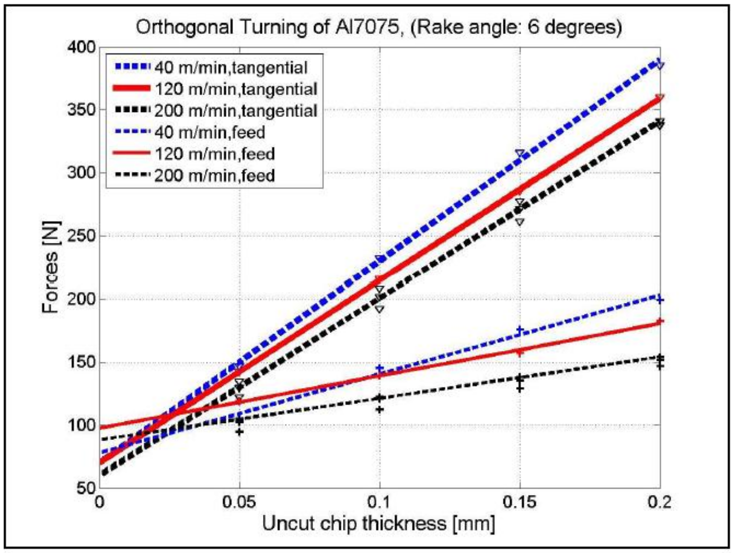

Figure 4.3 - Cutting forces measured during orthogonal cutting of Al-7075 for 6º rake angle

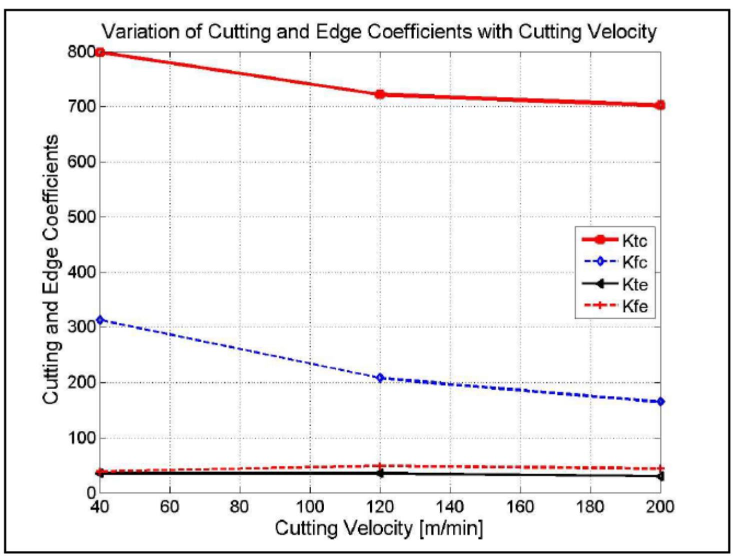

Figure 4.4 – Variation of cutting and edge coefficients with cutting velocity in Al-7075 for 6º rake angle

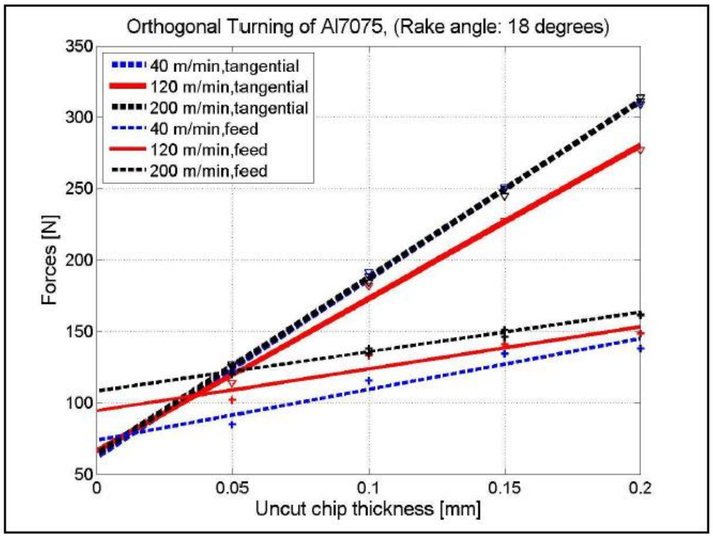

Figure 4.5 - Cutting forces measured during orthogonal cutting of Al-7075 for 18º rake angle

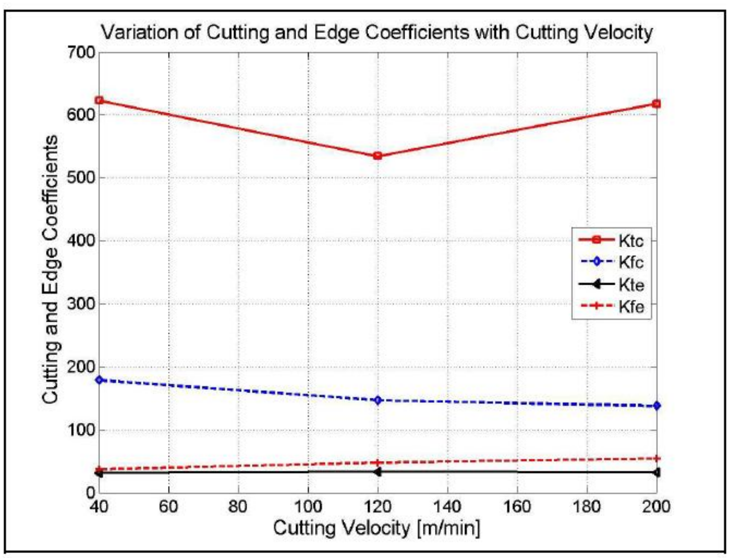

Figure 4.6 – Variation of cutting and edge coefficients with cutting velocity in Al-7075 for 18º rake angle

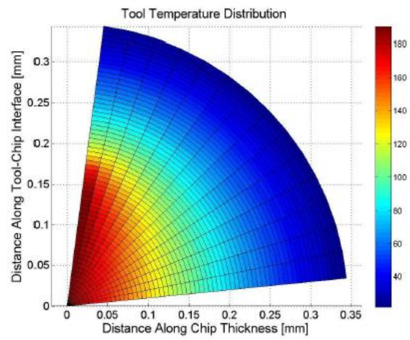

Figure 4.7 - Tool temperature distribution for experiment 1 by Dinc

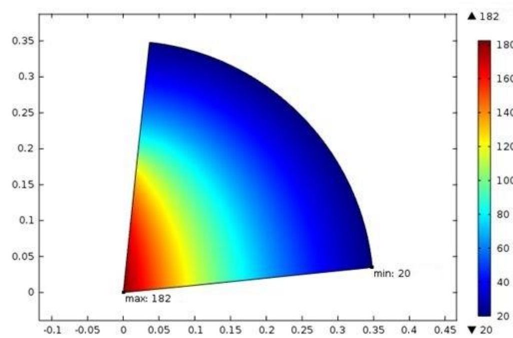

Figure 4.8 - Tool temperature distribution for experiment 1 by Bugdayci

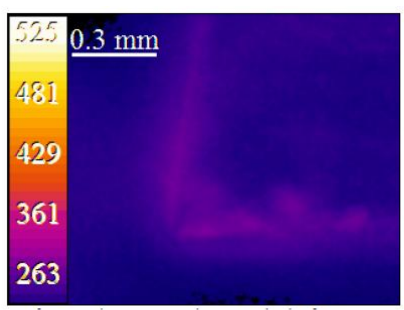

Figure 4.9 - IR image for experiment 1. Maximum tool rake face temperature is measured to be 235 ºC.

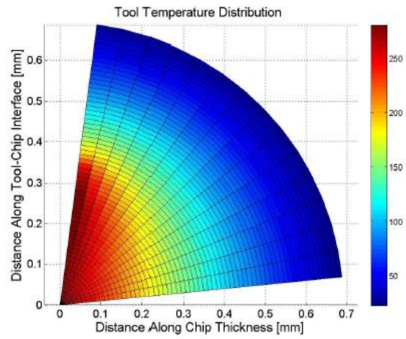

Figure 4.10 - Tool temperature distribution for experiment 2 by Dinc

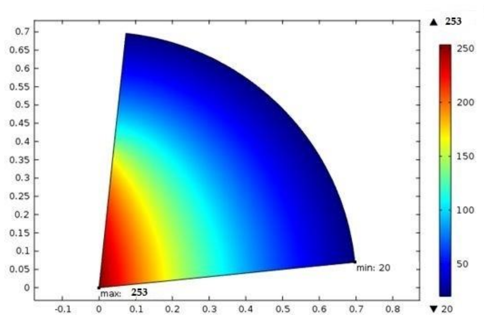

Figure 4.11 - Tool temperature distribution for experiment 2 by Bugdayci

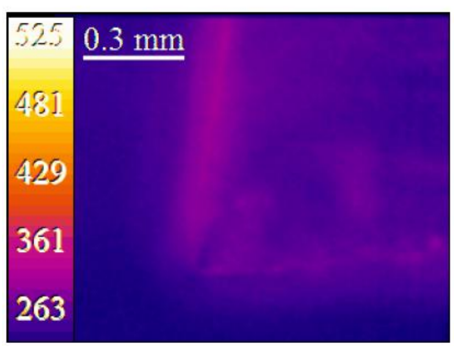

Figure 4.12 - IR image for experiment 2. Maximum tool rake face temperature is measured to be 288 ºC.

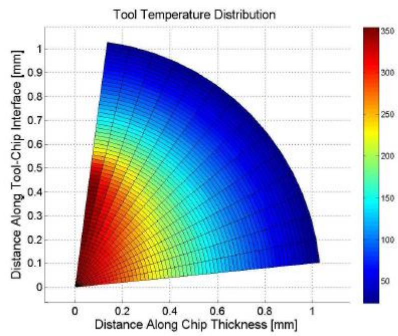

Figure 4.13 - Tool temperature distribution for experiment 3 by Dinc

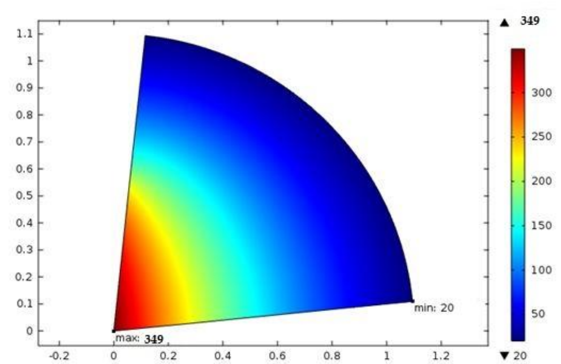

Figure 4.14 - Tool temperature distribution for experiment 3 by Bugdayci

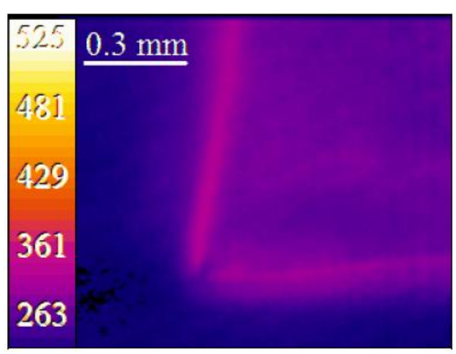

Figure 4.15 - IR image for experiment 3. Maximum tool rake face temperature is measured to be 310 ºC.

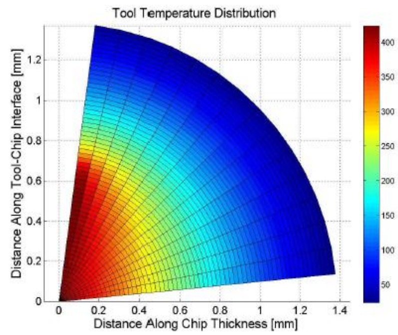

Figure 4.16 - Tool temperature distribution for experiment 4 by Dinc

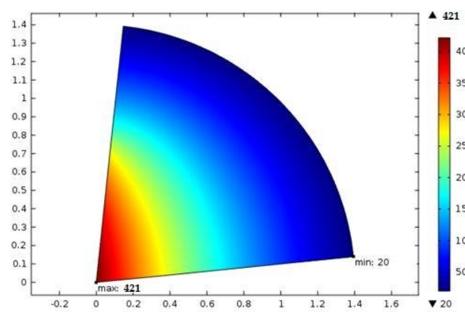

Figure 4.17 - Tool temperature distribution for experiment 4 by Bugdayci

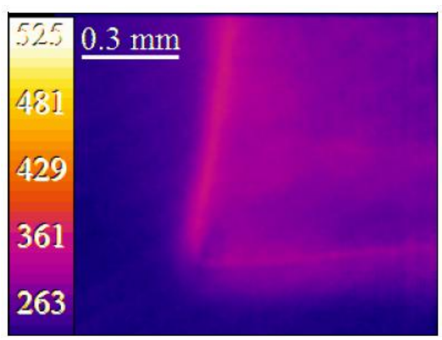

Figure 4.18 - IR image for experiment 4. Maximum tool rake face temperature is measured to be 344 ºC.

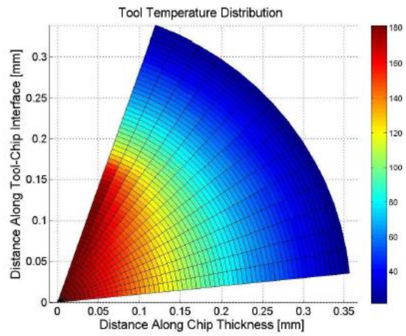

Figure 4.19 - Tool temperature distribution for experiment 5 by Dinc

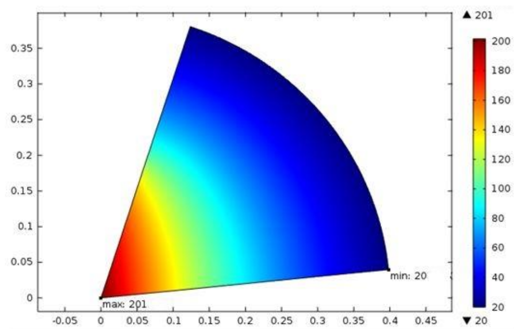

Figure 4.20 - Tool temperature distribution for experiment 5 by Bugdayci

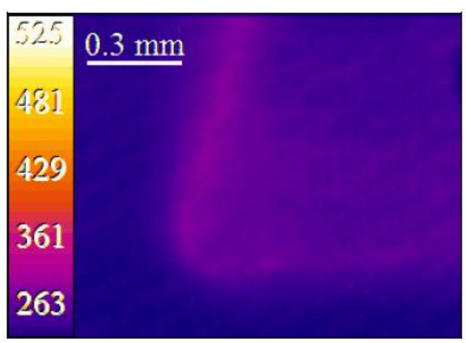

Figure 4.21 - IR image for experiment 5. Maximum tool rake face temperature is measured to be 262 ºC.

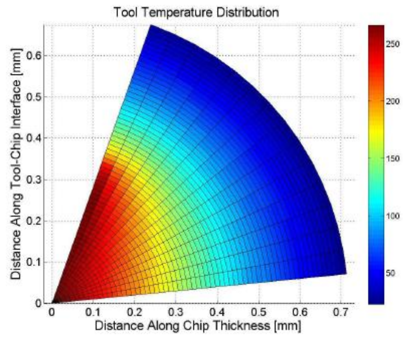

Figure 4.22 - Tool temperature distribution for experiment 6 by Dinc

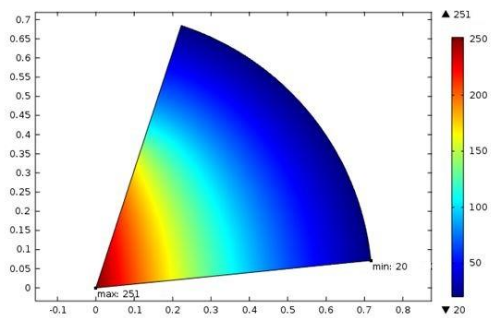

Figure 4.23 - Tool temperature distribution for experiment 6 by Bugdayci

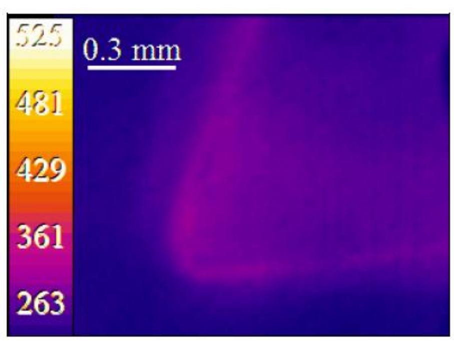

Figure 4.24 - IR image for experiment 6. Maximum tool rake face temperature is measured to be 281 ºC.

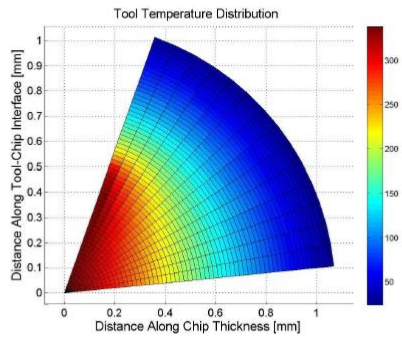

Figure 4.25 - Tool temperature distribution for experiment 7 by Dinc

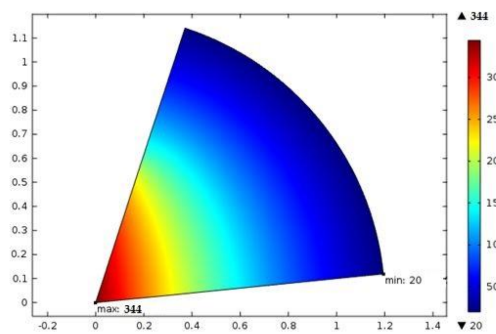

Figure 4.26 - Tool temperature distribution for experiment 7 by Bugdayci

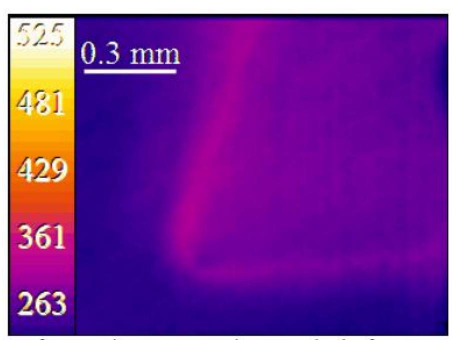

Figure 4.27 - IR image for experiment 7. Maximum tool rake face temperature is measured to be 308 ºC.

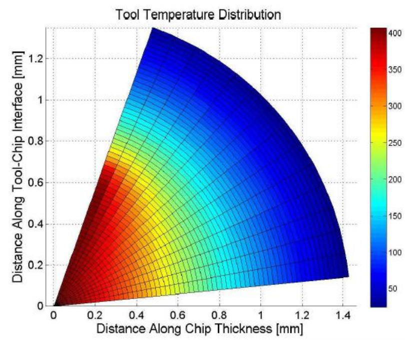

Figure 4.28 - Tool temperature distribution for experiment 8 by Dinc

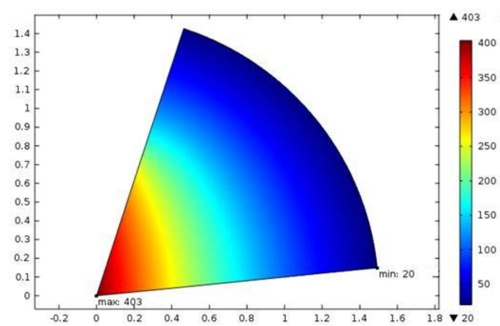

Figure 4.29 - Tool temperature distribution for experiment 8 by Bugdayci

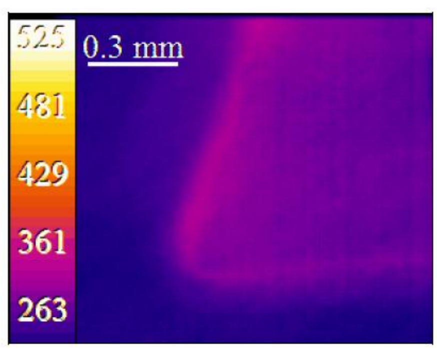

Figure 4.30 - IR image for experiment 8. Maximum tool rake face temperature is measured to be 317 ºC.

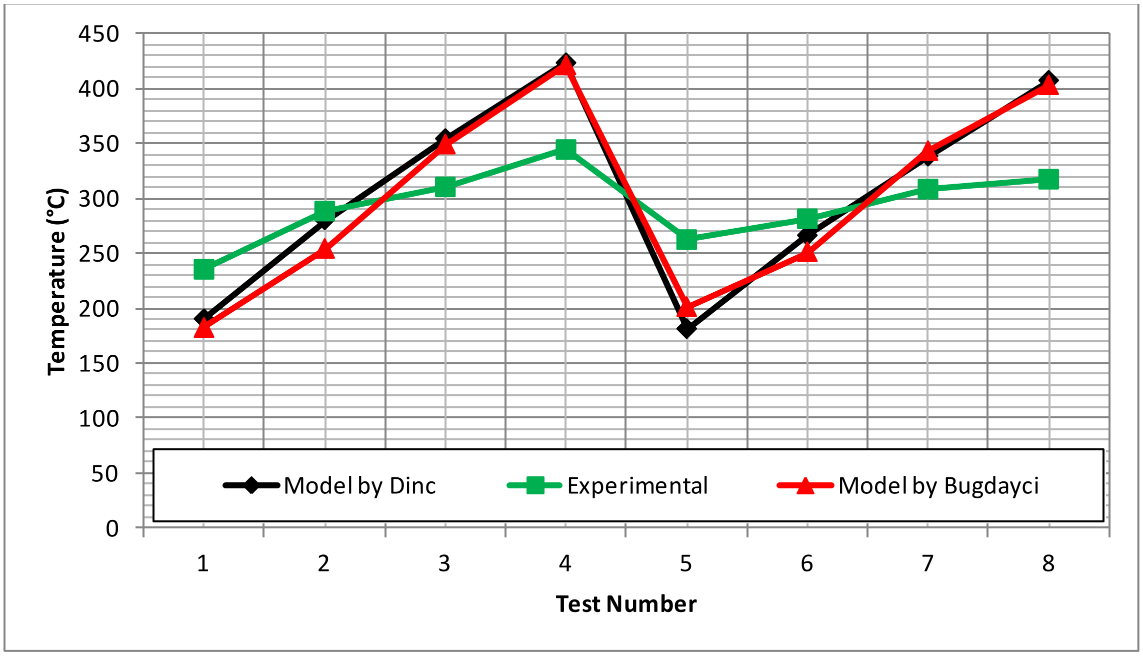

Figure 4.31 – Comparison of the models and experimental temperature values.

It is shown that the proposed finite element model gives very similar results compared with the finite model developed by Dinc. However when compared with the experimental values there are deviations for both of the rake angles at the lowest and highest feed rates. Overall the model has a good agreement with the experimental results and thus the temperature prediction model is validated.

4.5.2 Slot milling simulations

For the milling case, since there are no reliable data in the literature, only the results of the solutions are given. In the model only a single flute of the cutter is modeled due to symmetry in order to decrease computation time. The cutter lip is divided into discs similar to force modeling and contribution of each disc is calculated assuming continuous orthogonal cutting conditions. Since the main objective of this thesis is to model the flank wear, only the temperature field on the rake face is calculated.

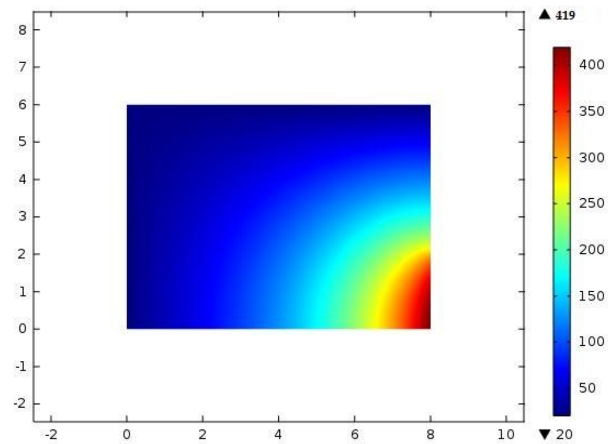

Figure 4.32 – Sample temperature distribution neglecting bottom edge effect for Tool A. Maximum temperature simulated is 419ºC.

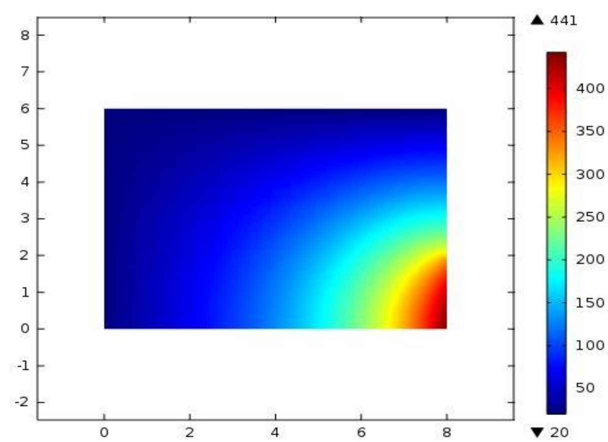

Figure 4.33 – Sample temperature distribution including bottom edge effect for Tool A. Maximum temperature simulated is 441ºC.

From Figures 4.32 and 4.33 it is clearly seen that the addition of the bottom edge cutting effect creates a shift in the temperature gradient towards the bottom edge, which is expected. The inclusion of the bottom edge effect transforms the temperature distribution from an "I" shape to "L", which is more realistic as seen from the picture of a used tool in Figure 4.34. In this figure, it is seen that the contact area where the chip slides over the rake face of the tool is brighter, due to the friction. The dimensions of this area are the axial depth of cut in the axial (z) direction and the feed per tooth value in the radial (r) direction. The simulated temperature fields also show a good agreement in this manner.

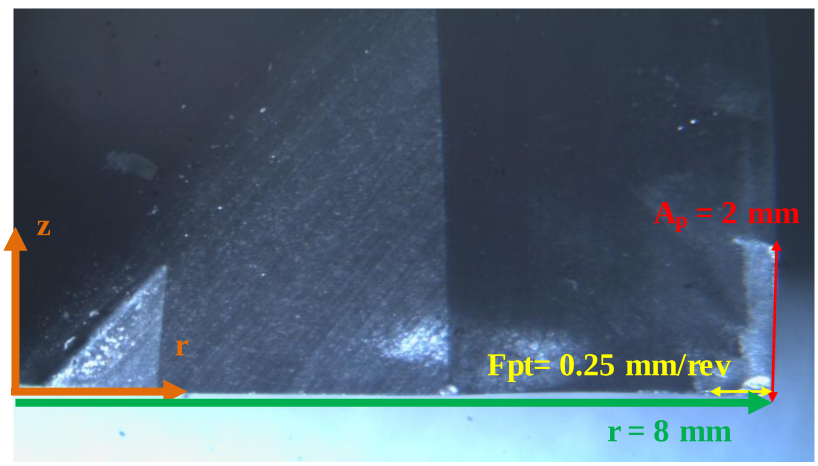

Figure 4.34 - Heat effected zone on a used tool

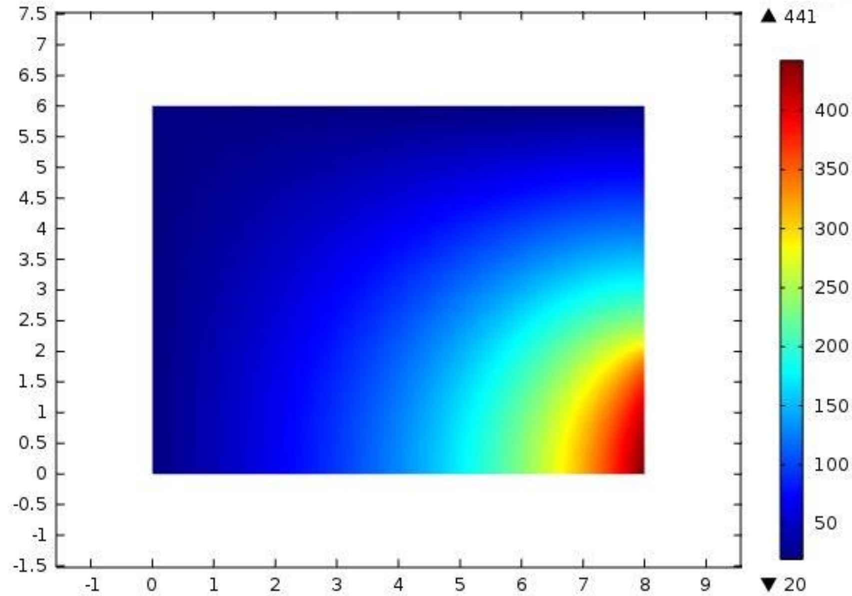

Figure 4.35 - Temperature distribution of tool A at 8000 rpm, 0.25 mm/rev. Maximum simulated temperature is 441ºC.

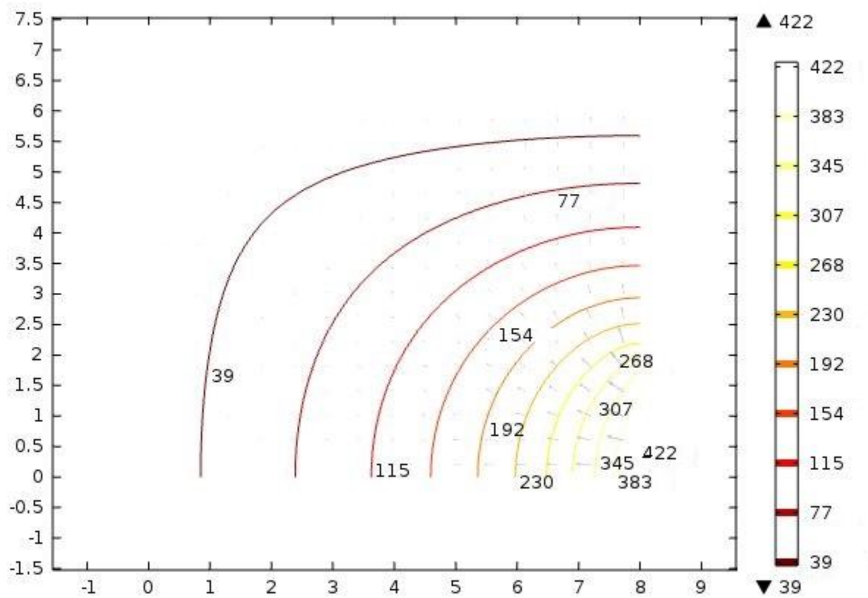

Figure 4.36 – Isothermal contours of tool A at 8000 rpm, 0.25 mm/rev

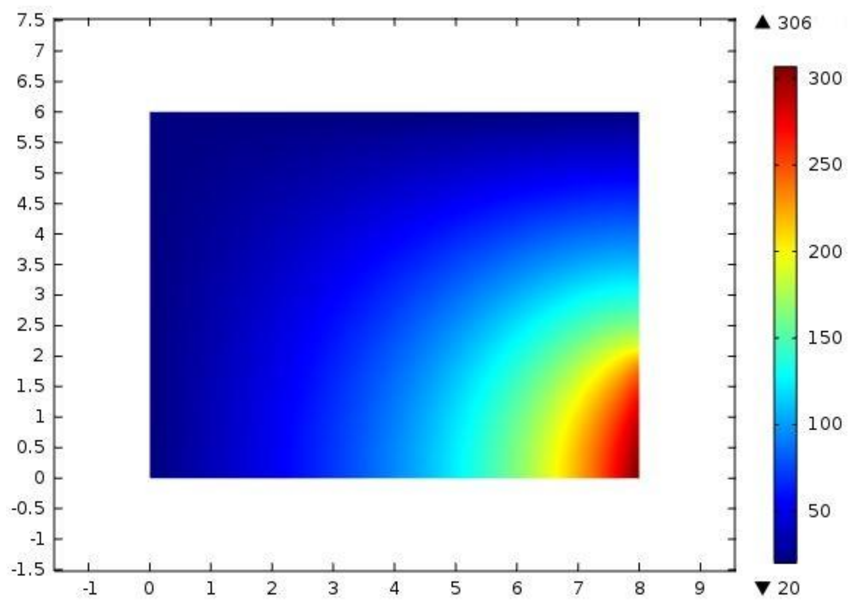

Figure 4.37 - Temperature distribution of tool B at 8000 rpm, 0.25 mm/rev. Maximum simulated temperature is 306ºC.

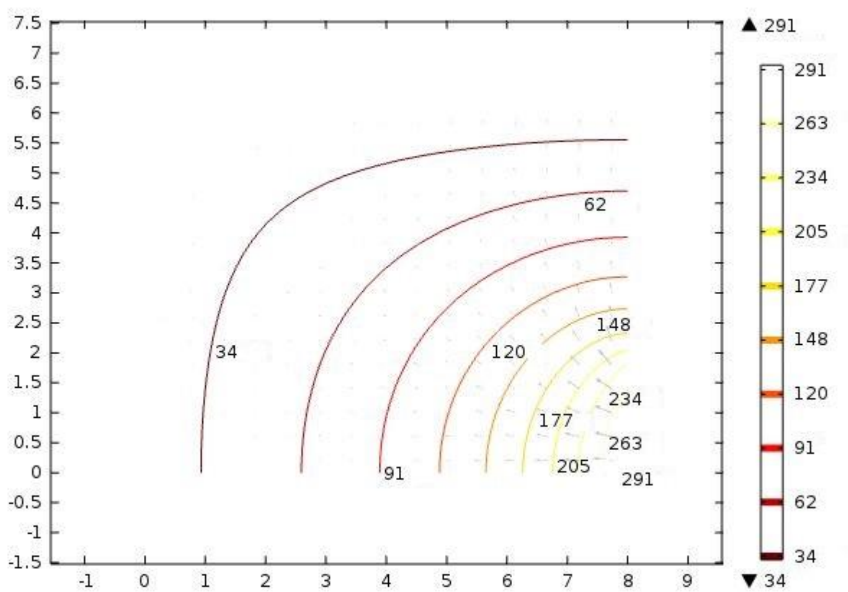

Figure 4.38 – Isothermal contours of tool B at 8000 rpm, 0.25 mm/rev

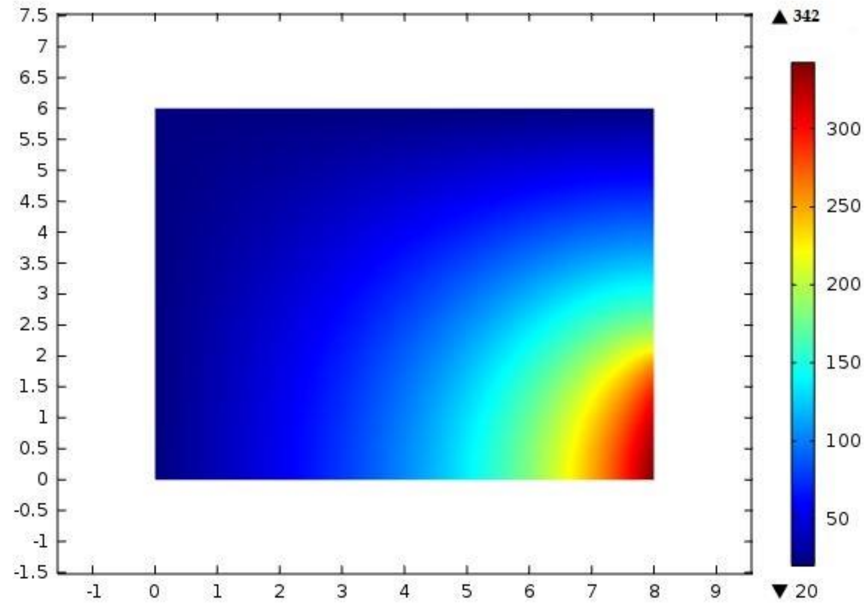

Figure 4.39 - Temperature distribution of tool C at 8000 rpm, 0.25 mm/rev. Maximum simulated temperature is 342ºC.

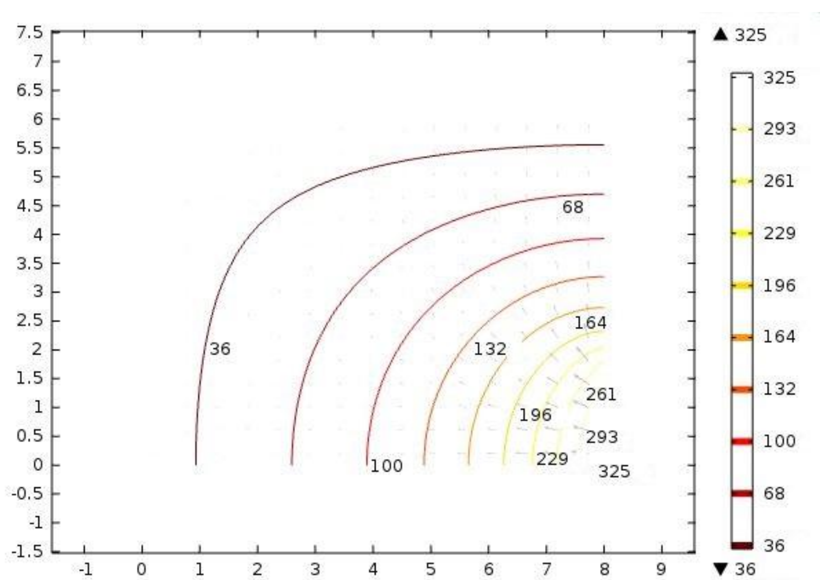

Figure 4.40 – Isothermal contours of tool C at 8000 rpm, 0.25 mm/rev

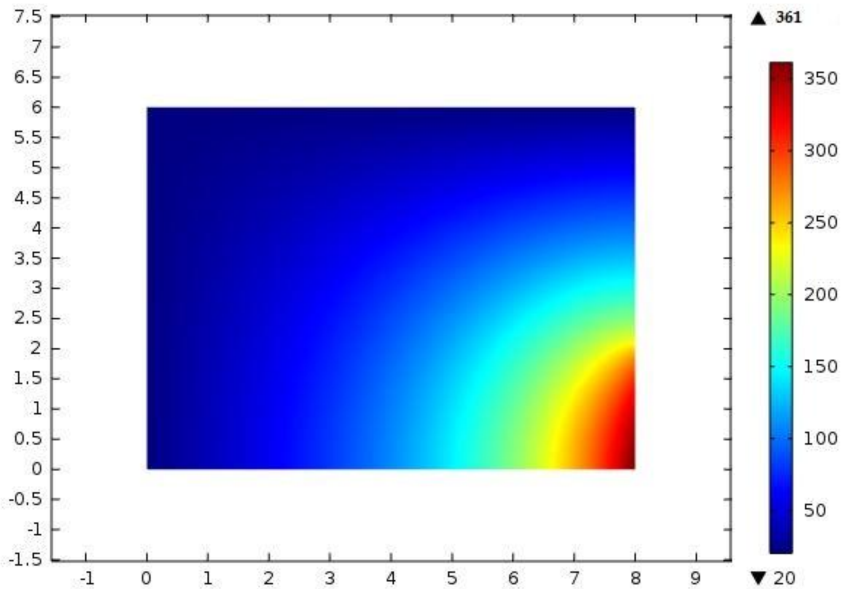

Figure 4.41 - Temperature distribution of tool D at 8000 rpm, 0.25 mm/rev. Maximum simulated temperature is 361ºC.

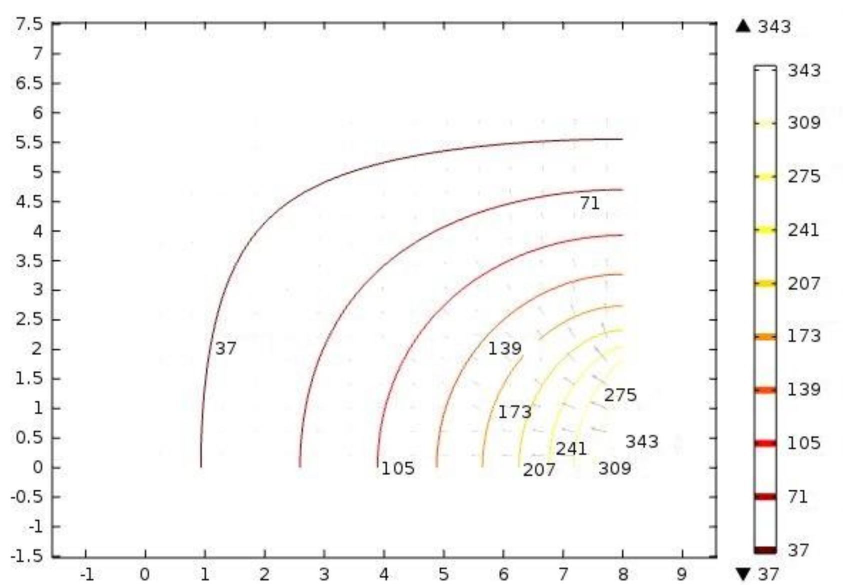

Figure 4.42 – Isothermal contours of tool D at 8000 rpm, 0.25 mm/rev.

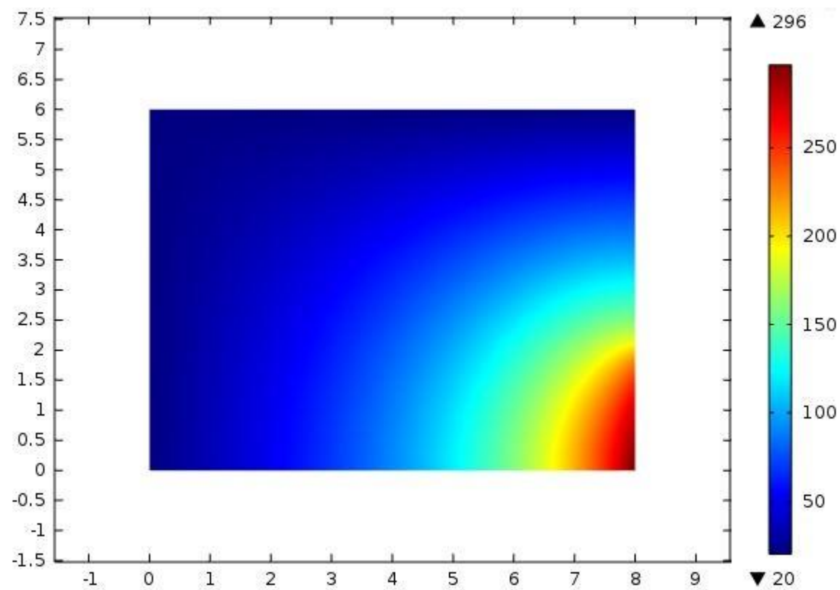

Figure 4.43 - Temperature distribution of tool E at 8000 rpm, 0.25 mm/rev. Maximum simulated temperature is 296ºC.

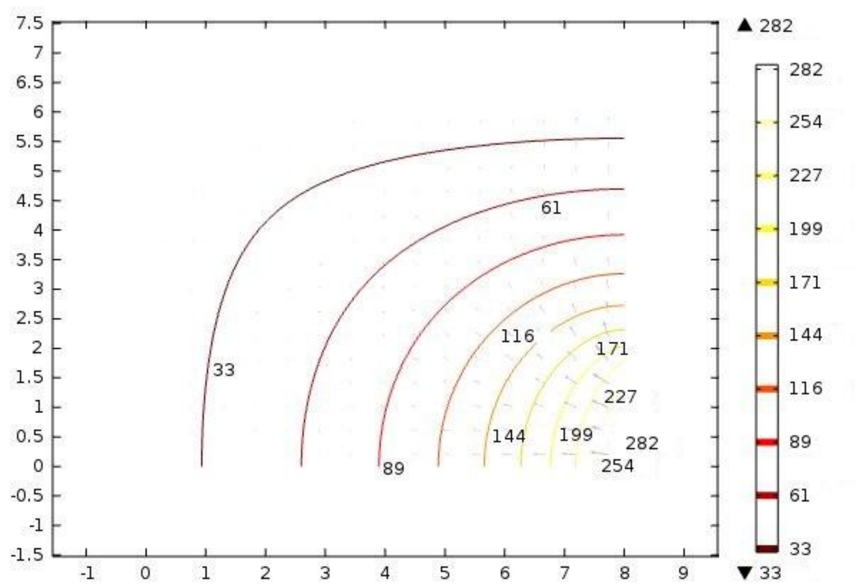

Figure 4.44 - Isothermal contours of tool E at 8000 rpm, 0.25 mm/rev

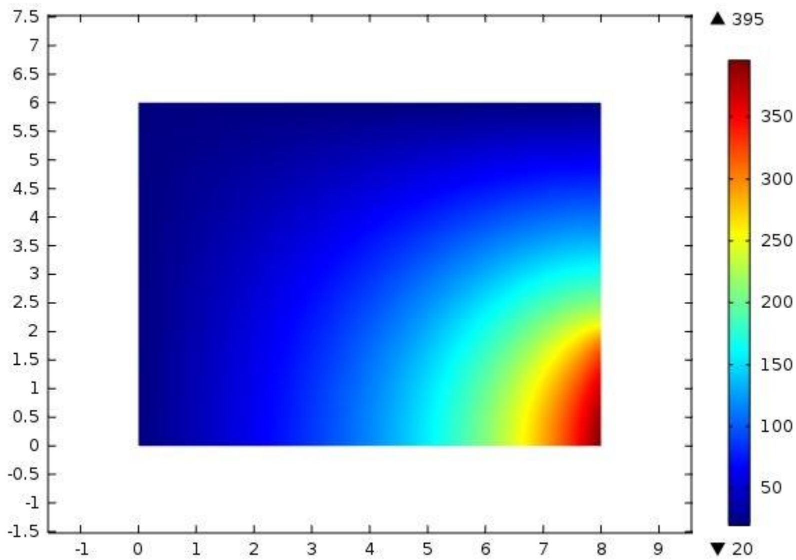

Figure 4.45 - Temperature distribution of tool F at 8000 rpm, 0.25 mm/rev. Maximum simulated temperature is 395ºC.

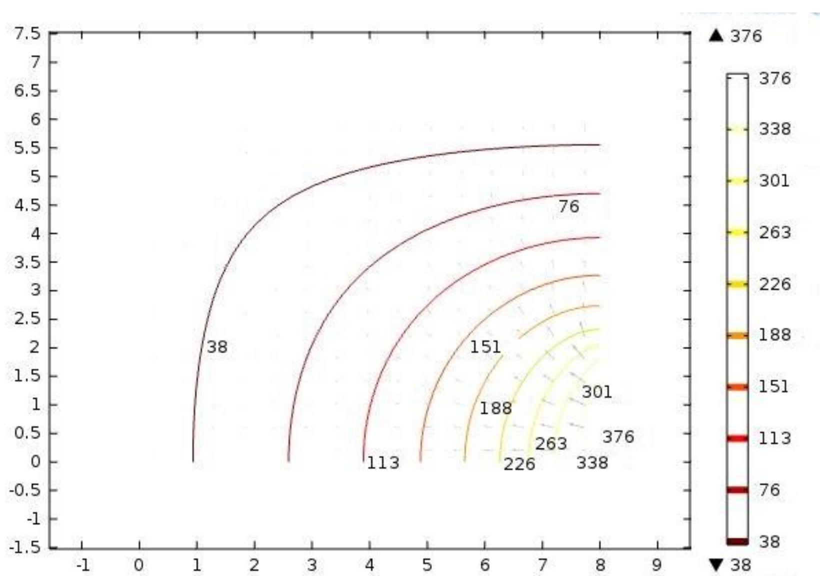

Figure 4.46 - Isothermal contours of tool F at 8000 rpm, 0,25 mm/rev

Table 4.4 - Simulated milling temperatures

Tool Name	Resultant Cutting Force [N]	Tool Density [kg/m^3]	Tool Thermal Conductivity [W/mK]	Simulated Maximum Temperature [ºC]
A	588	14330	105	441
B	388	14330	105	306
C	487	14330	105	342
D	432	14620	90	361
E	383	14330	105	296
F	579	14330	105	395

Overall, the inclusion of the bottom edge cutting effect shows an improvement in the temperature distribution compared with the image of the worn tool. Also it is noticed that as the cutting force increases the cutting temperature increases with the exception of tool D, which have a different material microstructure [92].

In this study, the friction between the bottom edge and the workpiece during the non-cutting period of the flute is not considered. Considering that and conducting a time-dependent analysis will likely to increase the magnitude of the maximum temperature and shift the location of that temperature closer to the bottom edge. On the other hand, accurate modeling of the cooling during the non cutting period of the cutting cycle will likely to improve the results obtained. However, the lack of experimental data on this topic is still an important void to be addressed in the machining research community.

Chapter 5

ANALYSIS OF TOOL LIFE

5.1 Introduction

With the increasing competition in the industry of manufacturing, process modeling becomes more and more important to avoid costly and time consuming trial and error approach. There are thousands of researchers around the world working with the aim of predicting the cutting forces, vibrations, residual stresses etc prior to actual machining operation in order to avoid any undesired outcomes and optimize the process. Accordingly, studies on tool wear mechanisms and tool life predictions contribute to a large portion of machining research. With the accurate prediction of tool wear, the catastrophic failure of the tool can be prevented and/or the tool designs can be altered to find the optimum parameters for a longer tool life. The first step towards the wear modeling is the identification of the wear mechanism. There are several mechanisms resulting in tool wear. Tool wear may occur as a result of one mechanism dominating the overall or it may result as a combination of these mechanisms. The main types of wear mechanisms are explained in the following subsections briefly.

5.2 Wear mechanisms

5.2.1 Abrasion Wear

Abrasion occurs when a harder material removes particles from the softer work material during sliding contact. At the same time softer work material also removes particles from the harder tool material although at a smaller rate. Tools and work materials generally contain carbides, oxides, and nitrides which are hard microstructures that cause abrasion wear during machining [11].

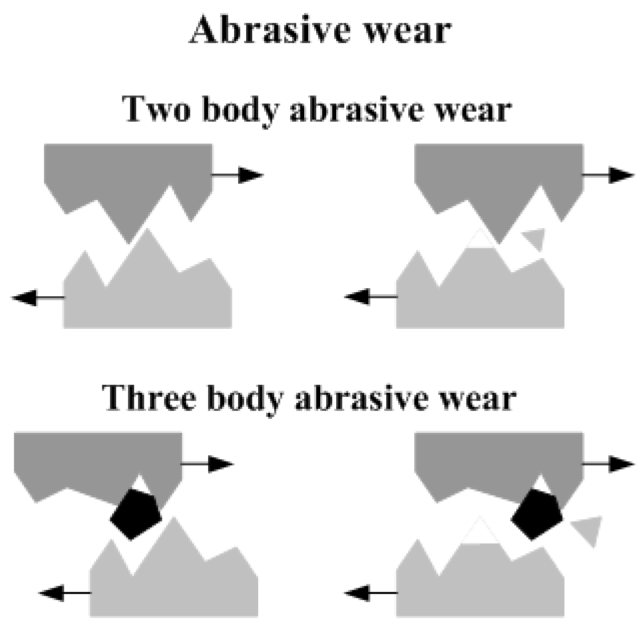

Figure 5.1 – Illustration of abrasive wear [89]

5.2.2 Adhesion Wear

Adhesion wear occurs when there is a relative motion between the two bodies that are under the normal load. In adhesion wear small fragments of softer work material adhere to the harder tool during machining. However, the adhered material is unstable and when it is separated from the cutting tool it removes along small fragments of the tool material. In machining this phenomenon is called the built-up edge (BUE) when part of the chip material welds to the cutting edge. This built-up edge may increase the cutting forces by acting as a duller tool or decrease the forces by changing the effective rake angle from negative to positive. Accurate prediction of temperature in machining is also critical for identifying the cutting speed at which BUE is minimum [11].

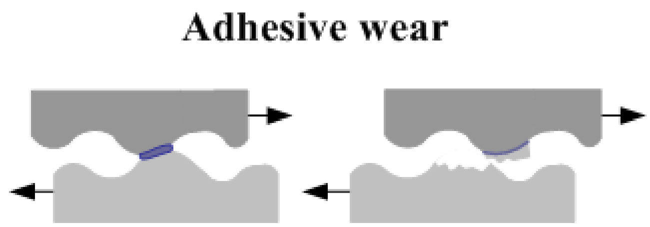

Figure 5.2 – Illustration of adhesive wear [89]

5.2.3 Diffusion Wear

When the temperature of the environment increases at the contact zones, the atoms in the two materials become unstable and migrate to the opposite material where the concentration is less.

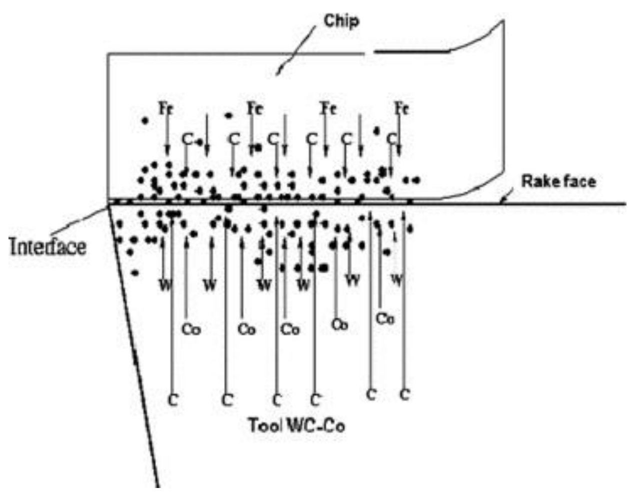

Figure 5.3 – Illustration of diffusion wear [90]

In cemented carbide tools, carbide (C) provides the hardness, while cobalt (Co) binds the tungsten carbide (WC) grains. For example in machining steel carbon diffuses to the moving steel chips, which have less concentration of the same atoms. This diffusion of tool materials leads to a weakened cutting edge and eventual chipping or breakage of the tool.

5.3 Wear types in machining

5.3.1 Crater Wear

At the tool-chip contact area where the tool is subject to friction forces due to the moving chip and high temperatures, crater wear occurs. It is considered that the diffusion is the main driving mechanism in crater wear since the greatest amount of crater wear occurs near the midpoint of the tool chip contact length where the temperature is greatest. Crater wear does not directly affect surface quality and tolerances but since it weakens the cutting edge and causes chipping of the tool, it is important to minimize crater wear. Therefore it is important to select a tool material with the minimum affinity to the workpiece material in terms of diffusion.

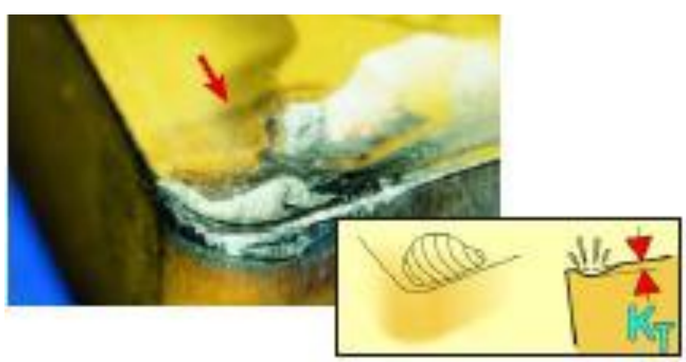

Figure 5.4 – Illustration of crater wear [91]

5.3.2 Flank Wear

The main cause of flank wear is the friction between the flank face (primary clearance face) of the tool and the machined workpiece surface. At the tool flank-workpiece contact zone, tool particles adhere to the workpiece surface and shear away from the tool. Abrasive wear may also occur when hard substances in the work or tool material scratch the flank and workpiece surface as they move across the contact area. Although adhesive and abrasive wear mechanisms are predominant in flank wear in machining traditional materials, some diffusion wear also exists. As flank wear increases, the tool-workpiece contact area becomes larger resulting in a poor surface finish, high friction forces and high temperatures. This eventually leads to tool breakage.

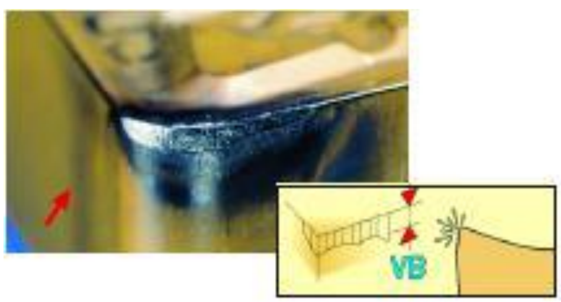

Figure 5.5 – Illustration of flank wear [91]

Since with the increasing flank wear portion of the sharp cutting edge is removed, the accuracy of the finished workpiece dimension is lost this amount. Therefore it can be concluded that the flank wear is more critical than crater wear. However, the volume that is worn away in crater wear is generally higher than for flank wear; if not controlled crater wear may also cause that total destruction of the tool.

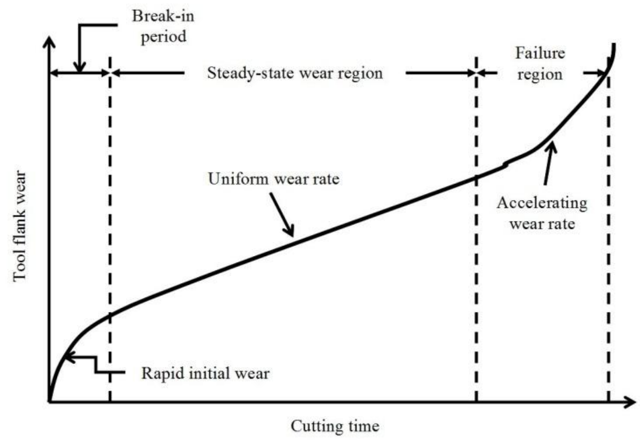

Figure 5.6 – General tool wear vs time graph [87]

The flank wear land is measured as the width of wear land on the primary clearance face [11]. A typical tool life curve is shown in Figure 5.6. The history of flank wear with machining time may be split into three regions. In the break in period the very sharp edge of the tool is worn rapidly after the cutting starts. This is followed by a steady-state region in which the wear rate is uniform and tool wear is approximately linear with increasing cutting time. After the wear land reaches a critical limit, the flank wear exponentially increases in the failure region. The tool must be replaced before reaching the critical limit to avoid catastrophic tool failure. The corresponding cutting time to this limit is called the tool life and was expressed first by Taylor [8] as a function of cutting conditions.

$$T_t = \frac{C_t}{V^{p'} \cdot c^{q'}} \tag{5.1}$$

Where T_t is the tool life, V is the cutting speed, and c is the feed rate, C_t, p' and q' are constants for a given tool-workpiece material pair and are identified from machining tests. It is stated that for constant feed rate (c) or constant speed *(V)*, logarithmic tool life charts can be prepared for the appropriate selection of feeds and speeds for a desired tool life performance by Altintas [11].

In this thesis, the tool lives of 6 different tungsten carbide helical end mills are analyzed. Using experimental wear data, an empirical relation for each tool that relates wear with maximum cutting temperatures, machining time and tool material is obtained. The effect of cutting temperature and material structure on tool life is presented.

5.4 Wear tests

In order to obtain a relation for the flank wear of the tools wear tests are conducted under the conditions given in Table 5.1. During the wear tests 16 mm diameters slots are cut using the tools and after each 64m of cutting distance, the tool flank wear is measured using an optical microscope.

Table 5.1 – Wear test conditions

Spindle Speed	*8000 rpm*
Feed per tooth	*0.25 mm/rev*
Wear Criteria	*300 micron in the flank face*
Measurement Interval	*20 min*

Table 5.2 – Tool wear of tool A

Tool A			
Radial Clearance Face - Flute 1			
Material Removed (cm^3)	Distance (m)	Time(min)	Wear (μm)
0	0	0	0
2048	64	20	36
4096	128	40	37
6144	192	60	39
8192	256	80	46
10240	320	100	47
12288	384	120	51
14336	448	140	53
16384	512	160	186
18432	576	180	188
20480	640	200	195
22528	704	220	199
24576	768	240	200
26624	832	260	201
28672	896	280	201
30720	960	300	205
32768	1024	320	207
34816	1088	340	207
36864	1152	360	209
38912	1216	380	211
40960	1280	400	211
43008	1344	420	212
45056	1408	440	212

Table 5.3 – Tool wear of tool B

Tool B			
Radial Clearance Face - Flute 2			
Material Removed (cm^3)	Distance (m)	Time(min)	Wear (µm)
0	0	0	0
2048	64	20	31
4096	128	40	38
6144	192	60	54
8192	256	80	83
10240	320	100	88
12288	384	120	92
14336	448	140	92
16384	512	160	96
18432	576	180	100
20480	640	200	102
22528	704	220	104
24576	768	240	104
26624	832	260	107
28672	896	280	108
30720	960	300	113
32768	1024	320	114
34816	1088	340	117
36864	1152	360	121
38912	1216	380	121
40960	1280	400	124
43008	1344	420	125
45056	1408	440	126

Table 5.4 – Tool wear of tool C

Tool C			
Radial Clearance Face - Flute 2			
Material Removed (cm^3)	Distance (m)	Time(min)	Wear (μm)
0	0	0	0
2048	64	20	16
4096	128	40	19
6144	192	60	23
8192	256	80	42
10240	320	100	56
12288	384	120	61
14336	448	140	67
16384	512	160	70
18432	576	180	72
20480	640	200	88
22528	704	220	97
24576	768	240	97
26624	832	260	101
28672	896	280	101
30720	960	300	102
32768	1024	320	104
34816	1088	340	106
36864	1152	360	110
38912	1216	380	111
40960	1280	400	111
43008	1344	420	114
45056	1408	440	120

Table 5.5 – Tool wear of tool D

Tool D			
Radial Clearance Face - Flute 2			
Material Removed (cm^3)	Distance (m)	Time(min)	Wear (µm)
0	0	0	0
2016	63	20	10
4032	126	40	10
6048	189	60	10
8064	252	80	10
10080	315	100	11
12096	378	120	11
14112	441	140	11
16128	504	160	12
18144	567	180	12
20160	630	200	12
22176	693	220	13
24192	756	240	14
26208	819	260	14
28224	882	280	15
30240	945	300	15
32256	1008	320	15
34272	1071	340	15
36288	1134	360	16
38304	1197	380	16
40320	1260	400	17
42336	1323	420	18
44352	1386	440	20
46368	1449	460	23

Table 5.6 – Tool wear of tool E

Tool E			
Radial Clearance Face - Flute 1			
Material Removed (cm^3)	Distance (m)	Time(min)	Wear (µm)
0	0	0	0
2016	63	20	11
4032	126	40	12
6048	189	60	14
8064	252	80	20
10080	315	100	21
12096	378	120	22
14112	441	140	38
16128	504	160	38
18144	567	180	38
20160	630	200	38
22176	693	220	39
24192	756	240	40
26208	819	260	42
28224	882	280	44
30240	945	300	45
32256	1008	320	47
34272	1071	340	51
36288	1134	360	51
38304	1197	380	53
40320	1260	400	55
42336	1323	420	61
44352	1386	440	64
46368	1449	460	67

Table 5.7 – Tool wear of tool F

Tool F			
Radial Clearance Face - Flute 2			
Material Removed (cm^3)	Distance (m)	Time(min)	Wear (µm)
0	0	0	0
2016	63	20	36
4032	126	40	37
6048	189	60	38
8064	252	80	40
10080	315	100	42
12096	378	120	44
14112	441	140	47
16128	504	160	48
18144	567	180	50
20160	630	200	51
22176	693	220	53
24192	756	240	54
26208	819	260	54
28224	882	280	56
30240	945	300	58
32256	1008	320	159
34272	1071	340	160
36288	1134	360	161
38304	1197	380	163
40320	1260	400	163
42336	1323	420	168
44352	1386	440	186
46368	1449	460	189

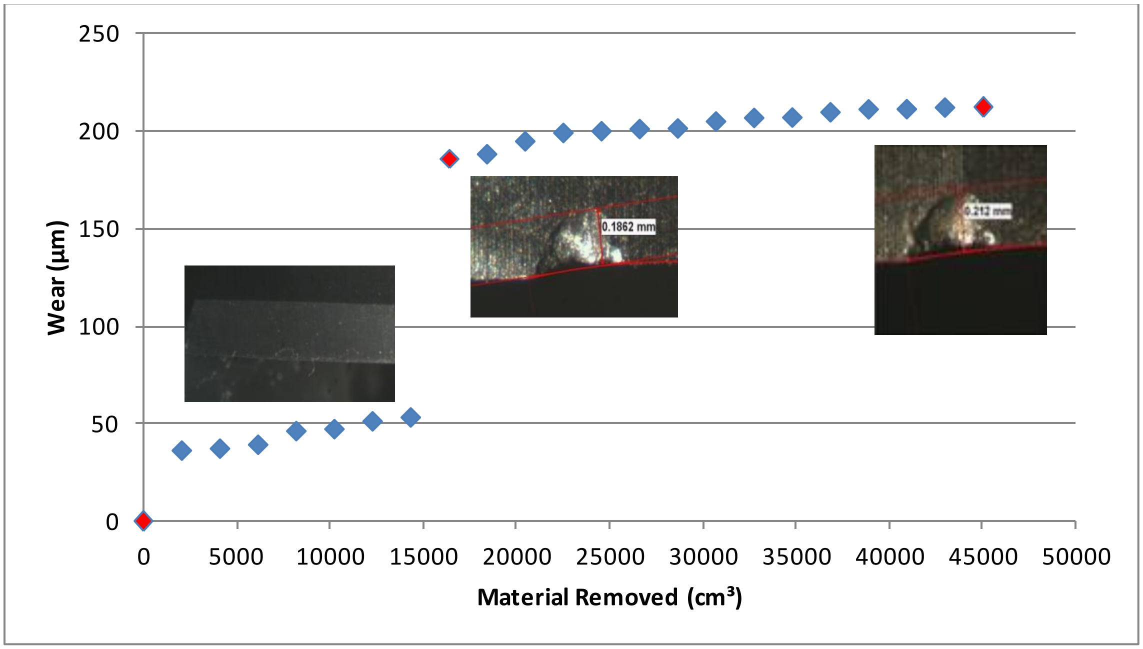

Figure 5.7 – Flank wear vs material removed for tool A

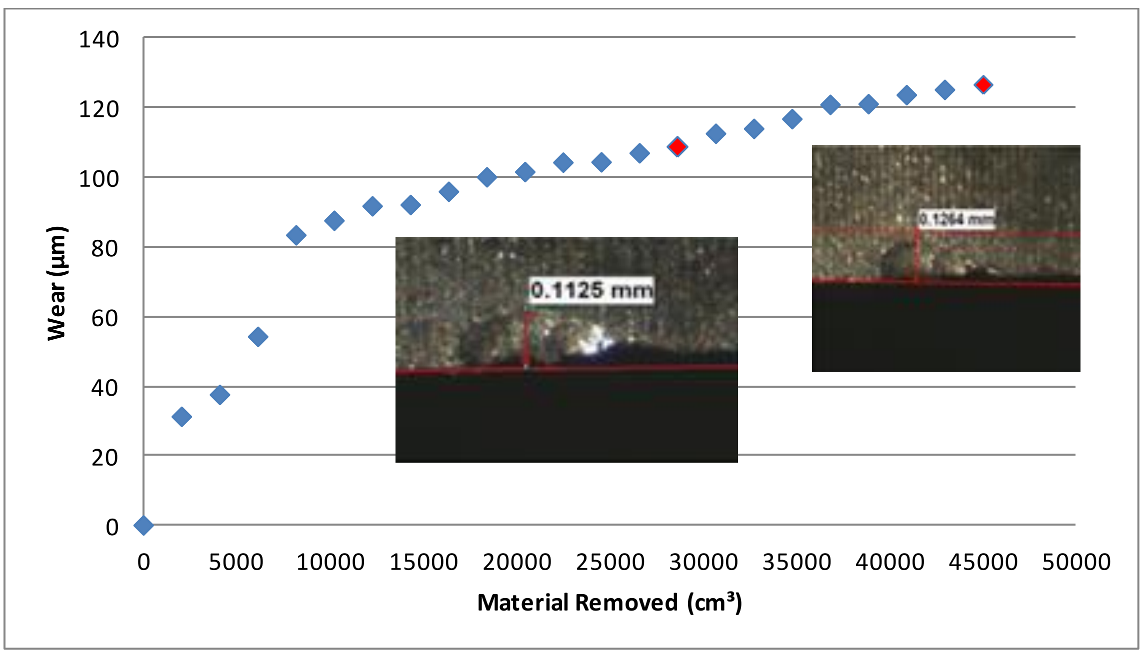

Figure 5.8 – Flank wear vs material removed for tool B

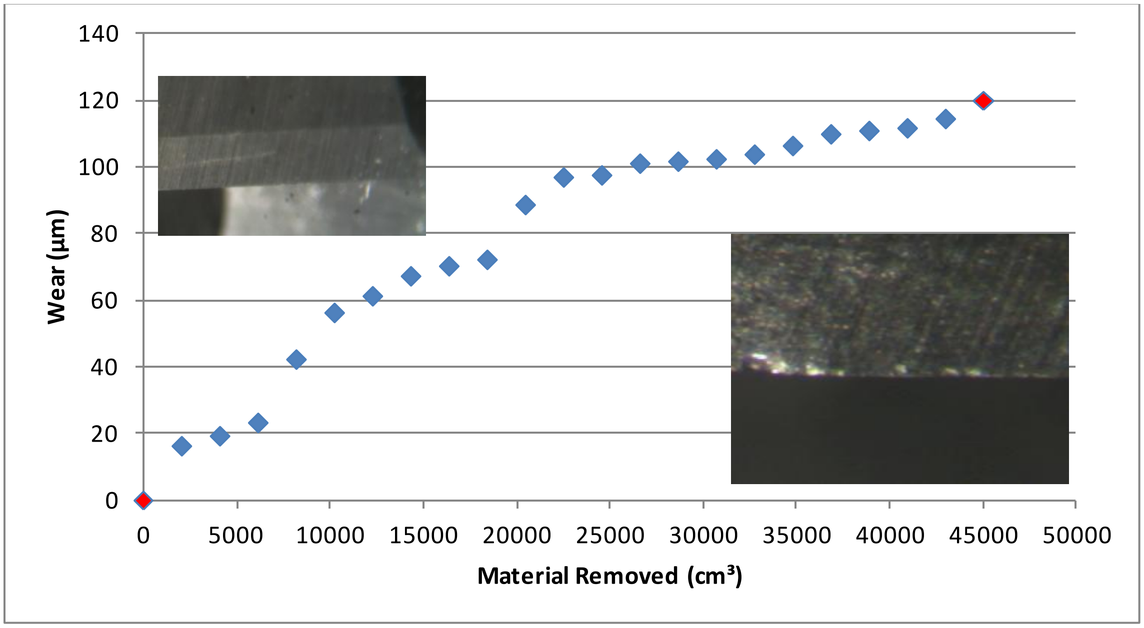

Figure 5.9 – Flank wear vs material removed for tool C

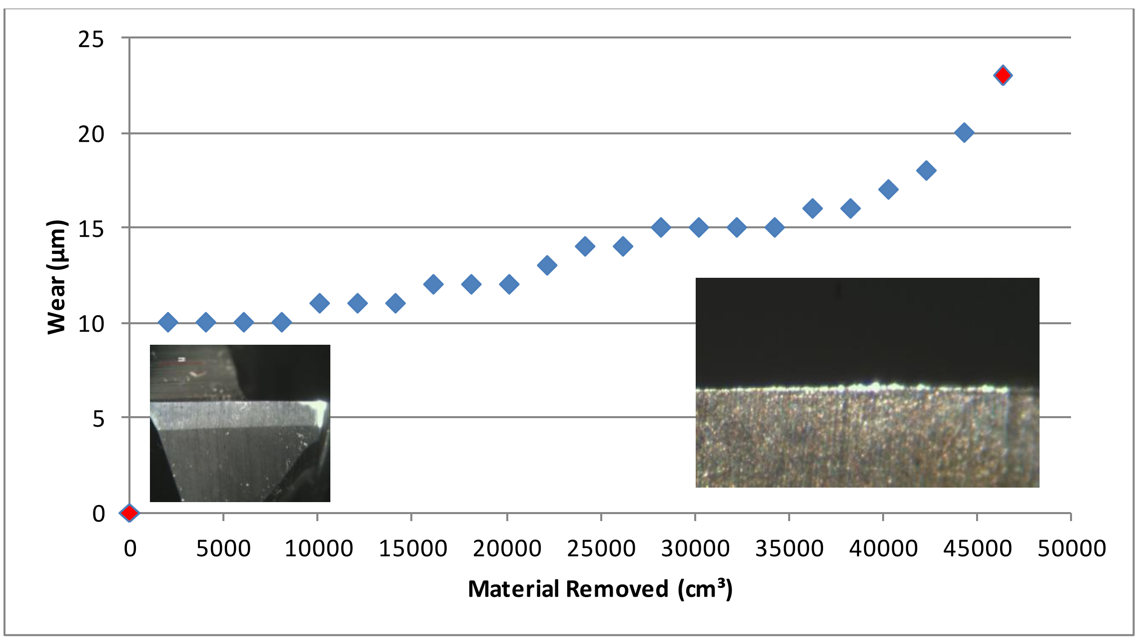

Figure 5.10 – Flank wear vs material removed for tool D

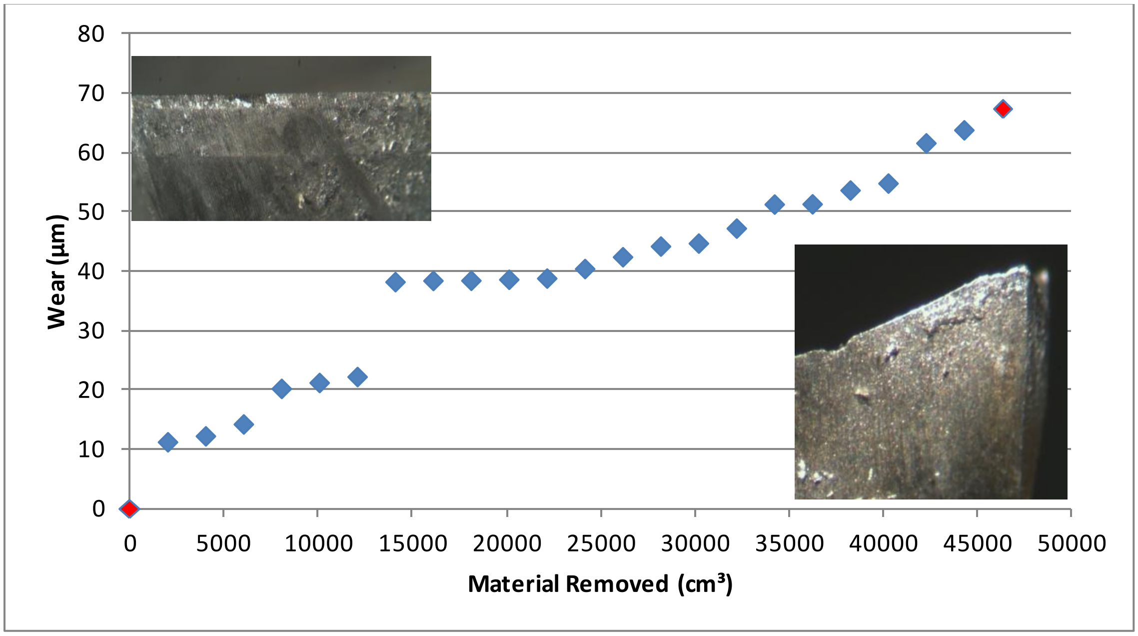

Figure 5.11 – Flank wear vs material removed for tool E

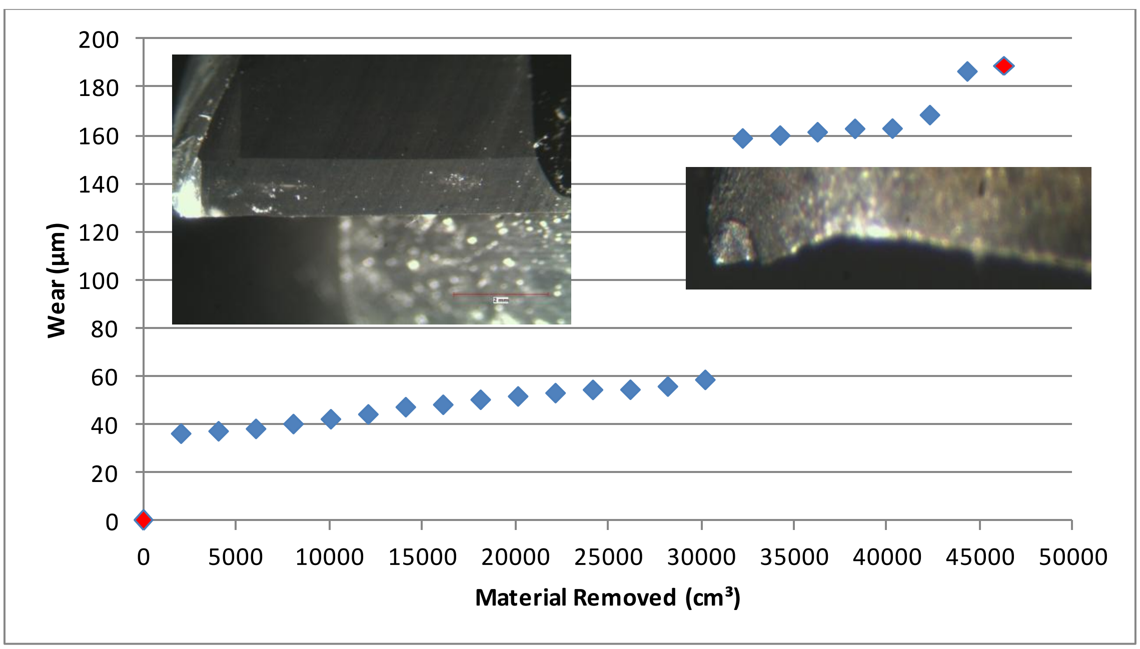

Figure 5.12 – Flank wear vs material removed for tool F

Using a logarithmic curve fit a relation between the tool flank wear and volume of material removed is obtained as follows;

$$V_b = C_1 \cdot \left(\frac{T_{c,\max}}{HV} \right) \cdot \ln(MR) - C_2 \qquad (5.2)$$

Where C_1 and C_2 are the empirical constants obtained from the cutting experiments, $T_{c,\max}$ is the maximum temperature on the flank face of the tool, HV is the Vickers Hardness of the tool material and MR is the material removed in cm^3.

Table 5.8 – Empirical constant for the wear equation

Tool Name	C1	C2	$T_{c,\max}$ [K]	Vickers Hardness [HV]	R^2
A	1,064	310,13	714	16	0,6338
B	0,640	130,04	579	15,9	0,9137
C	0,882	259,37	615	15,6	0,94
D	0,083	14,73	634	18,1	0,7932
E	0,463	125,32	569	15,7	0,8892
F	0,708	200,98	668	15,9	0,4258

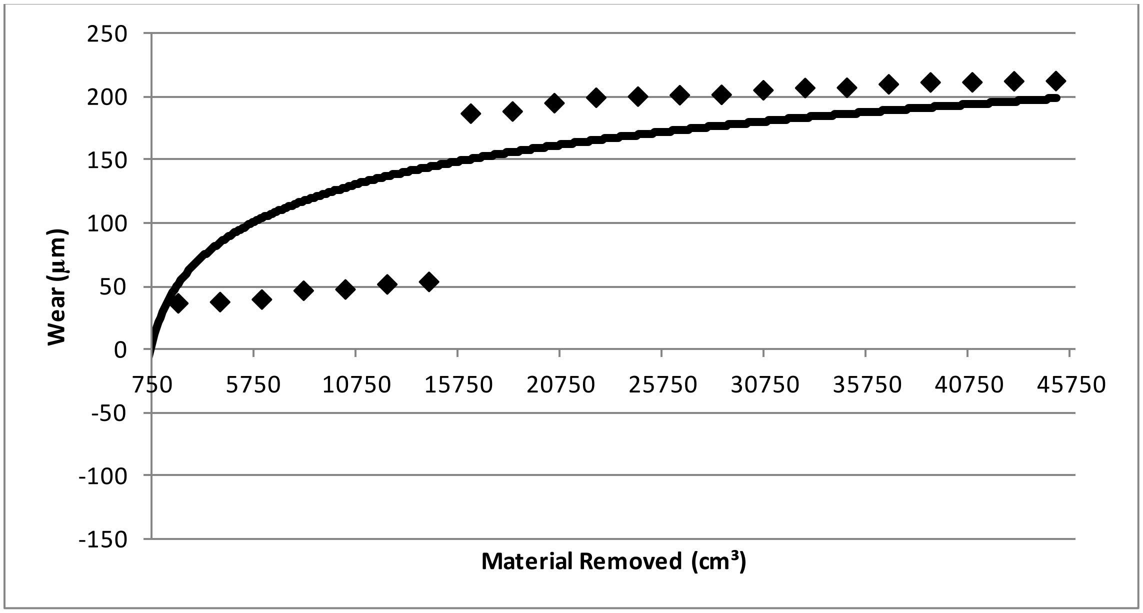

Figure 5.13 – Comparison of the simulated and the experimental data for tool A

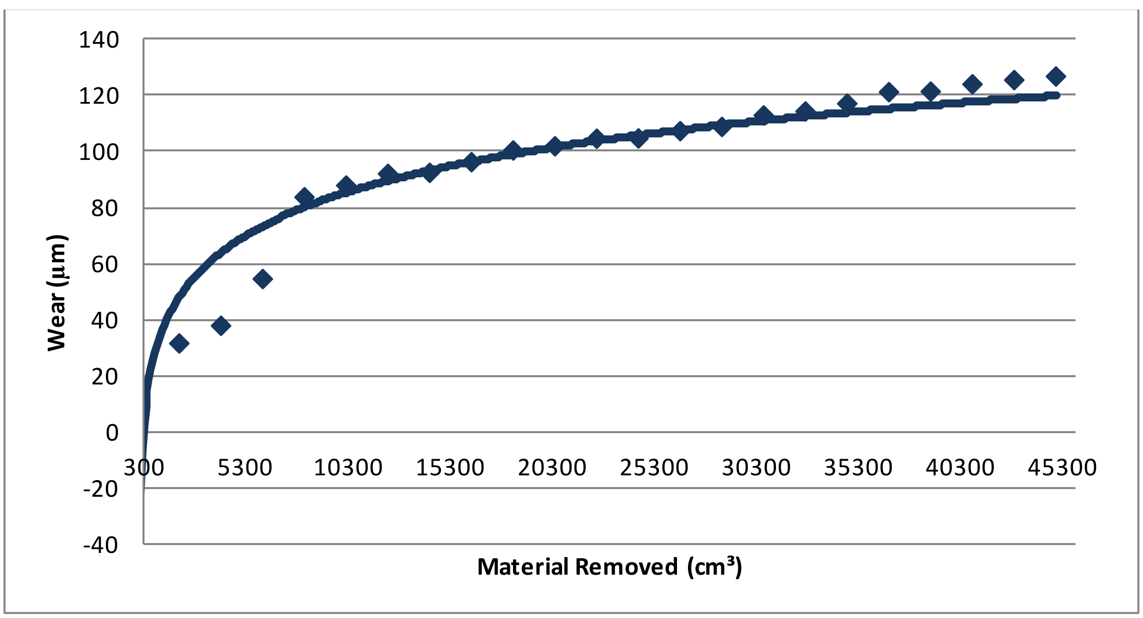

Figure 5.14 – Comparison of the simulated and the experimental data for tool B

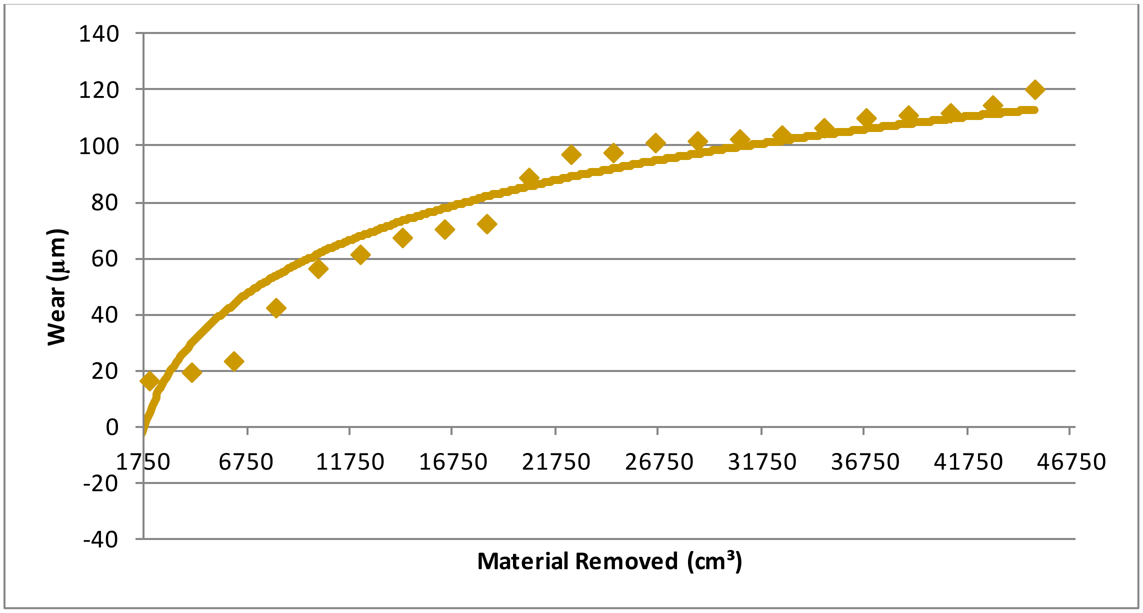

Figure 5.15 – Comparison of the simulated and the experimental data for tool C

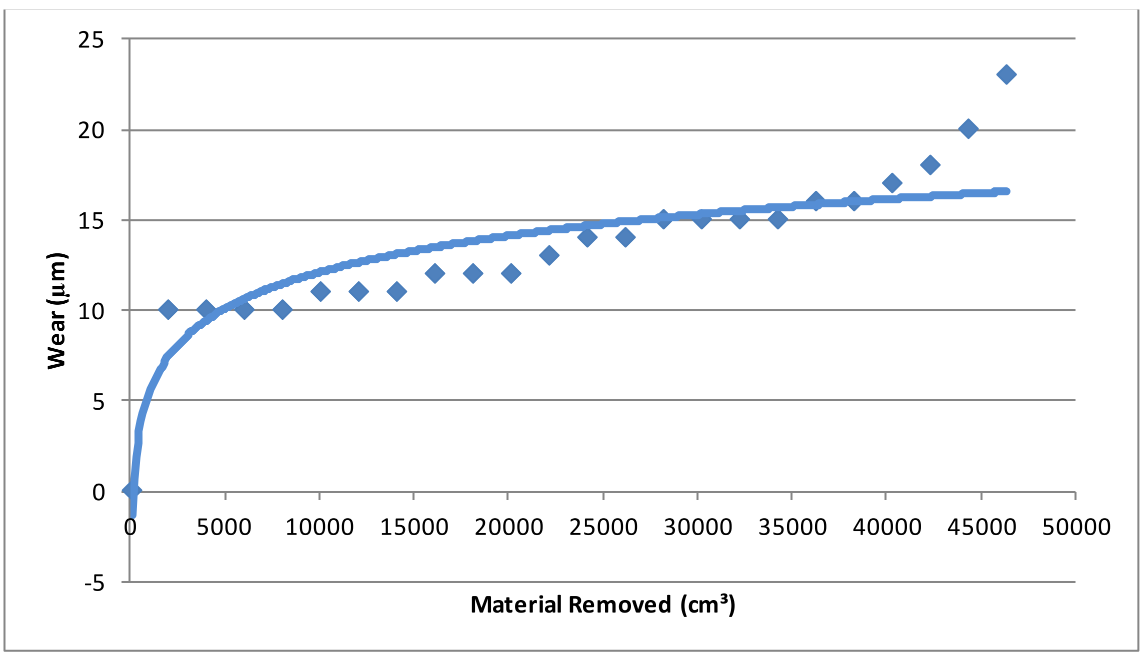

Figure 5.16 – Comparison of the simulated and the experimental data for tool D

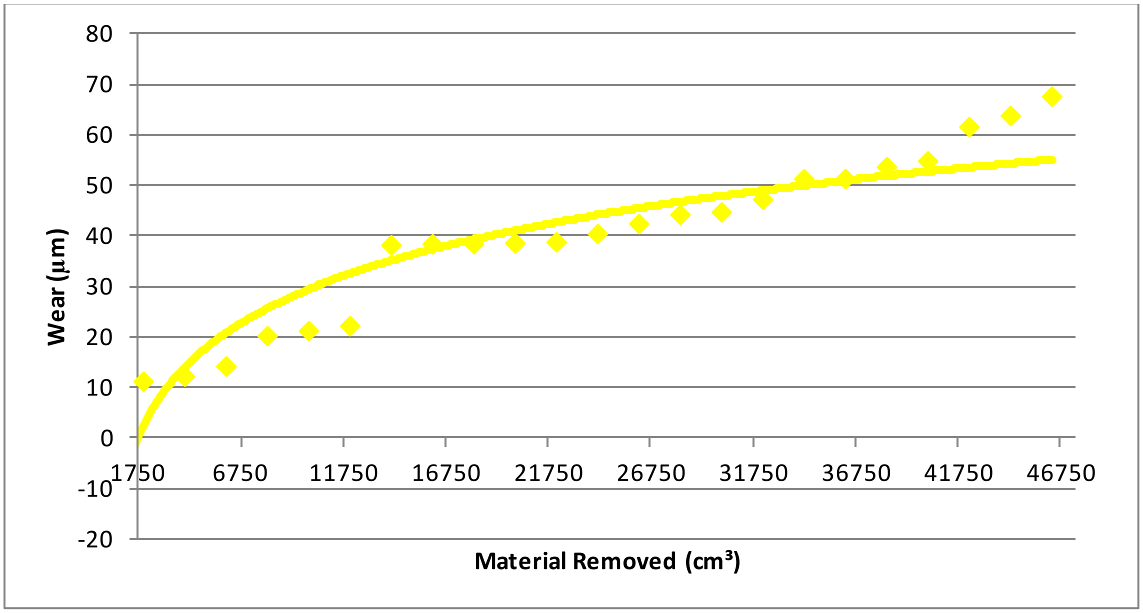

Figure 5.17 – Comparison of the simulated and the experimental data for tool E

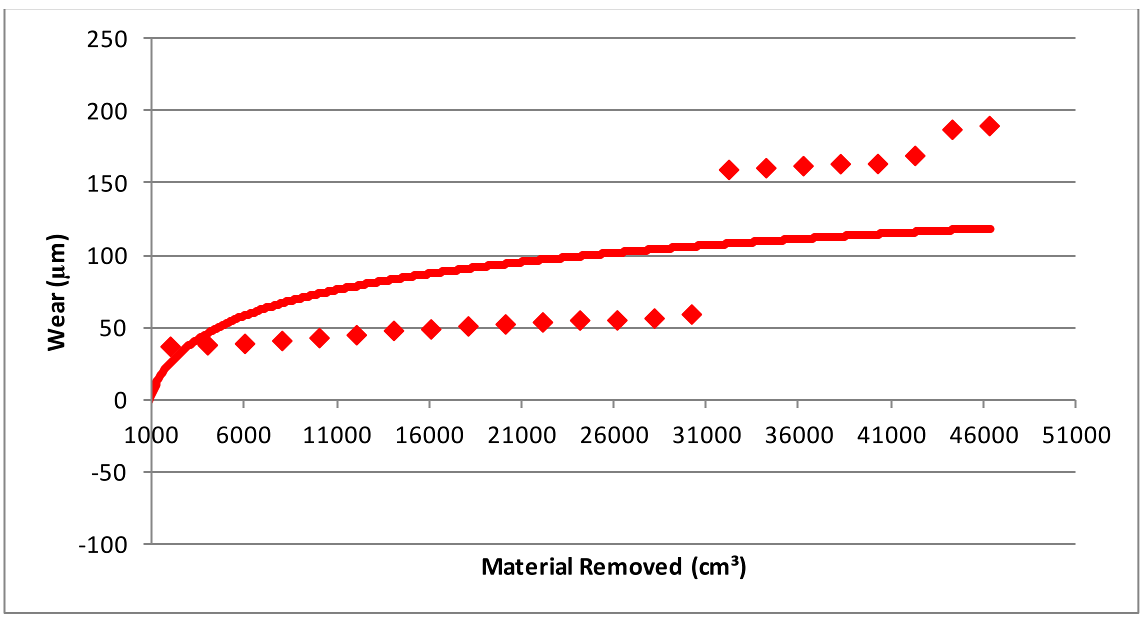

Figure 5.18 – Comparison of the simulated and the experimental data for tool F

It is seen that, in overall, simulated values are in good agreement with the experimental data as indicated by the coefficient of determination values (R^2) being closer to 1. However for tools A and F the equation has some deviations from the experimental data. When the tool wear graphs and wear images of tools A and F investigated carefully it is seen that there are sudden jumps in the tool wear graphs, indicating severe chipping and chip hammering of the cutting edge. The main reason of chip hammering is the deflection of chips against cutting edge. To prevent chip hammering it is suggested to alter the tool geometry, change the feed rate or increase the toughness of the tool material.

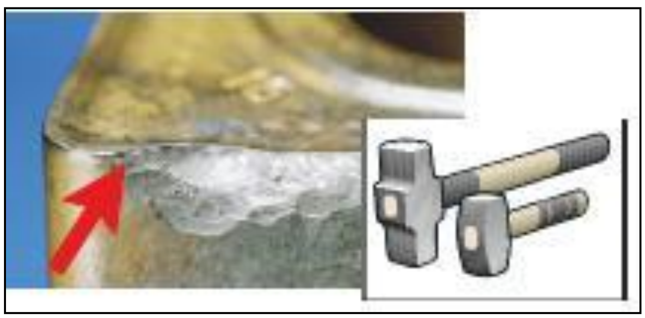

Figure 5.19 – Example chip hammering image

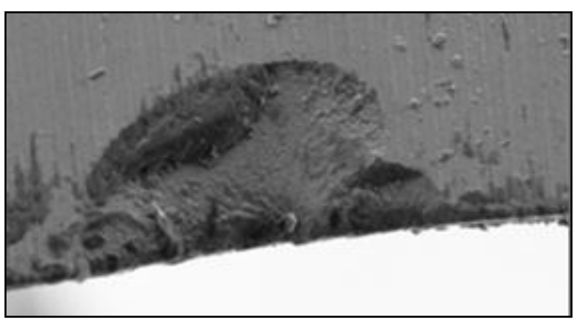

Figure 5.20 – Wear image for tool A

Taking the chip hammering into account, the tool life equations are modified as piecewise functions with a logarithmic function until the breaking point and a linear function thereafter, increasing the R^2 values above 0.90.

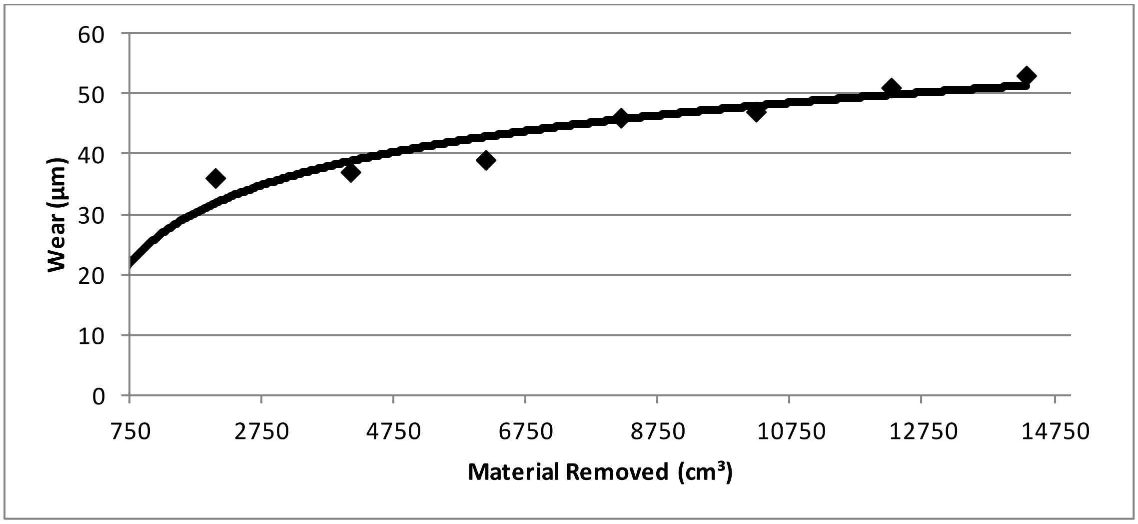

Figure 5.21 – Wear analysis for tool A until the breaking point.

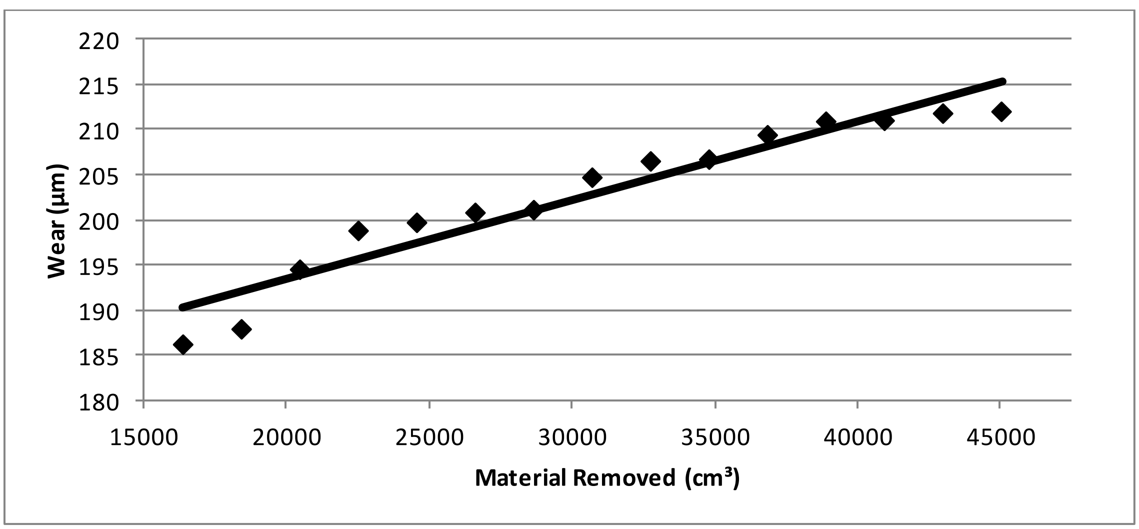

Figure 5.22 – Wear analysis for tool A after the breaking point.

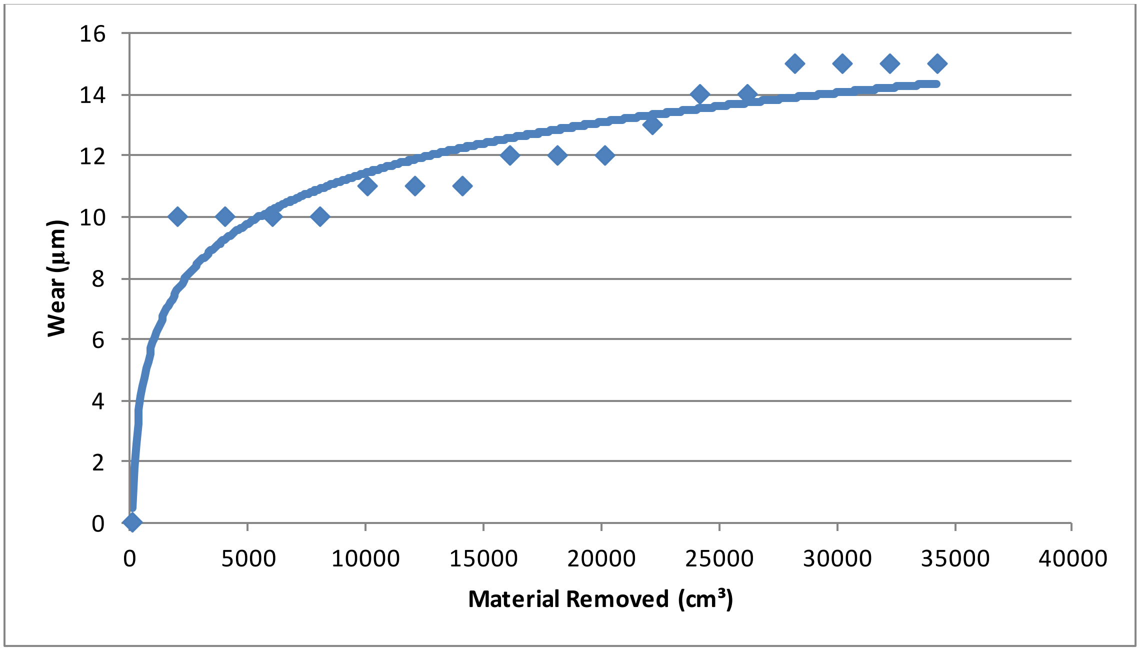

Figure 5.23 – Wear analysis for tool D until the breaking point.

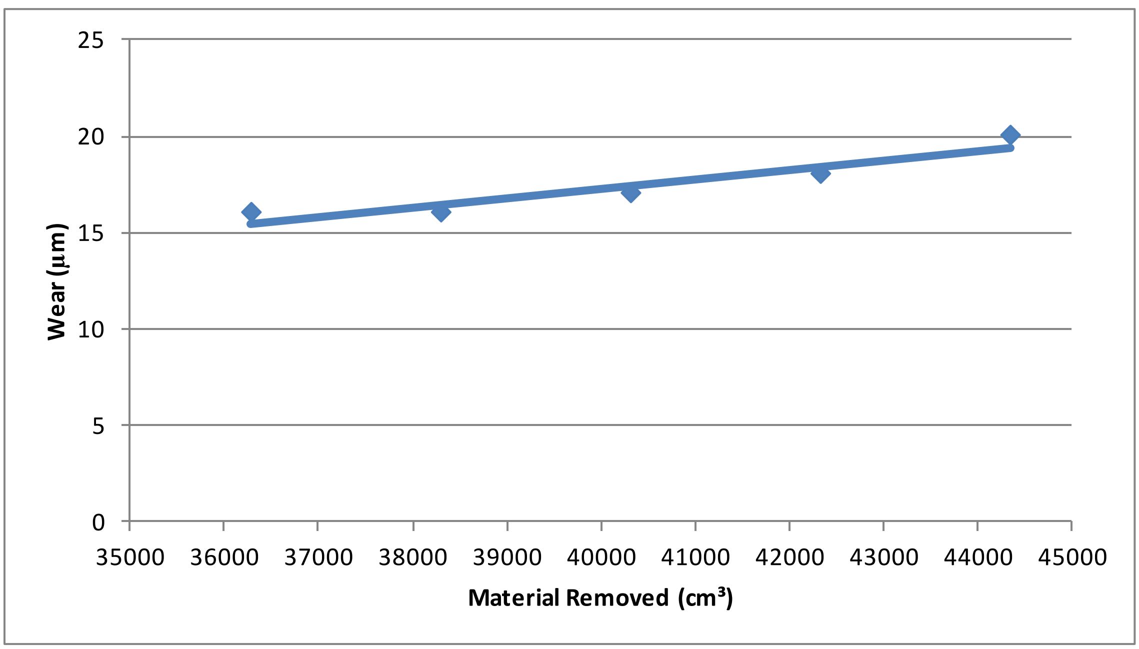

Figure 5.24 – Wear analysis for tool D after the breaking point.

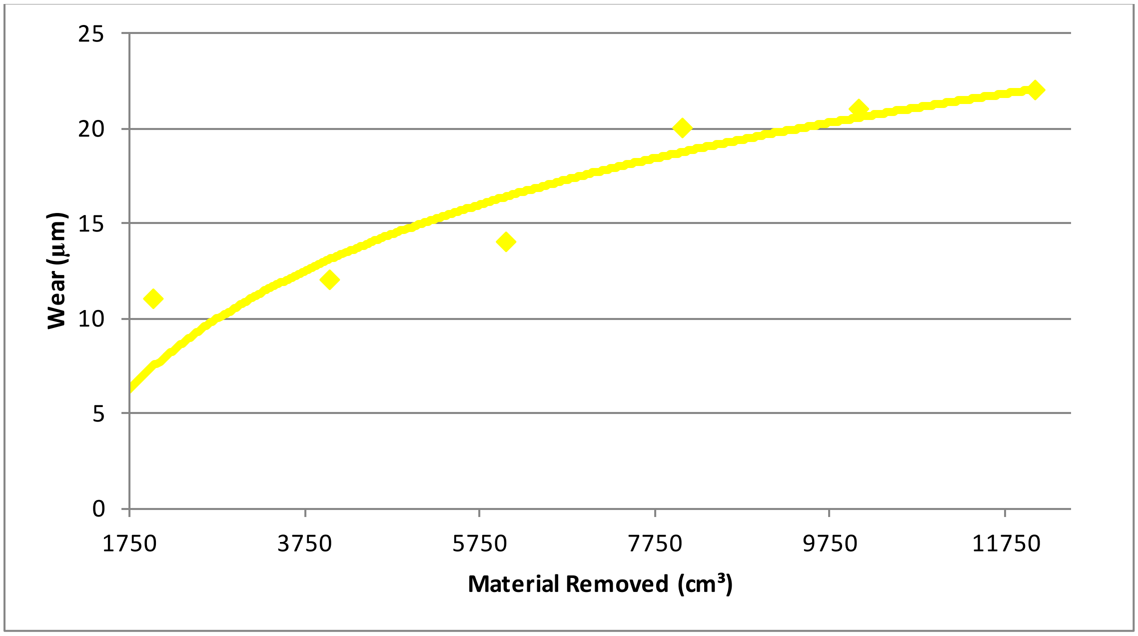

Figure 5.25 – Wear analysis for tool E until the breaking point.

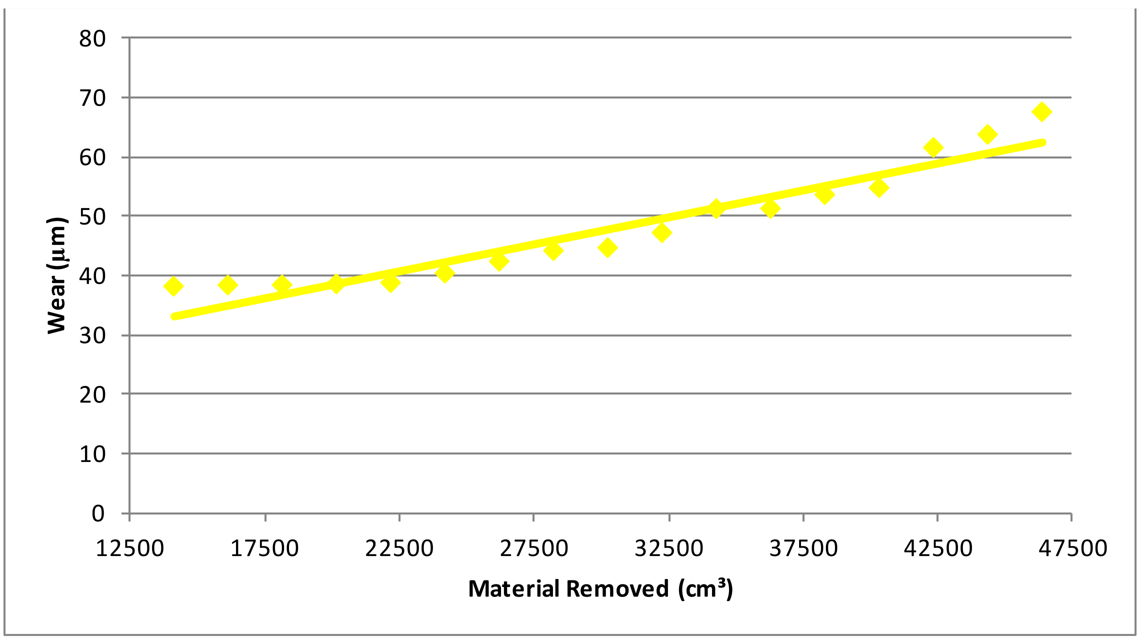

Figure 5.26 – Wear analysis for tool E after the breaking point.

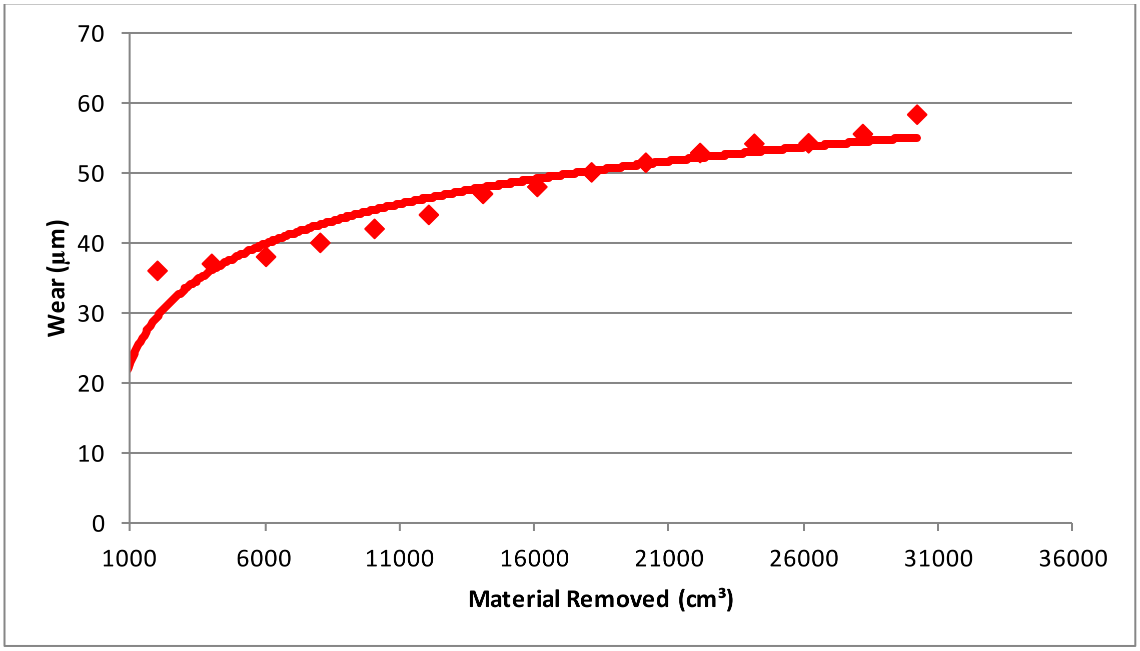

Figure 5.27 – Wear analysis for tool F until the breaking point.

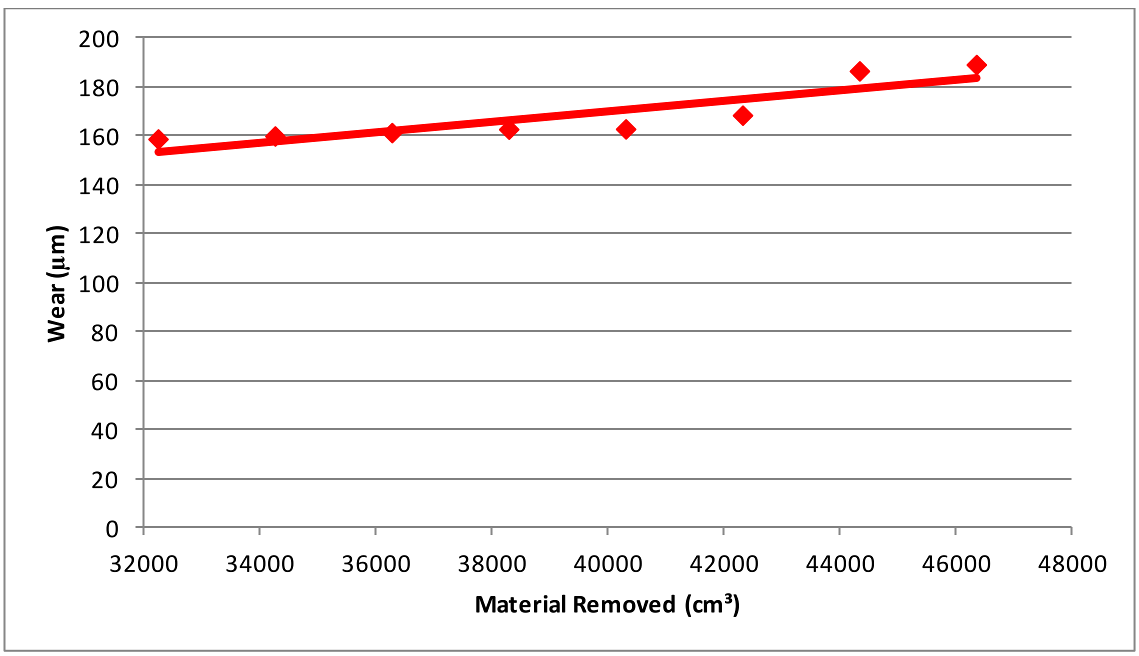

Figure 5.28 – Wear analysis for tool F after the breaking point.

Therefore the final form of tool life equations becomes;

For tools B and C:

$$V_b = C_1 \cdot \left(\frac{T_{c,\max}}{HV}\right) \cdot \ln(MR) - C_2$$

For tools A-D-E-F:

$$V_b = C_1 \cdot \left(\frac{T_{c,\max}}{HV}\right) \cdot \ln(MR) - C_2 \text{ before the breaking point}$$

$V_b = C_3 \cdot MR + C_4$ after the breaking point, with the coefficients C_3 and C_4 are given in table 5.9.

Table 5.9 – Empirical constant for piecewise wear equations

Tool Name	C3	C4	R^2
A	0,225	-44,741	0,9786
D	0,068	-10,497	0,9241
E	0,225	-54,634	0,9323
F	0,225	-42,457	0,9705

Chapter 6

INDUSTRIAL APPLICATIONS

6.1 Background of the project

In this chapter the industrial application of this study is presented. In 2011 a research partnership was established with Turkish Aerospace Industry (TAI) and Koç University Manufacturing and Automation Research Center (MARC) and a project to optimize the performances of helical end mills in milling Al-7050 is started. TAI has its production capacity full for the next ten to fifteen years for various projects from all over the world such as Joint Strike Fighter, Eurocopter, ANKA etc. Majority of the work done on these projects is pocketing operations in which 90-95% of the bulk material is removed to obtain complex geometries for the body and the wings of the airplanes and helicopters.

However the tool costs constitutes a large portion of the overall production cost. Up to this project, the tool selection criterion was mainly the cost of the tool in TAI. The objectives of this work were to describe the parameters that affect the tool life and improve the tool selection process. To achieve this, carefully designed cutting force and tool wear tests were conducted in Koç University MARC laboratory. In this chapter the results of these tests and the industrial outcomes of the project are presented.

6.2 Cutting force tests

Initially a quotation has been asked from the tool companies by TAI in order to create a database for the tool brands interested in supplying the tools. A total number of 141 different tools with 66 different geometries from various companies were collected.

Figure 6.1 – Picture of the tools supplied by the companies

Communicating with the Production Management department of TAI it was decided to perform cutting experiments on tools with 16 mm diameter since they were the most commonly used tool type in the factory and the dynamometer in MARC laboratory can hold tools with 16 mm diameter at maximum. Initially the tools are subjected to both slot milling and side milling tests to evaluate their cutting force performances.

Table 6.1 - Sample design of cutting force experiments

Tool Name	Average Cutting Forces			
	Slot Milling		Side Milling	
Spindle Speed [rpm] / Feed per tooth [mm/rev]	4000	8000	4000	8000
0.10	✓	✓	✓	✓
0.15	✓	✓	✓	✓
0.25	✓	✓	✓	✓

For the cutting force tests the tools are mounted on a rotary dynamometer which has piezoelectric material inside that sends electric signals when there is a force acting on it as shown in Figure 6.2. These signals are amplified via the charge amplifier and fed into the data acquisition card (DAQ card). Initially the tests are conducted at two different spindle speeds of 4000 rpm and 8000 rpm and 3 different feed rates of 0.10, 0.15 and 0.25 mm/rev. The force values for these conditions are shown in Figures 6.14-6.23.

Figure 6.2 - Experimental Setup

Table 6.2 - Sample Cutting Conditions

Tool Name	Spindle Speed	Feed per tooth	Feed
Tool A 2 flutes	8000rpm	0.25 mm/tooth	6000 mm/min

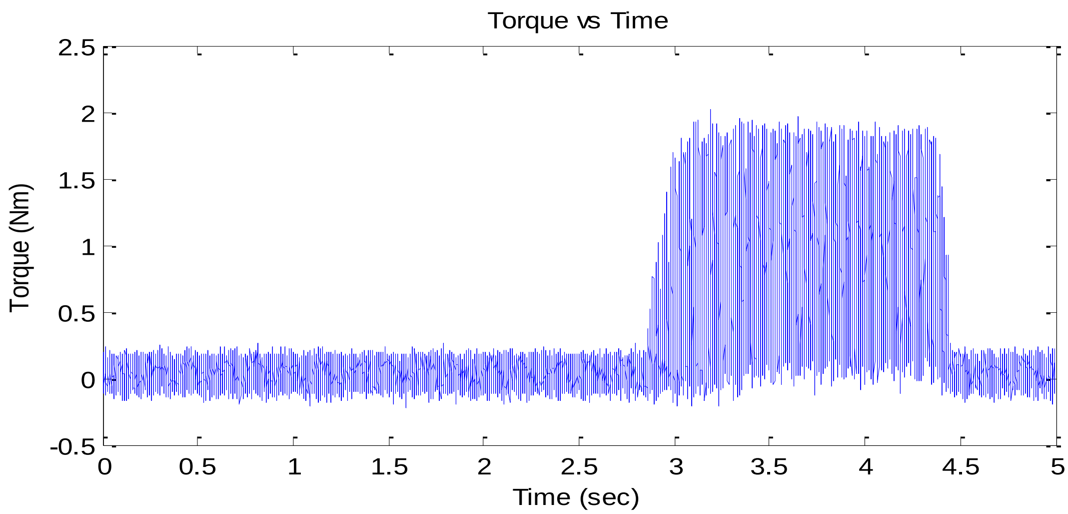

Figure 6.3 – Sample torque data vs time graph (Tool A)

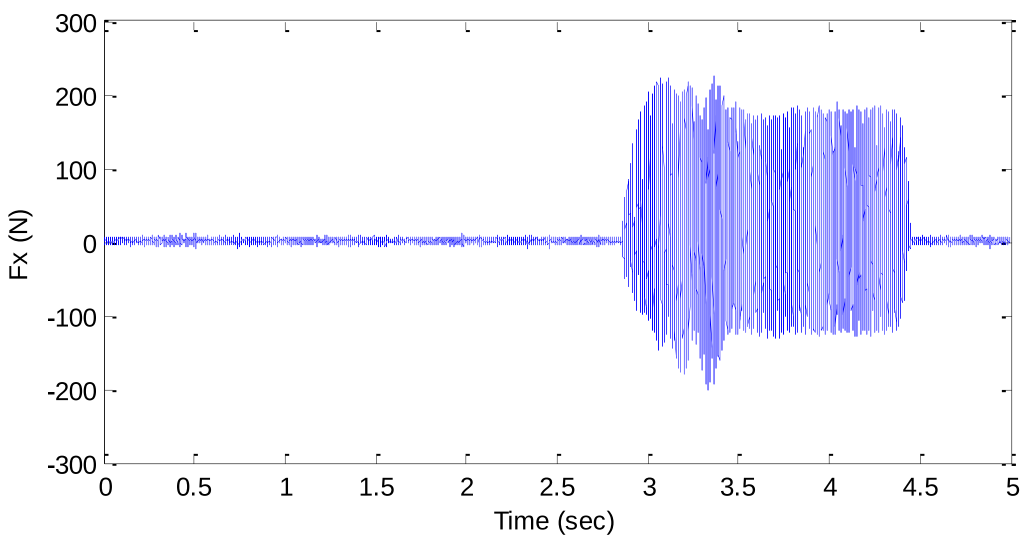

Figure 6.4 – Sample tangential cutting forces data vs time graph (Tool A)

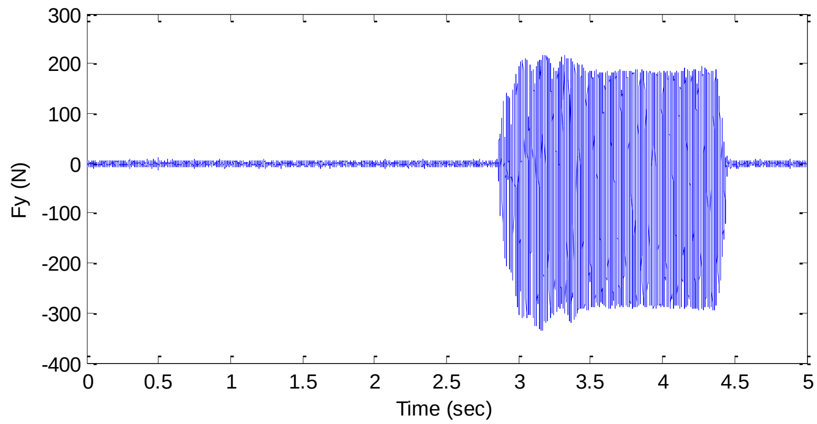

Figure 6.5– Sample radial cutting forces data vs time graph (Tool A)

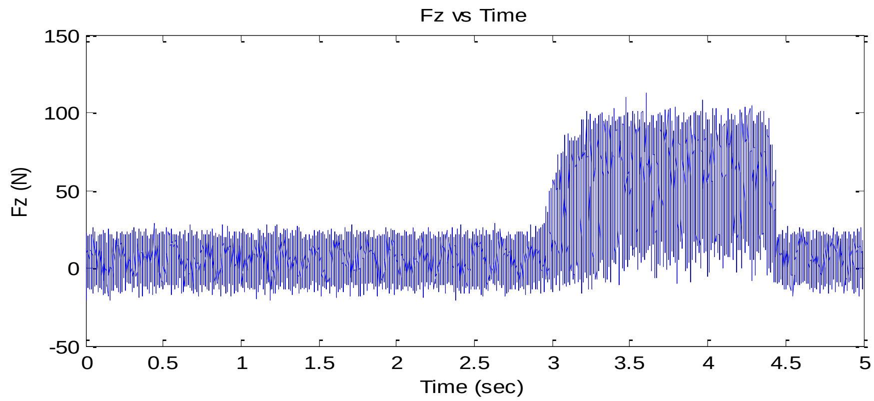

Figure 6.6 – Sample axial cutting forces data vs time graph (Tool A)

With the algorithm developed, the maximum and minimum force values are calculated.

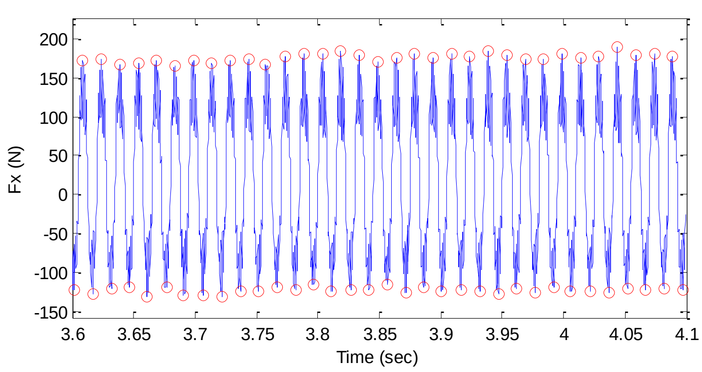

Figure 6.7 – Sample maximum tangential cutting forces vs time graph (Tool A)

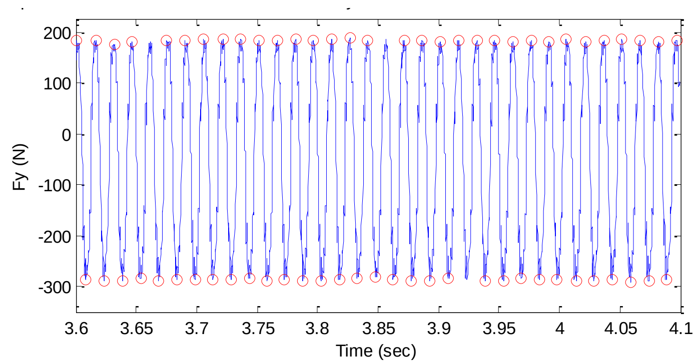

Figure 6.8 – Sample maximum radial cutting forces vs time graph (Tool A)

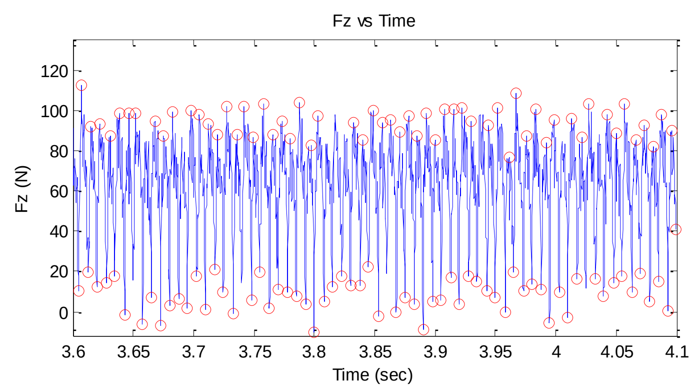

Figure 6.9 – Sample maximum axial cutting forces vs time graph (Tool A)

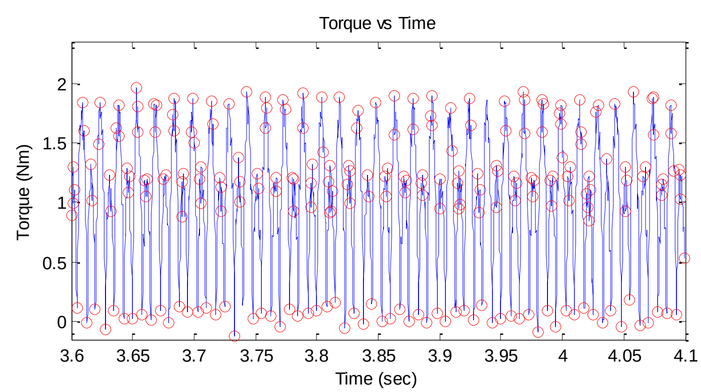

Figure 6.10 – Sample maximum cutting torque vs time graph (Tool A)

Using these data, characteristic force curves for each tool is obtained by plotting these force values with respect to the corresponding feed rate as shown in Figure 6.11-12.

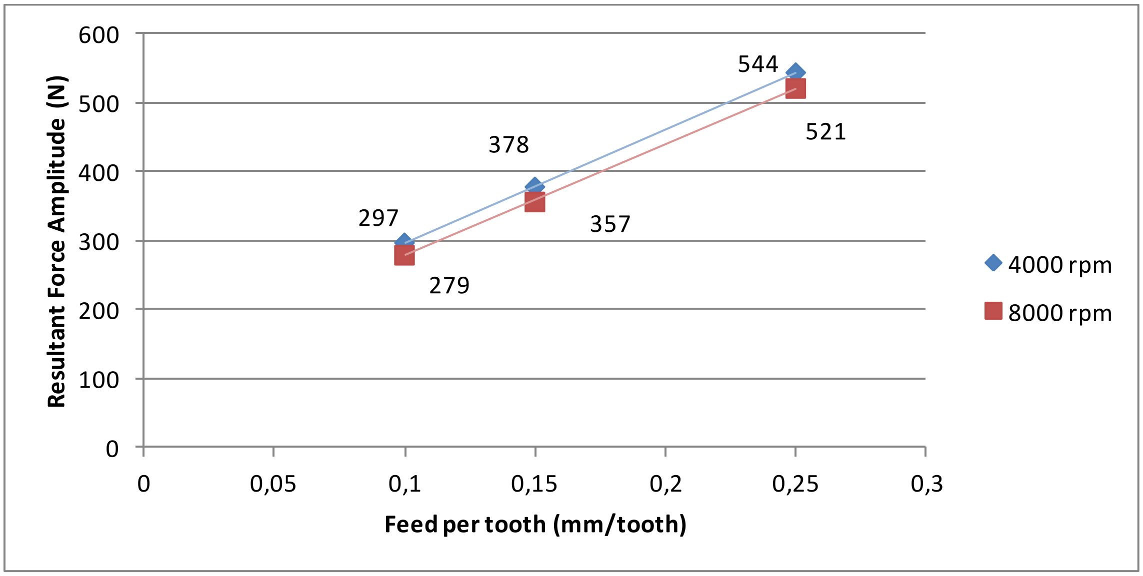

Figure 6.11 - Sample resultant cutting forces vs feed per tooth graph (Tool A)

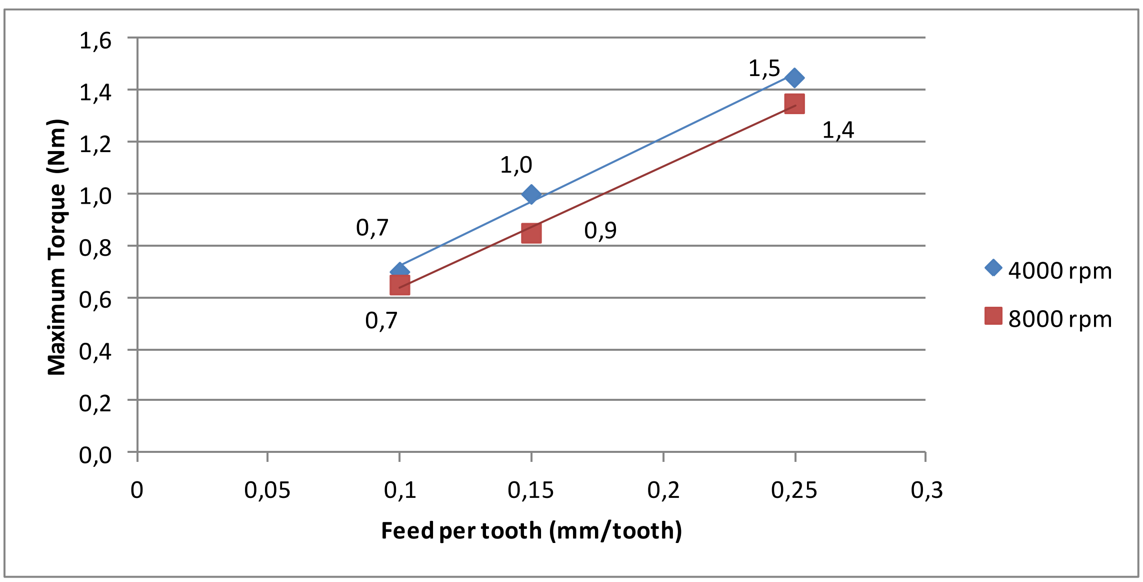

Figure 6.12 – Sample cutting torque vs feed per tooth graph

The first set of experiments was side milling tests where the process is down milling and half of the tool is immerged into the workpiece ($\phi_{st} = 90°, \phi_{ex} = 0°$). The second set was slot milling in which the process starts as up milling and after the maximum depth of cut turns into down milling ($\phi_{st} = 0°, \phi_{ex} = 180°$). For each test the total distance of cut was 20 mm and the axial depth of cut was 2 mm. After the first set of tests it is realized that the relative performances of the tools were independent of the cutting type as expected, therefore in order to use time more efficiently the tools are subjected to slot milling tests only for the remaining tests.

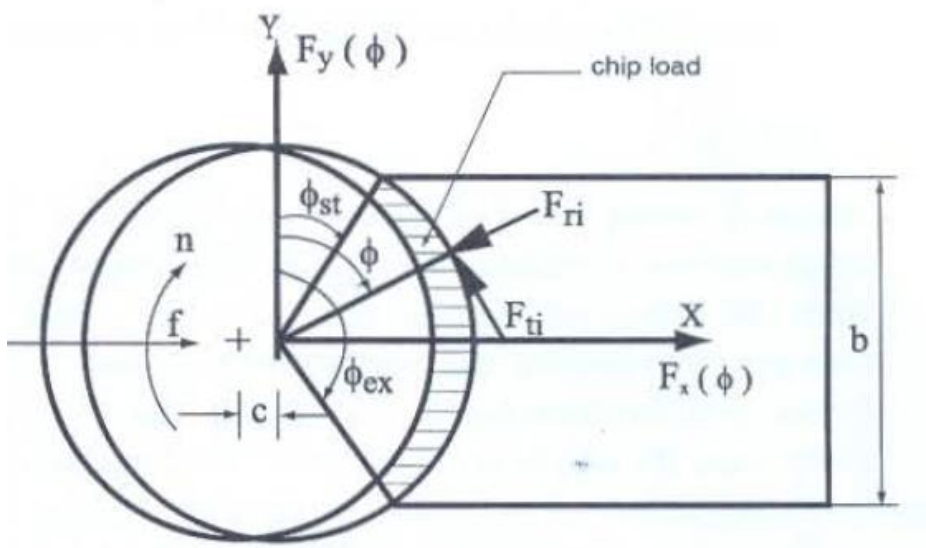

Figure 6.13 – Illustration of the entrance and exit angles for milling [11]

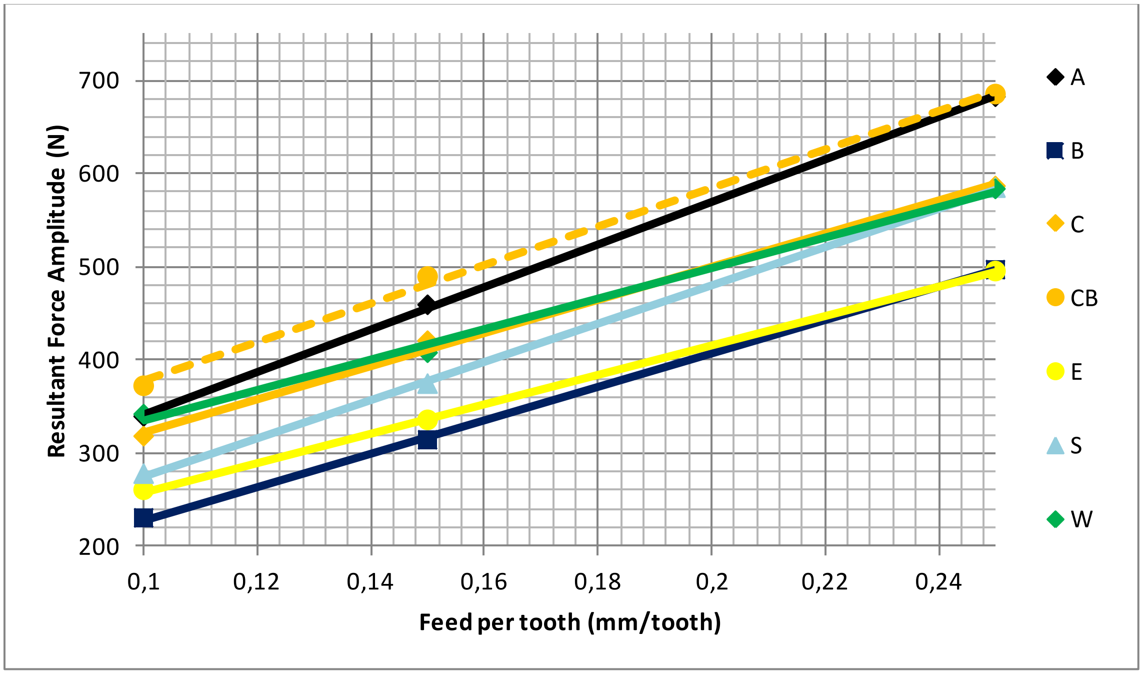

Figure 6.14 –Cutting forces vs feed per tooth graph for slot milling at 8000 rpm

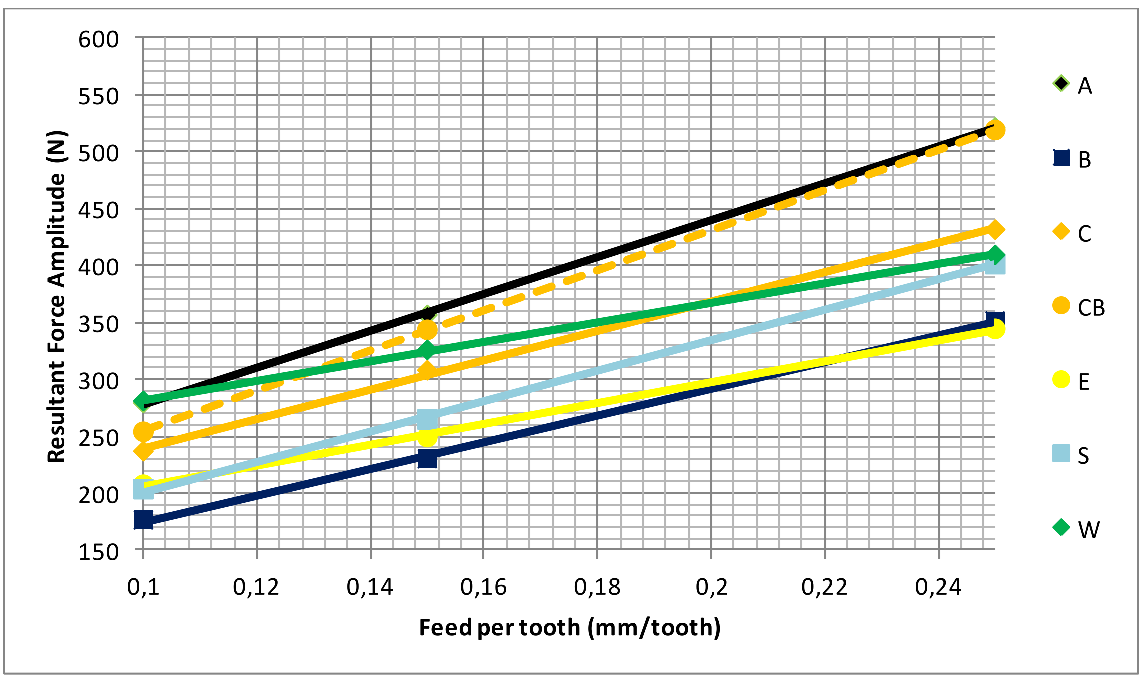

Figure 6.15 –Cutting forces vs feed per tooth graph for side milling at 8000 rpm

The results of the slot milling tests are given in Figures 6.16-6-21.

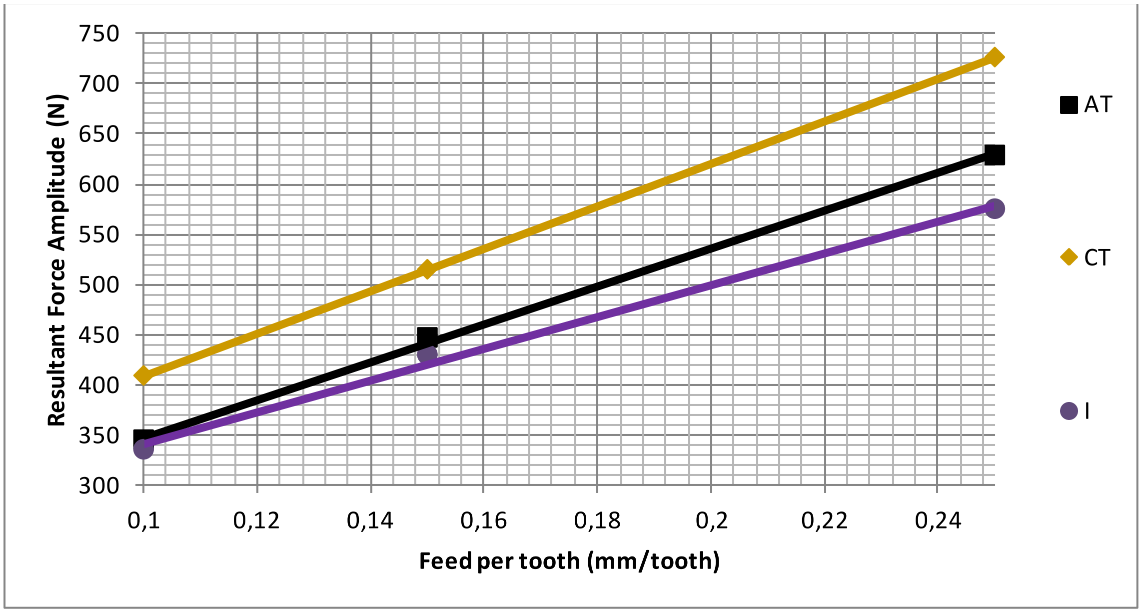

Figure 6.16 –Cutting forces vs feed per tooth graph for tools with 3 flutes at 4000 rpm

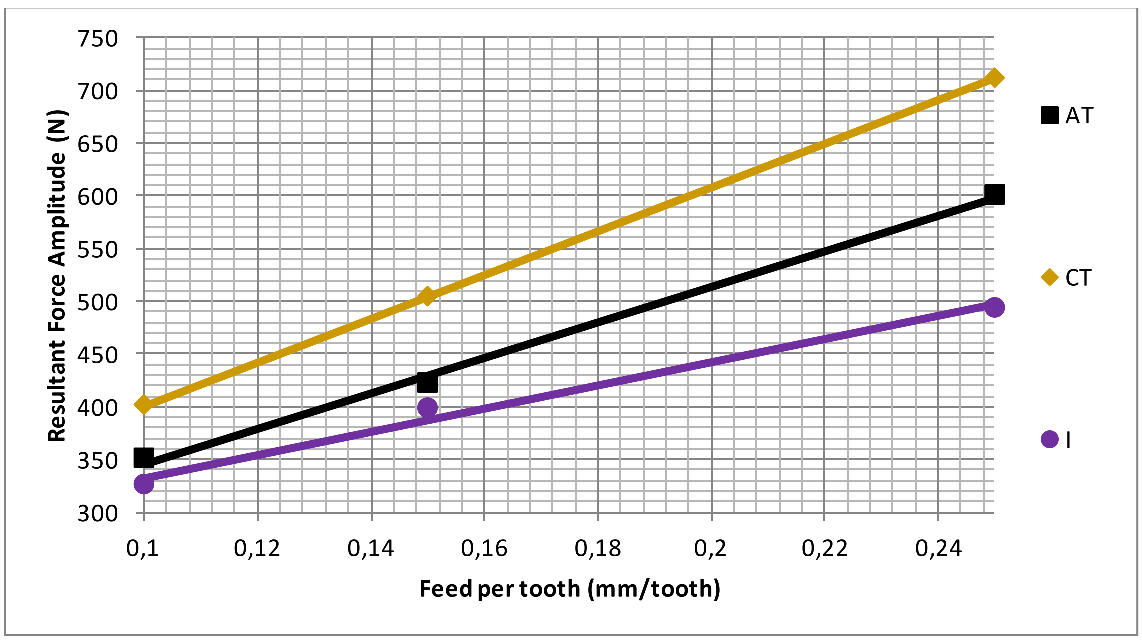

Figure 6.17 –Cutting forces vs feed per tooth graph for tools with 3 flutes at 8000 rpm

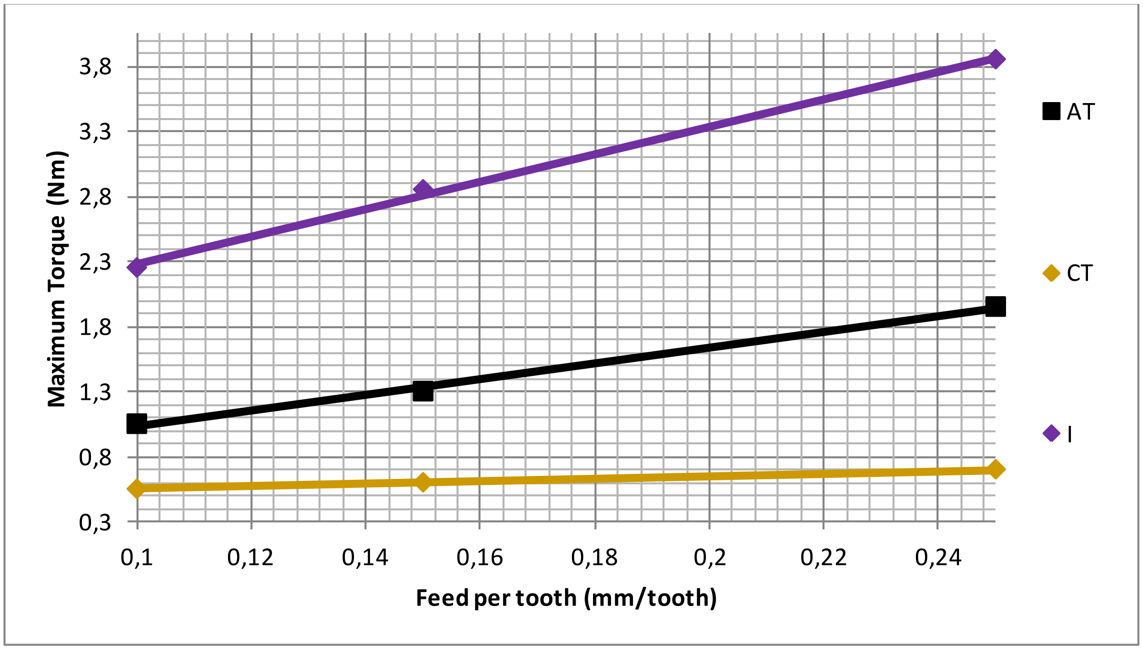

Figure 6.18 – Cutting torque vs feed rate for three fluted tools at 4000 rpm spindle speed

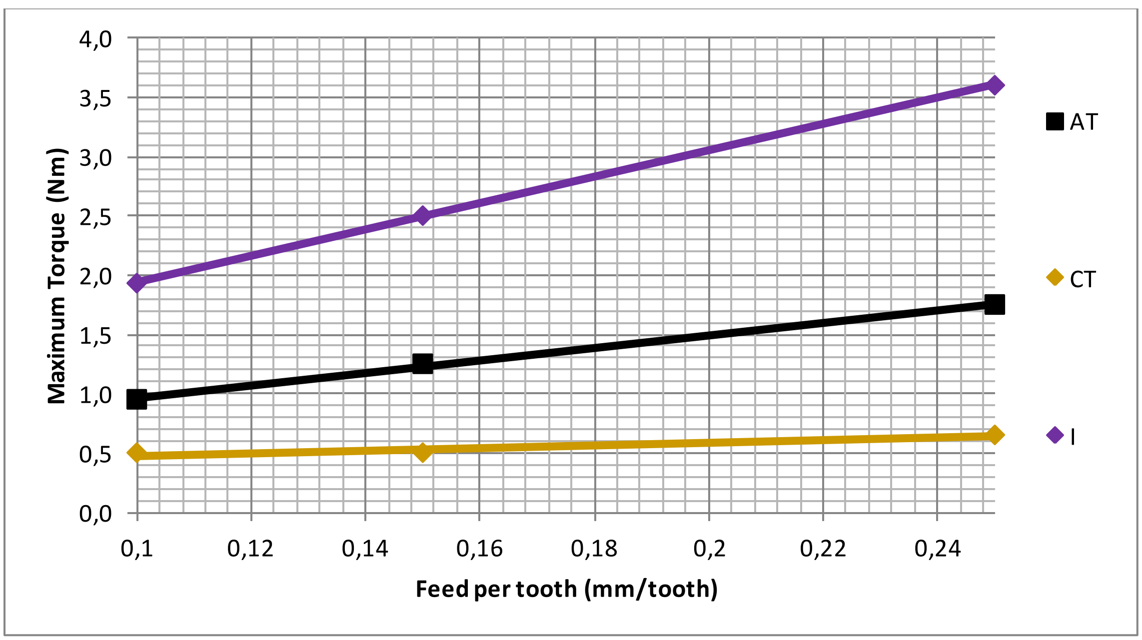

Figure 6.19 – Cutting torque vs feed rate for three fluted tools at 8000 rpm spindle speed

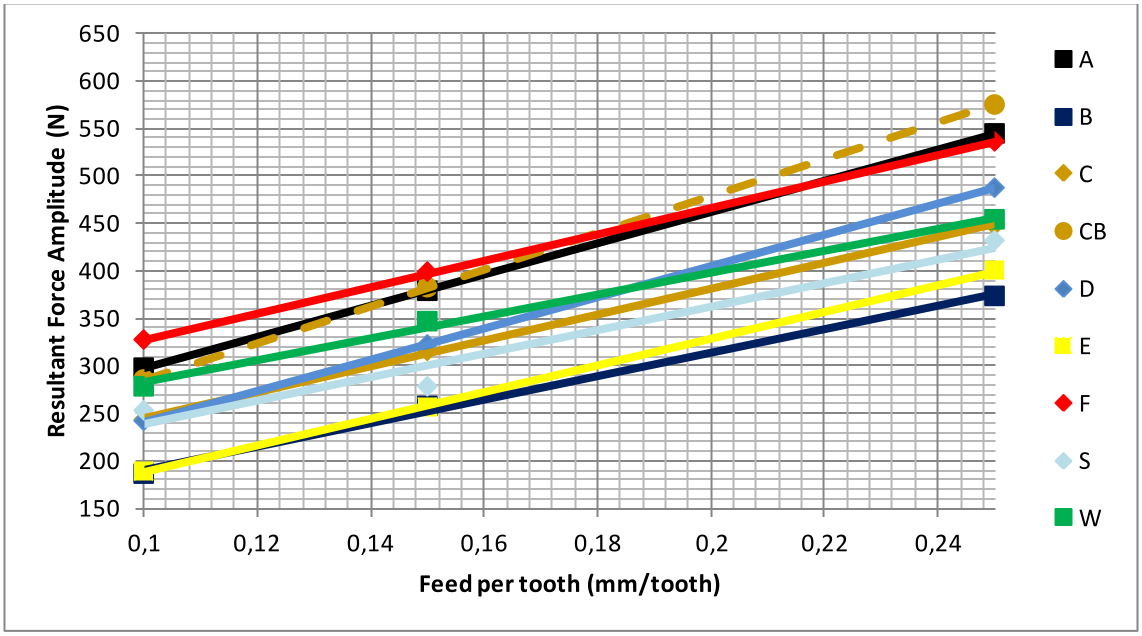

Figure 6.20 - Resultant forces vs feed rate graph for two fluted tools at 4000 rpm spindle speed slot milling

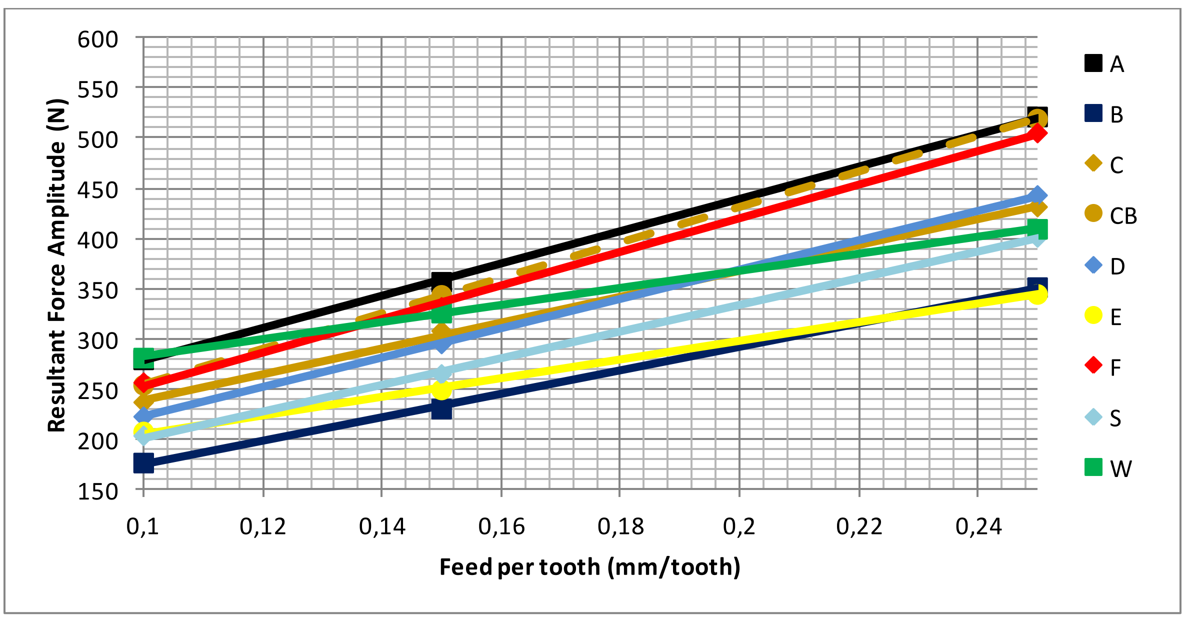

Figure 6.21 - Resultant forces vs feed rate graph for two fluted tools at 8000 rpm spindle speed slot milling

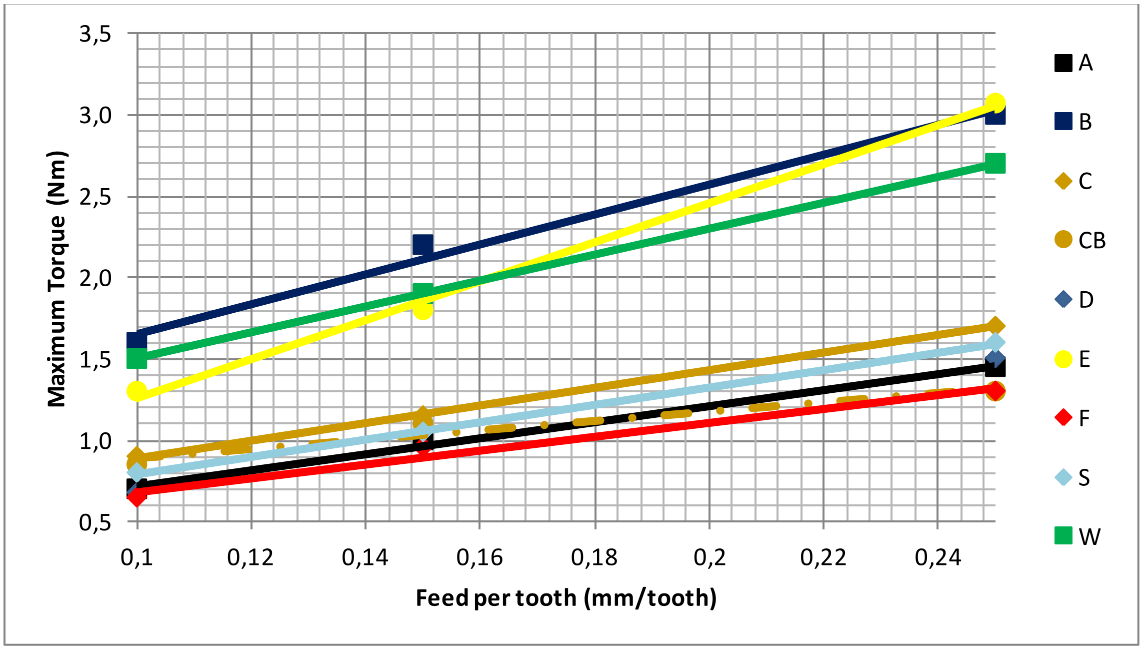

Figure 6.22 – Cutting torque vs feed rate for two fluted tools at 4000 rpm spindle speed

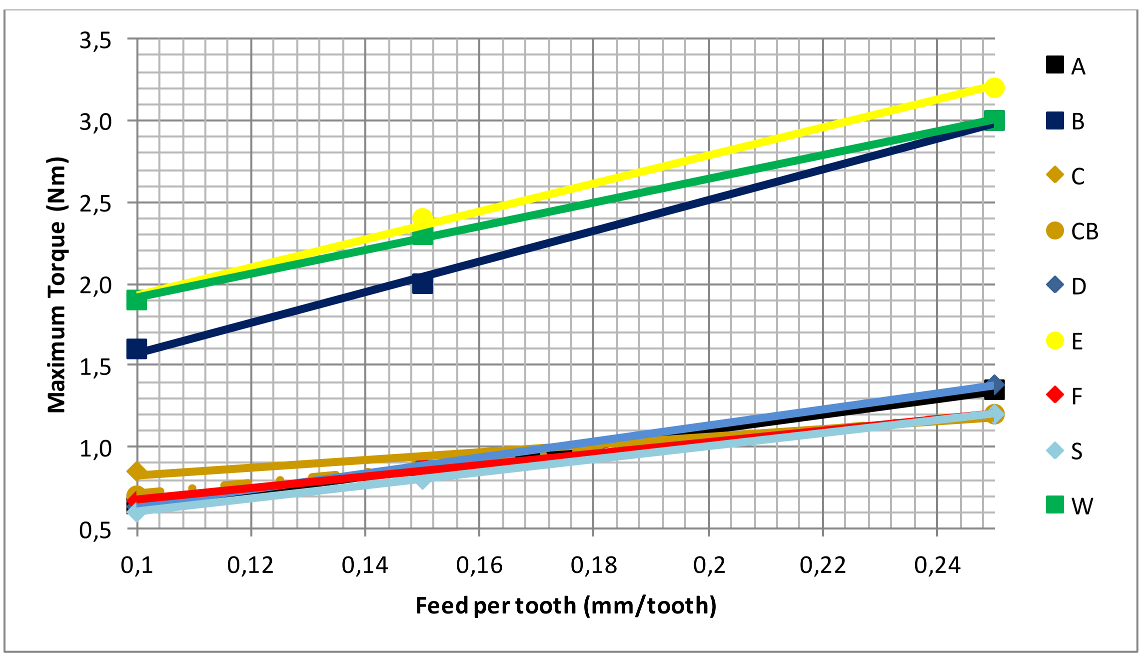

Figure 6.23 – Cutting torque vs feed rate for two fluted tools at 8000 rpm spindle speed

The cutting force performances of the tools are compared by plotting the characteristic curves in the same graph with respect to the corresponding feed rates. As expected there is a linear relation between the feed rate and cutting forces. As the feed rate increases the cutting forces and torques also increase. Also three fluted tools are subjected to larger forces than two fluted tools as expected. Additionally it is seen that the cutting forces and torques decrease slightly with increasing spindle speed. The impressive side of this study is the variation of cutting forces for different tool brands under the same conditions. In macro scale all of the tools are made up of same material (WC Cobalt), are at the same size (16 mm diameter) and specifically manufactured to cut the same material (Al-7050). However under same conditions the resultant forces exerted on a brand may be twice as large as another one.

Aside from the tungsten carbide end mills, three fluted end mills made up of Sialon are also tested in collaboration with the Anadolu University Materials Science and Engineering department. However during the tests the tools are broken due to their low impact resistances. Therefore it is concluded that for the near future Sialon tools cannot be considered as a replacement for tungsten carbide end mills.

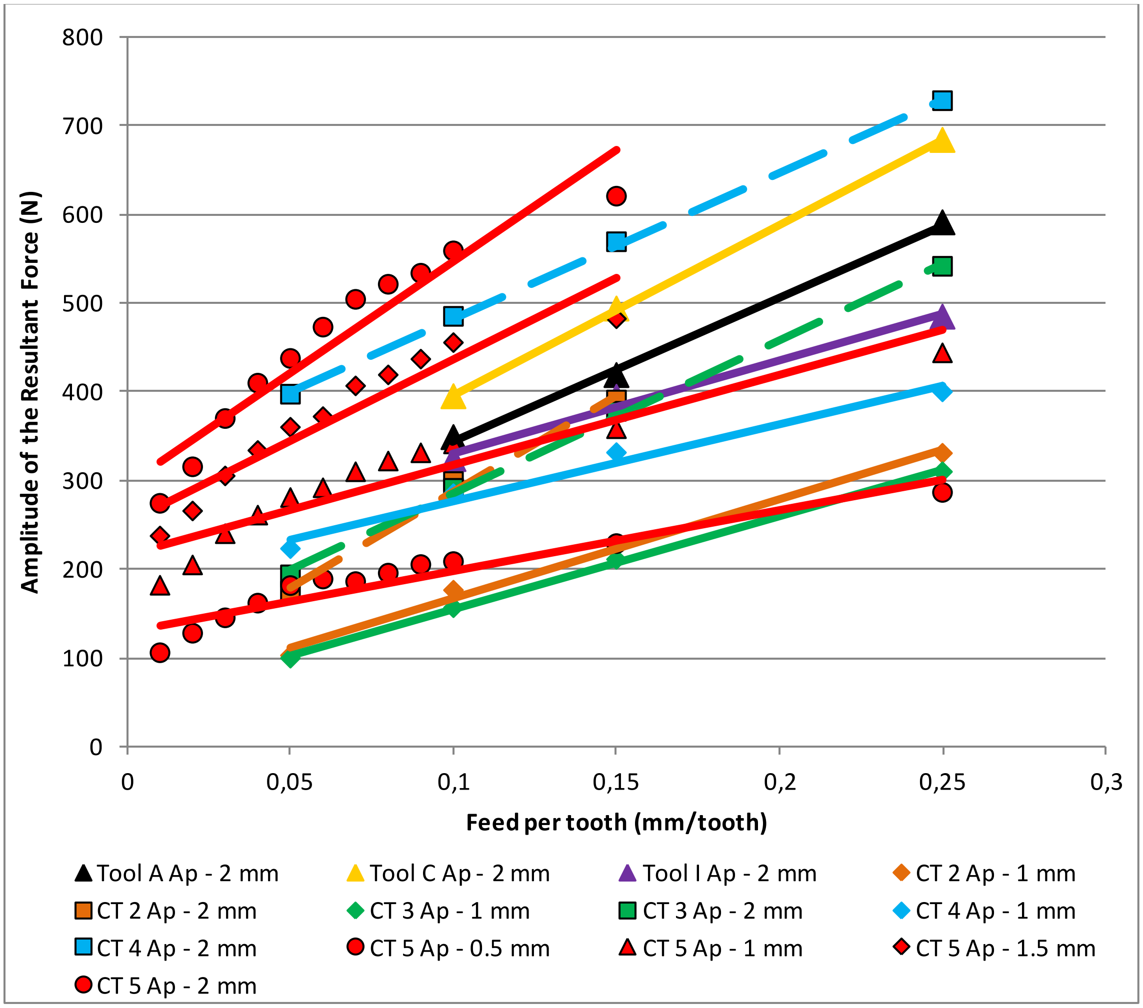

Figure 6.24 – Cutting force vs feed rate for three fluted Sialon tools at 8000 rpm spindle speed

6.3 Tool geometry measurements

In order to analyze the effect of tool geometry on cutting forces the main geometric parameters of the tools are measured using the optical microscope in MARC laboratory. The main geometric parameters shown in Figures 6.25 and 6.26 are measured for each tool. The results are tabulated in Table 6.3.

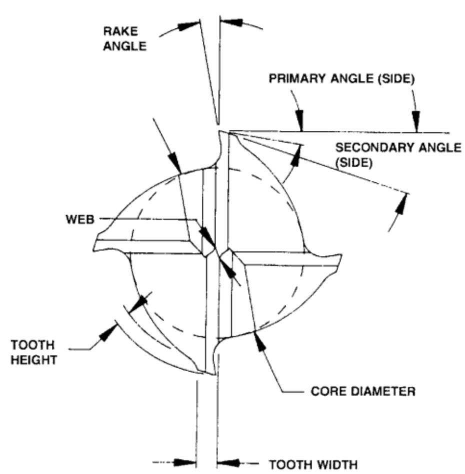

Figure 6.25 – Cutting tool parameters - Angles on an end mill [86]

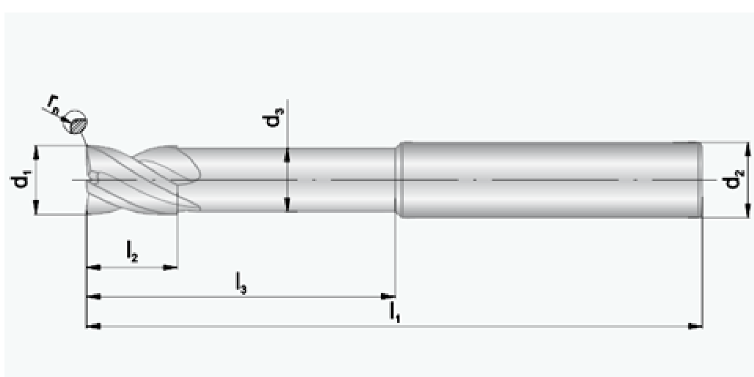

Figure 6.26 – Main dimensions of an end mill [87]

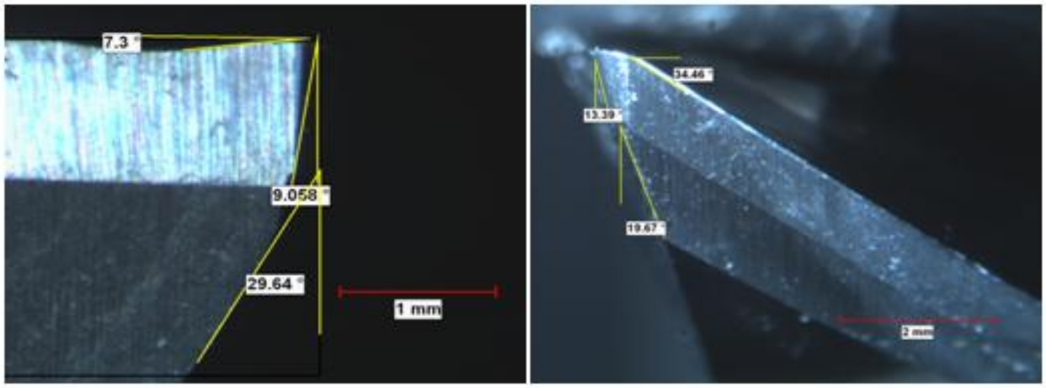

Figure 6.27 – Sample measurement images

Table 6.3 – Measured geometries of the tested tools

Tool Name	A	B	C	CB	D	E	F	I	W
Corner Radius [mm]	0,06	0,05	0,06	5	0,02	0,02	0,5	0,45	2
Axial Primary Clearance Angle	14	9	13	15	15	12	25	13	12
Axial Secondary Clearance Angle	26	23	20	27	26	29	14	22	30
Radial Rake Angle	8	25	12	0	5	18	34	3	13
Radial Primary Clearance Angle	10	10	23	12	10	16	15	14	12
Radial Secondary Clearance Angle	28	21	11	35	25	0	17	25	20
Helix Angle	33	33	34	20	20	20	16	35	18

However since the angles are different for each tool, the effect of a single angle could not be isolated. These measurements are then used in the modeling of the cutting forces.

6.4 Wear experiments

After the cutting forces are measured, a smaller group of tools is chosen for tool life tests. For the cutting conditions the severest of the condition in the cutting force tests was selected. The tool brands A-F are selected as TAI's request considering various factors such as the ease of logistics, prices of the tools and the origin of the tool brand.

Table 6.4 – Wear test conditions

Spindle Speed	*8000 rpm*
Feed per tooth	*0.25 mm/rev*
Wear Criteria	*300 micron in the flank face*
Measurement Interval	*20 min*

According to ISO standards a tool is accepted to complete its working life when the maximum wear depth reaches 300 micron in the flank face. However after over 7 hours of cutting with each tool it is concluded that the trends of the tool lives are obtained and there is no need to continue with the time consuming wear tests. The amount of time to pass for tool to complete its life is found by extrapolation.

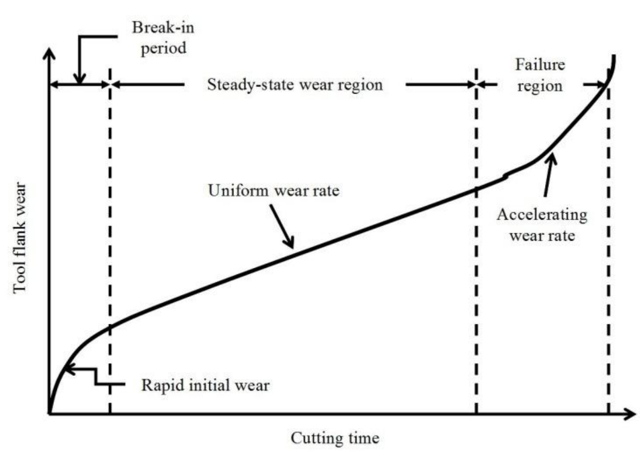

Figure 6.28 – General tool wear vs time graph [88]

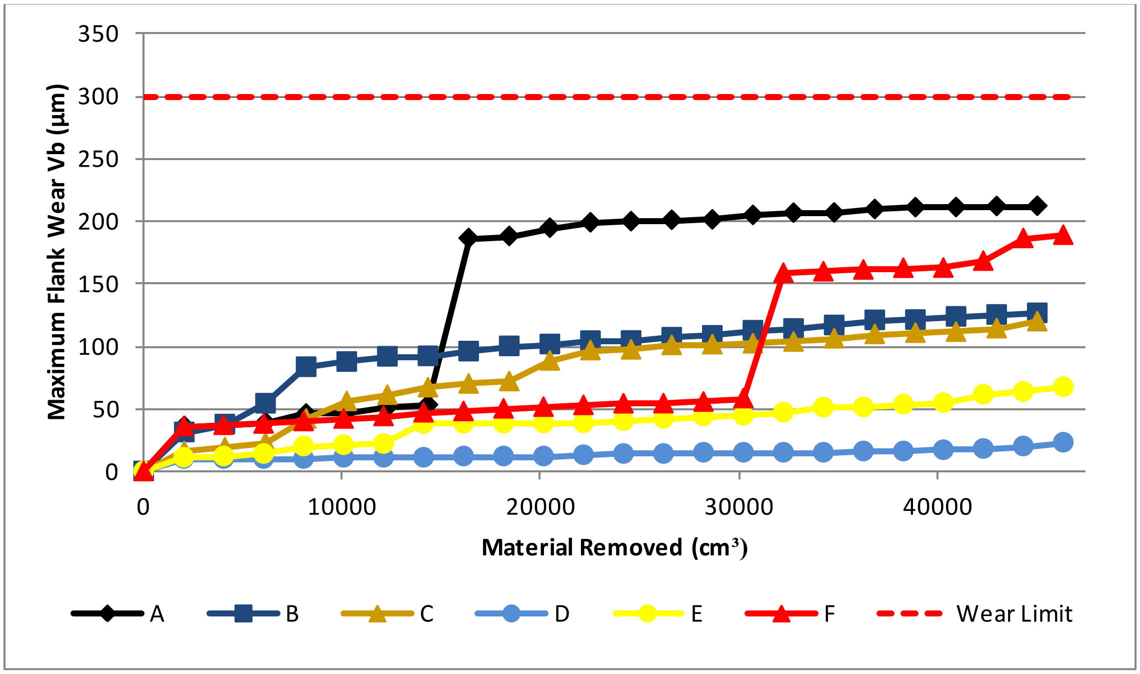

Figure 6.29 – Comparison of the flank wear of the tools

In all of the tests it is seen that the wear occurs at the bottom edge and it is asymmetrical in terms of flutes since always one flute wears out faster than the other one. The most important outcome of wear tests is that the wear of the tools is not directly related with the forces acting on the tool. This proves that even though the tools are all made up of WC Cobalt material there are definitely some differences between the tool materials. Especially the material of tool D shows a great resistance to wear. It is also important to underline the fact that the tools A and F have large jumps in their tool wear trends due to chipping. This may be related with poor chip evacuation and must be avoided for better performances. In order to prove that there is a difference in the tool materials, it is decided to make experiments on tool material identification.

6.5 Surface Roughness Measurements

Quality of the product is another crucial criterion in machining. Therefore in order to effectively judge the performances of the tools the surfaces after machining are also compared. The surfaces produced after the wear tests are measured by Mitutoyo SJ-301 surface contracer to both examine the surface qualities and also to observe the effect of tool wear on surface roughness. The surface profiles obtained after cutting are presented in Figures 6.37-6.42.

Figure 6.30 – Sample measurement of surface roughness with Mitutoyo SJ-301

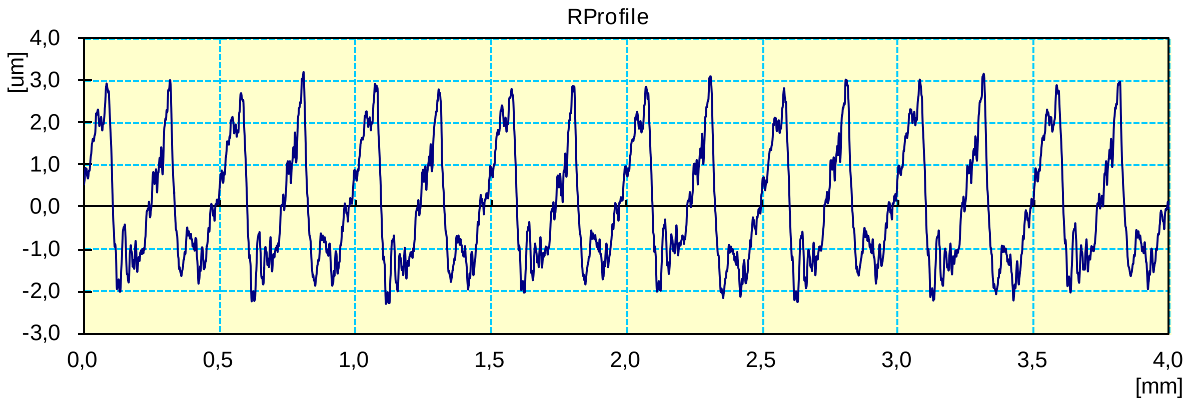

Figure 6.31 – Surface profile created by tool A

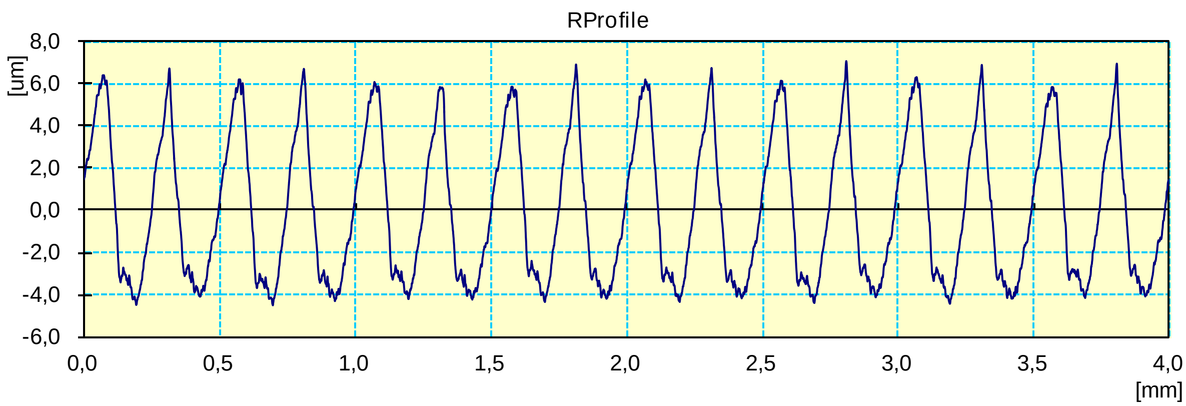

Figure 6.32 – Surface profile created by tool B

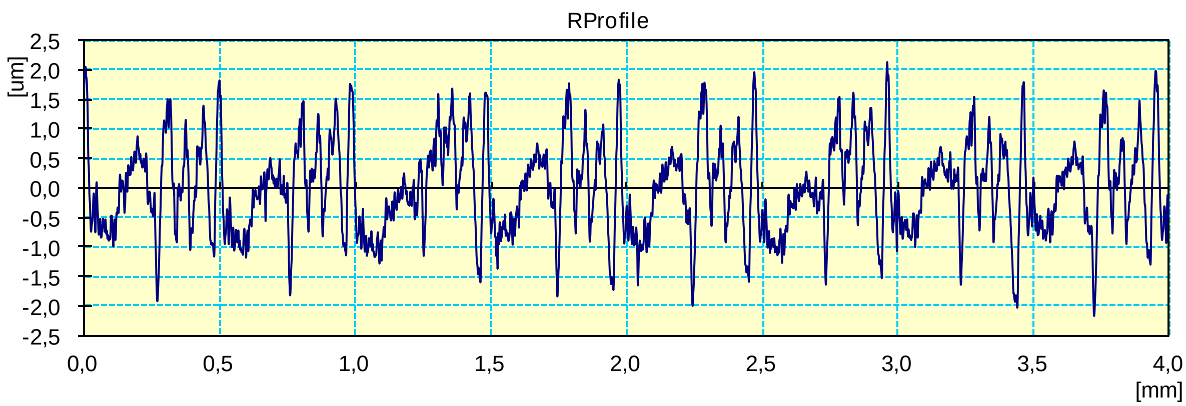

Figure 6.33 – Surface profile created by tool C

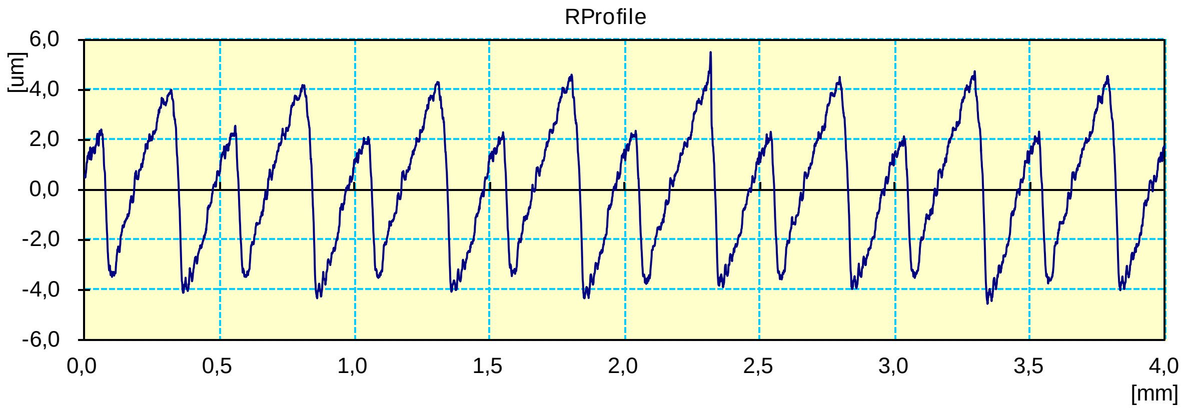

Figure 6.34 – Surface profile created by tool D

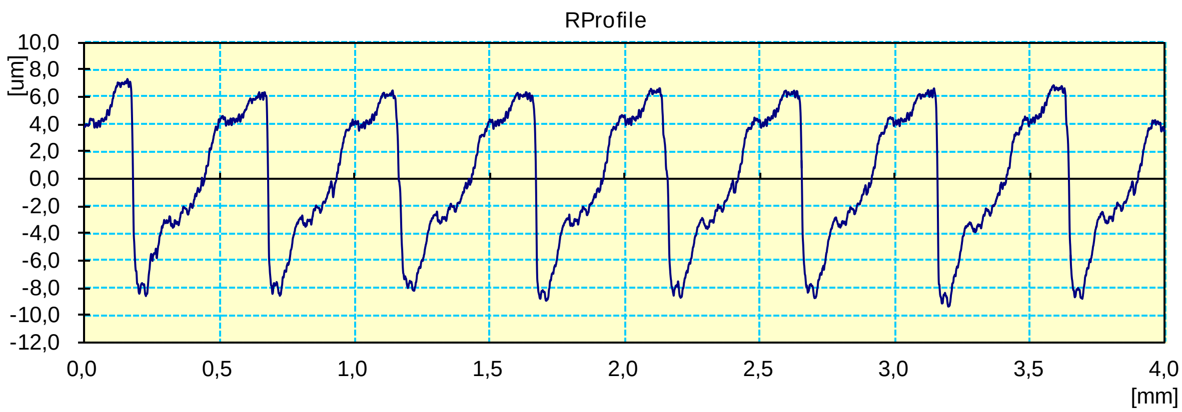

Figure 6.35 – Surface profile created by tool E

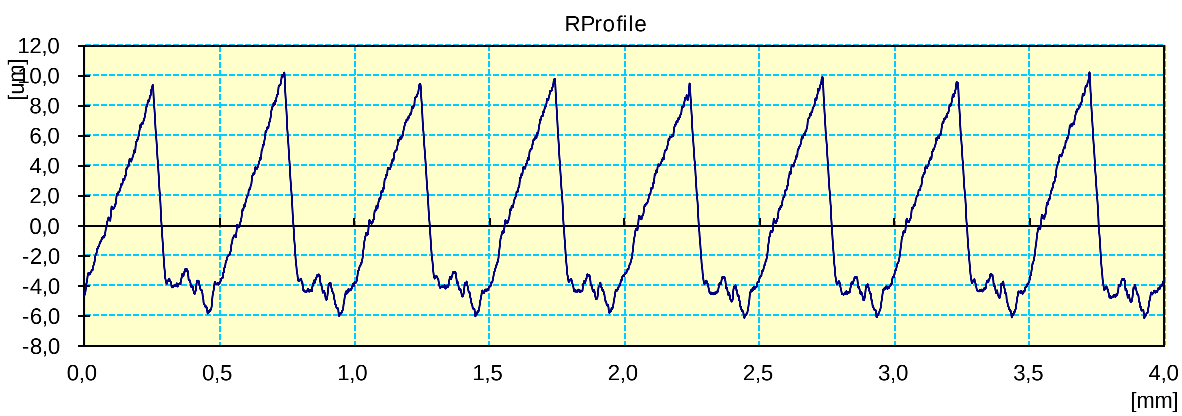

Figure 6.36 – Surface profile created by tool F

The measurements of surface contracer reflect the surface quality on the line that the contracer tip contacts with the material. In order to eliminate any error coming from the orientation of the contracer, the surfaces are also examined by using white light interferometer (WLI). Using WLI one can measure a surface topography instead of a single line.

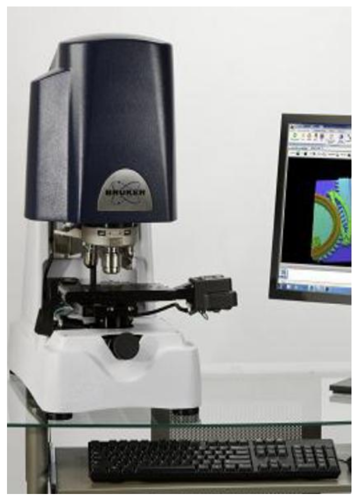

Figure 6.37 – White Light Interferometer (WLI)

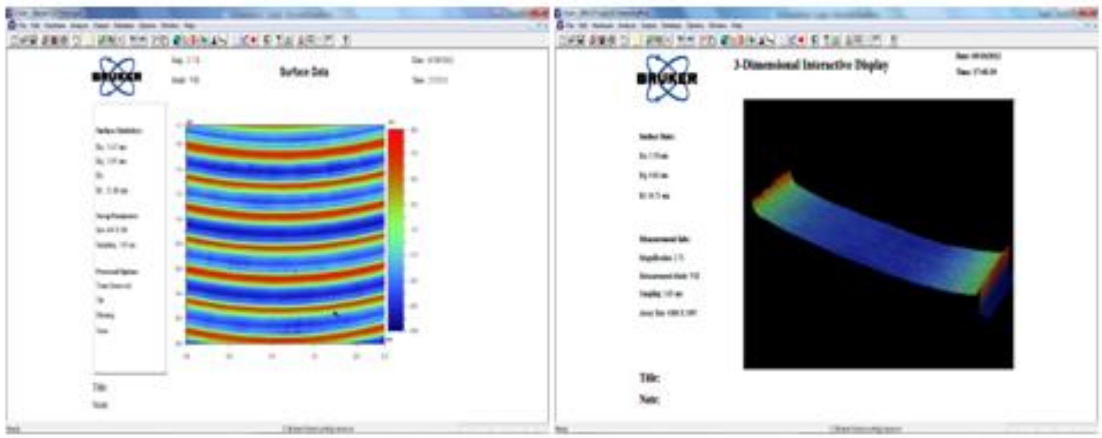

Figure 6.38 – Sample WLI image

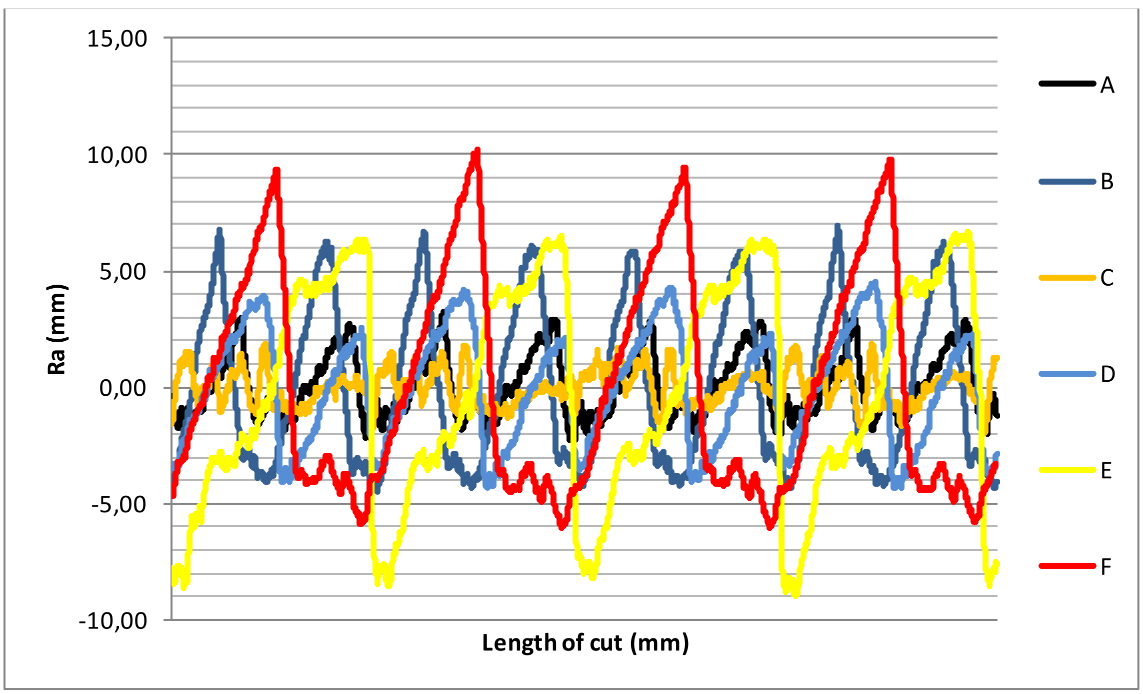

Figure 6.39 – Ra values from WLI taken at the centerline of slot (8000 rpm, 0.25 mm/rev)

The cutting forces of the worn tools are also measured and compared with their fresh states to show the increase of cutting forces with the tool wear.

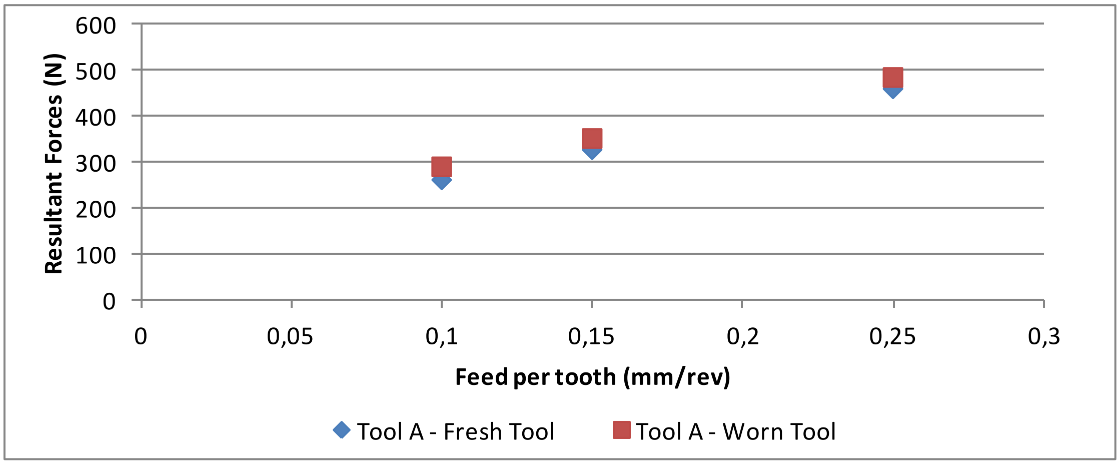

Figure 6.40 – Sample change of cutting forces with tool wear graph

Table 6.5 – (%) Increments of cutting forces for worn tools

Feed (mm/rev)	A	B	C	D	E	F
0,1	11	37	11	27	56	28
0,15	7	26	11	18	41	25
0,25	5	16	9	13	17	22

6.6 Material Identification

After the wear tests, in order to validate the measurements of optical microscope the tools are investigated using scanning electron microscope. During the measurements of flank wear it was also decided to examine the material properties of the tools using energy dispersive X-ray spectroscopy.

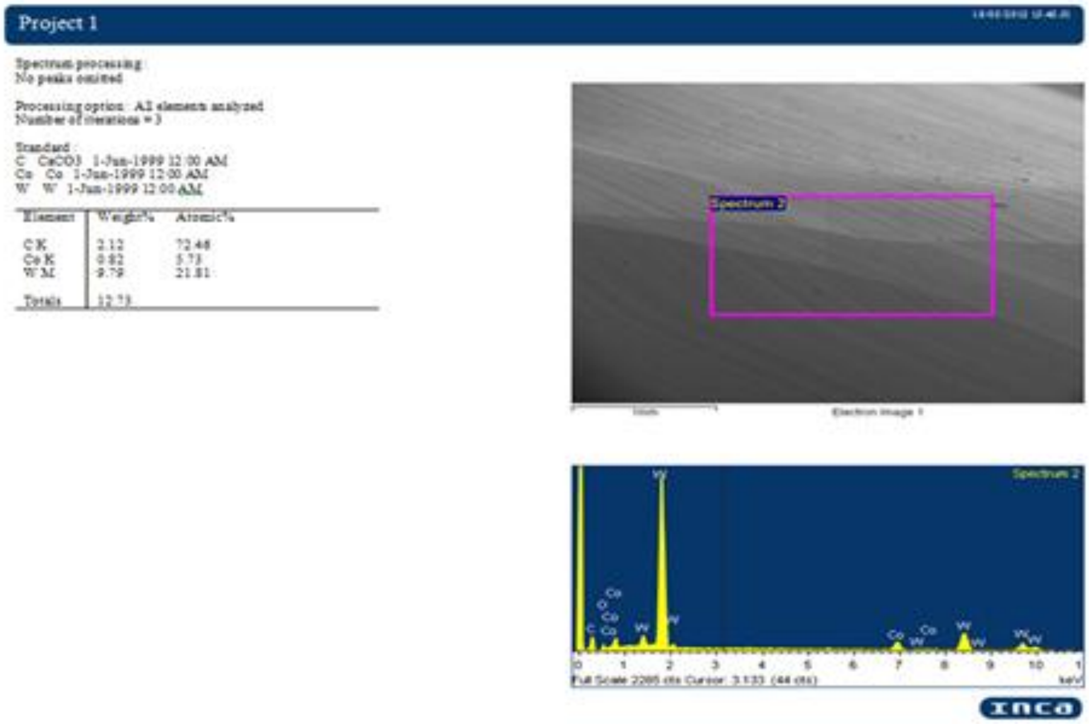

Figure 6.41 – Sample EDX analysis for tool B

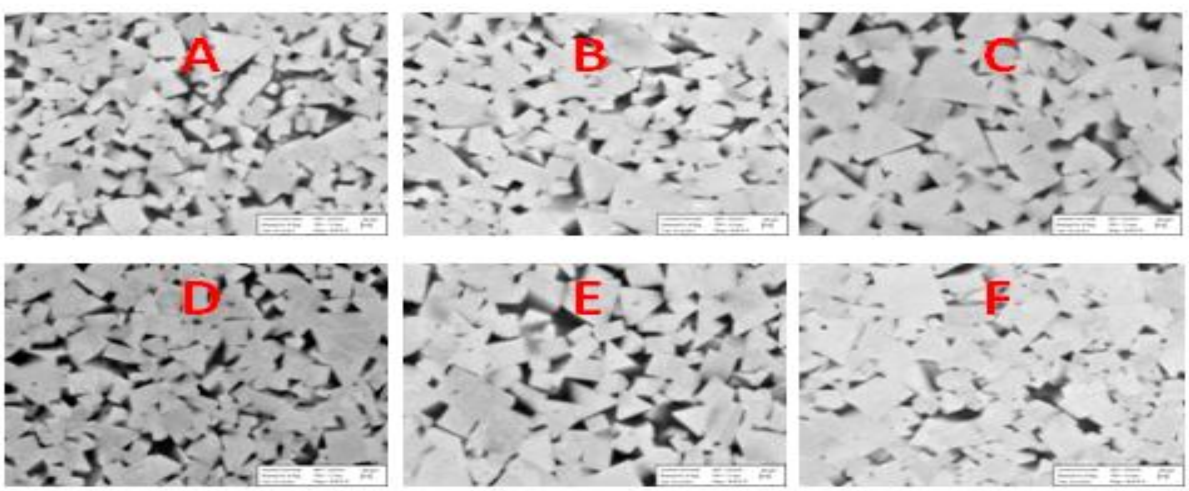

Figure 6.42 – Sample SEM images showing tool microstructures

Table 6.6 – Atomic and mass percentages of the tool materials

	W		C		Co	
	Weight	Atomic	Weight	Atomic	Weight	Atomic
A	79,8	30,4	9,9	57,4	10,4	12,3
B	83,1	37,0	7,3	49,5	9,7	13,5
C	83,6	38,9	6,6	46,7	9,3	13,6
D	84,4	35,3	8,7	55,6	**6,2**	**8,1**
E	82,2	35,6	7,6	50,7	10,2	13,8
F	83,9	40,4	6,0	44,2	9,5	14,3

It was concluded that tool D which showed superior performance compared with the other brands also has a different material concentration. In order to prove this the hardness of the tools were also examined. It is known that as the cobalt concentration decreases the hardness increases in tungsten carbide cobalt material. Using a microhardness tester it is shown that tool D has a lower cobalt concentration indeed.

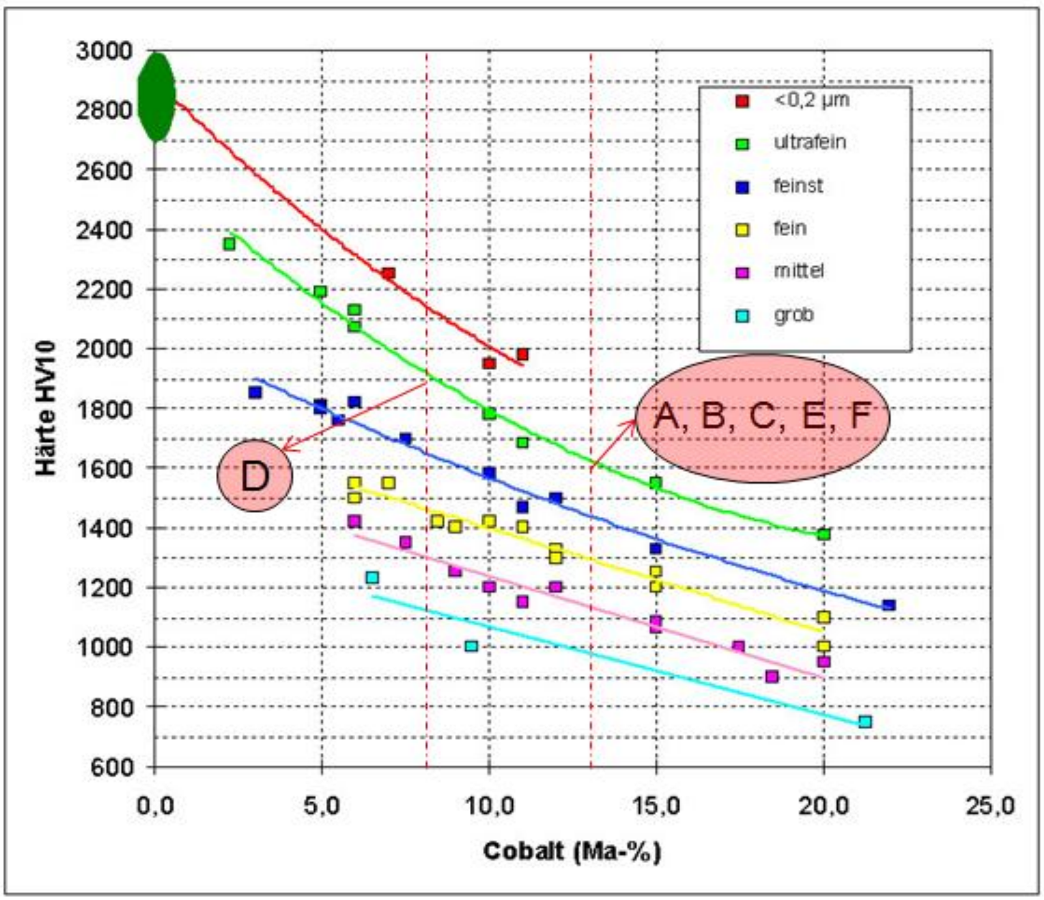

Figure 6.43 – Change of hardness with respect to cobalt concentration in different grain sized tungsten carbide cobalt

Figure 6.44 – Preparation of the samples for the hardness tests

Table 6.7 – Hardness values of the tools

	A	B	C	D	E	F
Hardness (GPa)	16,0	15,9	15,6	**18,1**	15,7	15,9

Figure 6.45 – Microhardness tests

6.7 Evaluation of the tool performances

In order to evaluate the performances of the cutters objectively two main criteria; tool wear and surface quality are compared. For the comparison the corresponding values of the tools are normalized by the tool that performs best for that specific category. For example in evaluating wear the tool that is worn out the least is considered the best tool. The wear values of the other tools are divided by the wear value of the best tool to obtain their wear ratings. Similar rating is done also on the surface qualities. The results of this evaluation are given in Figure 6.14. This evaluation shows that Tool D shows the best performance among the group. It is also important to emphasize that tool D shows 4 times better performance compared to tool F which has the same macro geometry and material classification. It is also important to add that this evaluation does not take the tool costs into account which is the main criterion for many cases.

Table 6.8 – Evaluation of the tool performances

	A	B	C	D	E	F
Wear	9,22	5,5	5,21	1	2,93	8,21
Surface Quality	1,94	4,84	1	3,27	6,71	6,70
TOTAL	11,16	10,34	6,21	**4,27**	9,64	14,91

6.8 Economical aspects of the study

Once the wear progression curves of the tools are obtained, a cost analysis is conducted by calculating the tool cost of unit material removed. The tool price information is supplied by TAI and by extrapolating the flank wear curves to the wear limit, the total amount of material to be removed in the whole life span of a tool is calculated. The tool costs obtained by dividing the tool prices to the material removed are presented in Table 6.9.

Table 6.9 – Tool cost for unit material removed

	A	B	C	D	E	F
Tool Cost (€/m^3)	651	569	459	120	840	755

Analyzing the results, it is crucial to underline the fact that the most expensive tools is not the best performing tool. As it can be seen from Table 6.15, just by changing the tool from one brand to another, one can decrease the tool costs for $1/7^{th}$, comparing tools D and E. This study clearly proves the importance of scientific evaluation in the selection of cutting tools. For future work this study can be extended to other tool-workpiece pairs.

Chapter 7

CONCLUSIONS

Tool wear modeling is one of the most complex subjects in the metal cutting literature. It is a multiphysics problem requiring the precise modeling of cutting forces, temperatures, contact mechanics and material behavior. Therefore, in order to have an improvement in the tool life model, all of these preliminary studies must be improved first.

In this study, the cutting forces during milling are modeled using average cutting coefficients obtained from mechanistic calibration tests at first. Although average coefficients give reliable solutions for a wide range, the model deviates from the experimental values at the extremes of the cutting forces. Therefore, in order to improve the precision of the model instead of using the average cutting coefficients, it is suggested to use the instantaneous cutting coefficients. On the other hand, the inclusion of the bottom edge effect is a major improvement in terms of reflecting the actual process. However, in this study the deflection of the tool and the cutter runout was not taken into account. The non cutting part of the bottom edge slides over the workpiece surface during the whole cutting cycle which may be significant if the tool deflection is also taken into account. Studies towards the modeling of this part would help to better understand the distribution of the temperature fields since it is obvious that any sliding force would create additional heat sources.

Secondly, the temperature field on the rake face of the tool is modeled. However, it is extremely difficult to develop a precise temperature prediction model in machining due to the facts that metal cutting is very highly localized and non-linear process which occurs at high temperatures, high pressures and strains. The complexity of the contact phenomena in the metal cutting process makes it extremely hard to predict temperature accurately and precisely. In this thesis, heat partition approach is utilized within the finite element method. The advantage of the model used in this thesis is that the finite element model only calculates the temperature distribution where the heat generation values are calculated analytically. This approach decreases the computation time significantly. For the simulations presented in this thesis the computation time was around a few seconds.

Apart from the temperature prediction, temperature measurement is an even more challenging part in the metal cutting research field. Most of the available data on metal cutting is on turning since it is a continuous process and the nature of turning allows sensors to be placed on the stationary cutting tool. Still it is very difficult to make temperature measurements very close to the cutting edge. Due to this lack of experimental data, validation of the proposed mathematical models becomes harder. Most of the published articles rely on the few published experimental data. Temperature measurement is even a tougher task to accomplish since the tool is rotating at very high speeds. Most of the study on milling temperature prediction is done either using sensors placed on the stationary workpiece, or using the cooling channels of special end mills at lower spindle speeds for data sampling concerns. Therefore, in this thesis the temperature model is validated using orthogonal turning data. It is clear that a study towards measuring the milling temperatures in milling would be a tough but a rewarding one, considering the great need of such experimental data.

Finally, an empirical relation correlating wear with milling temperature, tool material properties and the material removed is obtained using the experimental wear data. This relation shows the effect of milling temperature and material properties on tool life. As the temperature increases, the diffusion of the tool binder increases, leading to diffusion wear and decreased tool life. Similarly as the tool hardness decreases, the chipping of the tool increases, this also decreases tool life. Additionally in this study the relation of cobalt binder on tool wear is realized. In tungsten carbide tools cobalt binder not only directly affects the tool hardness, but the interaction of this cobalt with the aluminum workpiece also speeds up the diffusion process. It is experimentally proved that decreasing the cobalt concentration of the tool from 12% to 6% increases the tool life dramatically.

The industrial applications of this study clearly prove the importance of scientific evaluation in engineering applications. With the presented cost analysis it is shown that just by changing the tool supplier the tool cost analysis can be deducted to one seventh of the initial tool cost. Conducting similar analysis and other tool workpiece couples is strongly suggested for both economical concerns and utilization of the environmental resources.

BIBLIOGRAPHY

[1] Staley, J.T., 1974, “Aging kinetics of Aluminum Alloy 7050,” Metallurgical Transactions., 5, pp. 929-932.

[2] Hunsicker, H.Y., 1976, “Development of Al-Zn-Mg-Cu Alloys for Aircraft,” Philosophical Transactions of the Royal Society of London. Series A, Mathematical and Physical Sciences, 282 (1307), pp. 359-376.

[3] Schröter, K., 1925, “Hard-metal Alloy and the Process of Making Same,” U. S. Patent 1,549,615.

[4] Shearer, T. R., 2008, “The Designer’s Guide to Tungsten Carbide,” General Carbide: Greensburg PA.

[5] Weisberg, D. E., 2008, “The Engineering Design Revolution Chapter 3”.

[6] Mickelson, D., 2007, “Hard Milling & High Speed Machining: Tools of Change”.

[7] ISO Test standards. http://www.iso.org Accessed 02.07.2013.

[8] Taylor, F.V., 1906, “On the Art of Cutting Metals,” The American Society of Mechanical Engineers.

[9] Merchant, M.E., 1944, “Basic Mechanics of the Metal Cutting Process,” Journal of Applied Mechanics.

[10] Armarego, E.J., 1993, “Material Removal Processes – An Intermediate Course”.

[11] Altintas, Y., 2012, “Manufacturing Automation: Metal Cutting Mechanics, Machine Tool Vibrations and CNC Design,” Cambridge University Press.

[12] Shamoto, E. and Altintas, Y., 1999, “Prediction of Shear Angle in Oblique Cutting with Maximum Shear Stress and Minimum Energy Principles,” Journal of Manufacturing Science and Engineering, pp. 399-407.

[13] Soldani, X., Moufki, A., Molinari, A., Budak, E. and Özlü, E., “High Speed Machining of AISI 1050 Steel: Modeling and Experimental”.

[14] Mabrouki, T., Girardin, F., Asad, M. and Rigal, J.F., 2008, "Numerical and Experimental Study of Dry Cutting for an Aeronautic Aluminum Alloy (A2024-T351)," International Journal of Machine Tools & Manufacture, 48, pp.1187-1197.

[15] Ehmann, K.F., Kapoor, S.G., Devor, R.E. and Lazoglu, I., 1997, "Machining Process Modeling: A Review," Journal of Manufacturing Science Engineering, 119, pp. 655-663.

[16] Tuysuz, O., Altintas, Y. and Feng, H.Y., 2013, "Prediction of Cutting Forces in Three and Five-axis Ball-end Milling with Tool Indentation Effect," International Journal of Machine Tools & Manufacture, 66, pp. 66–81.

[17] Engin, S., and Altintas, Y., 2001, "Mechanics and Dynamics of General Milling Cutters. Part I: Helical End Mills," International Journal of Machine Tools & Manufacture, 41, pp. 2195–2212.

[18] Wang, S.M., Chiou, C.H. and Cheng, Y.M., 2004, "An Improved Dynamic Cutting Force Model for End-milling Process," Journal of Materials Processing Technology, 148, pp. 317–327.

[19] Li, H.Z., Zhang, W.B., and Li, X.P., 2001, "Modeling of Cutting Forces in Helical End Milling Using a Predictive Machining Theory," International Journal of Mechanical Sciences, 43, pp. 1711–1730.

[20] Wan, M., Zhang, W.H., Dang, J.W. and Yang, Y., 2010, "A Novel Cutting Force Modeling Method for Cylindrical End Mill," Applied Mathematical Modeling, 34, pp. 823–836.

[21] Azeem, A., Feng, H.Y. and Wang, L., 2004, "Simplified and Efficient Calibration of a Mechanistic Cutting Force Model for Ball-end Milling," International Journal of Machine Tools & Manufacture, 44, pp. 291–298.

[22] Hamade, R.F., Seifa, C.Y., and Ismail, F., 2006, "Extracting Cutting Force Coefficients from Drilling Experiments," International Journal of Machine Tools & Manufacture, 46, pp. 387–396.

[23] Fang, N., and Wu, Q., 2005, "The Effects of Chamfered and Honed Tool Edge Geometry in Machining of Three Aluminum Alloys," International Journal of Machine Tools & Manufacture, 45, pp. 1178–1187.

[24] Wan, M. and Zhang, W.H., 2009, "Systematic study on cutting force modeling methods for peripheral milling," International Journal of Machine Tools & Manufacture, 49, pp. 424–432.

[25] Yang, Y., Zhang, W.H. and Wan, M., 2011, "Effect of cutter runout on process geometry and forces in peripheral milling of curved surfaces with variable curvature," International Journal of Machine Tools & Manufacture, 51, pp. 420–427.

[26] Imani, B.M. and Layegh, E., 2008, "Comprehensive simulation of surface texture for an end-milling process," Scientia Iranica, 15, pp. 340-347.

[27] Anayet M., Patwari, U., Nurul Amin, A.K.M. and Waleed, F.F., 2011, "Influence of chip serration frequency on chatter formation during end milling of Ti6Al4V," Journal of Manufacturing Science and Engineering, 133.

[28] Budak, E. and Altintas, Y., 1998, "Analytical prediction of chatter stability in milling—Part I: General Formulation," Journal of Dynamic Systems, Measurement, and Control, 120, pp. 22-30.

[29] Budak, E. and Altintas, Y., 1998, "Analytical prediction of chatter stability in milling —Part II: Application of the General Formulation to Common Milling Systems," Journal of Dynamic Systems, Measurement, and Control, 120, pp. 31-36.

[30] Cao, Y. and Altintas, Y., 2007, "Modeling of spindle-bearing and machine tool systems for virtual simulation of milling operations," International Journal of Machine Tools & Manufacture, 47, pp. 1342–1350.

[31] Ko, J.H., Yun, W.S., Cho, D.W. and Ehmann, F.K., 2002, "Development of a Virtual Machining System, Part 1: Approximation of the Size Effect for Cutting Force Prediction," International Journal of Machine Tools & Manufacture, 42, pp. 1595–1605.

[32] Budak, E., Lazoglu, I. and Guzel, B.U., "Improving Cycle Time in Sculptured Surface Machining Through Force Modeling."

[33] Bao, W.Y. and Tansel, I.N., 2000, "Modeling micro-end-milling operations. Part I: analytical cutting force model," International Journal of Machine Tools & Manufacture, 40, pp. 2155–2173.

[34] Kang, I.S., Kim, J.S., Kim, J.H., Kang, M.C. and Seo, Y.W., 2007, "A mechanistic model of cutting force in the micro end milling process," Journal of Materials Processing Technology, pp. 250–255.

[35] Dang, J.W., Zhang, W.H., Yang, Y. and Wan, M., 2010, "Cutting force modeling for flat end milling including bottom edge cutting effect," International Journal of Machine Tools & Manufacture, 50, pp. 986–997.

[36] Hou, Z.B. and Komanduri, R., 2000, "General solutions for stationary/moving plane heat source problems in manufacturing and tribology," International Journal of Heat and Mass Transfer, 43, pp. 1679-1698.

[37] Komanduri, R. and Hou, Z.B., 2000, "Thermal modeling of the metal cutting process - Part I: Temperature rise distribution due to shear plane heat source," International Journal of Mechanical Sciences, 42, pp. 1715-1752.

[38] Komanduri, R. and Hou, Z.B., 2001, "Thermal modeling of the metal cutting process - Part II: Temperature rise distribution due to frictional heat source at the tool-chip interface," International Journal of Mechanical Sciences, 43, pp. 57-88.

[39] Komanduri, R. and Hou, Z.B., 2001, "Thermal modeling of the metal cutting process - Part III: Temperature rise distribution due to the combined effects of shear plane heat source and the tool-chip interface frictional heat source," International Journal of Mechanical Sciences, 43, pp. 89-107.

[40] Moufki, A., Molinari, A. and Dudzinski, D., 1998, "Modeling of orthogonal cutting with a temperature dependent friction law," J. Mech. Phys. Solids, 46, pp. 2103-2138.

[41] Lazoglu, I. and Altintas, Y., 2002, "Prediction of tool and chip temperature in continuous and interrupted machining," International Journal of Machine Tools & Manufacture, 42, pp. 1011–1022.

[42] Ulutan, D., Lazoglu, I. and Dinc, C., 2009, "Three-dimensional temperature predictions in machining processes using finite difference method," Journal of Materials Processing Technology, 209, pp. 1111-1121.

[43] Dinc, C., Lazoglu, I. and Serpenguzel, A., 2008, "Analysis of thermal fields in orthogonal machining with infrared imaging," Journal of Materials Processing Technology, 198, pp. 147–154.

[44] Lazoglu, I. and Islam, C., 2012, "Modeling of 3D temperature fields for oblique machining," CIRP Annals - Manufacturing Technology, 61, pp. 127–130.

[45] Majumdar, P., Jayaramachandran, R. and Ganesan, S., 2005, "Finite element analysis of temperature rise in metal cutting processes," Applied Thermal Engineering, 25, pp. 2152-2168.

[46] Usui, E. and Shirakashi, T., 1984, "Analytical prediction of cutting of tool wear," Wear, pp. 129 – 151.

[47] Dolinšek, S., Šuštaršic, B. and Kopac, J., 2001, "Wear mechanisms of cutting tools in high-speed cutting processes," Wear, 250, pp. 349–356.

[48] Zareena, A.R. and Veldhuis, S.C., 2012, "Tool wear mechanisms and tool life enhancement in ultra-precision machining of titanium," Journal of Materials Processing Technology, 212, pp. 560– 570.

[49] Wang, Z.G., Rahman, M. and Wong, Y.S., 2005, "Tool wear characteristics of binderless CBN tools used in high-speed milling of titanium alloys," Wear, 258, pp. 752–758.

[50] Thamizhmanii, S., Kamarudin, K., Rahim, E.A., Saparudin, A. and Hassan, S., 2007, "Tool wear and surface roughness in turning AISI 8620 using coated ceramic tool," Proceedings of the World Congress on Engineering 2.

[51] Yulian E., Adesta, T., Riza, M., Hazza, M. and Rosehan, D.A., 2009, "Tool wear and surface finish investigation in high speed turning using cermet insert by applying negative rake angles," European Journal of Scientific Research, 38, pp. 180-188.

[52] Gu, J., Barber, G., Tung, S. and Gu, R.J., 1999, "Tool life and wear mechanism of uncoated and coated milling inserts," Wear, pp. 273–284.

[53] Tang, Z.T., Liu, Z.Q., Pan, Y.Z., Wan, Y. and Ai, X., 2009, "The influence of tool flank wear on residual stresses induced by milling aluminum alloy," Journal of Materials Processing Technology, 209, pp. 4502–4508.

[54] Kountanya, R., 2011, "Surface finish and tool wear characterization in hard turning using a mathematical cutting tool representation," Machining Science and Technology: An International Journal, 15, pp. 429-452.

[55] Pavlov, A., Andonov, I., Qehaja, N. and Pavlov, I., 2007, "Simulation modeling of carbide tools wear," Fascicle of Management and Technological Engineering, 6(16).

[56] Umbrello, D., Filice, L., Micari, F., Matsumura, T. and Shirakashi, T., "Prediction of tool wear progress in machining of carbon steel using different tool wear mechanisms".

[57] Sivasakthivel, P.S., Murugan, V.V. and Sudhakaran, R., 2010, "Prediction of tool wear from machining parameters by response surface methodology in end milling," International Journal of Engineering Science and Technology, 2(6), pp. 1780-1789.

[58] Gatto, A., Bassoli, E. and Iuliano, L., "Performance optimization in machining of aluminum alloys for moulds production: HSM and EDM," Aluminum Alloys, Theory and Applications, pp. 355-376.

[59] Krain, H.R., Sharman, A.R.C and Ridgway, K., 2007, "Optimization of tool life and productivity when end milling Inconel 718TM," Journal of Materials Processing Technology, 189, pp. 153–161.

[60] Ozel, T., Karpat, Y., Figueira, L. and Davim, J.P., 2007, "Modeling of surface finish and tool flank wear in turning of AISI D2 steel with ceramic wiper inserts," Journal of Materials Processing Technology, 189, pp. 192–198.

[61] Lorentzon, J., and Jarvstrat, N., 2008, "Modeling tool wear in cemented-carbide machining alloy 718," International Journal of Machine Tools & Manufacture, 48, pp. 1072– 1080.

[62] Molinari, A. and Nouari, M., 2002, "Modeling of tool wear by diffusion in metal cutting," Wear, 252, pp. 135–149.

[63] Luo, X., Cheng, K., Holt, R. and Liu, X., 2005, "Modeling flank wear of carbide tool insert in metal cutting," Wear, 259, pp. 1235–1240.

[64] Sanchez, J.M., Rubio, E., Alvarez, M., Sebastian, M.A. and Marcos, M., 2005, "Microstructural characterization of material adhered over cutting tool in the dry machining of aerospace aluminum alloys," Journal of Materials Processing Technology, 164–165, pp. 911–918.

[65] Liew, W.Y.H. and Ding, X., 2008, "Wear progression of carbide tool in low-speed end milling of stainless steel," Wear, 265, pp. 155–166.

[66] Montgomery, S., Kennedy, D. and O'Dowd, N., 2009, "Analysis of wear models for advanced coated materials," Dublin Institute of Technology.

[67] Li, H.Z., Zeng, H. and Chen, X.Q., 2006, "An experimental study of tool wear and cutting force variation in the end milling of Inconel 718 with coated carbide inserts," Journal of Materials Processing Technology, 180, pp 296–304.

[68] Rao, B., Dandekar, C.R. and Shin, Y.C., 2011, "An experimental and numerical study on the face milling of Ti–6Al–4V alloy: Tool performance and surface integrity," Journal of Materials Processing Technology, 211, pp. 294–304.

[69] Li, B., 2012, "A review of tool wear estimation using theoretical analysis and numerical simulation technologies," Int. Journal of Refractory Metals and Hard Materials, 35, pp. 143–151.

[70] Lee, G.Y., Dharan, C.K.H. and Ritchie, R.O., 2001, "A physically-based abrasive wear model for composite materials," Lawrence Berkeley National Laboratory.

[71] Crosskey, M. and Gutierrez-Miravete, E., "A modeling study of diffusion wear of carbide tools in titanium machining".

[72] Shao, H., Wang, H.L. and Zhao, X.M., 2004, "A cutting power model for tool wear monitoring in milling," International Journal of Machine Tools & Manufacture, 44, pp. 1503–1509.

[73] Wang, Z.G., Wong, Y.S. and Rahman, M., 2005, "High-speed milling of titanium alloys using binderless CBN tools," International Journal of Machine Tools & Manufacture, 45, pp. 105–114.

[74] Bouzakis, K.D., Gerardis, S., Katirtzoglou, G., Makrimallakis, S., Michailidis, N. and Lili, E., 2008, “Increasing tool life by adjusting the milling cutting conditions according to PVD films’ properties,” CIRP Annals - Manufacturing Technology, 57, pp. 105–108.

[75] Xie, L.J., Schmidt, J., Schmidt, C. and Biesinger, F., 2005, “2D FEM estimate of tool wear in turning operation,” Wear, 258, pp. 1479–1490.

[76] Marksberry, P.W. and Jawahir, I.S., 2008, “A comprehensive tool-wear/tool-life performance model in the evaluation of NDM (near dry machining) for sustainable manufacturing,” International Journal of Machine Tools & Manufacture, 48, pp. 878–886.

[77] Fukui, H., Okida, J., Omori, N., Moriguchi, H. and Tsuda, K., 2004, “Cutting performance of DLC coated tools in dry machining aluminum alloys,” Surface & Coatings Technology, 187, pp. 70– 76.

[78] Liu, M., Takagi, J.I. and Tsukuda, A., 2004, “Effect of tool nose radius and tool wear on residual stress distribution in hard turning of bearing steel,” Journal of Materials Processing Technology, 150, pp. 234-241.

[79] Calatoru, V.D., Balazinski, M., Mayer, J.R.R., Paris, H. and L’Esperance G., 2008, “Diffusion wear mechanism during high speed machining of 7475-T7351 aluminum alloy with carbide end mills,” Wear, 265, pp. 1793-1800.

[80] Zhang, S., Li J.F., Deng J.X. and Li Y.S., 2009, “Investigation of diffusion wear during high-speed machining Ti-6Al-4V alloy with straight tungsten carbide tools,” Journal of Advanced Manufacturing Technologies, 44, pp. 17-25.

[81] Sarhan, A., Sayed R., Nassr, A.A. and El-Zahry, R.M., 2001, “Interrelationships between cutting force variation and tool wear in end-milling,” Journal of Materials Processing Technology, 109, pp. 229-235.

[82] Grzesik W., 2008, "Influence of tool wear on surface roughness in hard turning using differently shaped ceramic tools," Wear, 265, pp. 327-335.

[83] Rech, J., Yen T.-C., Schaff M.J., Hamdi H., Altan T. and Bouzakis K.D., 2005, "Influence of cutting edge radius on the wear resistance of PM-HSS milling inserts," Wear, 259, pp. 1168-1176.

[84] Bai W.J., Ke Y.L., Wu H.B. and Dong H.Y., 2009, "Experimental studies of cutting temperature during high-speed milling of aerospace aluminum," Key Engineering Materials, 392-394, pp 719-723.

[85] Guhring, End mill geometry: Helix Angle and Flutes from http://www.guhring.com/ELearning, retrieved in 05.08.2013

[86] Frezy CNC, from http://www.frezycnc.eu/, retrieved in 05.08.2013

[87] R. L. Vaughn, 1966, "Modern Metals Machining Technology," ASME Journal of Engineering for Industry, pp. 65-71.

[88] Dinc, C., 2006, "Analysis of thermal fields in orthogonal machining," MSc Thesis

[89] Mechanisms of wear, from http://www.substech.com/, retrieved in 05.08.2013

[90] Nouari, M., List, G., Girot, F. and Géhin, D., 2005, "Effect of machining parameters and coating on wear mechanisms in dry drilling of aluminum alloys," International Journal of Machine Tools and Manufacture, 45 (12–13), pp. 1436-1442.

[91] Tool wear, from http://www.sandvik.coromant.com, retrieved in 05.08.2013.

[92] Bonny, K., De Baets, P., Vleugels, J., Van der Biest, O., Lauwers, B. and Liu, W., 2009, "EDM machinability and dry sliding friction of WC-Co cemented carbides," Int. J. Manufacturing Research, 4 (4), pp.375–394.

Vita

Nevzat Bircan Buğdaycı completed high school in VKV Koc Lisesi with Inan Kırac Foundation Scholarship, in 2006. He received his B.Sc degree in Mechanical Engineering from Middle East Technical University (METU), Ankara, in 2011. Since 2011, he is in the M.Sc program in Mechanical Engineering at Koç University as a teaching/research assistant. He is expected to join Department of Mechanical and Process Engineering at ETH Zürich to pursue his PhD degree.